Wright, Mick (2024) *On the determination of mass density profiles for gravitational lenses from gravitational wave data*. PhD thesis.

https://theses.gla.ac.uk/84676/

On the Determination of Mass Density Profiles for Gravitational Lenses from Gravitational Wave Data

Mick Wright

Submitted in fulfillment of the requirements for
the Degree of Doctor of Philosophy

School of Physics and Astronomy
College of Science and Engineering
University of Glasgow

August 2024

A corpse…should be left well alone.
Oh, I know very well. How the secrets beckon so sweetly.
Only an honest death will cure you now. Liberate you, from your wild curiosity

Lady Maria of the Astral Clocktower
Bloodborne, Hidetaka Miyazaki

ABSTRACT

With the dawning of the age of gravitational wave astronomy, we are rapdily moving from the detection of a single event being extraordinary by itself to this being much more routine. This has opened the doors to a number of investigative avenues of the phenomena that may be probed using these signals or that affect these signals on their path from their source to us here on Earth.

One of these phenomena is gravitational lensing. This occurs when the signal passes by massive objects en-route, and General Relativity predicts that because massive objects warp spacetime this will change the path of the signal. This occurs in a similar fashion to the bending of light by a lens resulting in the name. This phenomenon has been seen in light for over a century, beginning with the first observations by Arthur Eddington in 1919 but has, as of the end of the third observing run of the current ground-based gravitational wave detector network not been observed.

In this thesis, I first aim to present the necessary foundations of gravitational physics and statistical analysis to understand the theory and analysis of gravitational waves and gravitational lensing thereof, before moving on to the work that I have done throughout the course of this degree to investigate what we may learn from future observations of gravitationally lensed gravitational wave signals.

In particular, I will first discuss the development of GRAVELAMPS—a framework that at inception, was designed to investigate gravitational wave signals to determine if there are any signatures of microlensing—gravitational lensing by small compact objects such as stars or black holes and in the case of such a detection, determine the most likely distribution of the mass of the lens which can tell us a great deal about the object that has served to lens the signal. I detail the design, philosophy, and initial testing done to validate the software.

With the framework available, I will then go on to discuss some of the first deployments of the GRAVELAMPS software on real gravitational wave signals. Specifically these were signals identified by the lensing investigations from the LIGO-Virgo-KAGRA Collaboration collaborations to be interesting—though in all cases these signals had been ultimately determined to be non-lensed upon thorough investigation of the possibility, as well as an interesting candidate from the, at time of writing, currently ongoing fourth observing run which also yields no support for the microlensing hypothesis.

I then turn my attention to the strong lensing regime—that where the lensing object is a galaxy or galactic cluster—to investigate how one may determine the mass density profile of the lens here. In this regime, multiple signals are produced that retain the frequency evolution but differ in magnification, time delay, and an overall phase shift. These signals must be analysed together to yield answers, and I demonstrate a means to acquire this information using the model agnostic outputs of strong lensing detection analyses. I show the demonstrations that this method is both valid and stable, and can be deployed at speed, given that it can be done without the need to re-sample an extended parameter space.

Finally, I turn the discussion to the question of gravity. General Relativity is currently the best theory of gravity available to us, but there have been many proposed alternatives that may result in some deviations from the expectations within it. I show an investigation of the possibility that events that GRAVELAMPS determines to be of interest from the perspective of the microlensing hypothesis could instead be the result of deviations from General Relativity. The conclusion of that investigation is that for certain scenarios—some ruled out by current constraints, others still possible—such a false positive can occur.

Ultimately, this work aims to show some of the development of investigations into not just the question of "*is a gravitational wave signal lensed*" but the question of the lens itself. With the ongoing increases in the sensitivities of the current detector network as well as the on-boarding of other detectors coming in the near future, the detection of gravitational wave lensing is just a matter of time and when it comes we will want to know as much about the lens from that signal as we can and this work aims to assist in ways to acquire that knowledge.

CONTENTS

LIST OF FIGURES

LIST OF TABLES

List of Acronyms

BBH	Binary Black Hole
BH	Black Hole
BNS	Binary Neturon Star
CBC	Compact Binary Coalescence
CE	Cosmic Explorer
CMB	Cosmic Microwave Background
EFE	Einstein Field Equations
EM	Electromagnetic
EMRI	Extreme Mass Ratio Inspiral
EOB	Effective-One-Body
ESA	European Space Agency
ET	Einstein Telescope
GR	General Relativity
GW	Gravitational Wave
HOM	Higher Order Modes
HST	Hubble Space Telescope
IMR	Inspiral, Merger, And Ringdown
ISCO	Innermost Stable Circular Orbit
JWST	James Webb Space Telescope
KAGRA	Kamioka Gravitational Wave Detector
KDE	Kernel Density Estimator
LIGO	Laser Interferometer Graviational Wave Observatory
LISA	Laser Interferometer Space Antenna
LVK	LIGO-Virgo-KAGRA Collaboration

MCMC	Markov Chain Monte Carlo
NASA	National Aeronautics And Space Administration
NFW	Navarro Frenk White
NR	Numerical Relativity
NS	Neutron Star
NSBH	Neutron Star-Black Hole
O1	First Observing Run
O3	Third Observing Run
O4	Fourth Observing Run
O5	Fifth Observing Run
PDF	Probability Density Function
PN	Post-Newtonian
PSD	Power Spectral Density
QNM	Quasinormal Mode
SIE	Singular Isothermal Ellipsoid
SIS	Singular Isothermal Sphere
SMBH	Super-Massive Black Hole
SNR	Signal-To-Noise Ratio
TGR	Testing General Relativity
TT	Transverse-Traceless

CONVENTIONS

The following outlines the conventions that will be used within this work.

Einstein Summation Convention

Where indices appear twice within a tensorial quantity and it is not otherwise specified, this indicates the summation over the possible values of the repeated index, i.e.

$$A^{\alpha}\,\overrightarrow{e_{\alpha}} = \sum_{\alpha} A^{\alpha}\,\overrightarrow{e_{\alpha}}\,.$$

Alphabet of Tensorial Indices

Unless otherwise specified, the usage of the Greek alphabet for Tensorial indices implies four-dimensional quantities specifically with the Latin alphabet being used otherwise.

Derivative Notation

Partial differentiation will be shortened to the use of a ',' with the following index denoting the parameter that the differentiation will be with respect to, e.g.

$$A^{\alpha}{}_{,\beta} := \frac{\partial A^{\alpha}}{\partial x^{\beta}}$$

Covariant differentiation will be shorted to the use of a ';', again, with the following indices denoting the parameters that the differentiation will be with respect to, e.g.

$$A^{\alpha}{}_{;\beta} := A^{\alpha}{}_{,\beta} + A^{\gamma}\Gamma^{\alpha}{}_{\gamma\beta},$$

where $\Gamma^{\gamma}{}_{\alpha\beta}$ denotes the relevant Christoffel symbol (see Section 2.4).

Geometerised Units

Where not directly specified otherwise, it may be assumed that the unit system employed in this work is that of *geometerised units* such that $c = G = 1$.

ACKNOWLEDGMENTS

This work, like any other, is not produced in a vacuum. Whilst it is my name that graces the front and whilst I am the one who typed the words that you see before you, I cannot say that I did so alone, so before we begin our discussions, there are people that I must thank for the support, help, and work that has aided me on the slow journey that has seen me claw my way here.

First and foremost, I must thank my supervisors, Martin Hendry and Graham Woan. Had they not agreed to supervise me as an initially unfunded student paying my way through the degree working in a Starbucks, I would not have made it through. Their support through the years has been steadfast and generous and I cannot thank you both enough for it. I hope that looking upon this work that you feel that effort was worth it.

As is detailed in the relevant Chapters, I have had a number of coauthors on many a joint piece of work in the past four years, and I issue my thanks to them all. In particular, I'd like to highlight Nathan K. Johnson-McDaniel, whose scripts formed part of the basis of the beautiful waveform plots that are in Chapter 9 for non-GR waveforms, as well, I'd also like to thank Otto A. Hannuksela who has always been an excellent person to work with and who welcomed me into the gravitational wave lensing community. Additionally, Chris van den Broeck who has taken the brave decision to allow me to continue my work on to my next chapter, I will be eternally grateful for that.

Next, I want to turn to thank the rest of the IGR within the University of Glasgow. No matter that I was frequently a departmental ghost joining meetings from my home away from campus, you have always made me feel welcome and connected to the rest of you and I thank you for that. It would have been very easy to have isolated away and become disconnected and I have never felt that way.

As much of this work features the GRAVELAMPS software, I want to issue my thanks to my main co-developers over the years, Eungwang Seo, Ania Liu, and Isaac Wong. Each of you has made an incredible contribution to it and I thank each of you for it. As I go on from this point and continue with its development, I will continue to always put each of you forward for the work that you have done on it. Particularly to Ania and Isaac, both of you could easily have made your own software and I particularly thank you for choosing to merge with our work in true communal spirit. I also wish to thank all of those developers who have worked on the pieces of software I have used to make GRAVELAMPS what it is—in particular, I thank Fredrik Johansson, a man I have never met, but whose work has made my own possible and the developers of BILBY.

Turning my attention a little further out professionally, I want to send my thanks to Laura Uronen, currently of CUHK. Whilst you are one of my newer friends, in these last few weeks and months you have provided one of a few needed sources of constant laughter and banter as I have worked to draft this thesis.

Finally, of my professional collaborators, I must thank my most frequent collaborator and dear friend, Justin Janquart. Whether I need someone to bounce an idea off of, to vent my frustrations, to joke around and slack off with, or anything, you have been and are always there to be both a colleague and as I say, dear friend. So thank you. And know that I will never, ever admit that again, so enjoy it.

Continuing on those who have always been there as close friends in this journey, I must mention Fiona Porter and particularly thank her for getting a poster for a conference in a blinding rush—I would not have been able to do it without you. For that, and so many other things over the years, thank you.

No list of my friends will ever be complete without Christopher "Kristoff" Duffy. My dear and beloved friend, I could probably write something the length of this thesis to thank you for being the best of friends. Between our long discussions be they our attempts at professional discourse or the time we 'solved Scottish politics' like the nerds we are, I can think of no one who would support me more in this journey.

Finally, I turn next to my family who have supported me far more than they should and without whom I literally would have been unable to do this—in my unfunded first year, my grandparents kindly stepped up and gave me my tuition. They've kept me going even at the very start of this journey when, being candid with you reader, I easily could have given up. Here we are at the end, when I will be moving out not just to another city but to another country, and it really is all because of them. I do not thank you enough, but here it is, in black and white in a place I cannot edit later. So you'll always know.

DECLARATION

The material herein was written by the author under the supervision of Professors Martin Hendry and Graham Woan in the University of Glasgow. All chapters of this thesis were written with some editorial input from Professor Martin Hendry. It has not been submitted for any other degree at the University of Glasgow, or at any other institution. Parts of this work were carried out in conjunction with other authors which have been listed in the relevant sections.

Each of the Chapters, beginning with Chapter 6 and concluding with Chapter 9 contain material in part from papers that have been or are in the process of being published in peer-reviewed journals. The paper(s) and journal in question have been noted at the beginning of each chapter.

Chapter 9 contains plots of non-General Relativity (GR) waveforms that were constructed using a plotting script written originally by Nathan K. Johnson-McDaniel. All other plots that are not attributed were generated using scripts written by the author personally.

1

Development of Gravitational Theory

> *If you wish to make an apple pie from scratch, you must first invent the universe*
>
> —Carl Sagan

Should you drop it, this thesis will fall down. It is not alone in that regard, many things will. The question we are concerned with is "*why* does it fall down" and the answer that we provide is *gravity*. Currently gravity is best described by Albert Einstein's theory of GR which describes all mass as existing within a four-dimensional space-time which is deformed into having curvature by the presence of that mass. That curvature determines how masses move, trying to reach the lowest point that they can and so small masses will fall towards larger ones. Currently this is the best description of gravity, the latest development from that which came before. We will therefore, begin with an exploration of the development of gravity—how we got here, and where we might go from here.

The development of the question of gravity has always been intertwined with the development of our view of the universe around us. In particular, the development of our understanding of the night sky, of the other planets in the Solar System, through to our current understanding of the large scale structure and history of the universe. As a result, the following discussion will also explore the development of cosmology contemporaneous to developments in attempts to describe gravity, in particular, how the former drive the latter.

The first recorded attempts to describe gravity were that of the Ancient Greeks. The first of these was that of Aristotle. In his view, outlined in his *Physics* (Aristotle, 1930b), all terrestrial things were comprised of a combination of the four elements of water, earth, fire, and air. A fifth element, aether, was the medium in which celestial bodies were held. He would go on in his work, *On the Heavens* (Aristotle, 1930a) to outline that to him, the celestial bodies, as well the Earth itself were stratified into a series of concentric celestial spheres, with the Earth sphere at the core—a depiction of this model is shown in Figure 1.1. Aristotelian gravity holds that the heavy elements of earth and water naturally tend towards this centre and thus cause objects to fall whereas the lighter elements of fire and air naturally tend to rise towards the next highest sphere—the Moon. In this model of gravity, objects should fall with a speed proportional to their weight, i.e. heavier objects should fall faster than lighter ones.

The celestial sphere model would be codified into predictions of the movement of the stars and planetary bodies in the night sky by Claudius Ptolemy in his Almagest (also known as the *Syntaxis Mathematica* Ptolemy, 1984). In this, the central Earth does not move with the fixed stars and mov-

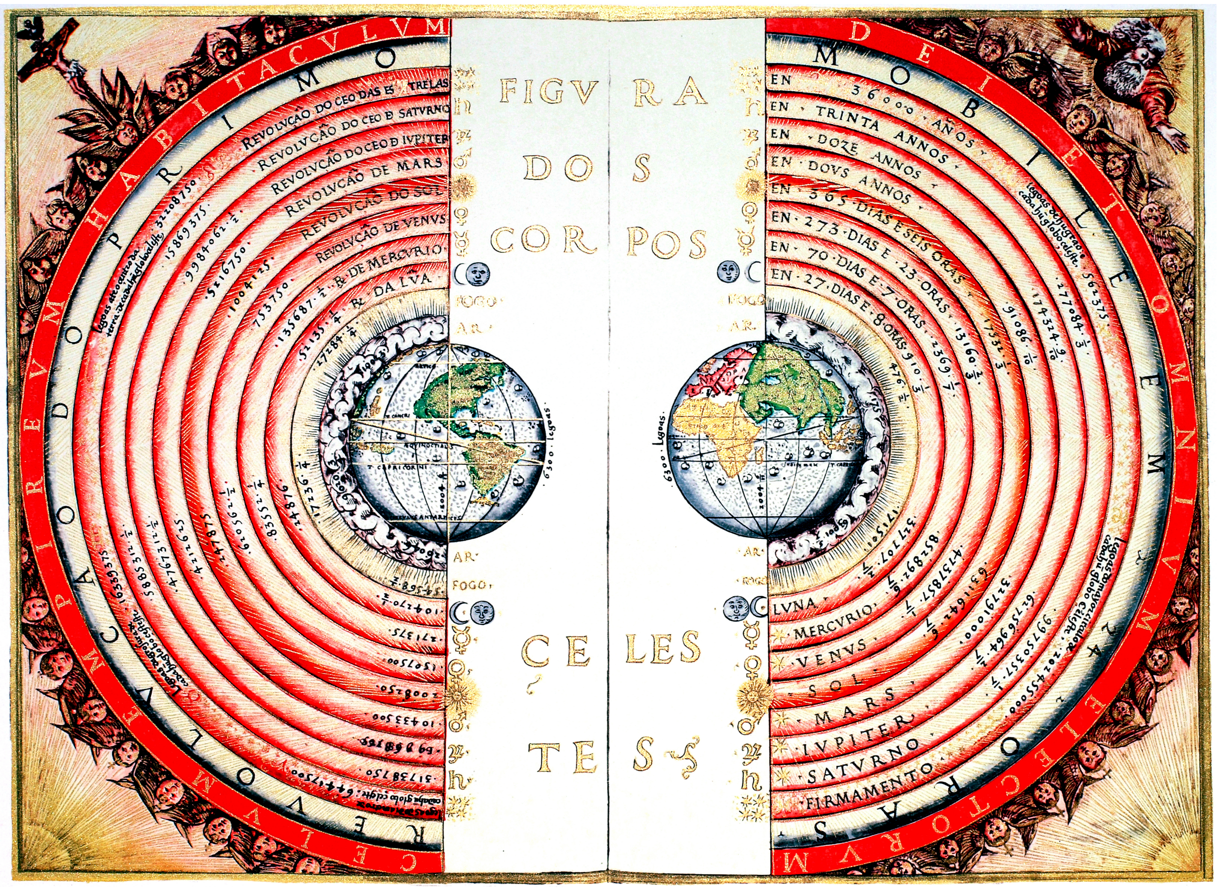

Figure 1.1: A depiction of the celestial sphere model by Bartolomeu Velho (Velho, 1568). The Earth is depicted at the centre of a series of concentric spheres containing the other bodies in the Solar system, then the fixed stars, then the Primum Mobile ("first movable") which caused the movement of stars, the day-night cycle, etc. Finally at the outermost sphere is the Empyrean—the place in which the Divine reside.

ing planetary bodies in their respective spheres. In order to explain the apparent backtracking in the night sky performed by the planetary bodies that seemed to suggest that they did not smoothly rotate around the Earth as the fixed stars seemed to, epicycles were introduced. The inclusion of these epicycles allowed the Ptolemaic model to predict the movements of bodies in the night sky with far greater accuracy than other theories at the time but did introduce significant complexity to the modelling. A depiction of this complexity is shown in Figure 1.2 which shows the paths of Mercury and Venus using an epicyclical model.

The combination of Aristotelian gravity and the Ptolemaic epicyclical model of the motion of the bodies in the night sky would be the prevailing beliefs for over a thousand years, though alternative thoughts were expressed during this period. For instance, Aristarchus of Samos proposed the first known heliocentric model which would be further developed by Seleucus of Seleucia. However, these proposals failed to sufficiently move the general view of the universe.

Heliocentrism would be revived by the publishing of *De revolutionibus orbium coelstium* or *On the Revolutions of the Heavenly Spheres* by Nicolaus Copernicus in 1543 (Copernicus, 1543) which placed

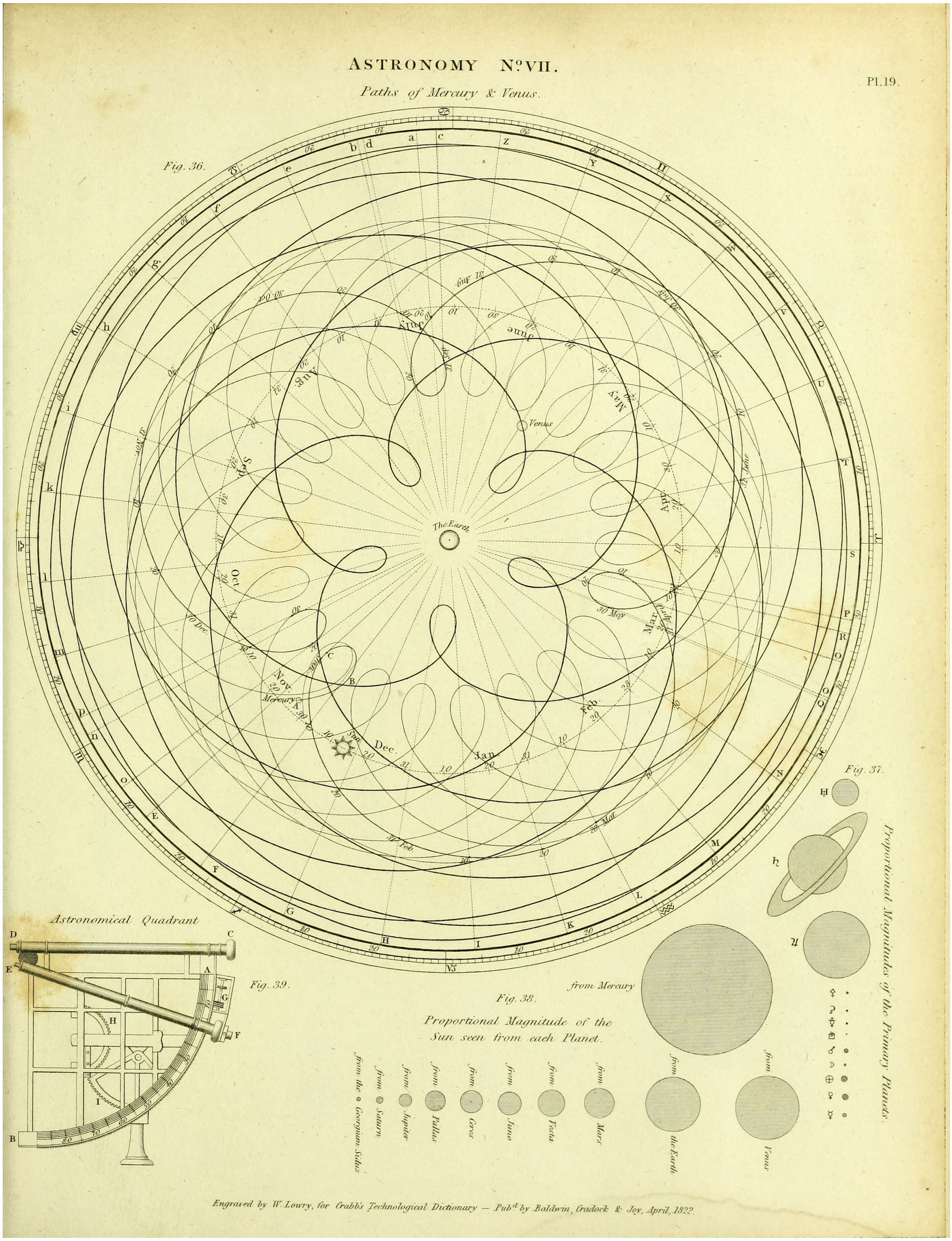

Figure 1.2: A depiction of the paths of Mercury and Venus using the epicyclical model used in Ptolemaic belief from the Universal Technical Dictionary by George Crabb (Crabb, 1843)

the Earth as the third planet out from the central Sun. The decades that followed would also produce the disproving of the Aristotelian belief that objects should fall at a speed proportional to their mass. The most famous demonstration of this are the fabled experiments of Galileo Galilei, in which he would determine that objects fall with the same *acceleration* (Galilei, 1954). He would also uncover the existence of the four Galilean Moons of Jupiter; Io, Europa, Callisto, and Ganymede. That these objects were definitively orbiting Jupiter rather than the Earth would put further evidence against the geocentric model of the Universe. He would also observe the phases of Venus, direct evidence for the planets orbiting the Sun.

Johannes Kepler would then develop his laws governing planetary motion which would provide a mathematical framework for the movement of objects in the Copernican model. These laws would suggest that the motion of the planets are elliptical with the Sun as one of the foci of the orbit. This would continue to explain the observed motion from Earth without the need for the complexity of the epicyclical model (Kepler, 1609, 1619). At the time, the Laws were empirically constructed by they would not remain so.

The next major theory of gravitation would be published on the 5th July 1687 in the *Philosophiæ Naturalis Principia Mathematica* or *the Mathematical Principles of Natural Philosophy* by Isaac Newton. In Newtonian gravity, all mass is responsible for gravity because it exerts a force which attracts all other mass with a strength inversely proportional to the separation between them. This force would act instantaneously in response to changes in the system. In addition to this universal law of gravitation, Newton also proposed his three laws of motion, and in combination the laws of motion and gravitation would result directly in the Keplerian laws of planetary motion, further solidifying these as a development of our understanding of the universe (Newton, 1972).

Next to change, was the model of the celestial spheres. Whilst the Copernican model had started a shift from the models of Aristotle, by removing the Primum Mobile and Empyrean, the planetary spheres and that of stars remained. By the introduction of the Keplerian laws, the planetary spheres would be placed at specific and different distances to each other, though the stellar sphere remained. This would change over time with improvements in understanding of the Milky Way. Galileo had shown that the Milky Way contained a vast number of faint stars, and in 1750 Thomas Wright would speculate that it was in fact a singular rotating system held together by gravitational forces much as the Solar System is, but on a significantly larger scale. He would also suggest that some of the nebulae were in fact not part of the Milky Way (Wright, 1750); these would be termed 'Island Universes' by Immanuel Kant when he expanded upon Wright's work in 1755 with his *Allgemeine Naturgeschichte und Theorie des Himmels* or *Universal Natural history and Theory of the Heavens* (Kant, 1981), though it would prove an unpopular view at the time.

The shift from a Milky-Way only view to that of multiple galaxies would not occur fully until the 1920s. Firstly, the work of Harlow Shapely would imply that the Sun was not in the centre of the Milky Way using the distances of globular clusters to instead estimate that the centre of the Milky Way was in the direction of the constellation Sagittarius (Shapley, 1919). Edwin Hubble would go on to show that Andromeda is outside of the Milky Way, and the picture of the universe shifted to that of many galaxies (Hubble, 1929b). His work would also show that the universe is expanding and that the Milky Way does not occupy a special place within the universe (Hubble, 1929a)—in fact that the expansion of the universe does not have a well-defined centre.

Over much of this period, Newtonian gravity had held sway as the dominant explanation for the force of gravity. However, some developments would occur that would suggest that this view was incomplete. In particular, the development of the theory of electromagnetism and specifically the Maxwell Equations would seem to be at odds with Newtonian mechanics. The development of electromagnetism would lead to the failure of the Michelson-Morley experiment to detect the lumniferous æther—the medium in which light had been believed to propagate through the universe (Michelson & Morley, 1887). A new alternative explanation would be arrived at by Albert Einstein in his 1905 work *Zur Elektrodynamik bewegter Körper* or *On the Electrodynamics of Moving Bodies* which would lay out the framework of Special Relativity in which the speed of light is fixed for inertial reference frames and that the laws of physics are invariant in these frames (Einstein, 1905).

A decade after the introduction of Special Relativity, in 1915, Einstein would revolutionise gravitational theory by publishing his general theory of relativity, GR. No longer was the attraction between masses something that was innate and instantaneous. Mass would now cause a curvature of space-time and this curvature would be responsible for gravitationally-based movement. This force would propagate at the speed of light, c. Importantly, in the cases of weak gravitational fields that are not moving at speeds where relativistic effects would become important, GR would simplify to the Newtonian case—providing both an explanation for why Newtonian gravity had been so successful up until that point whilst giving a framework to address those areas where Newtonian gravity had been unable to provide answers (Einstein, 1915a,b,c,d).

To become the most successful theory of gravity to-date, GR has been and still is subject to a number of both laboratory and astrophysical tests. Four of these, in particular, called the Four Classical Tests of General Relativity, showed some of the initial major successes of the theory and will be discussed below to illustrate some of the testing that has been done on GR.

The first of these tests was to explain the perihelion precession of the orbit of Mercury. The elliptical orbits that the planets trace around the Sun had been well described, and in the case of all of the other planets, their perihelion precession had been accounted for, largely by the presence of the other planets—in fact, observations of this phenomena in Uranus had successfully lead to the discovery of Neptune. However, Mercury had been observed to have an anomalous precession, and there had been no evidence of a proposed even more interior planet, named Vulcan. GR was able to explain this anomalous precession without the need for another planet, and importantly provided a theoretical basis for the discrepancy between the observed anomaly and the Newtonian prediction. An outline of this was provided by Einstein directly in his 1915 work, *Explanation of the Perihelion Motion of Mercury from General Relativity Theory* (Einstein, 1915c).

The next of these tests was the gravitational deflection of light passing by massive objects. Within the framework of Newtonian gravity it had been predicted, by Johann Georg von Soldner in 1804, that light would be deflected when passing by massive objects (von Soldner, 1804). This prediction would go largely ignored, however, as theories of light as a wave had taken root. In 1911, Einstein would predict the same result (Einstein, 1911) but in 1915 would correct his prediction to double that of the Newtonian result due to the curvature of space-time near the massive object compared with that far away from it. This would give a testable prediction, and in 1919 the Eddington experiment would be undertaken. In this, pictures were taken of the Sun and the surrounding star field during a total solar eclipse. These could be compared with pictures of the same star field when the Sun was not nearby it, in order to detect the difference between them. This experiment would ultimately find in favour of the Einsteinian prediction rather than the Newtonian (Dyson et al., 1920).

The third, and final of the originally proposed tests was verification of the prediction of *gravitational redshift*. Einstein predicted that light travelling out of a gravitational well should appear to lose energy, corresponding to an increase in wavelength (i.e. a *redshift*) (Einstein, 1908). Conversely, light travelling into a gravitational well should appear to gain it, corresponding to a decrease in wavelength (i.e. *blueshift*). This would be verified in a number of tests both experimentally and in laboratory, in particular, one example of this would be the Pound-Rebka experiment of 1959, in which the energy of gamma ray photons was examined at the bottom and top of a 22.5m (74 ft) tower which showed evidence of this wavelength shifting (Pound & Rebka, 1960). A depiction of the experimental setup for the Pound-Rebka experiment is shown in Figure 1.3.

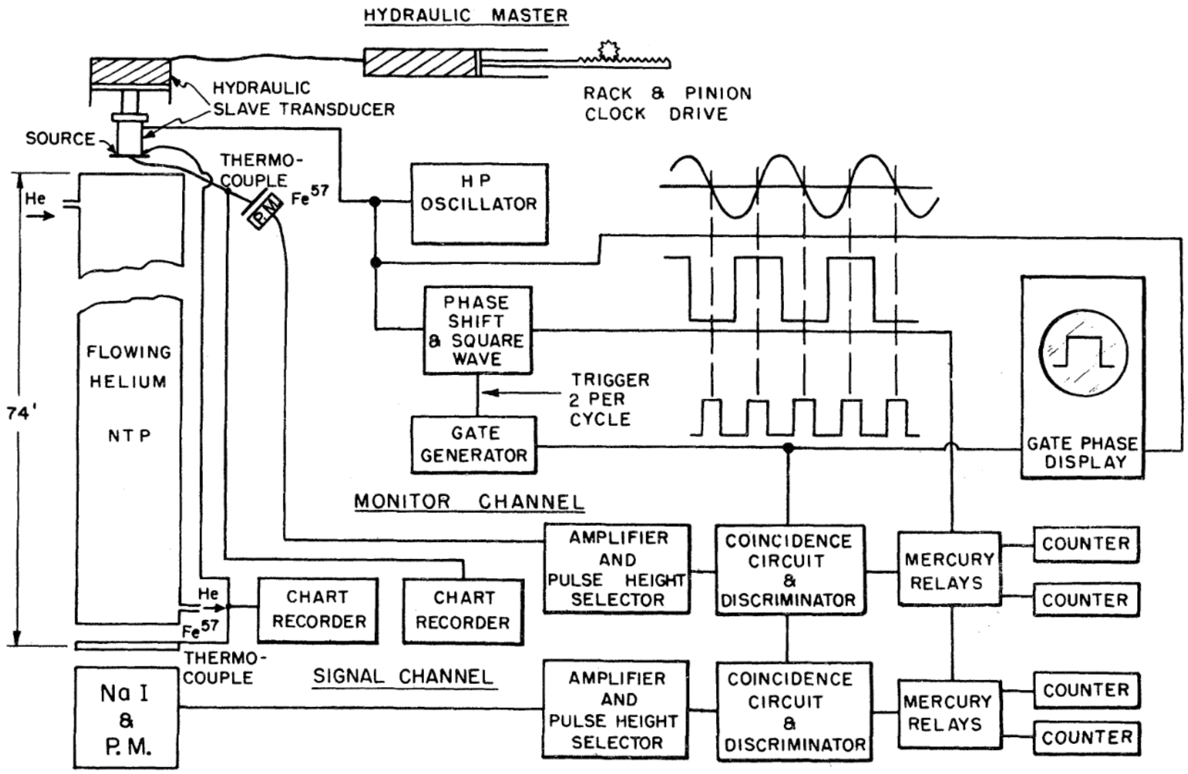

Figure 1.3: Depiction of the layout of the 1959 Pound-Rebka experiment to investigate gravitational redshift. Taken from Pound & Rebka (1960).

A fourth Classical Test of General Relativity was proposed by Irwin Shapiro in his 1964 work, *A Fourth Test of General Relativity*. GR predicts the phenomenon of gravitational time dilation. This time-dilation will cause a signal passing by a massive object to take longer than it would were that object not there. Shapiro proposed testing the delay on signals to Mercury and Venus and calculated that the time delays should be increased by $\sim 2 \times 10^{-4}$s under the assumption of GR (Shapiro, 1964). This experiment would be performed between 1966 and 1967 and the observed time-delay (now known as Shapiro delay) would be found to be compatible with the GR prediction (Shapiro et al., 1968).

Since the initial performance of these tests discussed here, each has been repeatedly retested and each has been found to be more and more consistent with the predictions of GR. These tests have also been joined by a host of other tests, all of which GR has passed and so, as stated at the beginning, it has been and remains the current best description of gravitation at the time of writing (Will, 2014; Berti et al., 2015). The ubiquity of GR's successes may now be seen in many images of the night sky with the phenomenon of *gravitational lensing*—the general phenomenon responsible for the second Classical Test. From that first detection in 1919, it is now a frequent sight in astronomical images, for instance, in the first revealed image from the JWST shown in Figure 1.4.

One of the other major successes of GR has been to provide a secondary means of looking out into the universe through the prediction of gravitational waves (GWs). These were first predicted by Einstein in 1916 (Einstein, 1916), but the road to observation would be a long one. Einstein had predicted that the acceleration of massive objects by gravity would allow for the production of gravitational radiation and in particular asymmetric motion, but he did not believe that detection would ever be possible due to the extremely small amplitude of the waves under all but the most cataclysmic of events.

The first major step towards the observation of gravitational waves would be finding a sufficiently compact object that an inspiralling binary of these might produce a loud enough signal. This step would be filled by the finding of evidence for the existence of black holes (BHs)—remnants of dead stars that are so dense not even light may escape them. This evidence would be found in X-ray observations and the discovery of Cygnus X-1 at the end of the 1960s and beginning of the 1970s which was found to most likely be a black hole (Brucato & Kristian, 1973; Shipman, 1975). In addition to black holes, there exist other very dense compact objects, in particular neutron stars (NSs) which are the product of the collapse of stars.

It should be noted that during this time, the first gravitational wave detectors were built by Joseph Weber. Initially, these consisted of large masses that could have vibrations induced by gravitational waves. He would then go on to design the Weber Bar—large aluminium bars that gravitational waves would again incite vibrations of. However, neither of these would yield a confident detection.

The search for gravitational waves would receive its first success by an indirect manner in 1974 when Russell Hulse and Joseph Taylor would discover what is now known as the Hulse-Taylor pulsar—a rapidly spinning neutron star that emits a jet of radiation from its magnetic poles that may be detected should the rotation of the neutron star point that jet towards the Earth (Hulse & Taylor, 1975). This particular pulsar was found to be in a binary with another neutron star and in particular was found to

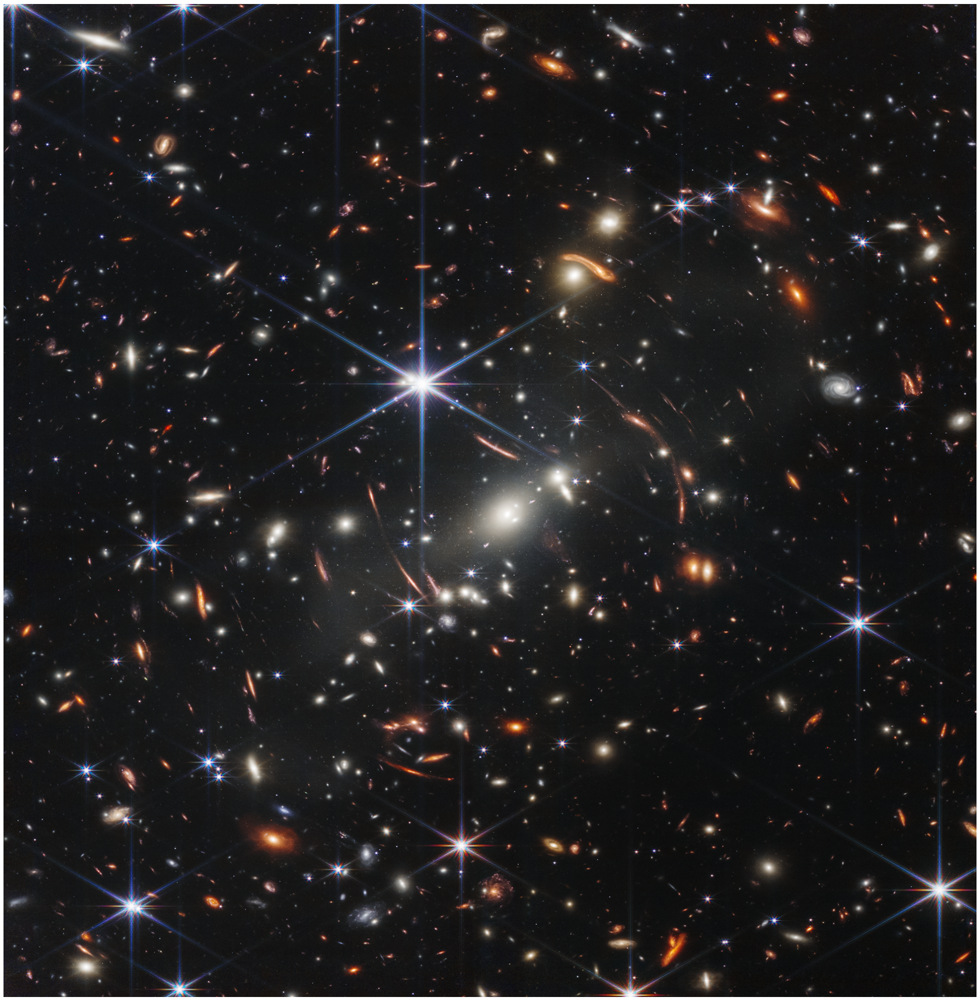

Figure 1.4: One of the first released images from the James Webb Space Telescope (JWST) specifically a deep field from the NIRCam instrument. Many of the galaxies that can be seen are smeared into arcs due to the effects of gravitational lensing. Image Credit: NASA/STSci

have a decaying orbit. This decay matches extremely well with the predictions of GR accounting for the emission of gravitational waves (Taylor & Weisberg, 1982).

The path to a direct detection of gravitational waves would require a return to an experiment that we have already touched on, albeit very briefly—the Michelson-Morley experiment. To give more detail on the nature of that experiment, as stated above it was designed to detect the presence of the lumniferous æther. It was believed at the time that this medium was ever-present in order to allow light to propagate through vacuum and therefore the motion of the Earth was motion through this medium and would introduce a slight difference in the time for light to travel in different directions. To detect this, Michelson and Morley constructed what is now known as a Michelson-Morley interferometer. Fundamentally, and at its most simple, this will consist of a light source, a beam-splitter, two mirrors, and a detector. The light source will shine a beam on to the beam-splitter to create two phase-aligned beams travelling in perpendicular directions with mirrors placed at the end of the beam paths directing the beams back towards the splitter, where they will be recombined and directed towards the detector, because both the length of the paths travelled and the fact that the beams were originally phase-aligned, this would allow any difference in the path length to be noted by examination of the interference pattern of the beams at the detector (Michelson & Morley, 1887).

To move from a detection of the lumnifeous æther to gravitational waves is merely a change of thought in the nature of the experiment. Rather than a medium causing a difference in the travel time between the two beams, instead a gravitational wave passing through the detector would cause the spacetime within the arms to be stretched and squeezed in differing amounts, meaning that the path lengths would alter and thus the interference pattern should change. The difficulty of the detection of this phenomenon, however, lies in the rigidity of spacetime which means that these changes are miniscule.

To detect gravitational waves using this method, gravitational wave observatories were built with significant upgrades compared with the simple outline of a Michelson-Morley interferometer given here. For example, the Laser Interferometer Graviational Wave Observatory (LIGO) detector uses power-boosted lasers injected into Fabry-Pérot cavities which artificially extend the length of the arms from 4km to over 1200km. This is not the only improvement that has been made in comparison with the original Michelson-Morley equipment; indeed a vast number of improvements have been made to achieve the necessary sensitivity (Aasi et al., 2015). This will be discussed in detail in Chapter 4.

The culmination of this effort would come on the 15th September 2014 when the two Advanced LIGO detectors—at Hanford and Livingston—would detect the signal GW150914 (Abbott et al., 2016a). This first direct detection of gravitational waves comes from a compact binary coalescence (CBC)—the inspiral and merger of two compact objects, in this case a binary black hole (BBH). This represented both the reward for a century of effort from the initial suggestion of gravitational waves as well as the opening of a brand new way of looking at the universe different from our electromagnetic (EM) observations.

Additional detections of gravitational wave events have taken place since, with two particular events of note being GW170817 which was the first detection of a binary neturon star (BNS) (Abbott et al., 2017b) and GW200105 which was the first detection of a neutron star-black hole (NSBH) binary (Abbott et al., 2021b). GW170817 was also important as, in the case of BNSs, we can also expect emission of EM radiation. The GW detector network—consisting of the two aforementioned detectors as well as the Virgo detector (Acernese et al., 2014)–as able to in this case given sufficient localisation information that EM astronomers were able to find co-incident events in all bands marking the first so called multi-messenger astronomical event and confirmation that the detection of gravitational waves are true detections (Abbott et al., 2017c). This multi-messenger event would be a primary driver of some of the first gravitational wave-based measurements of the expansion rate of the universe (Abbott et al., 2017a; Abbott et al., 2021a).

In the intervening years since the first detection, more and more gravitational waves events have been detected by the current ground-based detector network. At the publication of the most recent catalog of events by the LIGO-Virgo-KAGRA Collaboration (LVK) which covered until the end of the third observing run (O3) contained 90 candidates believed to have a probability of astrophysical origin greater than 50% (Abbott et al., 2023a). At time of writing, the O4 is underway and therefore this number will only increase.

As more and more detections occur, the detections themselves have moved from exceptional in their own right to routine and the focus is shifting to what more information can be gleaned from gravitational waves. One example of this already mentioned has been cosmological analysis and in particular estimation of the expansion rate of the universe, quantified in the Hubble constant, H_0 (Abbott et al., 2021a, 2023b). Another such example is investigation of the population of black holes and neutron stars (Abbott et al., 2019d, 2021c, 2023c). A third example that follows the themes of this chapter, however, is that gravitational waves offer a chance to test GR in the domain of strong gravitational fields—something that no laboratory may replicate allowing us to further hone in on how gravity works to continue answering the question of precisely *why* things fall (Abbott et al., 2016b, 2019e,f, 2021d,e).

The number of events detected will also continue to rise beyond the end of O4. In the short term, there will be the fifth observing run (O5) of the current detector network, but the network itself will expand over time. These include ground-based detectors such as the Kamioka Gravitational Wave Detector (KAGRA) (Akutsu et al., 2020), the LIGO-India Project (Iyer et al., 2011), the European Einstein Telescope (ET) (Punturo et al., 2010), and the American Cosmic Explorer (CE) (Reitze et al., 2019). Each of these will improve the sensitivity of the current ground-based detector network and in the particular cases of the latter two proposed detectors significantly improve the range that we expect to see GW events to which will allow improved investigation of all of the examples mentioned above as well as other developments in both GW and multi-messenger astornomy. The expansion of the network will also include space-based observatories such as the Laser Interferometer Space Antenna (LISA) (Babak et al., 2021), which has been adopted by European Space Agency (ESA) or the proposed Chinese detector TianQin (Luo et al., 2016). Expansion into space based detectors will allow access to a different frequencies from ground-based detectors, particularly below 1Hz, expanding the kinds of events we expect to see to include extreme mass ratio inspirals (EMRIs) and super-massive black holes (SMBHs) mergers.

With the successes of GR and the current developments in GW astronomy, it is worth bearing in mind that there remain a number of open questions both in gravitation and cosmology. GR whilst our best theory at present, may not remain so indefinitely. For instance, GR is a purely classical, geometric theory of gravity which cannot be fully reconciled with the developments of quantum mechanics and quantum field theory which have successfully unified the other three fundamental forces of nature into a combined quantised framework. In cosmology—developments in which, as have been shown, often spur developments in gravitational theory—there remain the questions over the nature of dark matter and dark energy and such grandiose questions as the ultimate fate of the universe. Gravitational waves may help in the developments of both fields in conjunction with our ongoing EM observations and experiments.

This thesis, however, will focus on one aspect of gravitation. In particular, it will focus on gravitational lensing. Whilst it has become a very commonplace observation in EM observations, it is not in principle restricted only to them and should affect gravitational wave signals as well. As of the end of the third observing run it has yet to be observed by the current ground-based detector network (Hannuksela et al., 2019; Abbott et al., 2021f, 2023d; Janquart et al., 2023b), however, with the improving sensitivities of the network as well as simply the increasing number of events it is probable that such a detection will occur relatively soon. This thesis will largely concern itself with the question of, should we detect a lensed GW signal, can we identify the nature of the massive object that has caused the lensing. In so doing, we may better understand the nature of many objects within the night sky and may shed some light on the question of dark matter.

This thesis comprises ten chapters, and the remaining are laid out as follows. Chapter 2 will elaborate on the principles of GR to lay the foundations of the work to come. Chapter 3 will give a brief introduction to probability and to Bayesian analysis setting the scene for the quantitative language that we use in the later analyses. Chapter 4 will build upon Chapter 2 by giving the basics of gravitational waves under the auspices of GR. Chapter 5 will close out our laying of the theoretical foundations of the work by discussing the formalism of gravitational lensing.

In the second part of the thesis, we move to the work that has been performed. We begin with Chapter 6 introducing the package that serves as the spine for the remainder of the work—GRAVELAMPS, which is designed to answer the question of what we can learn about a lensed signal. Chapter 7 shows this in action, discussing the first deployments of the GRAVELAMPS framework upon real events—specifically some candidate events from O3 and O4 that may have been interesting from the lensing persepective—though all are ultimately discarded. Chapter 8 then expands the reach of GRAVELAMPS from its original starting point in the microlensing regime to the strong lensing regime incorporating a methodology for analysing multiple images. Chapter 9 then carries us forwards into the alternate theories of gravity by examination of how deviations from GR would impact the GRAVELAMPS investigations, and we will finally give a brief conclusion and summary of some potential open threads in Chapter 10.

PART I

ASTROPHYSICAL AND MATHEMATICAL FOUNDATIONS

2

General Relativity

> *Have you ever questioned the nature of your reality?*
>
> —Bernard Lowe, *Westworld*
>
> Created for HBO by Jonathan Nolan and Lisa Joy

General Relativity is a *geometric* theory of gravity, so to begin to describe it we must first give a description of the mathematical objects used in the construction of geometry. The simplest mathematical object for geometry is a scalar. Scalars are quantities that are completely described by a single number i.e. the *magnitude* of that quantity. A prime example of a scalar quantity for gravitational consideration would be mass. However, the theory of gravity requires more than just magnitude and must also include direction such as velocity.

The following discussion draws inspiration from the following works which are recommended for their more detailed discussions of the topic:

- A First Course in General Relativity by Bernard Schutz (2009).
- Spacetime and Geometry: An Introduction to General Relativity by Sean Carroll (2013).
- Gravitation by Charles W. Misner, Kip S. Thorne, and John Archibald Wheeler (2017).

2.1 Vector Spaces

Quantities that also require direction may be described by *vectors*. Vectors are the next simplest example of a mathematical object used in geometry and are a typical exmaple of the wider category of object. This category of object is called a *vector space*. Objects within this category are constructed to contain the following properties:

Closure:	The addition and multiplication operations between two elements comprising the vector space must result in another element of the vector space.
Commutativity of Addition:	The result of addition between two objects in the vector space does not depend on the order of the addition, i.e. $$X + Y = Y + X$$

Inverse of Addition: For each element of the vector space, there must exist another element such that the addition of these two elements yields the identity, i.e.

$$\mathbf{X} + -\mathbf{X} = 0$$

Compatibility with Scalar Multiplication: The result of multiplication of an element of the vector space with any scalar value must be another element vector space.

Distributivity of Scalar Multiplication The result of a combination of the scalar multiplication and addition operations does not depend on the order of application of those operations, i.e.

$$\begin{aligned} a(\mathbf{X} + \mathbf{Y}) &= a\mathbf{X} + a\mathbf{Y} \\ (a + b)\mathbf{X} &= a\mathbf{X} + b\mathbf{X} \end{aligned}$$

Identity: For each of the addition and scalar multiplication operations there must exist an element of the vector space called the identity such that operating on another element with the identity will return the element, i.e.

$$\begin{aligned} \mathbf{X} + 0 &= \mathbf{X} \\ 1\mathbf{X} &= \mathbf{X} \end{aligned}$$

In addition to the standard vector, GR also uses a similar vector space object called a one-form (also known as a covector or covariant vector). These objects are a mapping from vectors to scalars. They are represented in a similar manner to vectors but perpendicularly. An overly simple way of viewing them may be to consider column vectors and row vectors as representing 'vectors' and 'one-forms'.

To visualise them more geometrically, vectors are often drawn as arrows in a space with the length indicating the magnitude. One-forms may be drawn in that same space as a series of parallel planes with the distance between them representing the magnitude—such as a gradient map or an air pressure map—as shown in Figure 2.1.

This visualisation may also give some intuition on the resultant scalar that the one-form maps the vector to. For instance, if one were to consider a topographical map which shows contours of constant elevation by applying a vector to that map, one could see the steepness between the two points at the ends of the vector by the number of those contours that are passed through. This is a direct example of the fact that the gradient is a one-form.

However, even these three object types are not sufficient to fully describe the geometry within GR. For this, we introduce the more general class of object that vectors and one-forms form the basis of—the tensor. Tensors are a function, linear in its arguments, that map a number of vectors and one-forms to a scalar. Specifically, each tensor is given a rank, $\binom{M}{N}$, which indicates that this tensor will map M one-forms and N vectors to a scalar. This notation makes clear that both vectors and one-forms are

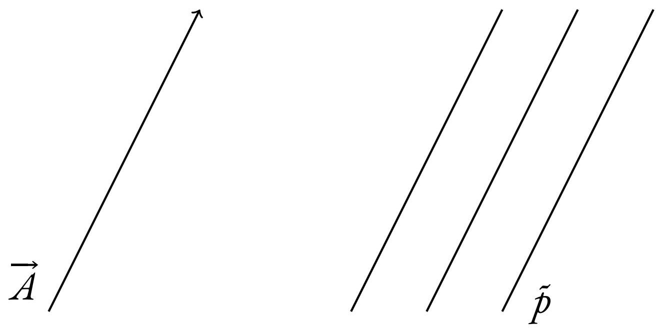

Figure 2.1: Depiction of a vector, $\vec{A}$, and a one-form, $\tilde{p}$. A vector is visualised in terms of an arrow with a direction and length specifying magnitude. A one-form is visualised a series of parallel planes with the spacing indicating the magnitude.

specific kinds of tensor, i.e. the rank $\binom{0}{1}$ and $\binom{1}{0}$ tensors respectively. Scalars may also be interpreted in tensorial notation as rank $\binom{0}{0}$ tensors. As will be discussed in more detail later, an example of a quantity that requires tensorial description would be curvature.

2.2 Manifolds

In the previous section, we have defined a number of objects capable of defining quantities in a space. We have not, however, defined an object that represents the space itself. This is done by introducing the concept of a *manifold*—a set of points that may for each point be described in terms of a specific number of parameters. The number of parameters needed to describe the manifold is called the *dimensionality* of that manifold. The most intuitive manifold is that of Euclidean space, i.e. the way that most of us consider the geometry around us—a flat space that may be described in terms of length, breadth, and height. More generally manifolds must look like Euclidean space locally but may globally be very different. An example of this would be the surface of the Earth. At human scales the curvature of the Earth is not noticeable so one may think in Euclidean terms but at a global scale the curvature may not be ignored.

Formally, an n-dimensional manifold allows the definition of a set of functions $\{x_1, ..., x_n\}$ called a chart that maps to a set of n scalars. This is the formal definition of a co-ordinate system for this manifold. A path in the space described by this manifold may be described in terms of a curve, $\lambda(t)$, that maps from the manifold to this path. This may be combined with the co-ordinate system to create the set of functions, $\{x^1(\lambda(t)), ..., x^n(\lambda(t))\}$, that describe the path in the defined co-ordinate system.

For the space-times used to describe GR, we may restrict ourselves to a subset of manifolds called *differentiable manifolds* which means that on small scales, it is possible to define a mapping to Euclidean space such that derivatives of functions on a point are preserved. This allows for the definition of local, but importantly not necessarily global, co-ordinate systems. This raises an important complication in manifolds—the lack of a global co-ordinate system complicates questions such as direction over large distances.

To illustrate such a complexity, we look at the concept of parallel transport. Given that two different points on the manifold may have differing co-ordinate systems, how could we determine whether or not two given paths are parallel. Our restriction to differentiable manifolds as we have said allows us to define local co-ordinate systems. So a vector at a point may be moved slightly whilst remaining parallel to its original position. This may be repeated to move a vector from a point A to a point B in a process called *parallel transport*. An illustration of this is shown in Figure 2.2, and we can see that by the time the vector has traversed from its starting point to point B then to point C and returning towards point A it has rotated.

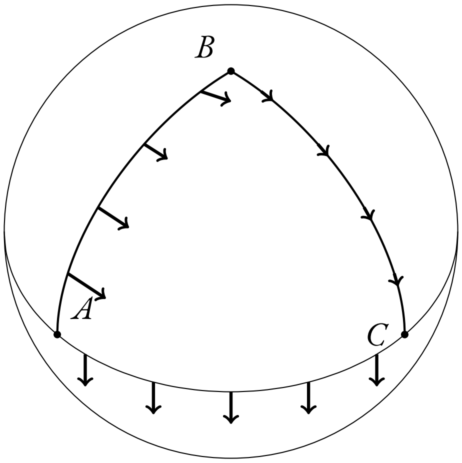

Figure 2.2: An illustration of parallel transport around the spherical triangle ABC. This illustrates that whilst local parallelism may be defined—global parallelism may not. This is not the case in regular, Euclidean geometry. Adapted from Figure 6.3 in Schutz (2009).

Repeating this process to go from point A to point C however, would not result in the same vector being generated, i.e. the rotation of the vector over the course of the parallel transport is dependent upon the path that has been taken. This is obviously not an effect that occurs in flat, Euclidean space, in which one may move a parallel line in any direction and retain the parallelism regardless of the path taken. This means that in general, one cannot define global parallelism; however, we do have a mechanism by which to transport vectors around a space.

2.3 The Metric

The simplest geometrical question is the distance between two points. As was stated in Section 2.2, in an N-dimensional space we may define a local co-ordinate system for each point requiring N functions. The functions that we choose are the *basis* of that co-ordinate system. In a four-dimensional flat space for a given frame $\mathcal{F}$ we may, for instance, choose to use the following basis vectors:

$$\begin{aligned}\vec{e_0} &\underset{\mathcal{F}}{\rightarrow} (1,0,0,0)\\ \vec{e_1} &\underset{\mathcal{F}}{\rightarrow} (0,1,0,0)\\ \vec{e_2} &\underset{\mathcal{F}}{\rightarrow} (0,0,1,0)\\ \vec{e_3} &\underset{\mathcal{F}}{\rightarrow} (0,0,0,1)\end{aligned} \tag{2.1}$$

Any point in that space may then be defined by a vector, $\vec{A}$, and in that frame may be expressed in terms of the basis vectors as:

$$\begin{aligned}\vec{A} &= A^0\,\vec{e_0} + A^1\,\vec{e_1} + A^2\,\vec{e_2} + A^3\,\vec{e_3}\\ &= A^\alpha\,\vec{e_\alpha}\,.\end{aligned} \tag{2.2}$$

Representing two points as $\vec{A}$ and $\vec{B}$, in that frame we define the interval between these two points as the *scalar product* (also known as the dot product) between the two vectors:

$$\begin{aligned}\vec{A}\cdot\vec{B} &= (A^\alpha\,\vec{e_\alpha})\cdot(B^\beta\,\vec{e_\beta})\\ &= A^\alpha B^\beta(\vec{e_\alpha}\cdot\vec{e_\beta}) \qquad .\\ &= A^\alpha B^\beta g_{\alpha\beta}\end{aligned} \tag{2.3}$$

We can see that the term, $g_{\alpha\beta}$, represents a set of numbers that are the output of the function that is defined as $\vec{e_\alpha}\cdot\vec{e_\beta}$. Recalling that our definition of a tensor is a function that will map a given number of vectors and one-forms to a scalar, we can see that this is a rank $\binom{0}{2}$ tensor. This tensor is called the *metric* since it allows the definition of length. Equation 2.3 also directly implies that the metric tensor is symmetric, i.e. $\mathbf{g}(\vec{A},\vec{B}) = \mathbf{g}(\vec{B},\vec{A})$.

Given that applying a single vector to a rank $\binom{0}{2}$ tensor will yield a $\binom{0}{1}$ tensor—i.e. a one-form, one may ask what that one-form would be. Considering the scenario, first yields

$$\mathbf{g}(\vec{A},-) \coloneqq \tilde{A}, \tag{2.4}$$

where given that we know from the above that $\mathbf{g}(\vec{A},\vec{B}) = \vec{A}\cdot\vec{B}$ means that $\tilde{A}(\vec{B}) = \vec{A}\cdot\vec{B}$. We can therefore define the components of $\tilde{A}$ as:

$$\begin{aligned}A_\alpha \coloneqq \tilde{A}(\vec{e_\alpha}) &= \vec{A}\cdot\vec{e_\alpha} = \vec{e_\alpha}\cdot\vec{A}\\ &= \vec{e_\alpha}\cdot(A^\beta\,\vec{e_\beta}) \qquad ,\\ &= (\vec{e_\alpha}\cdot\vec{e_\beta})A^\beta\end{aligned} \tag{2.5}$$

and employing the definition of, $g_{\alpha\beta}$ means

$$\therefore A_\alpha = g_{\alpha\beta} A^\beta. \tag{2.6}$$

The matrix that describes the components of the metric tensor is necessarily invertible. Defining the inverse matrix resulting from the metric components as $g^{\alpha\beta}$, we can therefore reverse the process, i.e.

$$A^\alpha := g^{\alpha\beta} A_\beta. \tag{2.7}$$

We can therefore see that by applying the metric or the inverse, we may map a vector to a one-form or vice-versa respectively and in so-doing we simultaneously lower or raise the index of the components. This result may be applied to higher ranked tensors as well to raise or lower indices more generally. An example of lowering and of raising is shown below:

$$\begin{aligned} A_\alpha{}^\beta{}_\gamma &= g_{\alpha\delta} A^{\delta\beta}{}_\gamma \\ A^{\alpha\beta}{}_\gamma &= g^{\alpha\delta} A_\delta{}^\beta{}_\gamma \end{aligned}. \tag{2.8}$$

An obvious question may therefore be what happens should one attempt to raise the index of the metric since the procedure may be applied to any tensor. In this case, this yields

$$g^\alpha{}_\beta = g^{\alpha\gamma} g_{\gamma\beta}, \tag{2.9}$$

which is, by definition, multiplying a matrix with its own inverse which simply yields the identity matrix and therefore we know that

$$g^\alpha{}_\beta = \delta^\alpha{}_\beta, \tag{2.10}$$

where $\delta^\alpha{}_\beta$ is the Kronecker delta—indicating 1 where $\alpha = \beta$ and 0 otherwise. If one were to repeat the process a second time, they would arrive at $g^{\alpha\beta} = g^{\alpha\beta}$ which is self-evident. The tensor the components of which correspond to $g^{\alpha\beta}$ is termed $\mathbf{g}^{-1}$ and it is unique amongst tensors for the relation between it and the metric, i.e. that the inverse tensor's components are the matrix inverse of the original and vice-versa.

2.4 Christoffel Symbols

It will often be the case that we are interested in how physical quantities vary over a space. We have in the previous section discussed the difficulties in comparing vectors over a space—however, we have noted that on local scales co-ordinate systems can be defined and we may transport vectors in these local systems which allows for local comparisons of vectors. Doing this repeatedly allow us to build to a definition of differentiation with respect to the basis vectors and thus with respect to a curve in the space. This is evaluated by the process of *covariant differentiation* and is given by following the product rule:

$$\frac{\partial \overrightarrow{A}}{\partial x^{\beta}} = \frac{\partial A^{\alpha}}{\partial x^{\beta}} \overrightarrow{e_{\alpha}} + V^{\alpha} \frac{\partial \overrightarrow{e_{\alpha}}}{\partial x^{\beta}}, \tag{2.11}$$

where the latter-most term denotes how the basis vectors themselves change over the space—it is not a requirement that the basis vectors remain static. This latter-most encoding is itself, a vector and therefore must be a combination of the basis vectors and some components, i.e.

$$\frac{\partial \overrightarrow{e_{\alpha}}}{\partial x^{\beta}} = \Gamma^{\gamma}{}_{\alpha\beta} \overrightarrow{e_{\gamma}}. \tag{2.12}$$

These components are termed the Christoffel symbols and given the fact that they are describing a property of the space, it will not be surprising that they have a connection with the metric tensor. To understand this connection, we can begin by connecting the covariant derivative of a one-form from its equivalent vector via the metric. This can be given by:

$$A_{\alpha;\beta} = g_{\alpha\gamma} A^{\gamma}{}_{;\beta}, \tag{2.13}$$

which can be arrived at by considering the lowering of the index by the matrix. We now consider again Equation 2.6. Taking the covariant derivative of this, and again applying the product rule, we get

$$A_{\alpha;\beta} = g_{\alpha\gamma;\beta} A^{\gamma} + g_{\alpha\gamma} A^{\gamma}{}_{;\beta}. \tag{2.14}$$

The combination of Equations 2.13 and 2.14 therefore requires that

$$g_{\alpha\gamma;\beta} = 0. \tag{2.15}$$

Remaining on the topic of the covariant derivative of the metric, we seek to define it more fully. We do this by considering that for a scalar, ϕ, we know the covariant derivative, $\nabla\phi$, must be equivalent to its derivative $d\phi$, because scalar quantities do not depend upon the basis vectors. We also know that the combination of the metric with two vectors yields a scalar. If we set that set of scalars to ϕ, we may write

$$\phi = g_{\alpha\beta} A^{\alpha} B^{\beta} \tag{2.16}$$

and thus the derivative becomes,

$$\begin{aligned} \implies \phi_{,\gamma} &= \frac{\partial g_{\alpha\beta}}{\partial x^{\gamma}} A^{\alpha} B^{\beta} + g_{\alpha\beta} \frac{\partial A^{\alpha}}{\partial x^{\gamma}} B^{\beta} + g_{\alpha\beta} A^{\alpha} \frac{\partial B^{\beta}}{\partial x^{\gamma}} \\ &= g_{\alpha\beta,\gamma} A^{\alpha} B^{\beta} + g_{\alpha\beta} B^{\beta} \left(A^{\alpha}{}_{;\gamma} - A^{\delta} \Gamma^{\alpha}{}_{\delta\gamma} \right) + g_{\alpha\beta} A^{\alpha} \left(B^{\beta}{}_{;\gamma} - B^{\delta} \Gamma^{\beta}{}_{\delta\gamma} \right) \\ &= g_{\alpha\beta,\gamma} A^{\alpha} B^{\beta} - g_{\alpha\beta} B^{\beta} A^{\delta} \Gamma^{\alpha}{}_{\delta\gamma} - g_{\alpha\beta} A^{\alpha} B^{\delta} \Gamma^{\beta}{}_{\delta\gamma} + g_{\alpha\beta} B^{\beta} A^{\alpha}{}_{;\gamma} + g_{\alpha\beta} A^{\alpha} B^{\beta}{}_{;\gamma} \\ &= \left(g_{\alpha\beta,\gamma} - g_{\delta\beta} \Gamma^{\delta}{}_{\alpha\gamma} - g_{\alpha\delta} \Gamma^{\delta}{}_{\beta\gamma} \right) A^{\alpha} B^{\beta} + g_{\alpha\beta} B^{\beta} A^{\alpha}{}_{;\gamma} + g_{\alpha\beta} A^{\alpha} B^{\beta}{}_{;\gamma} \end{aligned} . \tag{2.17}$$

From the fact the covariant derivative and derivative are equivalent, we can therefore conclude that the bracketed term of Equation 2.17 must be the covariant derivative of the metric tensor in full, i.e.

$$g_{\alpha\beta;\gamma} = g_{\alpha\beta,\gamma} - g_{\delta\beta} \Gamma^{\delta}{}_{\alpha\gamma} - g_{\alpha\delta} \Gamma^{\delta}{}_{\beta\gamma}, \tag{2.18}$$

and by combining Equations 2.18 and 2.15, we have tied the derivatives of the metric tensor to the Christoffel symbols:

$$g_{\alpha\beta,\gamma} = \Gamma^{\delta}{}_{\alpha\gamma} g_{\delta\beta} + \Gamma^{\delta}{}_{\beta\gamma} g_{\alpha\delta}. \tag{2.19}$$

We may finish wholly tying the Christoffel symbols to the metric by examining the combination of three index permutations of Equation 2.19. Specifically, we consider:

$$\begin{aligned} g_{\alpha\beta,\gamma} &= \Gamma^{\delta}{}_{\alpha\gamma} g_{\delta\beta} + \Gamma^{\delta}{}_{\beta\gamma} g_{\alpha\delta} \\ g_{\alpha\gamma,\beta} &= \Gamma^{\delta}{}_{\alpha\beta} g_{\delta\gamma} + \Gamma^{\delta}{}_{\gamma\beta} g_{\alpha\delta}, \\ -g_{\beta\gamma,\alpha} &= -\Gamma^{\delta}{}_{\beta\alpha} g_{\delta\gamma} - \Gamma^{\delta}{}_{\gamma\alpha} g_{\beta\delta} \end{aligned} \tag{2.20}$$

the sum of which yields

$$g_{\alpha\beta,\gamma} + g_{\alpha\gamma,\beta} - g_{\beta\gamma,\alpha} = \left(\Gamma^{\delta}{}_{\alpha\beta} - \Gamma^{\delta}{}_{\beta\alpha} \right) g_{\delta\gamma} + \left(\Gamma^{\delta}{}_{\alpha\gamma} - \Gamma^{\delta}{}_{\gamma\alpha} \right) g_{\delta\beta} + \left(\Gamma^{\delta}{}_{\beta\gamma} + \Gamma^{\delta}{}_{\gamma\beta} \right) g_{\alpha\delta}, \tag{2.21}$$

where we have used the symmetry of the metric tensor to note that $g_{\beta\delta} = g_{\delta\beta}$. Similarly we may now apply a symmetry of the Christoffel symbols which is that $\Gamma^{\alpha}{}_{\beta\gamma} = \Gamma^{\alpha}{}_{\gamma\beta}$—this may be demonstrated by considering the fact that $\phi_{,\beta,\alpha} = \phi_{,\alpha,\beta}$. Use of this symmetry allows us to simplify Equation 2.21 and define a Christoffel symbol purely in terms of the metric:

$$\Gamma^{\varepsilon}{}_{\beta\gamma} = \frac{1}{2} g^{\alpha\varepsilon} \left(g_{\alpha\beta,\gamma} + g_{\alpha\gamma,\beta} - g_{\beta\gamma,\alpha} \right), \tag{2.22}$$

where we have also multiplied both sides by $g^{\alpha\varepsilon}$ and employed Equation 2.10.

2.5 Parallel Transport

In Section 2.2, we discussed the notion of parallel transport in the context of demonstrating that parallelism may not be globally defined in certain spaces. However, beyond a qualitative description of parallel transport as a means to move vectors around locally that can be repeated for a more global transportation, we did not define what parallel transport is mathematically. Now equipped with the covariant derivative, we may do so.

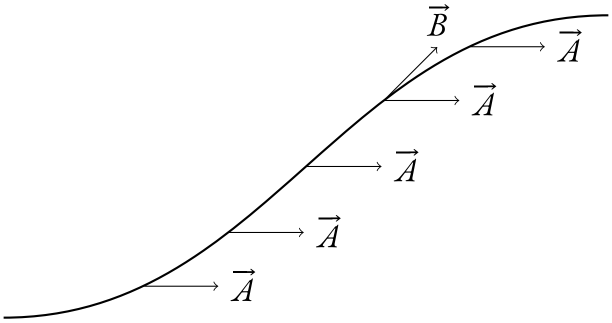

Figure 2.3: Illustration of the parallel transport of $\vec{A}$ along $\vec{B}$. Adapted from Figure 6.3 of Schutz (2009).

Figure 2.3 illustrates the process of parallel transport. We may locally define a co-ordinate system and in so doing may locally move a vector, $\vec{A}$ such that it remains parallel. To do this, we recall that curves are defined as functions of some parameter—in this example the curve is given as $\lambda(t)$. In addition to the vector $\vec{A}$, we may also define the vector $\vec{B}$ which is the *tangent* to any given point along the curve. This vector may also be described as $\frac{d\vec{x}}{dt}$.

In the local co-ordinate system in order for parallel transport to occur, the components of $\vec{A}$ must remain constant, so that the moved vector is parallel to the original, and so

$$\frac{dA^\alpha}{dt} = 0. \tag{2.23}$$

Applying the relation between the partial and covariant derivative, we may rewrite this as

$$\frac{dA^\alpha}{dt} = B^\beta A^\alpha{}_{,\beta} = B^\beta A^\alpha{}_{;\beta} - A^\gamma \Gamma^\alpha{}_{\gamma\beta} = 0 \tag{2.24}$$

Given that we have restricted ourselves to manifolds that on local scales must map to Euclidean space and in Euclidean space, $\Gamma^\alpha{}_{\gamma\beta} = 0$, we can therefore note that

$$B^\beta A^\alpha{}_{;\beta} = 0. \tag{2.25}$$

That the covariant derivative is zero in one co-ordinate system within the local frame, means that this must be the case in all co-ordinate system in that frame. Given that no specific point on the curve was chosen, this also therefore means that it will hold for all points in the manifold, and so therefore Equation 2.25 is a frame-invariant definition of parallel transport.

2.6 Geodesics

The shortest distance between two points is a straight line. This is one of the most basic statements about Euclidean geometry, but as we consider the manifolds we must ask the question of what the equivalent to a straight line might be—if there are any. We gain an insight into this by consideration of parallel transport.

In flat space, straight lines parallel transport their own tangents. The curves that perform this in the manifold are called geodesics. Employing Equation 2.25 we get

$$B^{\beta}B^{\alpha}{}_{;\beta} = B^{\beta}B^{\alpha}{}_{,\beta} + \Gamma^{\alpha}{}_{\gamma\beta}B^{\alpha}B^{\beta} = 0, \tag{2.26}$$

which may be rewritten in terms of a curve parameter, t, and the associated co-ordinate functions, x, as

$$\frac{d}{dt}\left(\frac{dx^{\alpha}}{dt}\right) + \Gamma^{\alpha}{}_{\gamma\beta}\frac{dx^{\gamma}}{dt}\frac{dx^{\beta}}{dt} = 0. \tag{2.27}$$

One may note that in flat spacetime, where the Christoffel symbol is zero, this will reduce to a straight line as expected—the straight line is the geodesic of flat space. In Equation 2.27, we have parameterised the expression in terms of t, but it is not a unique parameterisation. Any parameter that is a linear transformation, i.e. one that may be described as

$$t' = at + b, \tag{2.28}$$

where a and b are constant and independent of position within the curve, will also be solutions to Equation 2.27. The set of parameters which satisfy this are called the *affine parameters*.

With a candidate for the generalisation of straight lines to curved spaces we turn to interrogate whether geodesics are curves of extremal length. Starting from Equation 2.3 which defines the line element of the metric, we may get a measure of the length between two points on the curve corresponding to t_0 and t_1 as

$$l = \int_{t_0}^{t_1} \left| g_{\alpha\beta}\frac{dx^{\alpha}}{dt}\frac{dx^{\beta}}{dt} \right|^{1/2} dt. \tag{2.29}$$

This may be rewritten in the form

$$l = \int_{t_0}^{t_1} \mathcal{L}(x, \frac{dx}{dt})dt, \tag{2.30}$$

where $\mathcal{L}(x, \frac{dx}{dt}) = \sqrt{g_{\alpha\beta}\frac{dx^{\alpha}}{dt}\frac{dx^{\beta}}{dt}}$. In order for this curve to be of extremal length it must satisfy the *Euler-Lagrange equation*

$$\frac{d}{dt}\left(\frac{\partial\mathcal{L}}{\partial(dx^\alpha/dt)}\right)-\frac{\partial\mathcal{L}}{\partial x^\alpha}=0. \tag{2.31}$$

We solve this in stages, firstly looking at the derivatives of $\mathcal{L}$:

$$\begin{aligned}\frac{\partial\mathcal{L}}{\partial(dx^\alpha/dt)}&=\frac{1}{2\mathcal{L}}\left(g_{\alpha\beta}\frac{dx^\beta}{dt}+g_{\alpha\beta}\frac{dx^\alpha}{dt}\delta^\beta{}_\alpha\right)\\&=\frac{1}{\mathcal{L}}g_{\alpha\beta}\frac{dx^\beta}{dt}\end{aligned}, \tag{2.32}$$

$$\frac{\partial\mathcal{L}}{\partial x^\alpha}=\frac{1}{2\mathcal{L}}g_{\beta\gamma,\alpha}\frac{dx^\beta}{dt}\frac{dx^\gamma}{dt}. \tag{2.33}$$

To simplify the solution of the Euler-Lagrange equation, we may re-parameterise away from t to another affine parameter, u, such that $dt/du=\mathcal{L}$ which allows us to cancel the factor of $\mathcal{L}$ from both derivatives and so the Euler-Lagrange equation becomes

$$\begin{aligned}\frac{d}{du}\left(g_{\alpha\beta}\frac{dx^\beta}{du}\right)-\frac{1}{2}g_{\beta\gamma,\alpha}\frac{dx^\beta}{du}\frac{dx^\gamma}{du}&=0\\\implies g_{\alpha\beta}\frac{d^2x^\beta}{du^2}+g_{\alpha\beta,\gamma}\frac{dx^\gamma}{du}\frac{dx^\beta}{du}-\frac{1}{2}g_{\beta\gamma,\alpha}\frac{dx^\beta}{du}\frac{dx^\gamma}{du}&=0\end{aligned} \tag{2.34}$$

The next step is to contract Equation 2.34 with the inverse metric. We also note that the middle term of Equation 2.34 may be split into $\frac{1}{2}(g_{\alpha\beta,\gamma}+g_{\alpha\gamma,\beta})\frac{dx^\beta}{du}\frac{dx^\gamma}{du}$ due to it being symmetric. This yields

$$\frac{d^2x^\beta}{du^2}+\frac{1}{2}g^{\alpha\beta}\left(g_{\alpha\beta,\gamma}+g_{\beta\alpha,\gamma}-g_{\beta\gamma,\alpha}\right)\frac{dx^\beta}{du}\frac{dx^\gamma}{du}=0, \tag{2.35}$$

and using the definition of the Christoffel symbols

$$\implies\frac{d^2x^\beta}{du^2}+\Gamma^\alpha{}_{\beta\gamma}\frac{dx^\beta}{du}\frac{dx^\gamma}{du}=0, \tag{2.36}$$

in other words, the geodesic equation satisfies the Euler-Lagrange equation and is thus a curve of extremal length, i.e. the shortest distance between two points in a manifold is following the geodesic containing both points.

2.7 Curvature

In Section 2.2, and in particular in Figure 2.2, it was shown that parallel transport may result in a rotation of the vector over a closed loop—in that instance, it was over a spherical triangle. We also noted in that section that this rotation does not occur in flat spaces. That is because, this rotation allows us to define *curvature* in a geometrical framework.

To do this, we consider an infinitesimally small closed loop in a space. The four sides of this loop would be bounded by the co-ordinate lines, $x^1 = a$, $x^1 = a + \delta a$ and $x^2 = b$, $x^2 = b + \delta b$. We first parallel transport a vector $\vec{A}$ from the point with co-ordinates (a, b)— hereafter referred to as P—to the point with co-ordinates $(a + \delta a, b)$—hereafter Q—, the parallel transport equation (Equation 2.24) would be given as

$$\frac{dA^\alpha}{dx^1} = -\Gamma^\alpha{}_{\beta 1} A^\beta. \tag{2.37}$$

Integrating this between the two points would then allow the construction of the vector $\vec{A}$ at Q as

$$A^\alpha(Q) = A^\alpha(P_{\text{initial}}) - \int_{x^2=b} \Gamma^\alpha{}_{\beta 1} A^\beta dx^1 \tag{2.38}$$

This process may be repeated between the next two boundary points of the loop, denoted by R and S and finally back around to P—noting that in the latter two cases that there will be a sign change in the integral due to the fact that these are reversed direction compared with the first two—to yield that the change in the vector after parallel transportation around the loop compared with before is given by

$$\delta A^\alpha = \int_{x^1=a} \Gamma^\alpha{}_{\beta 2} A^\beta dx^2 - \int_{x^1=a+\delta a} \Gamma^\alpha{}_{\beta 2} A^\beta dx^2 + \int_{x^2=b+\delta b} \Gamma^\alpha{}_{\beta 1} A^\beta dx^1 - \int_{x^2=b} \Gamma^\alpha{}_{\beta 1} A^\beta dx^1. \tag{2.39}$$

To go further, we make the simplifications of working only to first order separation of the paths and caring only about the lowest order of the result which gives

$$\begin{aligned} \delta A^\alpha &\simeq -\int_b^{b+\delta b} \delta a \frac{\partial}{\partial x^1}\left(\Gamma^\alpha{}_{\beta 2} A^\beta\right) dx^2 + \int_a^{a+\delta a} \delta b \frac{\partial}{\partial x^2}\left(\Gamma^\alpha{}_{\beta 1} A^\beta\right) dx^1 \\ &\approx \delta a \delta b \left[-\frac{\partial}{\partial x^1}\left(\Gamma^\alpha{}_{\beta 2} A^\beta\right) - \frac{\partial}{\partial x^2}\left(\Gamma^\alpha{}_{\beta 1} A^\beta\right)\right] \end{aligned}, \tag{2.40}$$

which can be expanded out and using a combination of the product rule and Equation 2.37. Generalising the set of co-ordinates from 1 and 2 to γ and δ, this expansion yields after rearranging,

$$\delta A^\alpha = \delta a \delta b \left[\Gamma^\alpha{}_{\beta\gamma,\delta} - \Gamma^\alpha{}_{\beta\delta,\gamma} + \Gamma^\alpha{}_{\varepsilon\delta}\Gamma^\varepsilon{}_{\beta\gamma} - \Gamma^\alpha{}_{\varepsilon\gamma}\Gamma^\varepsilon{}_{\beta\delta}\right] A^\beta. \tag{2.41}$$

Looking at Equation 2.41, we may note that the bracketed term defines the components of a rank $\binom{1}{3}$ tensor that takes the vectors $\vec{A}$, $\delta a\, \vec{e_\delta}$, $\delta b\, \vec{e_\gamma}$, and the basis one-form $\tilde{\omega}$—which gives δA^α from $\delta \vec{A}$—and returns the changes in the components of the vector $\vec{A}$ after parallel transport. This tensor is called the Riemann-Christoffel tensor, or the Riemann curvature tensor,

$$R^\alpha{}_{\beta\delta\gamma} = \Gamma^\alpha{}_{\beta\gamma,\delta} - \Gamma^\alpha{}_{\beta\delta,\gamma} + \Gamma^\alpha{}_{\varepsilon\delta}\Gamma^\varepsilon{}_{\beta\gamma} - \Gamma^\alpha{}_{\varepsilon\gamma}\Gamma^\varepsilon{}_{\beta\delta}. \tag{2.42}$$

That the Riemann tensor is entirely composed of Christoffel symbols and their derivatives may come as no surprise given that Christoffel symbols describe the change in basis vectors over a space and our definition of curvature is how a vector changes after parallel transport around a loop. As with the other tensors discussed so far, the Riemann tensor has certain symmetries around index switches. These symmetries are:

- Antisymmetry in switches of the first two indices, i.e. $R_{\alpha\beta\gamma\delta} = -R_{\beta\alpha\gamma\delta}$.
- Antisymmetry in switches of the last two indices, i.e. $R_{\alpha\beta\gamma\delta} = -R\alpha\beta\delta\gamma$.
- Symmetry in switches of the first two indices with the last two indices, i.e. $R_{\alpha\beta\gamma\delta} = R_{\gamma\delta\alpha\beta}$.

This is most easily proven at a locally flat point, P, within the manifold at which the Christoffel symbols vanish, and their derivatives will be given by

$$\Gamma^{\alpha}{}_{\beta\gamma,\delta} = \frac{1}{2} g^{\alpha\varepsilon} \left(g_{\varepsilon\beta,\gamma\delta} + g_{\varepsilon\gamma,\beta\delta} - g_{\beta\gamma,\varepsilon\delta} \right). \tag{2.43}$$

which results in the Riemann tensor being given by, after the lowering of the first index being given by

$$R_{\alpha\beta\gamma\delta} = \frac{1}{2} \left(g_{\alpha\delta,\beta\gamma} - g_{\alpha\gamma,\beta\delta} + g_{\beta\gamma,\alpha\delta} - g_{\beta\delta,\alpha\gamma} \right) \tag{2.44}$$

This point, P, also allows the derivation of another important property of the Riemann-Christoffel tensor, which is the summation of the cyclic permutation of the last three indices

$$\begin{aligned} R_{\alpha\beta\gamma\delta} + R_{\alpha\delta\beta\gamma} + R_{\alpha\gamma\delta\beta} \\ = \frac{1}{2} \Big(& g_{\alpha\delta,\beta\gamma} - g_{\alpha\gamma,\beta\delta} + g_{\beta\gamma,\alpha\delta} - g_{\beta\delta,\alpha\gamma} + g_{\alpha\gamma,\delta\beta} - g_{\alpha\beta,\delta\gamma} \\ & + g_{\delta\beta,\alpha\gamma} - g_{\delta\gamma,\alpha\beta} + g_{\alpha\beta,\gamma\delta} - g_{\alpha\delta,\gamma\beta} + g_{\gamma\delta,\alpha\beta} - g_{\gamma\beta,\alpha\delta} \Big) \end{aligned} \tag{2.45}$$

and using the fact that partial derivatives commute, i.e. $g_{\alpha\beta,\gamma\delta} = g_{\alpha\beta,\delta\gamma}$, we can see that these cancel pairwise off, so that

$$R_{\alpha\beta\gamma\delta} + R_{\alpha\delta\beta\gamma} + R_{\alpha\gamma\delta\beta} = 0. \tag{2.46}$$

That Equation 2.46 is a tensorial equation means that because it holds in one co-ordinate system, it must hold in all of them, so this is a global property of the Riemann-Christoffel tensor.

A similar process to that that we have used to derive Equation 2.46 may be applied to the derivative of the Riemann tensor's co-ordinates in the locally flat space around a point, P, then from Equation 2.44, we would have

$$R_{\alpha\beta\gamma\delta,\varepsilon} = \frac{1}{2} \left(g_{\alpha\delta,\beta\gamma\varepsilon} - g_{\alpha\gamma,\beta\delta\varepsilon} + g_{\beta\gamma,\alpha\delta\varepsilon} - g_{\beta\delta,\alpha\gamma\varepsilon} \right). \tag{2.47}$$

By again performing the aforementioned process, we arrive at

$$R_{\alpha\beta\gamma\delta,\varepsilon} + R_{\alpha\beta\varepsilon\gamma,\delta} + R_{\alpha\beta\delta\varepsilon,\gamma} = 0, \tag{2.48}$$

which because we are in the flat space in which the Christoffel symbols are zero means that this expression is equivalent to

$$R_{\alpha\beta\gamma\delta;\varepsilon} + R_{\alpha\beta\varepsilon\gamma;\delta} + R_{\alpha\beta\delta\varepsilon;\gamma} = 0, \tag{2.49}$$

and much like Equation 2.46 because this is a tensorial equation, that it is valid in one system means that it is valid in all, and is therefore globally true. This particular Equation is called the *Bianchi identities*.

Whilst the Riemann-Christoffel tensor defines the curvature on a space, there are two additional curvature objects that are used in curved spaces. The first of these is the Ricci tensor, which is the contraction of the Riemann-Christoffel tensor in its first and third indices, i.e.

$$R_{\alpha\beta} = R_{\beta\alpha} \coloneqq R^{\gamma}{}_{\alpha\gamma\beta}. \tag{2.50}$$

Due to the symmetries of the Riemann-Christoffel tensor, all other contractions either vanish or will reduce to $\pm R_{\alpha\beta}$ meaning the Ricci tensor is functionally the only contraction of the Riemann-Christoffel tensor and hence the justification of singling it out. The symmetry of the Ricci tensor in its indices is a direct consequence of the symmetries of the Riemann-Christoffel tensor.

The second object is similarly the result of contraction—in this case contracting the Ricci tensor with the metric,

$$R = R^{\alpha}{}_{\alpha} = g^{\alpha\beta} R_{\alpha\beta}, \tag{2.51}$$

with the scalar value R being termed the Ricci scalar.

With the notion of contraction yielding the Ricci tensor from the Riemann-Christoffel tensor, this may also be done to Bianchi identities (Equation 2.49) to yield

$$\begin{aligned} g^{\alpha\gamma}\left[R_{\alpha\beta\gamma\delta;\varepsilon} + R_{\alpha\beta\varepsilon\gamma;\delta} + R_{\alpha\beta\delta\varepsilon;\gamma}\right] &= 0 \\ \implies g^{\alpha\gamma}\left[R_{\alpha\beta\gamma\delta;\varepsilon} - R_{\alpha\beta\gamma\varepsilon;\delta} + R_{\alpha\beta\delta\varepsilon;\gamma}\right] &= 0 \\ \implies R^{\gamma}{}_{\beta\gamma\delta;\varepsilon} - R^{\gamma}{}_{\beta\gamma\varepsilon;\delta} + R^{\gamma}{}_{\beta\delta\varepsilon;\gamma} &= 0, \\ \therefore R_{\beta\delta;\varepsilon} - R_{\beta\varepsilon;\delta} + R^{\gamma}{}_{\beta\delta\varepsilon;\gamma} &= 0 \end{aligned} \tag{2.52}$$

where we note that index raising and lowering is commutative with covariant differentiation due to a combination of Equation 2.15 and

$$\begin{aligned} g^{\alpha\gamma} g_{\gamma\beta} &= \delta^{\alpha}{}_{\beta} \\ \implies g^{\alpha\gamma} g_{\gamma\beta;\delta} + g^{\alpha\gamma}{}_{;\delta}\, g_{\gamma\beta} &= \delta^{\alpha}{}_{\beta;\delta} \\ \implies g^{\alpha\gamma}{}_{;\delta}\, g_{\gamma\beta} &= 0 \\ \implies g^{\alpha\gamma}{}_{;\delta}\, g_{\gamma\beta} g^{\beta\varepsilon} &= 0 \\ \implies g^{\alpha\gamma}{}_{;\delta}\, \delta_{\gamma}{}^{\varepsilon} &= 0 \\ \therefore\ g^{\alpha\varepsilon}{}_{;\delta} &= 0 \end{aligned} \tag{2.53}$$

Equation 2.52 is perhaps unsurprisingly called the contracted Bianchi identities. Contracting it again over the indices termed β and δ here yields

$$\begin{aligned} g^{\beta\delta}\left[R_{\beta\delta;\varepsilon} - R_{\beta\varepsilon;\delta} + R^{\gamma}{}_{\beta\delta\varepsilon;\gamma}\right] &= 0 \\ \implies g^{\beta\delta}\left[R_{\beta\delta;\varepsilon} - R_{\beta\varepsilon;\delta} - R^{\beta}{}_{\gamma\delta\varepsilon;\gamma}\right] &= 0 \\ \implies R_{;\varepsilon} - R^{\gamma}{}_{\varepsilon;\gamma} - R^{\gamma}{}_{\varepsilon;\gamma} &= 0\text{'} \\ \therefore \left(R^{\gamma}{}_{\varepsilon} - \frac{1}{2}\delta^{\gamma}{}_{\varepsilon} R\right)_{;\gamma} &= 0 \end{aligned} \tag{2.54}$$

where it is noted that for scalars, partial and covariant differentiation are equivalent. If a symmetric tensor, G, is defined such that

$$G^{\alpha\beta} = R^{\alpha\beta} + \frac{1}{2} g^{\alpha\beta} R, \tag{2.55}$$

then the twice-contracted Bianchi identities are directly

$$G^{\alpha\beta}{}_{;\gamma} = 0. \tag{2.56}$$

This final tensor, G, is known as the Einstein tensor and like the Riemann-Christoffel and Ricci tensors is a description of the curvature of the manifold.

2.8 Special Relativity

Before we may fully apply the geometric description of space-time to describe GR, we must first look at what happens without considering the effects of gravity. This is the domain of Einstein's Special Relativity which arises out of a combination of two postulates.

Postulate I: *Galilean Relativity*	Absolute velocity cannot be determined by experiment and the results of an experiment do not depend on the speed of the experiment relative

to other observers (Galilei, 1967).

Postulate II: *Universality of the Speed of Light* The speed of light relative to any non-accelerating observer is c regardless of the motion of the source of the light relative to the observer (Einstein, 1905).

In special relativity, space-time may be described a four dimensional co-ordinate system (t, x, y, z)—i.e. a four dimensional manifold with some metric. This metric must be measurable from the invariant interval over these four dimensions as given by Equation 2.3. The invariant interval in the four-dimensional space of SR is given by

$$\partial s^2 = -(c\partial t)^2 + \partial x^2 + \partial y^2 + \partial z^2. \tag{2.57}$$

Transferring to *natural units*, in which $c = 1$, allows us to define the metric as

$$\eta^{\alpha\beta} = \mathrm{diag}\left(-1, 1, 1, 1\right), \tag{2.58}$$

which is known as the Minkowski metric and directly tells us that this space-time is flat. Note that equally the metric can be defined with inverse signs as $\mathrm{diag}\left(1, -1, -1, -1\right)$.

Next, we introduce the concept of the *inertial frame*. Whilst Postulate I requires that the result of an experiment cannot determine absolute velocity, it can determine *acceleration*, and inertial frames are those that are not accelerating. Specifically, we are imposing requirements on t, and (x, y, z):

I. The spatial distance between two points P, which corresponds to (x_1, y_1, z_1), and Q, corresponding to (x_2, y_2, z_2) is not time-dependent.

II. Clocks within the frame are synchronised and the rate of change of t is not position-dependent.

III. The geometry at any single time t is Euclidean.

We may visually represent a series of events over their position and time, through a space-time diagram. An example of this is shown in Figure 2.4. In these space-time diagrams, straight lines represent paths of constant velocity with their slopes indicating the speed. Curves represent accelerations through the space, and each point represents a specific event. Light travels in a straight line at a 45° angle such that $\partial s^2 = 0$ and so lines in the space-time diagram of this nature are called *light-like*. Lines corresponding to travelling slower than the speed of light are called *time-like*, and those travelling faster are called *space-like*.

We now look at the second of the requirements we have imposed which requires that the clocks are synchronised and ask the question of what synchronisation means. To do this consider sending a beam of light between two points P and Q—this is illustrated in Figure 2.5. Clocks at position x_1 and position x_2 are considered synchronised if

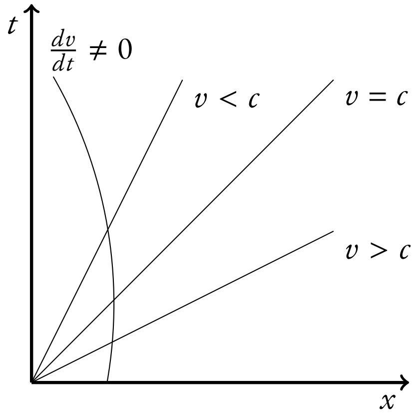

Figure 2.4: An example of a space-time diagram, showing the lines of three objects at constant velocity, one at c, as well as one above and below it. As well a fourth object with non-constant velocity is shown as a curve

$$t_2 = \frac{1}{2}\left(t_1 + t_1'\right). \tag{2.59}$$

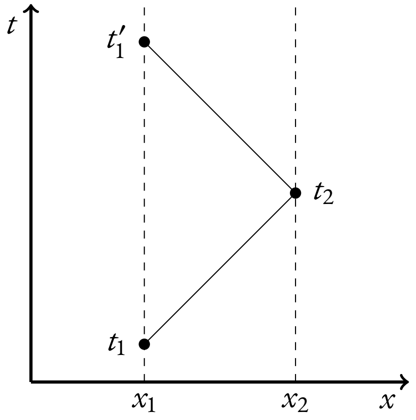

Figure 2.5: Space-time diagram depicting the reflection of light between two points. A clock at x_2 is synchronised with one at x_1 if t_2 is halfway between t_1 and t_1'.

There is an important result that arises from considering observing Figure 2.5 in another frame, $\mathcal{F}_2$, that is moving with some velocity v relative to the original frame, $\mathcal{F}_1$. The temporal axis, $\bar{t}$, of $\mathcal{F}_2$ may be considered as a rotation compared to that of $\mathcal{F}_1$ by some angle ϕ such that $\tanh\phi = v$. As a consequence of Postulate II, in the space-time diagram, light remains at travelling at a 45° angle. Extending out the lines in this way allows us to construct where to place the x-axis in $\mathcal{F}_2$ and looking at the illustration of this in Figure 2.6 we note that this has rotated up—also by ϕ. This means that events that are simultaneous in $\mathcal{F}_1$ are *not* simultaneous in $\mathcal{F}_2$ and vice-versa.

To understand how to transform between the co-ordinates in $\mathcal{F}_1$ and $\mathcal{F}_2$, we first define that a general linear transformation between two co-ordinate systems may be given by

$$x^{\alpha} = \Lambda^{\alpha}{}_{\beta}x^{\beta}. \tag{2.60}$$

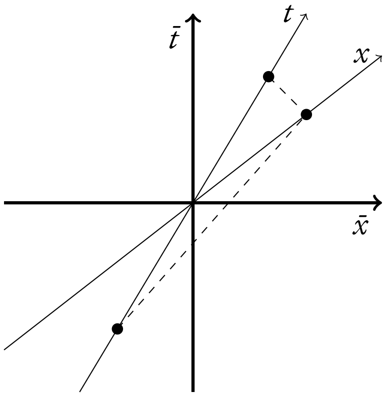

Figure 2.6: Illustration of the reflection of light between two points as seen from an observer in a frame moving with relative velocity to the original frame.

We may, without loss of generality, specifically consider the case where the velocity difference in the new frame is purely along the x-axis. In the construction of Figure 2.6 we have illustrated that this is a rotation in the t and x-axes. We may also note that one may define invariant hyperbolae in t and x which means that the transformation from one frame to another which preserves the interval as required may thus be described in terms of a hyperbolic rotation of these two axes, and so

$$\Lambda^{\alpha}{}_{\beta} = \begin{pmatrix} \cosh\phi & -\sinh\phi & 0 & 0 \\ -\sinh\phi & \cosh\phi & 0 & 0 \\ 0 & 0 & 1 & 0 \\ 0 & 0 & 0 & 1 \end{pmatrix}. \tag{2.61}$$

Employing Equation 2.61 therefore means that the non-trivial changes are given by

$$\begin{aligned} t' &= t\cosh\phi - x\sinh\phi \\ x' &= -t\sinh\phi + x\cosh\phi \end{aligned} \tag{2.62}$$

and considering the line $t' = 0$ we may note that $v = \tanh\phi$ which allows us to rewrite Equation 2.62 as

$$\begin{aligned} t' &= \cosh\phi\,(t - xv) \\ x' &= \cosh\phi\,(x - tv) \end{aligned} \tag{2.63}$$

and therefore by the hyperbolic identity $\cosh x = \frac{1}{\sqrt{1-\tanh^2 x}}$, we arrive at the *Lorentz transformation*

$$\begin{aligned} t' &= \gamma\left(t - xv\right) \\ x' &= \gamma\left(x - tv\right) \\ y' &= y \\ z' &= z \end{aligned}, \tag{2.64}$$

where obviously $\gamma = \frac{1}{\sqrt{1-v^2}}$. This transformation encodes two of the most important effects of Special Relativity—time dilation and length contraction. To an inertial observer, a moving clock would appear to be running more slowly. Simultaneously attempts to measure the length of a moving object would yield an apparently shorter measurement.

2.9 Energy and Momentum

Much of the discussion thus far has concerned space-time as a concept. However, space-time is not an empty space on which things occur. It contains within it particles, fluids, etc., and the mass that needs to be present for gravitational interactions. We begin our discussion on matter with the simplest form of matter, a massive particle.

Massive particles must, remain below the speed of light c, and therefore are required to have time-like worldlines on a space-time diagram. This path may be defined in our four-dimensional co-ordinate system as $x^{\alpha}(\lambda)$ i.e. some function over an affine parameter. That it is a time-like path necessarily means that a convenient affine parameter to use is the *proper time*, τ, given by

$$(\delta\tau)^2 = -\eta_{\alpha\beta}\delta x^{\alpha}\delta x^{\beta}, \tag{2.65}$$

i.e. the time interval as measured by an observer in an inertial frame. This is just the negative of Equation 2.57, which makes a convenient choice since it must necessarily be positive for time-like curves. We may define a four-dimensional equivalent to velocity as the tangent to its path on the space-time diagram. This four dimensional velocity is termed the four-velocity,

$$U^{\alpha} = \frac{dx^{\alpha}}{d\tau}. \tag{2.66}$$

We may note therefore that $\eta_{\alpha\beta}U^{\alpha}U^{\beta} = -1$ by construction and the implication therefore is that whilst one may have any velocity through space, one travels through space-time at a particular, constant rate. This is made more obvious by considering a particle's rest frame in which it will obviously have co-ordinates $(1, 0, 0, 0)$. We may combine this with the notion of mass by defining the *momentum* four-vector as

$$p^{\alpha} = mU^{\alpha}, \tag{2.67}$$

where m is the mass that is measured in the particle's rest frame. The spatial components of the momentum four-vector are obviously the spatial momentum. The temporal component is termed the *energy* of the particle, and is given by

$$E = mc^2 \tag{2.68}$$

in its rest frame. Moving to a collection of particles, which we term a *fluid*, a single four-velocity or four-momentum is obviously insufficient to describe the entire fluid. The object that fulfills this role is the *energy-momentum* tensor, $T^{\alpha\beta}$, which may be described as the flux of four-momentum, p^{α}, across a surface of constant x^{β}.

The components of this tensor describe a number of the properties that one associates with a fluid. To describe them, we first consider the most obvious question in a collection of particles—how many particles are there in some small volume? In the rest (or momentarily co-moving reference) frame this may be given by the *number density*, n, which is simply counting the number of particles in that volume. This may obviously change over the fluid since some regions may be more or less dense than others.

Given that the number density was defined in the context of the rest frame, one may ask about a frame experiencing some velocity, v. Each particle would appear to have that constant velocity. This would affect the volume that a given number of particles would take due to Lorentz contraction. So the number density in the frame would also be reduced by a factor of γ.

We may define a four-vector similar to the four-momentum for the number density

$$N^{\alpha} = nU^{\alpha}. \tag{2.69}$$

Again considering the Lorentz transformation for a frame that has some velocity (v^x, v^y, v^z) would yield that in that frame, the components of N^{α} would be

$$N^{\alpha} = \left(\frac{n}{\gamma}, \frac{nv^x}{\gamma}, \frac{nv^y}{\gamma}, \frac{nv^z}{\gamma}\right) \tag{2.70}$$

where the temporal component is clearly the number density, and the spatial components are the fluxes for each direction—i.e. how many particles cross a unit area of the surface in a unit time. Thus $\overrightarrow{N}$ is termed the number flux. It may be multiplied by other parameter to yield parameter-fluxes such as the momentum-fluxes that we require.

Returning to our definition of the energy-momentum tensor as the flux of four-momentum, p^{α} across a surface of constant x^{β}. The components are therefore in the rest frame:

T^{00}	The energy density, $\rho = mn$
$T^{0\alpha}$	The energy flux. In the rest frame context this corresponds to any heat conduction within the fluid.

$T^{\alpha 0}$ The momentum density. Given the equivalency of mass and energy, this is directly equivalent to the energy flux.

$T^{\alpha\beta}$ Momentum flux. This represents the forces on adjacent fluid elements due to things such as viscosity. It is in general called the *stress*.

In GR, we do not generally require dealing with the most general kind of fluid. We may restrict ourselves to *perfect fluids*. These are defined as fluids that in their rest frame have neither heat conduction nor viscosity and may be defined purely in terms of their energy density, and an isotropic pressure, p. Therefore, the components of the energy-momentum tensor for a perfect fluid must be

$$T^{\alpha\beta} = \begin{pmatrix} \rho & 0 & 0 & 0 \\ 0 & p & 0 & 0 \\ 0 & 0 & p & 0 \\ 0 & 0 & 0 & p \end{pmatrix} \tag{2.71}$$

so the general form of the tensor for a perfect fluid may be written

$$T^{\alpha\beta} = (\rho + p)U^{\alpha}U^{\beta} + p\eta^{\alpha\beta}. \tag{2.72}$$

When dealing with energy and momentum it is important to remember that these are *conserved quantities*. This is encoded within a requirement of the energy-momentum tensor that

$$T^{\alpha\beta}{}_{,\beta} = 0. \tag{2.73}$$

2.10 The Einstein Field Equations

In the examination of Special Relativity, space-time has been interpreted in the geometrical framework that this chapter has described as a four-dimensional flat Minkowski space, and we have in particular focused on inertial frames as non-accelerating frames.

Acceleration is possible within this framework as the result of forces, however, one would not be able to define a frame in which an accelerating particle would appear at rest for more than a particular moment (the frame in which this is true for a moment is known as the Momentarily Co-moving Reference Frame) but this does not pose any direct problems. What does pose an issue to the framework is the presence of gravity.

As discussed in Chapter 1, the Pound-Rebka experiment (Pound & Rebka, 1960) experiment demonstrated that light travelling out of a gravitational well should be redshifted. A basic assumption if Special Relativity holds in gravitation would be that the laboratory frame is an inertial frame. The gravitational field does not change between both crests which means that the paths followed by the crests should be congruent and $\Delta t_b = \Delta t_t$. However, because frequency is just the inverse of time, the fact that redshifting has occurred means that $\Delta t_t > \Delta t_b$. Thus the conclusion must be the lab frame is not an inertial frame.

This may be complicated further by consideration of the fact that objects at constant velocity should remain as such unless acted on by an external force. Gravity affects all matter in the same way, as we have discussed in Chapter 1, yielding the same acceleration—which is known as the Weak Equivalence Principle. This means that we may construct a frame in which objects in the gravitational field are at constant velocity—that which falls freely with the same acceleration imparted by gravity. This provides a candidate for an inertial frame.

Such a frame *cannot* be *global* and remain both inertial and rigid. The vertical and horizontal extent of the frame are obviously constrained since the acceleration due to gravity changes with height above the object and if extended too horizontally, the edges will no longer be falling horizontally. As the distance over which the frame may extend changes as the frame approaches the centre of the object, the frame may only have a certain extent temporally. In other words, such a frame may only be defined *locally*. That on local scales, a free-falling frame is indistinguishable from the Minkowski inertial frames of special relativity is known as the Einstein equivalence principle.

Therefore, between those requirements for our description of Special Relativity and those we have just discussed for the inclusion of gravity we have

I. Spacetime is a four-dimensional manifold with some metric.

II. This metric may be measured by the invariant interval.

III. The Weak Equivalence Principle.

IV. The Einstein Equivalence Principle.

from which it may become apparent that the presence of gravity is inferring a requirement for *curvature* in the framework that we have discussed. We therefore require a mechanism by which a gravitational field may have an effect on the metric to introduce this curvature. In Newtonian gravity, the field is related to the mass density, ρ, of an object by the Poisson equation for the Newtonian potential,

$$\nabla^2\Phi = 4\pi G\rho, \tag{2.74}$$

where G is Newton's gravitational constant. We are therefore seeking a replacement for this equation. In a general relativistic context, the replacement for the second derivative of the field would be a tensor that is the second derivative of the metric. Fortunately, we have already discussed such a tensor—the Riemann-Christoffel tensor. On the right hand side of the equation, we require a tensor that forms the generalisation of energy density, and we have discussed this also with the energy-momentum tensor.

The conservation of energy and momentum, as we noted requires that the derivative of the energy-momentum tensor be zero. So we would therefore require that the tensor we use as the replacement for the field also be zero. We have noted that this is the case for the Einstein tensor, and so we arrive at the Einstein field equations (EFE)

$$G^{\alpha\beta} = \kappa T^{\alpha\beta}. \tag{2.75}$$

The requirement that this must return to the Newtonian result in the limit of flat space yields that $\kappa = -8\pi G$. This is the central tenet of GR encoding everything that has been discussed in this chapter and forming the basis for the discussions ahead.

3

Bayesian Analysis

> *The coin spun and spun.*
> *Oponn whirled two faces to the cosmos but it was the Lady's bet.*
> *Spin on, silver, spin on*
>
> —*Gardens of the Moon*
> Steven Erikson

3.1 Propositions

Jane Austen's Pride and Prejudice opens with the statement "*It is a truth universally acknowledged, that a single man in possession of a good fortune, must be in want of a wife*". In much of science, we are concerned with the formalism of what something being "*a truth*" is. In statistics, these are formalised as states of a *proposition*. Propositions—for the moment—may be considered as either 'true' or 'false' and are generally represented by a single capital letter.

A general assertion that something is true, may for instance be denoted, A. The contrary assertion that said statement is false, i.e. that Pride and Prejudice's single man is not in want of a wife, would be denoted by $\overline{A}$. We may also assign these statements the values '1' and '0' respectively to denote their truthiness.

Statements are rarely singular, indeed, looking again at our Pride and Prejudice example, it is actually the combination of two propositions that lead to the man being in want of a wife, i.e. the proposition that the man is single and that the man is in possession of a good fortune. If we denote that A refers to the former and B refers to the latter, then we make the following identifications to denote the following scenarios

A, B	The assertion that A and B are true, i.e. the man is single *and* in possession of a good fortune. This is known as the *logical product*.
$A + B$	The assertion that either A is true, or B is true, or A and B are true, i.e. the man is at least single or in possession of a good fortune, and may be both. This is known as the *logical sum*.
$A, \overline{B} + \overline{A}, B$	The assertion that either A is true or B is true, but not both, i.e. the man is *either* single *or* in possession of a good fortune but not both. This is the *exclusive logical sum*.

$A, \overline{A}$	The assertion that something is simultaneously true and false i.e. the man is single *and* not single. This is an *impossible statement* which is always false.

We can therefore construct an expression that would correspond to Jane Austen's assertion in the following formulation. Defining

A	The man is single.
B	The man is in possession of a good fortune.
C	The man is in want of a wife.

then in this framework, she is saying that

$$A, B \implies C, \tag{3.1}$$

where the $\implies$ operator denotes *implies*. That is, if A and B are true, then C is true.

3.2 Boolean Algebra

The above discussion forms the basis of Boolean Algebra, a mathematical formalism for the discussion of the truthfulness of statements in statistics. Like the discussion of vector spaces in Section 2.1, Boolean algebra adheres to a number of mathematical rules and identities from which operations may be conducted. These are as follows (Boole, 1847):

Idempotence The repeated application of the logical operators on a proposition to itself do not affect the proposition, i.e.

$$\begin{aligned} A, A &= A \\ A + A &= A \end{aligned},$$

which may be repeated ad infinitum.

Commutativity The ordering of the propositions around the operator is irrelevant to the result of the expression, i.e.

$$\begin{aligned} A, B &= B, A \\ A + B &= B + A \end{aligned}.$$

Associativity The ordering of the operator evaluations for the same operator is irrelevant to the result of the expression, i.e.

$$\begin{aligned} A, (B, C) &= (A, B), C = A, B, C \\ A + (B + C) &= (A + B) + C = A + B + C \end{aligned}.$$

Distributivity Where an operator is applied to an expression of the other operator, this is equivalent to the outer operator being applied to the propositions and then the inner operator being evaluated, i.e.

$$\begin{aligned} A,(B+C) &= A,B + A,C \\ A+(B,C) &= (A+B),(A+C) \end{aligned}.$$

Duality An expression is equivalent to the expression where all propositions are replaced with its opposite and all operators are replaced with their counterparts, i.e.

$$\begin{aligned} &\text{If} \quad C = A,B \quad \text{then} \quad \overline{C} = \overline{A} + \overline{B} \\ &\text{If} \quad C = A+B \quad \text{then} \quad \overline{C} = \overline{A},\overline{B} \end{aligned}.$$

From this we may perform any number of logical operations to evaluate any combinations of a series of propositions from their implications. Where this can be done with certainty this would be known as deductive reasoning.

3.3 Probability

The discussion that we have had so far has been based on propositions that are either true or false. However, it is not generally the case that such definitive statements can be made. Returning to our Pride and Prejudice example it is obvious that there are any number of reasons why a single man in possession of good fortune may not be in want of a wife. This corresponds to the notion that the rather than the '0' and '1' that we have used to describe absolute falsehood and absolute truth, we would like something in between. This value is the *probability* of that statement.

There have been, and still are, several ways of viewing probability. These are called *probability theories*. Historically, there have been three major probability theories—the Classical, Frequentist, and Bayesian definitions of probability.

The Classical definition of probability, defines probability as a consequence of the Principle of Indifference. The Principle states that in the absence of evidence to the contrary, one should assume that all outcomes of a given event are equally likely. Probability in the classical sense is the ratio of the number of times that the event occurs compared to the number of times it *should* occur under the case of indifference (Laplace, 1812). There were a number of criticisms that were historically levelled at the Classical definition of probability, such as the notion that for matters that do not immediately present physical symmetries in the manner of dice, cards, coins, etc there is no natural way to apply the Principle of Indifference—in particular in matters of law (Gigerenzer et al., 1989). For instance, in our Pride and Prejudice example, what factors would need to be even for the Principle to apply and is it reasonable to make those factors even.

Seeking a more empirical or "objective" definition of probability paved the way for the development of the Frequentist definition of probability. Rather than a comparison to the principle of indifference, frequentism defined probability as the relative frequency of the result of an event over a number of trials (Venn, 1888). Specifically, it views the notion that in the limit of infinite trials, the relative frequency tends to the probability of the result, i.e.

$$p(A) = \lim_{n\to\infty} \frac{n_A}{n}, \tag{3.2}$$

where n represents the number of trials that have taken place and n_A the number of trials in which A was true. It is therefore the case that in frequentist probability the proposition varies in the repeated trials, e.g. in the Pride and Prejudice example the man is in want of a wife in some number of trials and not in want of a wife in others.

Frequentism represented the dominant view of probability through the nineteenth and much of the twentieth centuries—and remains a widely used probability theory even now. It is an extremely useful tool in fields where the application of repeated trials is easily performed. For instance, medical statistics or in the analysis of games of chance. However, in the astrophysical realm, it is often the case that we seek to describe statistically phenomena which we cannot repeat in a laboratory setting.

To answer the desire for such a definition of probability, we turn to the third and final definition of probability. The Bayesian definition. It is much more similar to the Classical definition, and indeed the work of the Reverend Thomas Bayes (Bayes, 1763) for whom this definition is named was contemporaneous with that of the Classical definition. In this "subjective" definition of probability, it is viewed as the *degree of belief* or *plausibility* of the statement.

This differs from Frequentism in that Bayesian propositions are either wholly true or wholly false, and the probability is assigning how plausible each state is, e.g. each examined man is either in want of a wife or not, and our check of many of them would reveal how plausible it is for the next man to want a wife. Indeed, this definition does not require multiple trials in order to arrive at a statement of plausibility, with even complete ignorance being a perfectly acceptable starting point from a Bayesian perspective.

Because each proposition must either be true or false, it does therefore follow in this view of probability that

$$p(A|I) + p(\overline{A}|I) = 1, \tag{3.3}$$

where A remains our proposition, I indicates any supporting beliefs or background information (for instance, in the Austen example we are presupposing that the individual is a man) and | indicates that presupposition relationship and is termed the *conditional probability*—that is, it may be read as "the probability of A conditioned on I being true". Equation 3.3 is known as the *sum rule*.

The secondary rule concerns *joint probability*, i.e. $p(A, B|I)$. We are often times interested in the question of how this is related to the probability of individual propositions. The *product rule* informs that this is constructed as

$$\begin{aligned} p(A, B|I) &= p(B|A, I) \times p(A|I) \\ &= p(A|B, I) \times p(B|I) \end{aligned}, \tag{3.4}$$

i.e. "the probability of both A and B is equal to the product of the probability of one proposition given the other and the probability of that other proposition".

The relationship between joint and conditional probability shown in Equation 3.4 and in particular the symmetry in the two forms leads directly to the most central tenet of Bayesian probability, Bayes Theorem (Bayes, 1763):

$$p(A|B, I) = \frac{p(A|I)\,p(B|A, I)}{p(B|I)}. \tag{3.5}$$

This simple relationship encodes the notion of updating our belief in something given new information. For instance, returning to our Austen example, we may now update our belief in the notion that the man is in want of a wife to learning more information about him—say learning that he is single or in possession of good fortune. This is also how we may say that in Bayesian analysis, the state of total ignorance is an acceptable starting point—an advantage over a Frequentist framework.

3.4 Hypothesis Spaces & Probability Density Functions

Thus far, such as in the Austen example, we have considered a space that has a number of specific propositions that have discrete states, i.e. the man is single or the man is not single. A more general system may have n such discrete states, and we would be concerned with the probability of a given *hypothesis*, $\mathcal{H}$, that the system will be in one of these states. In the Austen example, these states are purely binary and thus the sum rule directly shows that the total probability that must be 1. This remains true in general systems, where the total probability of the system being in one of the states must be 1. This is termed a *discrete hypothesis space*, and this requirement is termed *normalisation*, i.e.

$$\sum_{i=1}^{n} p(\mathcal{H}_i|I) = 1 \tag{3.6}$$

However, in many cases we will be interested in spaces that have an arbitrarily large number of possible states. For instance, this would be the case when we consider the value of a parameter in a system such as any physical quantity. Here these are termed to be in the *continuum* limit and thus form a *continuous hypothesis space*. In this case, when we consider $p(A|I)$, it is no longer a specific probability but a probability density function (PDF) which may be given by (Gregory, 2005)

$$p(A|I) = \lim_{\delta a \to 0} \frac{p(a < A < a + \delta a|I)}{\delta a}. \tag{3.7}$$

The probability that the parameter A is within the range given by a to $a + \delta a$ is thus given by $p(A|I)\delta a$, and so for a proposition B that the value of parameter A lies between a and b, the probability would be given by

$$p(B|I) = \int_a^b p(A|I)dA \tag{3.8}$$

The requirement for normalisation remains, with the summation of Equation 3.6 being replaced with the integral over the range of hypotheses, $\Delta\mathcal{H}$,

$$\int_{\Delta\mathcal{H}} p(\mathcal{H}|I)d\mathcal{H} = 1 \tag{3.9}$$

We may relate PDFs for two different parameters A and B that are related such that a function, f exists that uniquely maps a value of A to a value of B, i.e. $b = f(a)$. In this case the relation between $p(b)$ and $p(a)$ is

$$p(b) = p(a)\left|\frac{\partial a}{\partial b}\right|. \tag{3.10}$$

3.5 Marginalisation

As we have noted, it is often the case that hypotheses consist not only of a single parameter, but of several. It is also the case that we do not always care equally about all of the parameters that make up the hypothesis; we may view some of these parameters as *nuisance parameters*. We may seek to eradicate these parameters through the process of *marginalisation*.

To construct the mathematics of marginalisation, we will consider a relatively small problem, where our hypothesis consists of two parameters, A and B, and we are of the view that A is useful and B is a nuisance parameter. For the sake of simplicity in this illustration, we will assume that B is a discrete parameter that may take one of n states. If we have some background information, I, and have acquired some useful data, D, then we would start from the joint probability for the model parameters, i.e. $p(A, B|D, I)$, and we aim for the single parameter probability $p(A|D, I)$.

From our joint probability, we may use Equation 3.4 to split this into the conditional probability

$$p(A, [B_1 + \ldots + B_n]|D, I) = p([B_1 + \ldots + B_n]|D, I) \times p(A|[B_1 + \ldots + B_n], D, I), \tag{3.11}$$

where we have separated B into the set of values that B may take. The requirement for probability to be normalised tells us that the first term of Equation 3.11 is simply 1. In the second term, the truth of $[B_1 + \ldots + B_n]$ is actually contained within our background information given that we are presupposing the truth of our model and that in this model the parameter B may only take one of these n values. It may therefore be replaced with $p(A|D, I)$, i.e. our goal.

Rearranging Equation 3.11 we have an expression for our goal as

$$p(A|D, I) = p(A, [B_1 + ... + B_n]|D, I). \tag{3.12}$$

Deploying the distributivity of the logical product as established in Section 3.2, the joint probability may be rewritten as $p(\{A, B_1\} + ... + \{A, B_n\}|D, I)$. We may split this apart, by considering the sum and product rules to form the *extended sum rule* which may be derived for a general set of propositions by employing the sum and product rules as:

$$\begin{aligned}
p(X+Y|Z) + p(\overline{X+Y}|Z) &= 1 \\
\implies p(X+Y|Z) &= 1 - p(\overline{X}, \overline{Y}|Z) \\
&= 1 - p(\overline{X}|Z)p(\overline{Y}|\overline{X}, Z) \\
&= 1 - p(\overline{X}|Z)\left(1 - p(Y|\overline{X}, Z)\right) \\
&= 1 - p(\overline{X}|Z) + p(\overline{X}|Z)p(Y|\overline{X}, Z) \\
&= p(X|Z) + p(Y, \overline{X}|Z) \\
&= p(X|Z) + p(Y|Z)p(\overline{X}|Y, Z) \\
&= p(X|Z) + p(Y|Z)\left(1 - p(X|Y, Z)\right) \\
&= p(X|Z) + p(Y|Z) - p(Y|Z)p(X|Y, Z) \\
\therefore\ p(X+Y|Z) &= p(X|Z) + p(Y|Z) - p(X, Y|Z)
\end{aligned} \tag{3.13}$$

Considering Equation 3.13, one may note that in the case where X and Y are mutually exclusive, the joint probability is zero, reducing it to the sum of the two individual probabilities. We have noted that the parameter B in our discussion is discrete and takes one of these n states, so therefore the propositions in the set are in fact mutually exclusive, allowing Equation 3.12 to be rewritten as

$$\begin{aligned}
p(A|D, I) &= p(A, B_1|D, I) + ... + p(A, B_n|D, I) \\
p(A|D, I) &= \sum_{n=1}^{N} p(A, B_n|D, I)
\end{aligned}. \tag{3.14}$$

This is the mathematical description of marginalisation in the discrete case. It extends into the continuum limit as may be expected by replacing the summation with the integration over the space that the parameter B may occupy, i.e.

$$p(A|D, I) = \int_{\Delta B} p(A, B|D, I)db. \tag{3.15}$$

The ability to perform this marginalisation represents an advantage that Bayesian statistical analysis has over Frequentist statistical analysis as the latter has no general way of handling these nuisance parameters. Being able to deal with these nuisance parameters significantly speeds up analysis given that each parameter that must be analysed increases the computational cost of the analysis.

3.6 Bayesian Inference

We may now return to Bayes Theorem (Equation 3.5) in the context of the hypothesis spaces that we have discussed in section 3.4.

3.6.1 Parameter Estimation

Firstly we consider the problem of *parameter estimation*. This is the problem where we have some hypothesis, $\mathcal{H}$, that depends on a set of parameters θ, and we are interested in how our knowledge of this set of parameters is updated by acquiring some data, $\mathcal{D}$. Rewriting Bayes Theorem for this case, we have

$$p(\theta|\mathcal{D},\mathcal{H}) = \frac{p(\theta|\mathcal{H})p(\mathcal{D}|\theta,\mathcal{H})}{p(\mathcal{D}|\mathcal{H})}, \tag{3.16}$$

and we now turn to discuss each of the terms of Bayes Theorem in more detail.

Posterior $p(\theta|\mathcal{D},\mathcal{H})$ represents the state of our knowledge about the model parameters, *after* the inclusion of the data that we have gathered, hence *posterior*. To examine the individual state of knowledge about a given parameter in the parameter set θ, one may marginalise this posterior over the others, i.e.

$$p(\theta_1|\mathcal{D},\mathcal{H}) = \int p(\theta_1, ..., \theta_n|\mathcal{D},\mathcal{H}) d\theta_2 ... d\theta n. \tag{3.17}$$

This will be used in particular to show the probability density for individual parameters in the following chapters.

To summarise the posterior, we may look at a few specific values, the first of which is the mean which may be given by

$$\langle\theta\rangle = \int_{\theta_{\min}}^{\theta_{\max}} p(\theta|\mathcal{D},\mathcal{H})\theta d\theta. \tag{3.18}$$

In cases where the mean of the posterior is not as useful, such as where there is multi-modality in the posterior which may result in the mean ending up in a point of low probability, one may also consider the median of the posterior, θ_{med} which is defined such that

$$\int_{\theta_{\min}}^{\theta_{\text{med}}} p(\theta|\mathcal{D},\mathcal{H}) d\theta = 0.5. \tag{3.19}$$

We may also define a *confidence interval* which expresses the probability that the parameter is within the given interval. This is constructed as

$$\gamma_x = \int_{\theta_{\text{low}}}^{\theta_{\text{high}}} p(\theta|\mathcal{D}, \mathcal{H})d\theta, \tag{3.20}$$

where x represents the percentage of the probability density included in the region defined by θ_{low} and θ_{high}. This is often referred to as the x%-confidence interval, and commonly we are concerned with the 68%, 95%, and 99% confidence intervals.

Prior $p(\theta|\mathcal{H})$ represents the state of our knowledge about the model parameters, *prior* to the inclusion of the data. As we have noted in the previous sections this state may be one of total ignorance. The simplest means of representing this state is by returning to the Principle of Indifference discussed in the context of Classical probability. This results in the application of the Uniform distribution, i.e. all outcomes are equally likely. However, there exists a probability distribution known as the *Jeffreys Prior* (Jeffreys, 1946) which will be invariant under re-parameterisations of the model parameters, θ, which allows for a more generalised description of ignorance.

Likelihood $p(\mathcal{D}|\theta, \mathcal{H})$ is the probability of the data given the hypothesis and the set of parameters. It is frequently also given the notation, $\mathcal{L}(\theta)$.

Evidence $p(\mathcal{D}|\mathcal{H})$ is the probability of the data given only the hypothesis. It is frequently given the notation, $\mathcal{Z}$. We may define the evidence, by deploying the notion of marginalisation, specifically Equation 3.15, to say that

$$\mathcal{Z} \equiv p(\mathcal{D}|\mathcal{H}) = \int p(\mathcal{D}, \theta|\mathcal{H})p(\theta|\mathcal{H})d\theta. \tag{3.21}$$

It is for the reason that this is an integration of the likelihood over the prior space, that the evidence is also known as the *marginalised likelihood*.

Each of the constituent components of the Bayes Theorem for a given set of data, hypothesis, and parameters may be more or less difficult to compute which may make the problem of Bayesian inference more or less tractable.

3.6.2 Model Selection

There are often cases in which more than just a single model, there are a number of potential models that will solve a given problem. In which case, we would wish to have a framework to identify the most likely model. Bayesian statistical analysis may easily extend to that as well. This is done through the *posterior odds ratio*, which as the name implies is simply the ratio of the posterior probabilities for the models, i.e.

$$O_{ij} = \frac{p(\mathcal{H}_i|\mathcal{D})}{p(\mathcal{H}_j|\mathcal{D})}, \tag{3.22}$$

for hypothesis $\mathcal{H}_i$ and $\mathcal{H}_j$. Applying Equation 3.5 to this, we may rewrite O_{ij} as

$$O_{ij} = \frac{p(\mathcal{D}|\mathcal{H}_i)p(\mathcal{H}_i)}{p(\mathcal{D}|\mathcal{H}_j)p(\mathcal{H}_j)} = \frac{\mathcal{Z}_i}{\mathcal{Z}_j}\frac{p(\mathcal{H}_i)}{p(\mathcal{H}_j)}, \tag{3.23}$$

where we may note that the denominator of Bayes theorem has cancelled out, leaving us with two factors, the ratio of the evidences $\frac{\mathcal{Z}_1}{\mathcal{Z}_2}$ which is termed the *Bayes Factor*, $\mathcal{B}$, and the *prior odds ratio*. The priors of a model selection problem are frequently chosen such that the prior odds ratio is unity allowing it to be eliminated from the calculation.

We have shown in Equation 3.21 that the evidence is the marginalisation of the likelihood over all of the parameters of the hypothesis. This has the mathematical consequence of encoding an implementation of the principle of parsimony, or Occam's Razor which may be summarised as that "*the simplest explanation is usually the correct one*". This is encoded as penalising unnecessary parameters to counter the fact that any data set could be explained by an arbitrarily large number of fine-tuned parameters—for instance by the construction of a spline.

To demonstrate this we consider a simple scenario where we have two competing hypotheses: $\mathcal{H}_1$ which consists of a simple free parameter θ, and $\mathcal{H}_2$ which fixes this parameter to a specific value θ_0. We first consider the prior, if we assume a uniform prior over a range $\Delta\theta$ then the requirement for the normalisation of the prior will give

$$\begin{aligned} \int_{\Delta\theta} p(\theta|\mathcal{H}_1)d\theta = p(\theta|\mathcal{H}_1)\Delta\theta = 1 \\ \therefore\ p(\theta|\mathcal{H}_1) = \frac{1}{\Delta\theta} \end{aligned}. \tag{3.24}$$

The likelihood for this parameter, $\mathcal{L}(\theta)$, will have some characteristic distribution width, $\delta\theta$, which is defined as (Gregory, 2005)

$$\int_{\Delta\theta} p(\mathcal{D}|\theta, \mathcal{H}_1)d\theta = p(D|\widehat{\theta}, \mathcal{H}_1) \times \delta\theta = \mathcal{L}(\widehat{\theta}) \times \delta\theta, \tag{3.25}$$

where $\widehat{\theta}$ denotes the value of θ that has *maximised likelihood*, i.e. the value of θ most likely to produce the data. Combining Equations 3.24 and 3.25 with Equation 3.21 means that

$$\mathcal{Z}_1 \approx \mathcal{L}(\widehat{\theta})\frac{\delta\theta}{\Delta\theta}. \tag{3.26}$$

The case of $\mathcal{H}_2$ given that it has no free parameters would be equivalent to the likelihood of $\mathcal{H}_1$ specifically at the value θ_0, i.e. $\mathcal{L}(\theta_0)$, which means that the Bayes factor between the two would be given by

$$\mathcal{B}^1_2 = \frac{\mathcal{L}(\widehat{\theta})}{\mathcal{L}(\theta_0)}\frac{\delta\theta}{\Delta\theta}, \tag{3.27}$$

where we have the ratio of the likelihoods and the ratio of the likelihood and prior widths. Given that, as we noted, the likelihood of $\mathcal{H}_2$ is a subset of the likelihood of $\mathcal{H}_1$, the likelihood ratio will always favour the more complex hypothesis. However, the likelihood width is *significantly* narrower than the prior width which has the effect of boosting support for the simpler model.

3.7 Markov Chain Monte Carlo

The most obvious approach to construction a posterior distribution would be to sample uniformly across the prior space of each of the parameters and construct a grid from which to calculate the posterior. This approach is known as *grid searching* and will always produce a complete posterior; however, as it scales exponentially—sampling N points for M parameters will require N^M samples—, it rapidly becomes computationally intractable for all but the simplest problems—especially where calculation of the likelihood is non-trivial.

One approach for a more efficient method of parameter estimation which targets the *un-normalised* posterior distribution $p(\theta|\mathcal{D},\mathcal{H}) \propto \mathcal{L}(\theta)p(\theta|\mathcal{H})$ which avoids the need to calculate the Bayesian evidence, $\mathcal{Z}$, through integration involves Markov Chain Monte Carlo (MCMC) methods. MCMC methods sample from the probability distribution in such a way as to produce samples that are distributed proportionally to this un-normalised posterior.

There are a number of implementations of MCMC methods such as Gibbs sampling (Geman & Geman, 1984; Gelfand & Smith, 1990) or Hamiltonian Monte Carlo (Duane et al., 1987; Betancourt, 2018) as well as extensions to the method such as Reversible Jump Monte Carlo (Green, 1995). However, to introduce the concept, we focus on the Metropolis-Hastings algorithm (Metropolis et al., 1953; Hastings, 1970).

Firstly, we split the MCMC term into its constituent components i.e. *Markov chains* and *Monte Carlo integration*:

Monte Carlo Integration As the name implies, this is a means of performing integration. In this case, for a function $\mathcal{F}(\theta)$ that we wish to integrate, sampling n points uniformly over the volume, V, that we wish to integrate over allows the approximation of the integral as (Gregory, 2005)

$$\int_V \mathcal{F}(\theta)d\theta \approx V \times \langle\mathcal{F}(\theta\rangle \pm V \times \sqrt{\frac{\left\langle\mathcal{F}^2(\theta)\right\rangle - \langle\mathcal{F}(\theta)\rangle^2}{n}}, \tag{3.28}$$

where

$$\begin{aligned}\langle \mathcal{F}(\theta) \rangle &= \frac{1}{n}\sum_{i=1}^{n}\mathcal{F}(\theta_i) \\ \left\langle \mathcal{F}^2(\theta) \right\rangle &= \frac{1}{n}\sum_{i=1}^{n}\mathcal{F}^2(\theta_i)\end{aligned} . \tag{3.29}$$

The precision of the result is ultimately dependent on the value of n so it may be increased or decreased in order to achieve a desired speed or accuracy.

Markov Chains A Markov Chain is a chain of samples where the sample θ_{i+1} is dependent only upon the previous sample θ_i. This means it is a random or *stochastic* sampling of the space. The dependency between the samples is dictated by the *transition kernel*, $p(\theta_{i+1}|\theta_i)$ which is presumed to be time-independent—i.e. no matter where in the chain one is, one can transition freely from one sample to the next.

The Metropolis-Hastings implementation of MCMC works by first selecting a new candidate sample for the chain from a *proposal distribution*, $p(\Theta|\theta_i)$, that is easy to sample from and accepting this as the new sample with a probability determined by the *acceptance ratio* (Gregory, 2005)

$$r = \frac{p(\Theta|\mathcal{D},\mathcal{H})\,p(\theta_i|\Theta)}{p(\theta_i|\mathcal{D},\mathcal{H})\,p(\Theta|\theta_i)} \tag{3.30}$$

which may be done by simultaneously sampling from the uniform distribution between 0 and 1 and accepting the proposed sample if the uniform sample is less than or equal to the acceptance ratio. This is shown algorithmically in Algorithm 1.

This algorithm may be deployed on both symmetric and asymmetric proposal distributions which allow the chains to be guided towards regions of higher probability. As the chain progresses, after an initial period of *burn-in* which may be discarded it will produce samples that are proportional to the target distribution.

A disadvantage of this approach is that, in the case of significantly multi-modal distributions, the chain may get stuck in one area of the modes. Additionally, this approach does not provide an estimate of the Bayesian evidence, $\mathcal{Z}$, given the target is the posterior. Both of these limitations may be alleviated by the use of a process called *tempering* (Goggans & Chi, 2004).

This process introduces an annealing parameter, β, known as the *temperature* to the target distribution, i.e.

$$p(\theta|\beta,\mathcal{D},\mathcal{H}) \propto p(\theta|\mathcal{H})\mathcal{L}(\theta)^{\beta} \tag{3.31}$$

Creating a number of chains with different temperatures in parallel and then combining the chains

Algorithm 1: The Metropolis-Hastings Algorithm

```
$\theta_0 \leftarrow$ Initial value;
$i \leftarrow 0$;
$n \leftarrow$ Target number of samples;
while $i < n$ do
    $\Theta \leftarrow$ sampled from $p(\Theta|\theta_i)$;
    $r \leftarrow$ from Equation 3.30;
    $U \leftarrow$ sampled from Uniform distribution between 0 and 1;
    if $U \leq r$ then
        $\theta_{i+1} \leftarrow \Theta$;
    else
        $\theta_{i+1} \leftarrow \theta_i$;
    end
    $i \leftarrow i + 1$;
end
```

to achieve the final estimate. This is known as *parallel tempering*. This helps to alleviate the former limitation as chains with lower β are exploring a space that more strongly resembles the prior which means they are more likely to explore the entire space and not get stuck in individual peaks of the posterior. This may be propagated to the chains with higher β by periodically swapping chain locations (Veitch et al., 2015).

The parallel tempering process also allows an estimation of the natural logarithm of the evidence, $\mathcal{Z}$, to be calculated as (Friel & Pettitt, 2008)

$$\log \mathcal{Z} = \int_0^1 \mathcal{E}_{\theta \sim p(\theta|\beta)} \left(\log \mathcal{L}(\theta) \right) d\beta, \tag{3.32}$$

i.e. the integration of the *expectation value* of the log of the likelihood for samples of θ drawn from the target distribution. The expectation value of a quantity, θ, with associated probability density function $p(\theta)$, is given by

$$\mathcal{E}_\theta = \int_{-\infty}^{\infty} \theta p(\theta) d\theta. \tag{3.33}$$

3.8 Nested Sampling

Nested sampling is an alternative approach to solving the problems of Bayesian parameter estimation and model selection proposed by John Skilling (Skilling, 2004, 2006). Where the MCMC approach focuses on the production of the posterior, the nested sampling approach focuses on the calculation of the evidence and in so doing produces the posterior as a by-product. Algorithm 2 provides a summary of the implementation supplemented by the following discussion.

It introduces a new quantity called the *prior volume* or *prior mass*, x, which is the amount of the prior space that is associated with likelihood greater than some value L and can be calculated as

Algorithm 2: Nested Sampling

```
$\mathcal{Z} \leftarrow 0$;
$x_0 \leftarrow 1$;
$\mathcal{L} \leftarrow 0$;
$i \leftarrow 0$;
Sample $N$ live points, $\{\theta_1, ..., \theta_N\}$, from $p(\theta|\mathcal{H})$;
while termination criterion not met do
    $i \leftarrow i + 1$;
    $\mathcal{L}_i \leftarrow \min\left\{\mathcal{L}(\theta_i)\right\}$;
    Remove $\theta$ corresponding to $\mathcal{L}_i$ from live point set;
    Compute $t_i$, $x_i$, and $w_i$ for $\mathcal{L}_i$;
    $\mathcal{Z}_i \leftarrow \mathcal{Z}_i + \mathcal{L}_i w_i$;
    Sample new live point from $p(\theta|\mathcal{H})$ with constraint that $\mathcal{L}(\theta) > \mathcal{L}_i$;
end
for $\theta_i$ in final live point set do
    $\mathcal{L}_i \leftarrow \mathcal{L}(\theta_i)$;
    $N \leftarrow N - 1$;
    Compute $t_i$, $x_i$, and $w_i$ for $\mathcal{L}_i$;
    $\mathcal{Z}_i \leftarrow \mathcal{Z}_i + \mathcal{L}_i w_i$;
end
```

$$x(L) = \int_{\mathcal{L}(\theta)>L} p(\theta|\mathcal{H}) d\theta. \tag{3.34}$$

It may be obviously noted that the extremes of L are defined by 0 and $\mathcal{L}_{\max}$ and that at these extremes the values of $x(L)$ are 1 and 0 respectively. We may therefore note that an infinitesimal slice of this prior volume, dx, will associate with likelihoods in the range $[L, L + dL]$. Defining the inverse function $L(x)$, we may see that this will result in a positive decreasing function such that $L(0) = \mathcal{L}_{\max}$ and $L(1) = 0$. This allows us to rewrite the evidence as (Skilling, 2004)

$$\mathcal{Z} = \int_0^1 L(x) dx \tag{3.35}$$

and so the goal of the nested sampling algorithm is to estimate the area under the curve defined by $L(x)$. This may be done by considering a set of N points, $\{x_1, ..., x_n\}$, known as *live points* which are ordered so as to have decreasing prior volume and from which the equivalent series of likelihood values, $\mathcal{L}_i$ may be calculated. This allows estimation the evidence as the weighted sum

$$\mathcal{Z} \leftarrow \sum_{i=1}^{N} w_i \mathcal{L}_i \tag{3.36}$$

where the weights may be estimated using for instance the trapezoidal rule, $w_i = \frac{1}{2}(x_{i-1} - x_{i+1})$ with reflective boundary conditions $x_0 = 2 - x_1$ and $x_{N+1} = -x_N$ (Skilling, 2006). An illustration of this is shown in Figure 3.1.

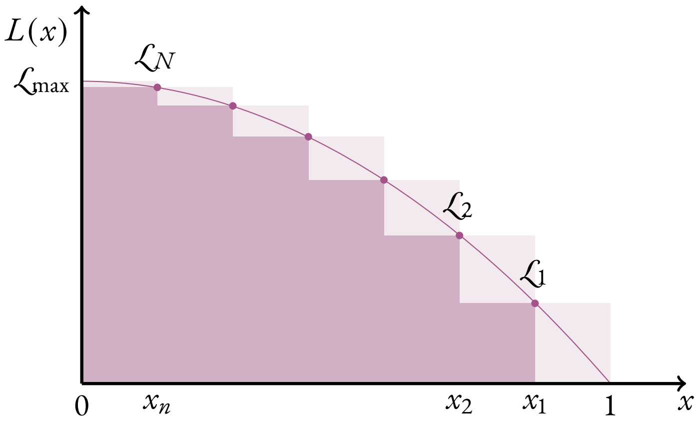

Figure 3.1: An illustration of the prior volume and likelihood relationship. The shaded rectangles correspond to the two values used to apply the trapezoidal rule to illustrate the approximation of the area under the curve. Adapted from Skilling (2006).

We have noted the requirement that the prior volume samples must be ordered in decreasing value. This would therefore allow us to construct the next sample as

$$x_i = t_i x_{i-1}, \tag{3.37}$$

where $0 < t_i < 1$ is termed the *shrinkage ratio*. Noting that $t_1 = x_1$, one may then construct the series as the geometric sum of these t_i. In principle to find the next live point, x_i one would sample from the uniform distribution, $\mathcal{U}(0, 1)$, and then evaluate the sample x_i and sort it into correct positioning. However, in order to do this, this would require a function that would map $x \rightarrow \mathcal{L}(\theta) \rightarrow \theta$ and to performing the sorting which is inefficient.

To avoid this, we may therefore invert this relation and consider that the constraint that $x_i < x_{i-1}$ is equivalent to $\mathcal{L}(\theta)_i > \mathcal{L}(\theta)_{i-1}$, and instead sample θ from the prior to gain a sample that meets this constraint and then compute the prior volume, x_i. The sampling of the prior to achieve the likelihood constraint may be done by MCMC methods (Skilling, 2006).

With the set of N samples drawn, we may then remove the point with the lowest $\mathcal{L}$ as a *dead point*. This dead point is used to update the estimate for the evidence, and then a new sample is drawn from the prior with the requirement that $\mathcal{L} > \mathcal{L}_{\text{dead point}}$. This process is repeated until it reaches some *termination criterion*. This may be set in terms of the contribution of the new dead point to the evidence which may be evaluated as (Skilling, 2006; Speagle, 2020)

$$\Delta \log \widehat{\mathcal{Z}}_i \equiv \log\left(\widehat{\mathcal{Z}}_{\text{live}} + \widehat{\mathcal{Z}}_i\right) - \log \widehat{\mathcal{Z}}_i \tag{3.38}$$

where $\widehat{\mathcal{Z}}_{\text{live}} = \mathcal{L}_{\max} x_i$ is the evidence resulting from the current maximum likelihood value of the live points and $\widehat{\mathcal{Z}}_i$ is the evidence contribution from the current dead point. The specific value to use for the termination criterion is arbitrary but for two of the major GW data analysis pipelines—LALInference (Veitch et al., 2015) and Bilby (Ashton et al., 2019)—a value of 0.1 is considered the default and sufficient for use.

Once the termination criterion has been met, the evidence estimate may be updated using the remaining live point additions to the likelihood which should form a relatively small correction assuming the termination criterion is sensibly chosen (Skilling, 2006; Speagle, 2020).

As noted, this process allows the posterior weight for each sample to be calculated as a by-product for each sample once the final evidence estimate is reached as

$$p_i = \frac{\mathcal{L}_i w_i}{\mathcal{Z}}. \tag{3.39}$$

4

Gravitational Waves

> *In the darkness, two shadows, reaching through the hopeless, heavy dusk. Their hands meet, and light spills in a flood, like a hundred golden urns pouring out the sun.*
>
> —*The Song of Achilles*
>
> Madeline Miller

We now turn our discussions to gravitational waves. We have in Chapter 2 discussed the fact that in the theory of GR the presence of mass deforms space-time into having curvature and this is the reason for gravity. This means that, unlike in the Newtonian view, space-time is now an elastic medium. One might picture this like a ball on a sheet of fabric. It causes a dip in the fabric around it creating a "well". If one now pictures a second ball on this fabric and then spiraling the two balls in towards each other, they will see this cause a rippling of the fabric. Returning to space-time, this ripple is a gravitational wave. These waves represent an entirely different way of examining the broader universe. One may think of this as the difference between "seeing" the universe with EM and "hearing" it with GWs.

4.1 Nearly-Flat Space-time

We know that, in the absence of massive objects, space-time is flat and may be described by the Minkowski metric of Special Relativity, $\eta_{\alpha\beta}$. It therefore stands to reason that very weak gravitational fields should result in a space-time that's *nearly* flat. The metric of such a space-time may be described in terms of a *perturbation* to the Minkowski metric, i.e.

$$g_{\alpha\beta} = \eta_{\alpha\beta} + h_{\alpha\beta} \tag{4.1}$$

where $|h_{\alpha\beta}| << 1$ describes the amount that the space-time is perturbed from flatness. To head towards an explanation for GW, we may examine the effects of this perturbation to linear order, neglecting the higher order terms at this time.

For this metric, we may calculate the Riemann-Christoffel tensor from Equation 2.42. To linear order, this will result in (Maggiore, 2008)

$$R_{\alpha\beta\delta\gamma} = \frac{1}{2}\left(h_{\alpha\delta,\gamma\beta} + h_{\beta\gamma,\alpha\delta} - h_{\beta\delta,\alpha\gamma} - h_{\alpha\gamma,\beta\delta}\right), \tag{4.2}$$

which is a similar form to that for flat space given by Equation 2.44. Continuing on from this point, we may compute the Ricci tensor from Equation 2.50, i.e. contracting over the first and third indices, which yields

$$\begin{aligned} R_{\alpha\beta} &= \frac{1}{2}\left(h^{\gamma}{}_{\beta,\gamma\alpha} + h^{\gamma}{}_{\alpha,\gamma\beta} - h_{\alpha\beta,\gamma\gamma} - h^{\gamma}{}_{\gamma,\alpha\beta}\right) \\ &= \frac{1}{2}\left(h^{\gamma}{}_{\beta,\gamma\alpha} + h^{\gamma}{}_{\alpha,\gamma\beta} - \Box h_{\alpha\beta} - h_{,\alpha\beta}\right) \end{aligned} \tag{4.3}$$

where we have defined $h = \eta^{\alpha\beta}h_{\alpha\beta} = h^{\alpha}{}_{\alpha}$ and the *d'Alembertian* operator, $\Box$, as the second derivative in flat space, i.e. $\Box = -\partial_t^2 + \partial_x^2 + \partial_y^2 + \partial_z^2$. To complete the set of curvature quantities, we may contract again to reach the Ricci scalar which will yield (Maggiore, 2008)

$$R = h^{\alpha\beta}{}_{,\alpha\beta} - \Box h. \tag{4.4}$$

Recalling the definition of the Einstein Tensor (Equation 2.55), in the nearly-flat space-time this will therefore be given by

$$G_{\alpha\beta} = \frac{1}{2}\left(h^{\gamma}{}_{\beta,\gamma\alpha} + h^{\gamma}{}_{\alpha,\gamma\beta} - \Box h_{\alpha\beta} - h_{,\alpha\beta} - \eta_{\alpha\beta}h^{\delta\varepsilon}{}_{\delta\varepsilon} + \eta_{\alpha\beta}\Box h\right). \tag{4.5}$$

This can be directly inserted into the EFE (Equation 2.75) to achieve a solution to linear order for this perturbed space-time. However, given that expressions must hold in *all* co-ordinate systems, we are free to choose one that simplifies this expression to allow us to more easily solve the system. In this instance, we choose to use the *Lorenz Gauge* in which we require that (Maggiore, 2008)

$$\bar{h}^{,\beta}{}_{\alpha\beta} = 0, \tag{4.6}$$

where $\bar{h}_{\alpha\beta} = h_{\alpha\beta} - \frac{1}{2}\eta_{\alpha\beta}h$. Moving to the Lorenz Gauge, will thus yield (Schutz, 2009)

$$G_{\alpha\beta} = \frac{1}{2}\Box\bar{h}_{\alpha\beta}, \tag{4.7}$$

which means that the EFE become

$$\Box\bar{h}_{\alpha\beta} = -16\pi T^{\alpha\beta}, \tag{4.8}$$

which may be known as the *linearised EFE* given our requirement of keeping things to linear order. As noted in Chapter 2, there are sixteen elements of these tensors which indicates up to sixteen independent components. The symmetries that are required for the EFE reduce this to ten (Maggiore, 2008). The choice of the Lorenz gauge has introduced four additional constraints, i.e. Equation 4.6 reducing the number of independent components to six.

4.2 Gravitational Wave Equation

We are now ready to directly show the existence of GWs which we do now by considering the case of the vacuum far away from the source of the gravitational field. In such a case, the energy-momentum tensor reduces to 0, and thus 4.8 simply becomes, after expanding out the d'Alembertian operator and exiting natural units,

$$\left(-\frac{1}{c^2}\frac{\partial}{\partial t^2}+\frac{\partial}{\partial x^2}+\frac{\partial}{\partial y^2}+\frac{\partial}{\partial z^2}\right)\bar{h}_{\alpha\beta}=0, \tag{4.9}$$

this is directly a wave equation. These gravitational waves are also directly implied to be travelling at the speed of light. This equation will permit any solution of the form (Schutz, 2009)

$$\bar{h}_{\alpha\beta}=A_{\alpha\beta}\exp\left(ik_\alpha x^\alpha\right), \tag{4.10}$$

where $A_{\alpha\beta}$ are the components of a tensor, k_α are the components of a one-form, and x^α are as always the components of the position vector. We may demonstrate that our suggested solution is indeed a solution to Equation 4.9 by considering its derivatives

$$\begin{aligned} \bar{h}_{\alpha\beta,\gamma} &= ik_\gamma \bar{h}_{\alpha\beta} \\ \implies \eta^{\gamma\delta} h_{\alpha\beta,\gamma\delta} &= -\eta^{\gamma\delta} k_\gamma k_\delta \bar{h}_{\alpha\beta} \end{aligned}, \tag{4.11}$$

this will be a solution of the expression if the pre-factor is zero. This can only be the case if

$$\eta^{\gamma\delta}k_\gamma k_\delta = k^\delta k_\delta = 0 \tag{4.12}$$

i.e. if the four vector k^α associated with the one-form k_α is a *light-like* vector indicating it must travel along the same world-lines as photons and therefore the wave must travel at the speed of light, c. We may identify the temporal component of this vector as the *frequency* of the wave, ω. The spatial components of the vector k^i indicate the *direction of propagation of the wave*.

We may also note that the choice of the Lorenz Gauge requires that the upper expression of Equation 4.11 must also evaluate to zero, which requires that

$$k^\beta A_{\alpha\beta}=0, \tag{4.13}$$

the physical interpretation of which is that $A_{\alpha\beta}$ must be orthogonal to $\vec{k}$. With the physical interpretations of the k_α and x^α in place, we may also note that the physical interpretation of $A_{\alpha\beta}$ indicates the *amplitude* of the gravitational wave.

With our solution in mind, we return to our statement that as of Equation 4.8 we have six independent components. We may reduce that further by noting that the Lorenz Gauge condition may still be met if we transform for the co-ordinates x^α to $x^\alpha+\xi^\alpha$ where we require that

$$\Box\xi_\alpha = 0. \tag{4.14}$$

This will produce a change in $\bar{h}_{\alpha\beta}$ given by

$$\bar{h}^{\text{New}}_{\alpha\beta} = \bar{h}^{\text{Old}}_{\alpha\beta} - \xi_{\alpha,\beta} - \xi_{\beta,\alpha} + \eta_{\alpha\beta}\xi^{\gamma}{}_{,\gamma}\,. \tag{4.15}$$

We may note that the d'Alembertian operator for flat space commutes with partial differentiation which means that $\Box\xi_{\alpha\beta} = 0$ where $\xi_{\alpha\beta}$ is given by the last three terms of Equation 4.15. Given that we have a solution for Equation 4.9, we may directly note that Equation 4.14 implies that a solution exists of the form

$$\xi_\beta = B_\beta \exp\left(ik_\alpha x^\alpha\right), \tag{4.16}$$

where B_β is a constant vector and k^α remains the same vector as in Equation 4.10. This solution may be inserted into Equation 4.15 alongside Equation 4.10 to note two additional restrictions on the tensor $A_{\alpha\beta}$ (Schutz, 2009):

$$\begin{aligned} A^{\alpha}{}_{\alpha} &= 0 \\ A_{\alpha\beta}U^{\beta} &= 0 \end{aligned}, \tag{4.17}$$

for a chosen fixed four-velocity U^β. The gauge defined by these restrictions atop the choice of the Lorenz Gauge is called the *Transverse-Traceless (TT)* gauge. We may note that in this gauge,

$$\bar{h}^{\text{TT}}_{\alpha\beta} = h^{TT}_{\alpha\beta}, \tag{4.18}$$

from our definition of $\bar{h}$.

In the TT gauge if we consider a wave where we orient ourselves such that the wave is propagating entirely in the z-direction, then the vector k^α will take the form $(\omega, 0, 0, \omega)$ given the light-like requirement of this vector. The TT gauge condition from the lower expression in Equation 4.17 requires that $A_{\alpha 0} = 0$, again for all α. Combining this with the Lorenz gauge condition then requires $A_{\alpha z} = 0$, again for all α. This leaves only A_{xx}, A_{yy}, and $A_{xy} = A_{yx}$ as non-zero components, and we may deploy the upper expression of Equation 4.17 to note that $A_{yy} = -A_{xx}$, which thus leaves only two independent components of $A_{\alpha\beta}$ from the original sixteen, i.e. we have reduced $A_{\alpha\beta}$ to

$$A_{\alpha\beta} = \begin{pmatrix} 0 & 0 & 0 & 0 \\ 0 & A_{xx} & A_{xy} & 0 \\ 0 & A_{xy} & -A_{xx} & 0 \\ 0 & 0 & 0 & 0 \end{pmatrix}. \tag{4.19}$$

4.3 Effects on Matter

Solutions to the gravitational wave equation (Equation 4.9) may all be transformed into super-positions of the plane wave solution (Schutz, 2009). This means that it is always possible to reduce the system to have only the two independent components h^{TT}_{xx} and h^{TT}_{xy} and so may transfer to this frame to consider the effect of a free particle encountering a GW. This free particle by definition travels along the geodesic as defined by Equation 2.27 which in this instance would be

$$\frac{dU^{\alpha}}{d\tau} + \Gamma^{\alpha}{}_{\beta\gamma} U^{\beta} U^{\gamma} = 0. \tag{4.20}$$

Upon interaction with the GW, the particle would have an acceleration imparted on it given by $-\Gamma^{\alpha}{}_{00}$. However, our requirements for the TT gauge have required that $h^{TT}_{\beta 0} = 0$ which means the particle remains at rest. This argument may be continued ad infinitum which suggests that the effect of the GW does not change the co-ordinates of the particle in this frame. This is not particularly, surprising given that, as was noted in Chapter 2, the basis vectors of a co-ordinate system need not remain constant over time. This apparent stillness is the consequence of the frame choice.

Aside: Geodesic Deviation

We have noted in Chapter 2 that global parallelism does not exist in curved spaces. Therefore, it may come as no surprise to learn that when extending a pair of geodesics they do not maintain their separation and that this is related to the curvature of the considered space—given that we know that in the flat space limit they must maintain their separation. The amount that their separation changes over the space is known as *geodesic deviation*, and may be derived from consideration of a connecting vector of the type we discuss here.

For two geodesics that begin locally parallel with tangent vectors $\vec{A}$ and $\vec{A}'$, we will consider two points P and P' linked by the *connecting vector*, $\vec{\xi}$ meaning that both points are the result of the same value of the affine parameter. Adopting the locally inertial frame at P, $V^{\alpha} = \delta^{\alpha}{}_{0}$. The Christoffel symbols vanish at this point, so the geodesic equation at the point P is

$$\left.\frac{d^2 x^{\alpha}}{d\lambda^2}\right|_{P} = 0. \tag{4.21}$$

The Christoffel symbols do not vanish at other points, so for the point P', the equivalent expression, maintaining that $V^{\alpha} = \delta^{\alpha}{}_{0}$, is

$$\left.\frac{d^2 x^{\alpha}}{d\lambda^2}\right|_{P'} + \Gamma^{\alpha}{}_{00}(P') = 0, \tag{4.22}$$

where we may insert that the Christoffel symbol due to the connection vector may be expressed as $\Gamma^{\alpha}{}_{00,\beta}\xi^{\beta}$ evaluated at P. Given that the difference between the x^{α} evaluated at points P and P' define the components of ξ, this means that

$$\frac{d^2\xi^\alpha}{d\lambda^2} = -\Gamma^\alpha{}_{00,\beta}\xi^\beta \tag{4.23}$$

which may be converted to the second covariant derivative as follows

$$\begin{aligned} A^0\xi^\alpha{}_{;0} &= A^0\xi^\alpha{}_{,0} + \Gamma^\alpha{}_{\beta 0}\xi^\beta \\ \implies A^0A^0\xi^\alpha{}_{;0;0} &= A^0\left(A^0\xi^\alpha{}_{,0} + \Gamma^\alpha{}_{\beta 0}\xi^\beta\right)_{;0} \\ &= A^0A^0\xi^\alpha{}_{,0;0} + A^0\left(\Gamma^\alpha{}_{\beta 0}\xi^\beta\right)_{;0}, \end{aligned} \tag{4.24}$$

where we here note that the right hand expression must be zero since the Christoffel symbols vanish when evaluated at P. Recalling that the derivatives commute we thus proceed

$$\begin{aligned} A^0A^0\xi^\alpha{}_{;0;0} &= A^0A^0\xi^\alpha{}_{;0,0} \\ &= A^0A^0\left(\xi^\alpha{}_{,0} + \Gamma^\alpha{}_{\beta 0}\xi^\beta\right)_{,0} \\ &= A^0A^0\left(\xi^\alpha{}_{,0,0} + \Gamma^\alpha{}_{\beta 0,0}\xi^\beta + \Gamma^\alpha{}_{\beta 0}\xi^\beta{}_{,0}\right). \end{aligned} \tag{4.25}$$

We next insert Equation 4.23, note that the requirement for initial parallelism between the two geodesics means that $\xi^\beta{}_{,0} = 0$, and finally recall the definition of the Riemann-Christoffel tensor (Equation 2.42) to arrive at

$$\xi^\alpha{}_{;0;0} = R^\alpha{}_{00\beta}\xi^\beta, \tag{4.26}$$

which may be generalised to other bases from this point to (Schutz, 2009)

$$A^\beta A^\zeta\xi^\alpha_{;\beta;\zeta} = R^\alpha{}_{\gamma\delta\varepsilon}A^\gamma A^\delta\xi^\varepsilon. \tag{4.27}$$

We may examine the effects of the GW on particles more completely by considering a two particle system rather than a single particle. These particles are separated for simplicity only in the x-axis by a co-ordinate distance ε. Considering the case of two freely falling particles, we note that each of these is travelling along a separate geodesic and so we may define the connecting vector, $\vec{\xi}$ between them. If we examine the TT gauge again, we will see that the particles appear to be at rest and the connecting vector will remain unchanged which does not help more than the single particle examination.

If, however, we consider not the TT gauge, but the local inertial frame at the origin of the connecting vector. In this frame, to linear order the co-ordinate distance is equivalent to the *proper distance*—the spatial equivalent to the proper time described in Section 2.9. This simplifies the left hand side of Equation 4.27 due to the Christoffel symbols vanishing in this frame which reduces the covariant derivative to the ordinary derivative, i.e.

$$\frac{d^2\xi^\alpha}{d\tau^2} = R^\alpha{}_{\gamma\delta\beta}U^\gamma U^\delta \xi^\beta, \tag{4.28}$$

where the vector $\vec{U}$ is the four-velocity of the two particles to linear order. This means that $\vec{U} \to (1,0,0,0)$ and in the initial moment that $\vec{\xi} \to (0,\varepsilon,0,0)$, and so Equation 4.28

$$\frac{d^2\xi^\alpha}{d\tau^2} = R^\alpha{}_{00x}\varepsilon = -R^\alpha{}_{0x0}\varepsilon. \tag{4.29}$$

The Riemann-Christoffel tensor is frame and gauge invariant, which would therefore imply that there must be a gauge invariant meaning behind the left hand side of the expression as well. This meaning is that the ξ^α indicate the proper distances over the four co-ordinates for the interval spanned by the connecting vector, i.e. between the particles. We may insert Equation 2.42 to transfer the Riemann tensor into $h_{\alpha\beta}$ which yields

$$\begin{aligned}\frac{\partial^2}{\partial\tau^2}\xi^x &= \frac{1}{2}\varepsilon\frac{\partial^2}{\partial\tau^2}h^{TT}_{xx}\\ \frac{\partial^2}{\partial\tau^2}\xi^y &= \frac{1}{2}\varepsilon\frac{\partial^2}{\partial\tau^2}h^{TT}_{xy}.\end{aligned} \tag{4.30}$$

This tells us that the proper distance between these two particles will change over time as an effect of the wave. That it is the proper distance that is changing means that this effect can thus be measured by experiment. We may also go one step further and understand the physical meanings of the two independent components of $h_{\alpha\beta}$. First, we note that repeating the above process for the two particles separated by the same co-ordinate distance in the y-axis only will result in

$$\begin{aligned}\frac{\partial^2}{\partial\tau^2}\xi^x &= \frac{1}{2}\varepsilon\frac{\partial^2}{\partial\tau^2}h^{TT}_{xy}\\ \frac{\partial^2}{\partial\tau^2}\xi^y &= -\frac{1}{2}\varepsilon\frac{\partial^2}{\partial\tau^2}h^{TT}_{xx}\end{aligned}. \tag{4.31}$$

Consider a ring of particles in the $x-y$ plane encountering a GW propagating in the z-direction that is such that only one of h_{xx} or h_{xy} non-zero. The effects of this are clearly the superposition of the two above effects. This is shown below in Figure 4.1 where we may note that the two cases are 45°rotations of each other. Given that h_{xx} and h_{xy} are independent, the interpretation of this is that these are two *linear polarisation* states.

For a more general separation of particles in this scenario, Equation 4.10 informs us that the h_{ij} in this scenario would be given by

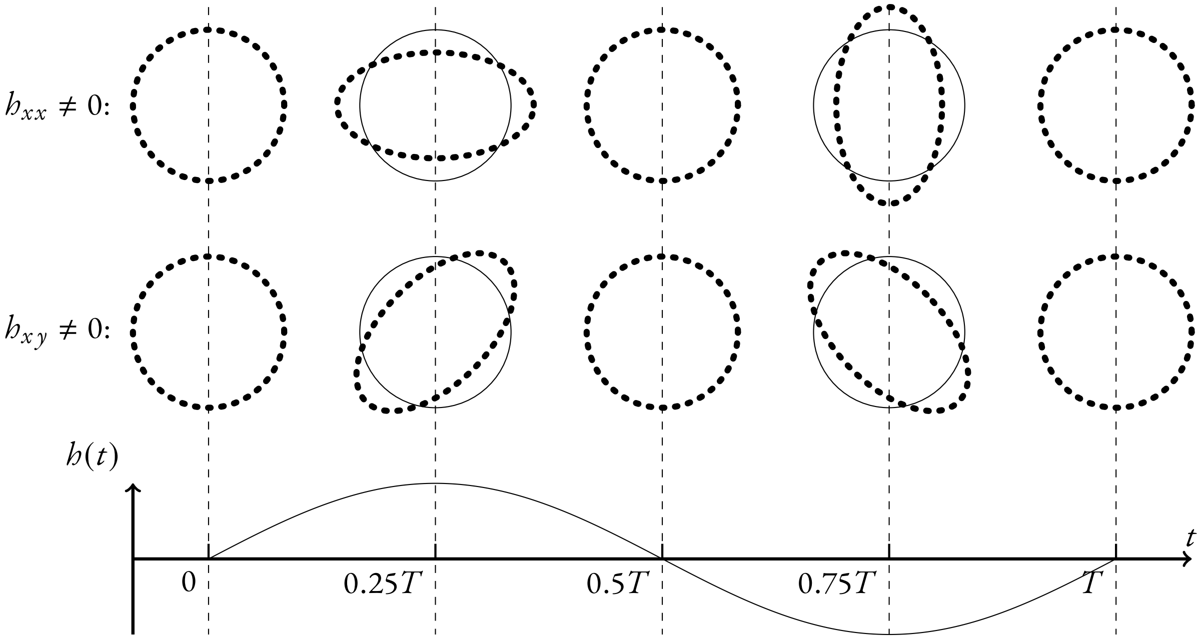

Figure 4.1: Illustration of the effects of a GW on a ring of particles, for the case where only one of h_{xx} and h_{xy} is non-zero, over the course of a period (T) of the wave. As may be noted the effects for each case are at a 45°rotation to each other.

$$\begin{aligned}
h_{ij} &= \begin{pmatrix} A_{xx} & A_{xy} & 0 \\ A_{xy} & -A_{xx} & 0 \\ 0 & 0 & 0 \end{pmatrix} \exp\left(-iw(ct-z)\right) \\
&= \left(\begin{pmatrix} A_{xx} & 0 & 0 \\ 0 & -A_{xx} & 0 \\ 0 & 0 & 0 \end{pmatrix} + \begin{pmatrix} 0 & A_{xy} & 0 \\ A_{xy} & 0 & 0 \\ 0 & 0 & 0 \end{pmatrix} \right) \exp\left(-iw(ct-z)\right) \\
&= \begin{pmatrix} 1 & 0 & 0 \\ 0 & -1 & 0 \\ 0 & 0 & 0 \end{pmatrix} a \exp\left(-iw(ct-z)\right) + \begin{pmatrix} 0 & 1 & 0 \\ 1 & 0 & 0 \\ 0 & 0 & 0 \end{pmatrix} b \exp\left(-iw(ct-z)\right) \\
&= h_{+} e^{+}_{ij} + h_{\times} e^{\times}_{ij}
\end{aligned} \tag{4.32}$$

where we have introduced the notation + and × to refer to the two polarisation states.

4.4 Generation of Gravitational Waves

We now turn to the question of how GWs would be generated. This requires solving the linearised EFE in the presence of matter, i.e. a non-zero energy-momentum tensor. This is done by employing a *Green's function*, $G(x-x')$, which is defined as the solution to the equation

$$\Box_x G(x-x') = \delta^4(x-x'), \tag{4.33}$$

which would make the solution to the linearised EFE, exiting natural units, be given by

$$\bar{h}_{\alpha\beta}(x) = -\frac{16\pi G}{c^4}\int G(x-x')T_{\alpha\beta}(x')d^4x'. \tag{4.34}$$

To proceed further and fully solve Equation 4.34 we must impose a boundary condition which allows us to select the Green's function. The condition that we impose is that there is no incoming radiation at the source of the gravitational waves, i.e. that the source of the gravitational waves is only a source and not also a sink. The imposition of this condition results in the Green's function being the *retarded Green's function* (Maggiore, 2008)

$$G(x-x') = -\frac{1}{4\pi|\vec{x}-\vec{x}\,'|}\delta(ct_{\text{ret}}-ct'), \tag{4.35}$$

where t_{ret} is termed the *retarded time* and is given by

$$t_{\text{ret}} = t - \frac{|\vec{x}-\vec{x}\,'|}{c}. \tag{4.36}$$

Inserting this into Equation 4.34 then yields

$$h_{\alpha\beta}(t,x^i) = \frac{4G}{c^4}\int \frac{1}{|\vec{x}-\vec{x}\,'|}T_{\alpha\beta}(t_{\text{ret}},\vec{x})d^3x'. \tag{4.37}$$

We may transfer this solution to the TT gauge by applying a co-ordinate transformation tensor, $\Lambda_{ij,kl}$, similar to that in Equation 2.60. This yields

$$h_{ij}^{TT} = \frac{4G}{c^4}\Lambda_{ij,kl}(\hat{x})\int \frac{1}{|\vec{x}-\vec{x}\,'|}T_{kl}(t_{\text{ret}},\vec{x})d^3x', \tag{4.38}$$

where $\hat{x}$ indicates the direction perpendicular to that of $\vec{x}$. We may now define $r = |\vec{x}|$ and note that in the limit of very large distances that r is significantly larger than the characteristic size of the source and so to leading order $|\vec{x}-\vec{x}\,'| = r$, and so Equation 4.38 becomes

$$h_{ij}^{TT} = \frac{4G}{c^4 r}\Lambda_{ij,kl}(\hat{x})\int T_{kl}(t_{\text{ret}},\vec{x})d^3x'. \tag{4.39}$$

Our attention, must therefore turn to the integral of the energy-momentum tensor. We begin by Fourier transforming the energy-momentum tensor

$$T_{kl}(t_{\text{ret}},\vec{x}) = \int \frac{1}{(2\pi)^4}\tilde{T}_{kl}(\omega,\vec{k})e^{-i\omega t_{\text{ret}}+i\vec{k}\cdot\vec{x}}. \tag{4.40}$$

In the so-called *slow motion* limit where the velocities within the source are significantly less than the speed of light, the exponential of the retarded time may be expanded as (Maggiore, 2008)

$$e^{-i\omega t_{\text{ret}}} = e^{-i\omega(t-r/c)}\left(1 - i\frac{\omega}{c}x'^i\hat{x}^i + \frac{1}{2}\left(-i\frac{\omega}{c}\right)^2 x'^i x'^j\hat{x}^i\hat{x}^j + \dots\right), \tag{4.41}$$

which is equivalent to the expansion of $T_{kl}(t_{\text{ret}},\vec{x})$ as (Maggiore, 2008)

$$T_{kl}(t_{\text{ret}}, \vec{x}) = T_{kl}(t - \frac{r}{c}, \vec{x}) + \frac{x'^i \hat{x}^i}{c}\frac{\partial T_{kl}}{\partial t} + \frac{x'^i x'^j \hat{x}^i \hat{x}^j}{2c^2}\frac{\partial^2 T_{kl}}{\partial t^2} + \ldots \tag{4.42}$$

We may now introduce the *momenta* of the energy-momentum tensor which are defined as (Maggiore, 2008)

$$\begin{aligned} S^{ij}(t) &= \int T^{ij}(t, \vec{x}) dx^3 \\ S^{ij,k}(t) &= \int T^{ij}(t, \vec{x}) x^k dx^3, \end{aligned} \tag{4.43}$$

and so on. We noted in Section 2.9 that the conservations of energy and momentum require that the derivatives of the energy-momentum tensor be zero (Equation 2.73). We therefore may note that this requires

$$T^{00}{}_{,0} = -T^{0i}{}_{,i} \tag{4.44}$$

which means that should we introduce the momenta, M, of the energy density, $\frac{1}{c^2}T^{00}$ and the momenta, P, of the linear momentum $\frac{1}{c}T^{0i}$ defined in a similar fashion to Equation 4.43, then these must be such that (Maggiore, 2008)

$$S^{ij} = \dot{P}^{i,j} = \frac{1}{2}\ddot{M}^{ij}, \tag{4.45}$$

which reduces Equation 4.39 at leading order to

$$h_{ij}^{TT}(t, \vec{x}) = \frac{2G}{c^4 r}\Lambda_{ij,kl}(\hat{x})\ddot{M}^{kl}(t - r/c), \tag{4.46}$$

or introducing the moment of inertia tensor, Q^{ij} given for mass density, ρ, by

$$\begin{aligned} Q^{ij} &\equiv M^{ij} - \frac{1}{3}\delta^{ij} M_{kk} \\ &= \int d^3x \rho(t, \vec{x}) \left(x^i x^j - \frac{1}{3} r^2 \delta^{ij} \right), \end{aligned} \tag{4.47}$$

to

$$h_{ij}^{TT}(t, \vec{x}) = \frac{2G}{c^4 r}\ddot{Q}_{ij}^{TT}. \tag{4.48}$$

The fact that the leading order is quadrupolar is a direct consequence of the conservation of energy and momentum which cause the monopolar and dipolar moments to be zero. The physical consequence of this is that motion that is spherically or axially symmetric will not produce gravitational waves as these do not produce a non-zero quadrupolar moment.

We may also combine Equations 4.46 and Equation 4.32 to note that, again to leading order, in the individual polarisation modes we we would have (Maggiore, 2008)

$$\begin{aligned} h_+ &= \frac{G}{c^4 r}\left(\ddot{M}_{11} - \ddot{M}_{22}\right) \\ h_\times &= \frac{2G}{c^4 r}\ddot{M}_{12}. \end{aligned} \tag{4.49}$$

We may note that the term $\frac{G}{c^4}$ is of the order 10^{-45}. This indicates that in general the amplitudes of GWs are extremely small and therefore only the most highly energetic systems would be able to produce a measurable effect—and that even for these systems measurement will require significant sensitivity.

4.5 Sources of Gravitational Waves

The requirement for extremely energetic systems pushes the potential sources of GWs into the astrophysical realm. Given that the only requirement is non-axisymmetric motion, one may envision any number of plausible scenarios to produce GWs. In general, the astrophysical sources of GWs may be divided into four categories of GW signal that they produce or contribute to. Each of these will be discussed in turn in the following sections.

4.5.1 Burst Signals

Generic transient signals may be produced by a wide array of astrophysical phenomena. These signals are typically referred to as *burst* signals and are sub-classified based on length into long duration and short duration. In contrast to the CBC signals discussed below which are also transient signals, burst signals may display a wide array of morphologies that may not necessarily have defined waveforms and may be complex to model. Whilst targeted searches for those models that do exist may be performed, burst signals may also be searched for using more generic search strategies (Abbott et al., 2017a, 2019a, 2021g).

Some examples of sources which would produce transient signals would be gamma ray bursts (Aasi et al., 2014), core-collapse supernovae (Abbott et al., 2020b), neutron star excitations (Abbott et al., 2019g), pulsar glitches (Abadie et al., 2011), non-linear memory effects from CBCs (Ebersold & Tiwari, 2020), parabolic or hyperbolic encounters of black holes (Cho et al., 2018), and the features of cosmic strings (Abbott et al., 2021h)—though this list is necessarily non-exhaustive since there may always be astrophysical processes of which we are unaware.

Searches for transient signals have been carried out concurrently with the searches for other signals during the observing runs of the current GW detector network. However, all signals that have been identified from the current searches have also been identified as CBC signals (Abbott et al., 2021g).

4.5.2 Continuous Waves

The requirement to produce GW signals is that of non-axisymmetric motion. The rotation of any non-axisymmetric neutron star would therefore be a source of GWs that would be extremely long duration and would produce a signal with amplitude given at a frequency f and a distance r from the source by (Maggiore, 2008)

$$h_0 = \frac{4\pi^2 G}{c^4}\frac{\varepsilon I_{zz} f^2}{r}, \tag{4.50}$$

where I_{zz} is the moment of inertia of the star with respect to its rotational axis, ε is the ellipticity which quantifies the asymmetry of the neutron star. We focus on neutron stars in particular given that they may be sufficient to produce measurable GW signals. Searches have been conducted for continuous GW signals from neutron stars in a variety of places but have not as yet conclusively identified any continuous wave signals (Abbott et al., 2021i,j, 2022a,b)

In addition to the rotation of neutron stars, another proposed source of continuous wave signals are boson clouds around spinning black holes. Again, searches have been conducted but have so far found no support for such signals (Abbott et al., 2022c).

4.5.3 The Stochastic Background

EM observations of the universe reveal the presence of the Cosmic Microwave Background (CMB); a nearly completely isotropic source of radio emission across the whole sky that is a result of the moment at which the early universe became optically thin. There is an analogous GW phenomenon in the form of the stochastic gravitational wave background which is a superposition of GW sources that is similarly isotropic across the whole sky though that may permit anisotropy at small scales (Abbott et al., 2019b).

There are a number of sources that may contribute to this background such as the unresolvable contributions from the other sources discussed in the surrounding sections. Other potential contributors to the stochastic background would be the inflation of the early universe (Turner, 1997), a preheating phase at the end of inflation (Easther et al., 2007), or phase transitions in the early universe (Marzola et al., 2017).

Searches have been conducted in the current GW detector network data for this background and upper limits have been placed on its potential strength (Abbott et al., 2017b; Abbott et al., 2019c, 2021k).

4.5.4 Compact Binary Coalescences

Consider the scenario of two compact objects, e.g. black holes or neutron stars, with masses m_1 and m_2 that are in a binary system with a common centre of mass and are separated by some distance r. In particular, we will assume that these objects are performing circular orbits with orbital frequency, ω_s, and choose co-ordinates such that the z-axis points in the direction of the observer and the origin is at the centre-of-mass. The angle between the z-axis and the direction perpendicular to the orbital plane will be termed the *inclination angle*, ι. An illustration of this scenario is given in Figure 4.2.

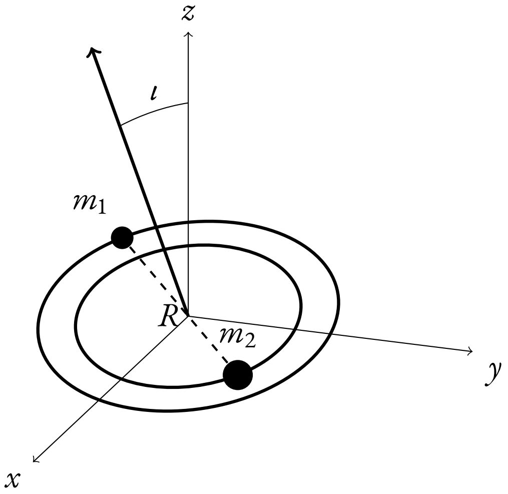

Figure 4.2: Illustration of two compact objects in circular orbits around a common centre of mass. These objects are seperated by distance R, and the binary has inclination angle, ι, with respect to the z-axis on which the observer is placed. Adapted from Figure 3.6 of Maggiore (2008).

We may define a *relative co-ordinate* for the two objects, $\overrightarrow{x_0} = \overrightarrow{x_1} - \overrightarrow{x_2}$, and choose that the trajectory of this relative co-ordinate in this scenario to be given by (Maggiore, 2008)

$$\begin{aligned} x_0 &= R\cos\left(\omega_s t + \frac{\pi}{2}\right) \\ y_0 &= R\sin\left(\omega_s t + \frac{\pi}{2}\right) \\ z_0 &= 0. \end{aligned} \tag{4.51}$$

Presuming that the objects are non-relativistic in orbital speed then, in the co-ordinate system that we have chosen, the second mass moment reduces to

$$M^{ij} = \mu x_0^i x_0^j, \tag{4.52}$$

where μ is the *reduced mass* given by $\mu = m_1 m_2/(m_1 + m_2)$. Inserting Equation 4.51 into Equation 4.52 yields that the only non-zero components of the second mass moment are

$$\begin{aligned} M_{11} &= \mu R^2 \frac{1 - \cos(2\omega_s t)}{2} \\ M_{22} &= \mu R^2 \frac{1 + \cos(2\omega_s t)}{2} \\ M_{12} &= \mu R^2 \frac{\sin(2\omega_s t)}{2}. \end{aligned} \tag{4.53}$$

Thus we see that we will have non-zero components of the second derivative given by

$$\begin{aligned} \ddot{M}_{11} &= 2\mu R^2 \omega_s^2 \cos 2\omega_s t \\ \ddot{M}_{22} &= -\ddot{M}_{11} \\ \ddot{M}_{12} &= 2\mu R^2 \omega_s^2 \sin 2\omega_s t. \end{aligned} \tag{4.54}$$

This will lead to, when accounting for the rotation of co-ordinates from the propagation in the z-axis used to compute Equation 4.49,

$$\begin{aligned} h_+ &= \frac{1}{r}\frac{4G\mu\omega_s^2 R^2}{c^4}\left(\frac{1+\cos^2\iota}{2}\right)\cos(2\omega_s t) \\ h_\times &= \frac{1}{r}\frac{4G\mu\omega_s^2 R^2}{c^4}\cos\iota\sin(2\omega_s t). \end{aligned} \tag{4.55}$$

We may also note that Kepler's third law requires that

$$\omega_s^2 = \frac{G(m_1+m_2)}{R^3}, \tag{4.56}$$

and by eliminating R in favour of ω_s, and defining the *chirp mass*

$$\mathcal{M}_c = \mu^{3/5}(m_1+m_2)^{2/5} = \frac{(m_1 m_2)^{3/5}}{(m_1+m_2)^{1/5}}, \tag{4.57}$$

we may rewrite Equation 4.55 as

$$\begin{aligned} h_+ &= \frac{4}{r}\left(\frac{G\mathcal{M}_c}{c^2}\right)^{5/3}\left(\frac{\omega_s}{c}\right)^{2/3}\left(\frac{1+\cos^2\iota}{2}\right)\cos(2\omega_s t) \\ h_\times &= \frac{4}{r}\left(\frac{G\mathcal{M}_c}{c^2}\right)^{5/3}\left(\frac{\omega_s}{c}\right)^{2/3}\cos\iota\sin(2\omega_s t). \end{aligned} \tag{4.58}$$

This scenario is a demonstration of the fact that even in circular orbits the two-body problem results in the emission of GWs. This would have an important consequence that has been neglected in the prior derivation—that the production of GWs would cause energy to leave the system and the orbits to slowly decay. This decay was first observed for the Hulse-Taylor pulsar (Hulse & Taylor, 1975; Taylor & Weisberg, 1982) providing the first indirect evidence for the existence of GWs.

The total power emitted by GWs in the above scenario may be given by Maggiore (2008)

$$P = \frac{32}{5}\frac{c^5}{G}\left(\frac{G\mathcal{M}_c\omega_{\rm gw}}{2c^3}\right)^{10/3}, \tag{4.59}$$

where $\omega_{\rm gw} = 2\omega_s$ is the rotational frequency of the GW. This energy must come from the orbital energy which is given by

$$E_{\text{orbit}} = -\frac{G m_1 m_2}{2R}, \tag{4.60}$$

and so therefore losses to the orbital energy must have corresponding losses in the separation between the two objects. This results in an increase in ω_s from Kepler's third law, which increases the power emitted by the GW. Consequently, this process will repeat until the two objects coalesce.

So long as the condition,

$$\dot{\omega}_s << \omega_s^2 \tag{4.61}$$

holds, then we may approximate the behaviour of this system as a circular orbit with a slowly varying radius. This is known as *quasi-circular motion*. By taking this approximation, we may use Kepler's third law, to rewrite the orbital energy as

$$E_{\text{orbit}} = -\left(\frac{G^2 \mathcal{M}_c^5 \omega_{\text{gw}}^2}{32}\right)^{1/3} \tag{4.62}$$

Equating the derivative with respect to time of Equation 4.62 and Equation 4.59, then converting from rotational frequency to GW frequency, $f_{\text{gw}} = \omega_{\text{gw}}/2\pi$, we arrive at

$$\dot{f}_{\text{gw}} = \frac{96}{5}\pi^{8/3}\left(\frac{G\mathcal{M}_c}{c^3}\right)^{5/3} f_{\text{gw}}^{11/3}. \tag{4.63}$$

Integrating Equation 4.63, there will be a finite time at which the frequency diverges. This is the *coalescence time*, t_c. The solution to the above—at observer time, t—in terms of this coalescence time is given by (Maggiore, 2008)

$$f_{gw}(t_c - t) = \frac{1}{\pi}\left(\frac{5}{256}\frac{1}{t_c - t}\right)^{3/8}\left(\frac{G\mathcal{M}_c}{c^3}\right)^{-5/8}. \tag{4.64}$$

The divergence of this expression is cut off by the fact that the compact objects have physical extent and cannot simply continue inspiralling indefinitely. After a certain point, they merge. We have noted in the derivation of this expression that we are taking the assumption of quasi-circular motion. It is clear that at some point this approximation will break down due to the strong gravitational fields near each of the compact objects. The last circular orbit possible is known as the Innermost Stable Circular Orbit (ISCO). The radius of this will be given by

$$r_{\text{ISCO}} = \frac{6G(m_1 + m_2)}{c^2}. \tag{4.65}$$

Beyond this radius the merger will occur. However, prior to that radius we may use a modification of Equation 4.58 to describe the produced waves. Defining the area swept out by the orbit over a period of time t as

$$\Phi(t) = \int_{t_0}^{t} \omega_{\text{gw}}(t')dt', \tag{4.66}$$

then we would have for each of the polarisation modes, an amplitude of (Maggiore, 2008)

$$\begin{aligned} h_+ &= \frac{1}{r}\left(\frac{G\mathcal{M}_c}{c^2}\right)^{5/4}\left(\frac{5}{c(t_c-t)}\right)^{1/4}\left(\frac{1+\cos^2\iota}{2}\right)\cos(\Phi(t_c-t)) \\ h_\times &= \frac{1}{r}\left(\frac{G\mathcal{M}_c}{c^2}\right)^{5/4}\left(\frac{5}{c(t_c-t)}\right)^{1/4}\cos\iota\sin(\Phi(t_c-t)). \end{aligned} \tag{4.67}$$

These systems are termed CBCs and in the searches conducted for these signals, as of the end of O3, the LVK Collaborations have found 90 signals, beginning with GW150914 (Abbott et al., 2016a), that have been identified as having a greater than 50% probability of astrophysical origin—i.e. being CBC signals (Abbott et al., 2023a). At time of writing, an additional confirmed CBC signal detection (The LIGO Scientific Collaboration et al., 2024) from the ongoing O4 has been released with there likely to be many others over the duration of the observing run.

4.6 Detection of Gravitational Waves using Interferometry

As has been noted in Chapter 1, the current ground based detector network consists of interferometer-based detectors. We now turn our discussion to this form of detector and how the detection of GWs occurs. Figure 4.3 illustrates the schematic breakdown of the LIGO detectors as they were at the time of the first GW detections.

The basic principle of the Michaelson interferometer, as discussed in Chapter 1, is that light travels from a source to the beam splitter, which sends two phase-aligned beams of light down each of the arms. Mirrors at the end of each arm reflect these beams back down the arms recombining the beams at the beam-splitter, and the results are directed towards a photodetector. Arms of the same length will result in destructive interference which means that the photodetector will receive no light. If however, the arms are slightly different lengths, then some light will reach the photodetector.

The response of the interferometer to a GW will depend on its orientation relative to the source. This allows the definition a function governing how sensitive the detector is across the sky, which is termed the *antenna response*. This is defined per-polarisation mode such that the measured strain of the interferometer is given by

$$h(t) = F_+(t)h_+(t) + F_\times(t)h_\times(t). \tag{4.68}$$

In addition to the sky location of the GW, it is also dependent upon ψ, termed the *polarisation angle* which indicates the rotation between the polarisation modes at the source and the polarisation modes at the detector. For an L-shaped interferometer such as the LIGO detectors, oriented such that

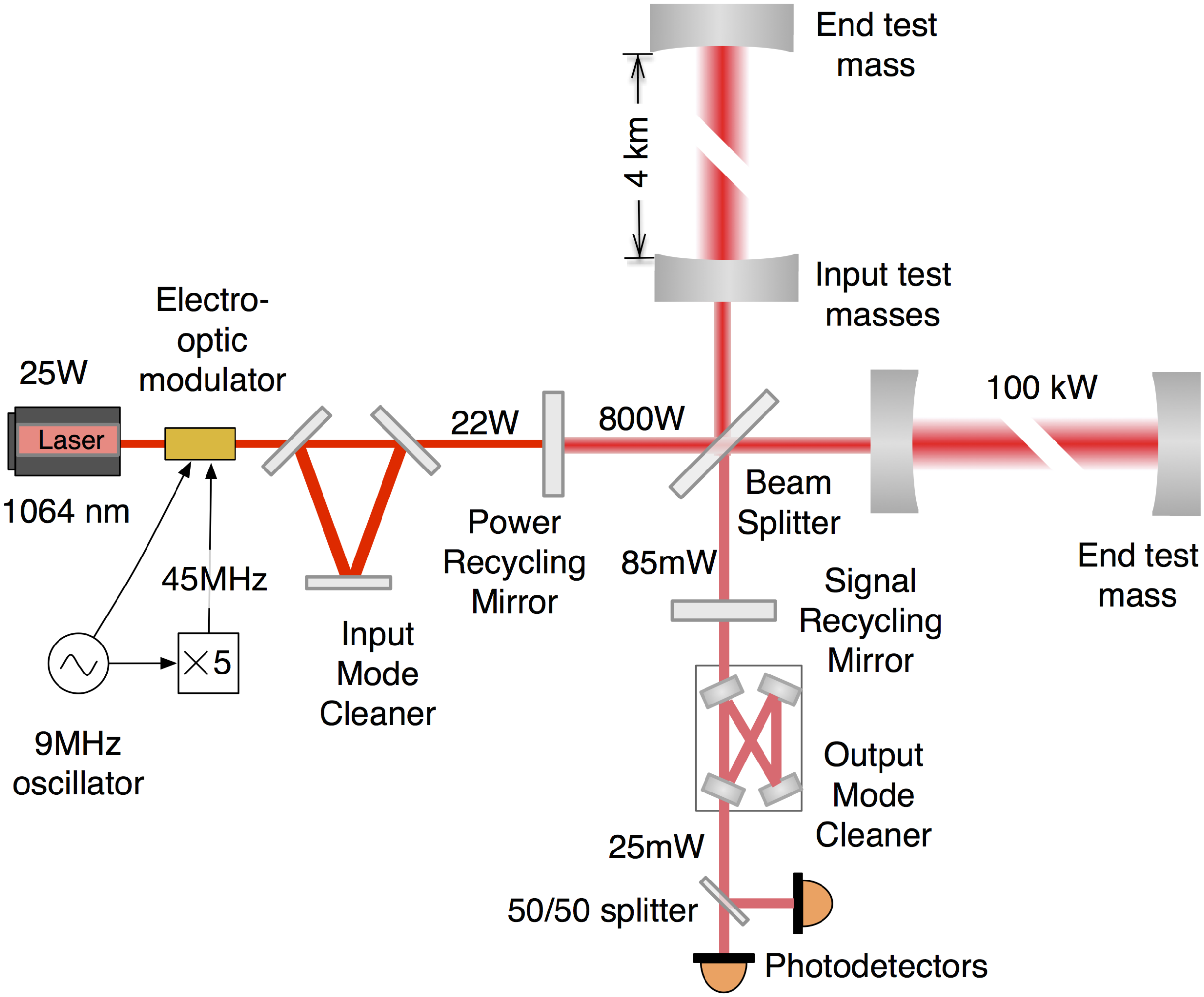

Figure 4.3: Schematic diagram of the Advanced LIGO detectors. The detector is a Michelson interferometer with 4km long arms. Fabray-Perot cavities within the arms amplify the signal. Additional measures such as power recycling and cleaning are used to further improve the sensitivity of the detector. Figure from Martynov et al. (2016).

the arms are on the x- and y-axes—illustrated in Figure 4.4—, the antenna response functions are given by (Schutz, 2011)

$$\begin{aligned} F_+ &= -\frac{1}{2}(1+\cos^2\theta)\cos 2\phi\cos 2\psi + \cos\theta\sin 2\phi\sin 2\psi \\ F_\times &= \frac{1}{2}(1+\cos^2\theta)\cos 2\phi\sin 2\psi + \cos\theta\sin 2\phi\cos 2\psi . \end{aligned} \tag{4.69}$$

We have discussed in Section 4.3 that GWs will cause the length of space to expand and contract, and in particular we illustrated the effect for a pair of masses separated vertically and horizontally in Figure 4.1. For a GW interferometer these masses are called the *input test mass* and *end test mass*, and the effect will differentially change the difference in the lengths of the arms. Specifically, for a pair of equal length, L,

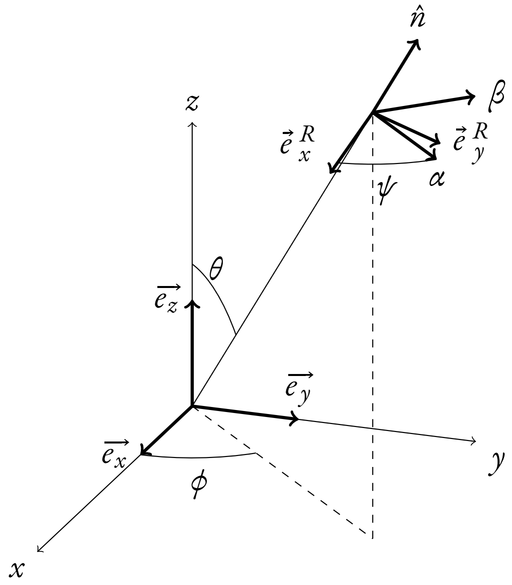

Figure 4.4: Illustration of the detector geometry resulting in the antenna response functions given in Equation 4.69. Figure adapted from Schutz (2011).

$$h = \frac{\Delta L}{L}. \tag{4.70}$$

We have already noted that h is an extremely small number. For instance, the detected strain for GW150914 was of the order 10^{-21} (Abbott et al., 2016a). The arm length of LIGO, as shown in Figure 4.3 is 4km, meaning that the change in the arm length would be of order 10^{-18}m. However, a number of strategies are employed to improve the sensitivity of the detector, some of which alter the effective length of the arms (Aasi et al., 2015; Acernese et al., 2014; Akutsu et al., 2020) which have allowed the detectors to reach the sensitivity required to detect GW signals. We briefly describe some of these strategies below.

Fabray-Pérot Cavity	Installed in each arm of the detector, these cavities reflect the input laser light repeatedly up and down the cavity before allowing the light to proceed, increasing the effective length of the arms. In the case of the LIGO interferometers, this increase is up to the order of 1100km.
Power Recycling	The placement of the power recycling mirrors form a resonance cavity with the source of the laser which increases the power of the laser significantly.
Signal Recycling	The placement of the signal recycling mirror reflects some of the output light from the signal back into the interferometer which has a similar effect to the above but at specifically the signal output which will improve the signal-to-noise ratio (SNR).

In addition to the low amplitude of GW signals, there are a number of sources of noise in the detectors that must be overcome to reach sufficient sensitivity for detection. The combination of these effects and the mitigation strategies against them ultimately determines the sensitivity of the detector. A breakdown of these noise sources into their contributions as a function of frequency for the LIGO detectors at the time of the first detections is shown in Figure 4.5.

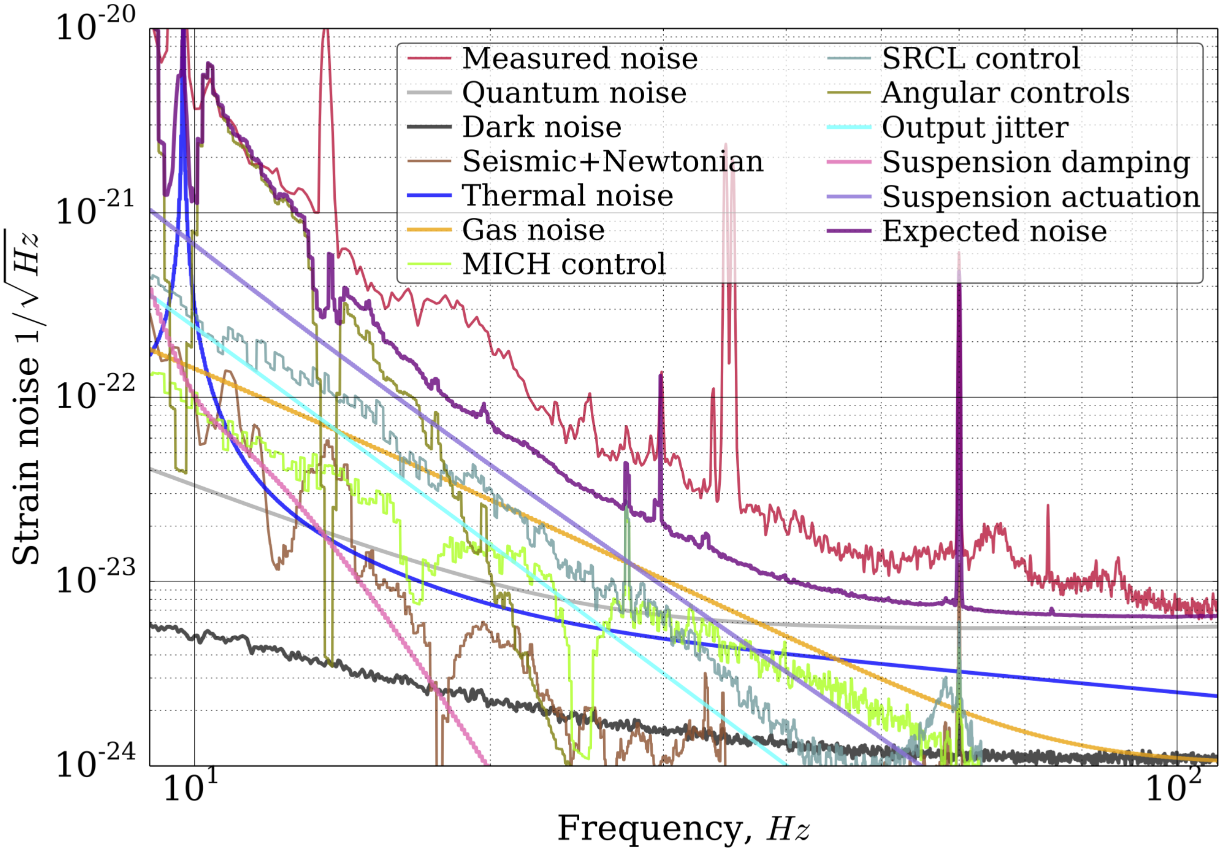

Figure 4.5: Plot of the contributing noise sources to the LIGO detectors at the start of O1. Figure from Martynov et al. (2016).

Below is a brief description of what some of the noise sources are:

Quantum Noise This is the result of fluctuations of the vacuum entering the interferometer. This results in two separate effects. The first of these is the causation of fluctuating radiation pressure on the test masses in the cavities which will physically move them (Buonanno & Chen, 2001). The strain sensitivity of radiation pressure noise is given, for a Michaelson interferometer with arm length L and test mass, M, , by (Maggiore, 2008)

$$S_n^{1/2}(f)\Big|_{\text{rad. pres.}} = \frac{1}{MLf^2}\sqrt{\frac{4\hbar P}{c\pi^3\lambda_L}}, \tag{4.71}$$

where P is the power of the incident laser at wavelength λ_L, and $\hbar$ is the reduced Planck constant.

The second resultant effect of the vacuum fluctuations is the shot noise—error in the output signal from the interferometer. In the same Michaelson interferometer as above, this results in a strain sensitivity of (Maggiore, 2008)

$$S_n^{1/2}(f)\Big|_{\text{shot}} = \frac{1}{L}\sqrt{\frac{\hbar c \lambda_L}{4\pi P}}. \tag{4.72}$$

The combination of these two effects is typically termed the Standard Quantum Limit, and represents a fundamental limit to the design sensitivity.

Seismic Noise This is the result of movement of the ground. There are a number of potential sources for this both geophysical seismic activity, such as Earthquakes or the micro-seismic background, and anthropogenic causes—such as nearby traffic. The strain sensitivity has the general form (Maggiore, 2008)

$$S_n^{1/2}(f)\Big|_{\text{seis}} = \frac{1}{L}10^{-7} f^{-2}. \tag{4.73}$$

As may be noted, this represents a significant potential source of noise and thus requires active mitigation. This is done in the current detector network in two forms, active and passive isolation. Passive isolation is achieved through the suspension of the optical components in a quadruple pendulum system (Aston et al., 2012). Active isolation is achieved by mounting the pendulum system on active platforms which are controlled by a seismometer (Martynov et al., 2016).

Thermal Noise This is the result of thermal vibrations of both the mirrors and the suspensions. The displacement spectral density for thermal noise may be given by (Maggiore, 2008)

$$x(\omega) = \frac{1}{\omega |Z(\omega)|}\left(4kT\Re(Z(\omega))\right)^{1/2}, \tag{4.74}$$

where T is the temperature, and Z is the *impedance* of the system—with $\Re$ denoting the real component. The impedance associated to a normal mode of an object with mass m and frequency, ω_0 can be generally modelled as (Maggiore, 2008)

$$Z = -\frac{im}{\omega}\left(\omega^2 - \omega_0^2 + i\omega^2\phi(\omega)\right), \tag{4.75}$$

where $\phi(\omega)$ is called the *loss angle*. These quantities would need to be computed for each of the components of the detector.

Newtonian Noise	This is the result of fluctuations in the local gravitational field around the test masses. These fluctuations are the consequence of all nearby motion around the detector. This may not be eliminated on a ground-based detector, though there are mitigation strategies such as operating underground or monitoring the fluctuations by means of a number of seismometers around the detector.
Gas Noise	This is the result of gas remaining the vacuum chambers in which the detector is operated. Residual gas will cause fluctuations in the refractive index scattering light from the lasers.
Transient Noise (Glitches)	A number of transient phenomena may occur in or around the detectors which may provoke a response in the detector which are known as *glitches*. These are obviously difficult to systematically, not least because certain scenarios may produce signals that mimic real GW events. One mitigation strategy against false positives from glitches is checking for coherency of the proposed candidate in multiple detectors since terrestrial phenomena may affect a subset or indeed only one of the detectors depending upon the source. Another is that various phenomena have distinct morphological structures that may be identified by human review or machine learning approaches.

Between these noise sources and the mitigation strategies employed to counter them, this ultimately yields the sensitivity of the detectors. The sensitivity of the LIGO detectors prior to the detection of the first GW signals, at the time of the first detections, and at full design sensitivity are shown in Figure 4.6.

4.7 Gravitational Wave Data Analysis

With an understanding of the response of the detector to a GW signal as well as potential sources of noise, we now turn to the question of extracting the GW signal from the noise in the detector. The total measured strain at the detector would be a combination of the signal as well as the total noise, i.e.

$$s(t) = h(t) + n(t), \tag{4.76}$$

or the equivalent relationship $\tilde{s}(f) = \tilde{h}(f) + \tilde{n}(f)$, in the frequency domain. Extracting the signal therefore will require models both of the signal and noise strains.

4.7.1 Modelling Noise

One simplification that is often made is to assume that the noise is both Gaussian in nature and stationary. Whilst this is in reality untrue, the approximation is sufficiently valid to allow its use with

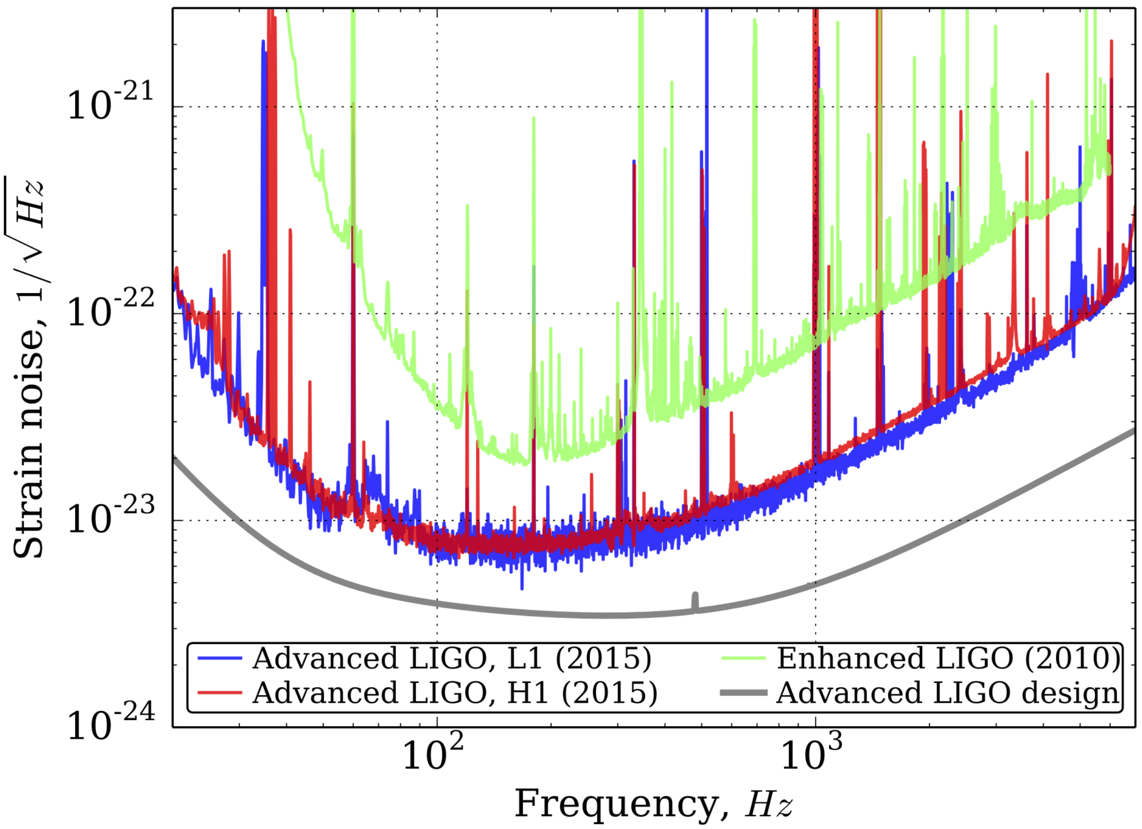

Figure 4.6: Sensitivity curves for the LIGO detectors in 2010 (Green), 2015 (Red and Blue), and at the design (Gray). Design sensitivity is expected to be achieved for O5. Figure from Martynov et al. (2016).

the caveat that it will lead to inefficiencies in searches. Under this assumption, the noise may be given by (Moore et al., 2014)

$$\left\langle \tilde{n}(f)\tilde{n}^{*}(f')\right\rangle = \frac{1}{2}\delta(f-f')S_n(f), \tag{4.77}$$

where the angular brackets are denoting an averaging over many realisations of the noise and $S_n(f)$ is called the one-sided noise *power spectral density (PSD)*. As we have assumed stationarity of the noise, this averaging may be replaced with a time averaging which may be done by repeatedly measuring the noise over a period, T, computing the Fourier transform, and then taking the average.

We have noted above about the glitches that may occur which contribute to the detector noise. Many of these may substantially alter the noise curve for brief durations and so these must be monitored for when performing this procedure since these will violate the assumptions of stationarity.

However, with this procedure formed and an understanding of the noise PSD, it is possible to extract the signal from the measured strain by constructing a Wiener filter (Wiener, 1949). This filter is given by (Moore et al., 2014)

$$\tilde{K}(f) = \frac{\tilde{h}(f)}{S_n(f)}. \tag{4.78}$$

Given that it requires knowledge of the model of the signal, it is also known as a *matched filter*. Under the usage of this filter, and with the knowledge that the squared SNR is given by the inner product of the signal with itself in the frequency domain, this yields the form

$$\rho^2 = \int_0^\infty 4\frac{|\tilde{h}(f)|^2}{S_n(f)} df. \tag{4.79}$$

4.7.2 Modelling CBC Waveforms

With the need for modelling the signal reinforced to extract the signal from the noise, we may now turn to the question of modelling the signals. We will specifically focus on CBC waveform modelling here, given that all currently detected signals have been CBCs and the modelling of these waveforms is the most advanced. As we have discussed in Section 4.5.4, a CBC begins with an inspiralling phase that eventually results in a merger. These are the first two phases of modelling a CBC signal, with a third being modelling of the *ringdown*, which are GWs produced by the motion post merger as the system settles.

CBC waveforms typically decompose the total strain into its *spin-weighted spherical harmonic modes*, h_{lm}, such that (Kidder, 2008)

$$h(t) = h_+(t) - ih_\times = \sum_{l=2}^{\infty} \sum_{m=-l}^{l} h_{lm}(t) {}_{-2}Y_{lm}(\theta, \phi), \tag{4.80}$$

where ${}_{-2}Y_{lm}$ are the -2-spin-weighted spherical harmonics. The (l, m) modes that produce the highest amplitudes are termed the *dominant modes* and these are the $(2, \pm 2)$ modes. The remaining modes are termed either *subdominant modes* or *higher order modes (HOM)*.

There are a number of techniques that may be employed to calculate these spin weighted spherical harmonics leading to a number of different "families" of waveforms. We summarise a few of these below including examples of waveforms using these approaches:

Post Newtonian Theory The post-Newtonian (PN) formalism of GR is an approximation of solutions to the EFE that are valid only in the weak-field and slow motion regimes. The solutions are constructed as corrections to the Newtonian solution to a given order of parameters in v/c. This validity restrictions mean that this approach may only be used for modelling the inspiral. This approach is used by the *Taylor* family of waveforms (Buonanno et al., 2009).

Numerical Relativity The most complete approach to producing waveform models would be to numerically simulate the two body problem in GR. This approach has been deployed to simulate a number of cases such as BBHs (Pretorius, 2005) and BNSs (Anderson et al., 2008). However, this approach is also extremely computationally intensive and as such, these waveforms are not typically used directly. Instead, most often *surrogates* are used instead—these are waveforms that interpolate between the numerical relativity (NR) waveforms. These are usually valid only in a restricted parameter space. An example of such a waveform is *NRSur7dq4* (Varma et al., 2019).

Effective-One-Body As the name implies, the effective-one-body (EOB) approach replaces the full two body problem to a single test particle with the reduced mass, μ, moving in an effective Kerr spacetime. Full modelling of the three components of the CBC can be done by also including the PN results. Further improvement may be made by calibrating against the NR waveforms. As may be expected the family of waveforms using this approach are known as the *EOB* waveforms, with the most recent being the *SEOBNRv5* series (Pompili et al., 2023).

Phenomenological Waveforms The final approach we discuss here is that of purely modelling the GW signal rather than modelling the dynamics of the system producing the waveform. In this approach, one models the inspiral, merger, and ringdown separately. The inspiral may be modelled using the PN formalism, and the merger and ringdown may be calibrated against the NR waveforms. The full waveform is then constructed by combining the three models together. This approach is flexible in allowing different physics to be modelled. A family of waveforms using this approach is the *IMRPhenom* family with the individual waveforms typically being named for the features associated—for instance *IMRPhenomD* (Khan et al., 2016) contains only the dominant mode and non-precessing signals, whereas *IMRPhenomXPHM* (Pratten et al., 2021) may be used for precessing signals containing HOM, with the X simply denoting a more efficient series of waveforms that have been developed compared with the original implementation (Pratten et al., 2020). Work in the following chapters will primarily use the *IMRPhenomXPHM* waveform model.

5

Formalism of Gravitational Lensing

> *Unthinkable complexity. Lines of light ranged in the nonspace of the mind, clusters and constellations of data. Like city lights, receding...*
>
> —*Neuromancer*
> William Gibson

Lensing is formally a process of the deflection of a signal by an object. We have discussed in the previous chapters that the presence of massive objects induces curvature and that curvature changes the geodesics of the space. We have also discussed that light-like curves that signals such as photons or GW signals travel follow these geodesic paths, so it may come as no surprise to learn that massive objects may act as lenses.

We have also noted in Chapter 1 that gravitational lensing was predicted by Einstein in his works on GR (Einstein, 1915a). In particular, GR predicts that light passing by a spherical body of mass, M, at a closest distance of ξ, will be deflected at an angle $\hat{\alpha}$ given by (Schneider et al., 1992)

$$\hat{\alpha} = \frac{4GM}{c^2 \xi}. \tag{5.1}$$

This angle is double the prediction that may be arrived at in Newtonian gravitation, as had been done by for instance Johann Georg von Soldner (von Soldner, 1804) and therefore measurement of this angle forms a direct test of GR. This test was first performed by Eddington, Dyson, and others during the Solar Eclipse on the 29th May 1919 in which they examined the stars close to the Sun to observe their deflection. Their measurements would correspond to that of the GR prediction and thus give a successful test of GR (Dyson et al., 1920).

Astrophysical lensing would take longer to observe. Einstein had initially believed that it would never be observed given that he purely considered the lensing of light from stars. However, in 1937, after the shifting of the view of the universe from that of only the Milky Way to that of multiple galaxies, Fritz Zwicky would posit that these galaxies could act as lenses and that they would provoke much more dramatic and thus observable effects (Zwicky, 1937). Such galactic lensing would be first observed in 1979 when examination of the spectra of the Twin Quasar pointed towards the apparent observed pair in fact being two gravitationally lensed images of the same object (Walsh et al., 1979).

In the intervening years it has become a common sight in images from the Hubble Space Telescope (HST) or now, the JWST, where as shown in Figure 1.4, gravitational lensing was present in the first revealed images. However, light is not alone in experiencing this deflection. As we have noted in Chapter 4, GWs travel at the speed of light too, hence along the same light-like curves as light and will also experience lensing. We may thus use the following discussions based on the case for light as a basis for that of GW gravitational lensing.

5.1 The Lens Equation

In the following discussions we will consider the following geometry—shown in Figure 5.1—of a source, displaced from the optical axis by a distance, $\vec{\eta}$, at an angular distance D_{OS}—meaning an angular displacement of β—from the observer passes at a distance $\vec{\xi}$ from an object of mass, M at an angular distance of D_{OL} from the observer. This will cause deflection at an angle $\hat{\alpha}$. From the observer's perspective, it will appear that the ray will have arrived from a source at an angular displacement, θ from the optical axis.

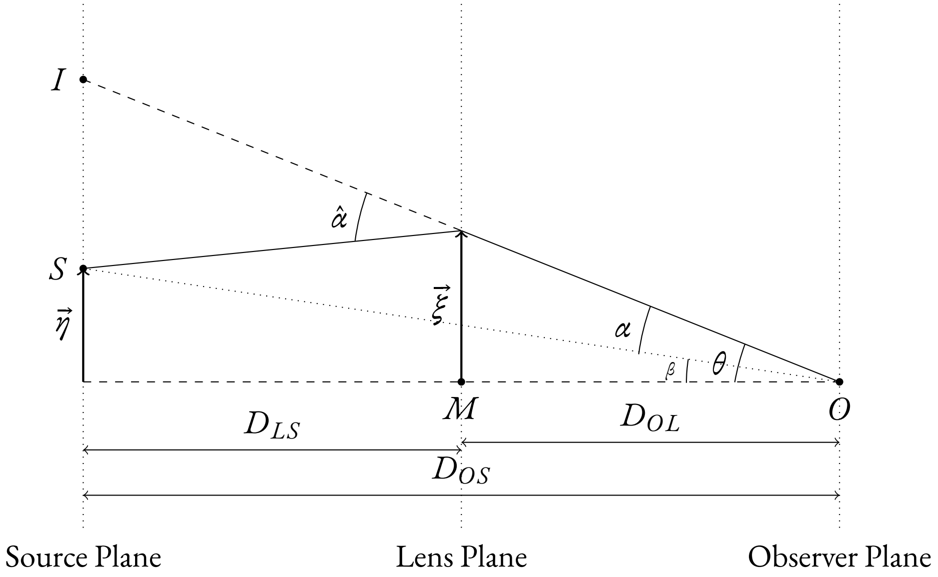

Figure 5.1: Illustration of the geometry of the deflection of light passing at a distance ξ to a body of mass, M.

Given that we are considering astrophysical scenarios, we may make the simplification that the physical size of the lens is significantly less than the distance between the source and the lens and the source and the observer. This is the so-called *thin-lens approximation*. Similarly we may be justified in using the *small angle approximation*.

Under both of these approximations, from examination of Figure 5.1 that the displacement between the positions of I and S will be given by

$$I - \eta = D_{OS} \tan\theta - D_{OS} \tan\beta, \tag{5.2}$$

and we may also note that

$$\begin{aligned} \tan\hat{\alpha} &= \frac{I-\eta}{D_{LS}}\cos\beta \\ \implies \hat{\alpha} &\simeq \frac{I-\eta}{D_{LS}} \\ \tan\alpha &= \frac{I-\eta}{D_{OS}}\cos\theta \\ \implies \alpha &\simeq \frac{I-\eta}{D_{OS}} \\ \therefore\ \alpha &\simeq \frac{D_{LS}}{D_{OS}}\hat{\alpha} \end{aligned} \tag{5.3}$$

where we term the angle, α, the *reduced deflection angle*. We may obviously from the construction of Figure 5.1 note that

$$\beta = \theta - \frac{D_{LS}}{D_{OS}}\hat{\alpha}. \tag{5.4}$$

Equation 5.4 is known as the *lens equation*. This may be also presented in terms of the displacement of the source and the *impact parameter* as (Schneider et al., 1992)

$$\vec{\eta} = \frac{D_{OS}}{D_{OL}}\vec{\xi} - D_{LS}\hat{\alpha}. \tag{5.5}$$

However, rather than either of these two forms, it is frequently the case that it will be more useful to consider a dimensionless equivalent. This is done by defining two *characteristic* length scales, one, ξ_0 for the lens plane, and the other, $\eta_0 = \xi_0 D_{OL}/D_{OS}$, for the source plane. Using these, we define the dimensionless *image position* and *source position* as,

$$\vec{x} = \frac{\vec{\xi}}{\xi_0}, \qquad \vec{y} = \frac{\vec{\eta}}{\eta_0}, \tag{5.6}$$

and can define the dimensionless lens equation as (Schneider et al., 1992)

$$\vec{y} = \vec{x} - \vec{\alpha}\,. \tag{5.7}$$

5.2 Magnification

As we have stated, lensing is a process of deflection. It is not a process of *absorption* and *re-emission*. As a result of being the response of the light-like travel-paths to a gravitational object, it would not only deflect a single ray but a bundle of rays. The propagation of such a bundle of rays may be discussed in terms of the *surface brightness*—the energy flux at a frequency, f, per unit area (perpendicular to the direction of propagation), time, solid angle, and frequency interval, i.e.

$$I(f) = \frac{dE}{dt\,dA\,d\Omega\,df}. \tag{5.8}$$

A light ray—or a bundle thereof—may also be described in terms of the flux of photons, i.e. the number of photons in a particular volume. This may be given by

$$F(\vec{x}, \vec{p}, t) = \frac{dN}{d^3\,\vec{x}\,d^3\,\vec{p}}, \tag{5.9}$$

where N is the number of photons in the volume of a cube with sides of length $\vec{x}$ which have momentum $\vec{p}$. This is also known as the *phase-space distribution function*. We may combine Equations 5.8 and 5.9 by noting the following identities:

- A beam of photons with energy dE is the result of dN photons with energy $E = cp = hf$ therefore $dN = dE/cp$ and $dp = (h/c)df$;
- The linear momentum density $d^3\,\vec{p}$ may be given by $p^2 dp d\Omega$;
- The volume element $d^3\,\vec{x}$ may be given by $cdAdt$;

and therefore

$$F(\vec{x}, \vec{p}, t) = \frac{dE}{hcp^3 dt\,dA\,d\Omega\,df} = \frac{I(f)}{hcp^3}. \tag{5.10}$$

The Liouville theorem applied to this bundle of rays states that "*the [volume] occupied by a given swarm of N particles is independent of location along the world line of the swam*" (Misner et al., 2017), i.e. that the surface brightness must be conserved by gravitational lensing.

The total flux of an object received at a telescope is given as the product of the surface brightness of the source and the solid angle that it subtends. Therefore any changes in flux resulting from the gravitational lensing effect must manifest themselves in the form of changes to the apparent solid angle. This means that the gravitational lensing of light is a process of *magnification*. The ratio of the apparent solid angle of the lensed image compared to the solid angle that would be subtended by the source is termed the *magnification factor*, μ.

In the gravitational wave case, an equivalent ratio may be defined which is that between the wave amplitudes, ϕ, of the lensed and unlensed signals. This is termed the *amplification factor*, F, and will be discussed in more detail in later sections.

5.3 Caustics, Critical Curves, and Image Parity

The lens equation is fundamentally a transformation equation between the co-ordinates of the source plane and those of the lens plane, i.e. between $\vec{\beta}$ and $\vec{\theta}$—the three-dimensional equivalents to the angles shown in Figure 5.1. It is therefore possible to define the *Jacobian* matrix for that transformation given by $\partial\vec{\beta}/\partial\vec{\theta}$. It may also be shown to be the case that the magnification factor is the inverse of the determinant of this Jacobian, i.e. (Schneider et al., 1992)

$$\mu = (\det \frac{\partial\vec{\beta}}{\partial\vec{\theta}})^{-1}, \tag{5.11}$$

by considering the area distortion for a bundle of rays. This may equivalently be defined in terms of $\partial\vec{x}/\partial\vec{y}$. The determinant of this matrix may be either positive, negative, or zero. Points which have finite positive or negative determinants produce an image that is deemed to have the respective *parity*. Those points that result in a vanishing determinant are called the *caustics* of the lens with the corresponding curves where the infinitely magnified image would appear being called the *critical curves*.

The importance of the caustic curves is that the number of images that gravitational lensing produces is related to the displacement of the source from the optical axis between the observer and the lens. At very large distance this must recover the non-lensing limit, i.e. only a single image. However, nearer the lens multiple images may be produced, specifically the number of images produced would increase by two for each caustic crossed between the given displacement and that far away displacement—this means that the number of images produced by gravitational lensing for general lensing objects must be odd, a result known as Burke's theorem (Burke, 1981). However, it must be noted that certain—technically oversimplified—lens profiles such as the isolated point mass, as will be shown in the next section, produce even numbers of images owing to their central singularity. It is also the case that whilst an odd number of images must be produced, not all will necessarily be detectable—central images for instance tend to be de-magnified or occluded by the foreground lens.

5.4 Multiple Image Example

To provide an example of the production of multiple images, we return to the situation depicted in Figure 5.1 and we explicitly identify the lens as an isolated point mass. In this case, the combination of Equations 5.1 and 5.3 yield that the reduced deflection angle is given by

$$\alpha = \frac{D_{LS}}{D_{OS}D_{OL}}\frac{4GM}{c^2}. \tag{5.12}$$

Restricting ourselves to the case of the source being on the optical axis of the lens and the observer, i.e. $\beta = 0$, then the solution to the lens equation is given by

$$\theta_E = \sqrt{\frac{D_{LS}}{D_{OS}D_{OL}}\frac{4GM}{c^2}}. \tag{5.13}$$

This describes a ring of radius, θ_E, termed the Einstein Ring. In the more general case of non-zero β, this will have two solutions that will be given by (Mollerach & Roulet, 2002)

$$\theta_{\pm} = \frac{\beta}{2} \pm \theta_E \sqrt{1 + \frac{\beta^2}{4\theta_E}}. \tag{5.14}$$

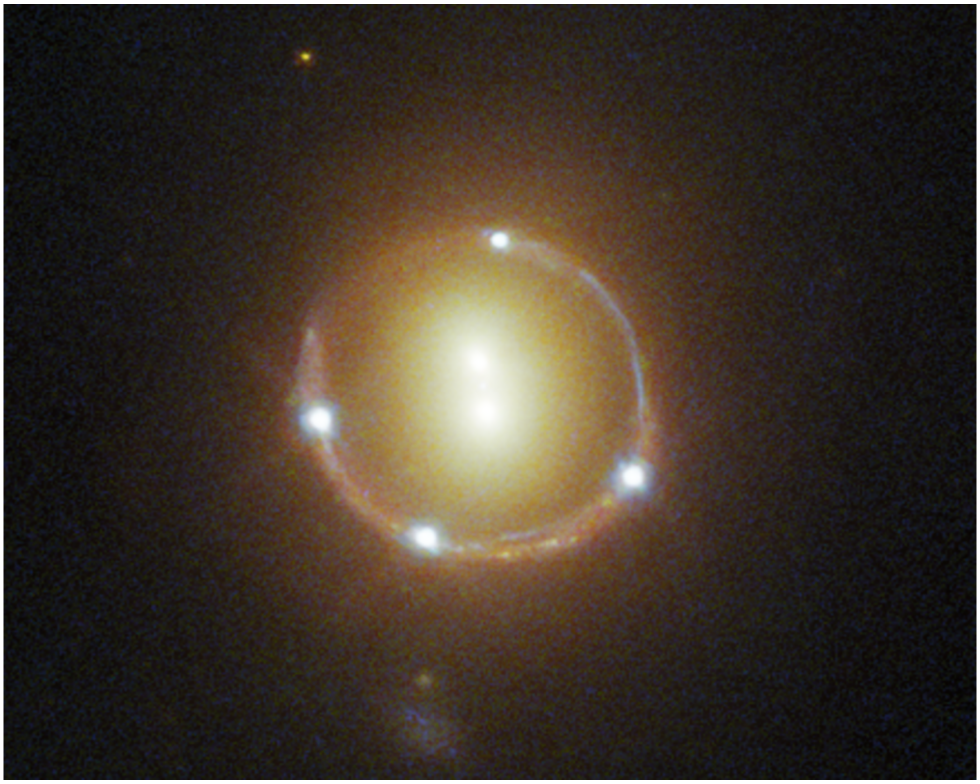

Figure 5.2: An example of the Einstein Ring formed from the lensing of the quasar 2M1310-1714. The four bright spots in the ring represent four of the produced lensed images. There is a fifth fainter image in the centre. Image Credit: ESA/Hubble & NASA, T. Treu

Figure 5.2 shows an example of the lensing of the quasar 2M1310-1714 (Lucey et al., 2018) by a foreground galaxy. There are four lensed images that are smeared out by the effect of the lensing forming the Einstein Ring. A fifth fainter image is present in the centre.

5.5 The General Lens

The discussions above have largely concerned the simplest case of an isolated point mass lens, however, realistic lenses may have any number of morphologies. In such cases we would in principle need to consider the full three dimensional structure of the lens. However, one simplification that we may continue to make is that given the distances between the lens, source, and observer vastly outstrip the size of the lens, we may continue to deploy the thin-lens approximation and treat the deflection as occurring all at once at the point $\vec{\xi}$.

By making this approximation, we no longer need to consider the complete three-dimensional mass density profile of the lensing object, $\rho\vec{x}$; we may instead consider the projection of this density profile on a two dimensional plane that is perpendicular to the line-of-sight of the source at the distance to the centre-of-mass of the object, i.e. (Mollerach & Roulet, 2002)

$$\Sigma(\vec{\xi}) = \int \rho(\vec{\xi}, z) dz, \tag{5.15}$$

where ρ is the three-dimensional mass density and z is the direction of the line-of-sight. This projection is called the *surface mass density*. This is once again defined in terms of physical quantities, and we may again rescale this to a dimensionless equivalent by the definition of the *critical surface density* which is given by (Schneider et al., 1992)

$$\Sigma_{\text{cr}} = \frac{c^2 D_{OS}}{4\pi G D_{OL} D_{LS}}, \tag{5.16}$$

and hence denote the dimensionless surface mass density, $\kappa(\vec{x})$, as

$$\kappa(\vec{x}) = \frac{\Sigma(\vec{\xi})}{\Sigma_{\text{cr}}}. \tag{5.17}$$

Aside: Derivation of Deflection Angle

Here, we briefly turn to the origins of Equation 5.1 to then consider the result for the general lens. We once again consider a nearly-flat metric in the non-relativistic limit and assuming the energy-momentum for a perfect fluid. We will use a slightly differing starting formulation of the nearly-flat metric than Equation 4.1, namely (Schneider et al., 1992)

$$g_{\alpha\beta} = \left(1 - \frac{1}{2}h\right) \eta_{\alpha\beta} + h_{\alpha\beta}, \tag{5.18}$$

Under the non-relativistic limit for the perfect fluid, Equations 2.71 and 5.18 means that the components of the energy momentum tensor may be approximated as

$$\begin{aligned} T^{00} &\simeq \rho c^2 \\ T^{0i} &\simeq c\rho v^i \\ T^{ij} &\simeq \rho v^i v^j + p\delta^{ij} \end{aligned} \tag{5.19}$$

neglecting the terms of higher order. Introducing two *retarded potentials*

$$\begin{aligned} U(t,\vec{x}) &= -G\int \frac{\rho\left(t-\frac{\vec{y}}{c},\vec{x}+\vec{y}\right)}{|\vec{y}|}d^3y \\ \vec{V}(t,\vec{x}) &= -G\int \frac{(\rho\vec{v})\left(t-\frac{\vec{y}}{c},\vec{x}+\vec{y}\right)}{|\vec{y}|}d^3y, \end{aligned} \tag{5.20}$$

where $\vec{v} = d\,\vec{x}/dt$, then the line element may be given by (Schneider et al., 1992)

$$\begin{aligned} ds^2 &= g_{\alpha\beta}dx^\alpha dx^\beta \\ &\simeq \left(1+\frac{2U}{c^2}\right)c^2dt^2 - 8cdt\frac{\vec{V}\cdot d\,\vec{x}}{c^3} - \left(1-\frac{2U}{c^2}\right)d\,\vec{x}^{\,2} \end{aligned} \tag{5.21}$$

If we consider the situation of lensing and make the assumption that during the time that the ray interacts with the lens that the matter distribution does not substantially change, then it may be assumed that the metric above is *stationary* which means that this metric will be conformal to a metric, $\widetilde{ds}^2$ of the form (Schneider et al., 1992)

$$\widetilde{ds}^2 = e^{2U}(dt - w_i dx^i)^2 - e^{-2U}\gamma_{ij}dx^i dx^j, \tag{5.22}$$

for some functions U, w_i, γ_{ij}, all of which are dependent only upon the spatial co-ordinates. In such a case, it is obvious that for $\widetilde{ds}^2 = 0$,

$$dt = w_i dx^i + e^{-2U}\gamma_{ij}dx^i dx^j. \tag{5.23}$$

This means that for a stationary observer, the *time of arrival* of a light-like curve emitted at $t = 0$ and the spatial projection of which is $\vec{\gamma}$ will be given by

$$t = \int_{\vec{\gamma}} w_i dx^i + e^{-2U}\gamma_{ij}dx^i dx^j. \tag{5.24}$$

We have discussed in Chapter 2 that light-like curves are the geodesics of the space meaning that they are the curves of extremal length (as shown in Section 2.6) meaning that they are invariant under small variations of $\vec{\gamma}$, i.e.

$$\delta\int_{\vec{\gamma}} w_i dx^i + e^{-2U}\gamma_{ij}dx^i dx^j = 0. \tag{5.25}$$

which is equivalent to the classical Fermat principle that ray paths are those of the least time under the requirement that an effective refractive index is given by (Schneider et al., 1992)

$$n = e^{-2U} + w_i\frac{dx^i}{dl}, \tag{5.26}$$

where $dl = \gamma_{ij} dx^i dx^j$ is viewed as the geometrical arc length. In the metric we are considering the effective refractive index will be given by (Schneider et al., 1992)

$$n = 1 - \frac{2U}{c^2} + \frac{4}{c^3}\vec{V} \cdot \vec{e}, \tag{5.27}$$

where $dl = |d\,\vec{x}|$ and $\vec{e} = d\,\vec{x}/dl$ is the tangent vector of the light-like curve. Constructing the Euler-Lagrange equation $\delta \int n dl = 0$ then yields that the derivative of the tangent vector with respect to the geometric arc length is

$$\frac{d\,\vec{e}}{dl} = -\frac{2}{c^2}\nabla U - \vec{e}(\vec{e} \cdot \nabla U) + \frac{4}{c^3}\,\vec{e} \times (\nabla \times \vec{V}), \tag{5.28}$$

where $\nabla = \left(\frac{d}{dx}, \frac{d}{dy}, \frac{d}{dz}\right)$.

The angle of deflection $\hat{\alpha}$ is obviously defined as the difference between the tangent vector before and after the deflection and may thus be given by

$$\hat{\alpha} = \frac{2}{c^2}\int \nabla U - \vec{e}(\vec{e} \cdot \nabla U) dl - \frac{4}{c^3}\int \vec{e} \times (\nabla \times \vec{V}) dl. \tag{5.29}$$

In general, we may neglect the latter $\vec{V}$ integral due to it being negligible compared with the already small contribution of the former integral (Schneider et al., 1992). In the case of the point mass, $U(\vec{x}) = -\frac{GM}{|\vec{x}|}$ integration over the unperturbed ray given by $\vec{x}(l) = \vec{\xi} + l\,\vec{e}$ where $\vec{\xi}$ is orthogonal to the tangent vector prior to the effect of lensing using that $U(\vec{x}) = -\frac{GM}{|\vec{x}|}$ leads to Equation 5.1.

We now turn to the deflection angle for the general lens. In the case where both $\hat{\alpha}$ is small and the thin-lens approximation may be made—both of which are justified in the astrophysical case—this allows us to again integrate over the unperturbed ray as we did in the point mass case, which reduces 5.29 to the integration of the Einstein angles for each element of the surface mass density, i.e. (Schneider et al., 1992)

$$\hat{\alpha} = \frac{4G}{c^2}\int_{\mathbb{R}^2} \frac{(\vec{\xi} - \vec{\xi'})\Sigma(\vec{\xi'})}{\left|\vec{\xi} - \vec{\xi'}\right|^2} d^2\xi'. \tag{5.30}$$

In terms of the dimensionless mass density this is given by

$$\hat{\alpha} = \frac{1}{\pi}\int_{\mathbb{R}^2} \kappa(\vec{x'}) \log\left|\vec{x} - \vec{x'}\right| d^2x'. \tag{5.31}$$

5.6 Time Delay

We noted in Equation 5.24 that lensing will change the time-of-arrival of a signal as compared to its non-lensed path. If we consider this in the context of the metric of Equation 5.22, again noting that $\vec{V}$

may be neglected, the time-of-arrival is given by (Schneider et al., 1992)

$$\begin{aligned} t &= \frac{1}{c}\int\left(1-\frac{2U}{c^2}\right)dl \\ &= \frac{l}{c}-\frac{2}{c^3}\int U dl, \end{aligned} \tag{5.32}$$

which we see has two contributing components—a geometric component and a potential based one which corresponds to Shapiro delay (Shapiro, 1964). The l in this instance is the path between S and O with the unbroken line in Figure 5.1. To establish the *time delay* induced by the lensing we compare this with the time-of-arrival for the non-deflected case which is just the geometrical contribution from the path given by the dotted line between S and O, i.e. the straight-line path between them which yields

$$t_d = \frac{\Delta l}{c} - \frac{2}{c^3}\int U dl = t_{\text{geo}} - t_{\text{Shap}}. \tag{5.33}$$

We examine both of these contributions in turn, starting with the geometrical time delay for which we need to establish the difference in path length. Examining Figure 5.1, this is done by first noting the point at which the line SO—the non-deflected path—crosses the lens plane, we term this point L. From L, one projects two lines up towards the deflected path such that two isosceles triangles are formed. This is illustrated in Figure 5.3.

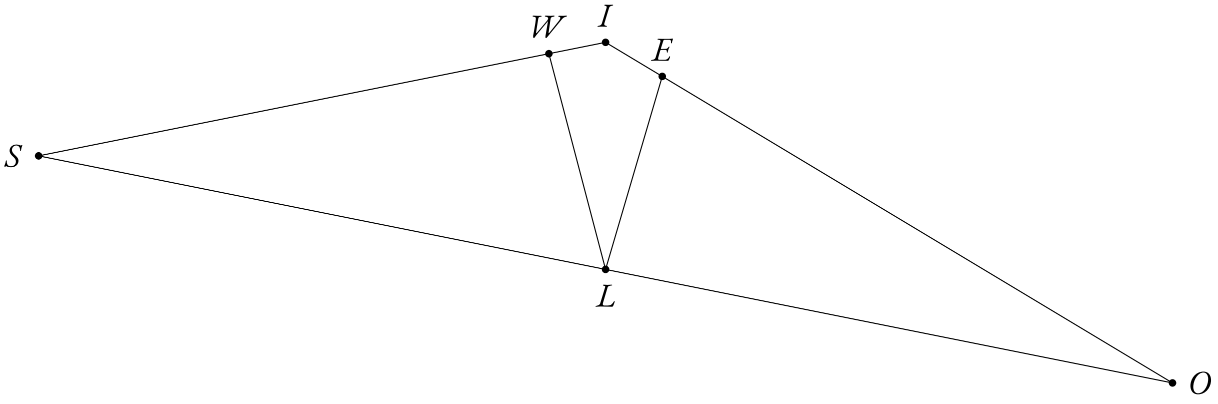

Figure 5.3: Illustration of the extra path length of the deflected ray. The extra path length is given by the path WIE where the triangles LSW and LOE are both isosceles.

As before we know that the angle SOE is $\theta - \beta$. Working through the trigonometry of the situation, and recalling the full picture of the geometry given by Figure 5.1 reveals that the geometrical time delay is given by (Mollerach & Roulet, 2002)

$$t_{\text{geo}} = \frac{1}{c}\frac{D_{OL}D_{OS}}{2D_{LS}}(\theta-\beta)^2 \tag{5.34}$$

Turning to the Shapiro delay, following the lead of Schneider et al. (1992), we may compute this by first considering the isolated point mass case and computing the integral between the points S and

I. This will be given by

$$\int_S^I U dl = GM \left[\log \frac{\left|\vec{\xi}\right|}{2D_{LS}} + \frac{\vec{\xi} \cdot (\vec{\eta} - \vec{\xi})}{\left|\vec{\xi}\right| D_{LS}} + O\left(\left(\frac{\vec{\eta} - \vec{\xi}}{D_{LS}} \right)^2 \right) \right]. \tag{5.35}$$

Under the assumptions and approximations that we have made for lensing, we may neglect the higher order terms and the second term, leaving only the first, i.e.

$$\begin{aligned} \int_S^I U dl &\simeq GM \log \frac{\left|\vec{\xi}\right|}{2D_{LS}} \\ &\simeq GM \left(\log \frac{\vec{\xi}}{D'} + \log \frac{D'}{D_{LS}} \right) \end{aligned} \tag{5.36}$$

where the distance D' is small relative to the astrophysical distance D_{LS} but is significant relative to $\vec{\xi}$. A similar process may be performed and a similar decomposition may be made. Combining the two results, and inserting the relationship between the mass and surface mass density will yield that the Shapiro time delay will be given by

$$t_{\text{Shap}} = -\frac{4G}{c^3} \int \Sigma(\vec{\xi'}) \log \left(\frac{\left|\vec{\xi} - \vec{\xi'}\right|}{\xi_0} \right) d^2\xi' + \text{const.} \tag{5.37}$$

where we may identify the distance D' as ξ_0. Taking one factor of c over to the left hand side, the non-constant quantity remaining on the right may be identified as the *deflection potential* of the lensing object and is generally given the identifier, $\hat{\psi}(\vec{\xi})$. This may be converted to dimensionless form

$$\begin{aligned} \psi(\vec{x}) &= \frac{D_{LS} D_{OL}}{D_{OS} \xi_0^2} \hat{\psi}(\vec{\xi}) \\ &= \frac{1}{\pi} \int_{\mathbb{R}^2} \kappa(\vec{x'}) \log \left|\vec{x} - \vec{x'}\right| d^2x, \end{aligned} \tag{5.38}$$

from which one may immediately note that the reduced deflection angle is the gradient of the dimensionless deflection potential.

From Equations 5.34 and 5.37 we now may construct that the total time delay is given by

$$ct_d = \frac{D_{OL} D_{OS}}{2D_{LS}} (\theta - \beta)^2 - \hat{\psi}(D_{OL}\theta) + \text{const.} \tag{5.39}$$

where the right hand side—neglecting the constant—is termed the *Fermat potential*, $\hat{\phi}$. This too may be rewritten in dimensionless form—though we must include the cosmological redshift to do so—as (Schneider et al., 1992)

$$\begin{aligned}\phi(\vec{x},\vec{y}) &= \frac{1}{1+z_L}\frac{D_{OL}D_{LS}}{D_{OS}\xi_0^2}\phi \\ &= \frac{1}{2}(\vec{x}-\vec{y})^2 - \psi(\vec{x}).\end{aligned} \tag{5.40}$$

One may note that the holding of the lens equation is a requirement that $\nabla\phi(\vec{x},\vec{y}) = 0$.

5.7 Lensing of Gravitational Waves

In Section 5.2 we discussed that the lensing of light is a process of magnification and defined the magnification factor. We noted in that section that the equivalent in the case of GW is the *amplification factor*—the ratio of the lensed wave amplitude vs the unlensed source wave amplitude. We here turn the discussion to the form of that amplification factor.

The previous discussion has introduced the majority of the language and the approximations that can be made in the context of GW lensing. However, to fully describe the amplification of GW in all generality, we must also consider the *wave optics* regime. The previous discussion has been purely geometrical and considered light as rays. Underpinning this has been assumption that the frequency is significantly higher than the inverse of the (redshifted) lens mass. In the GW case, this assumption does not always hold—specifically in the case of low mass objects.

In the wave optics regime, the amplification factor is given by the *diffraction* integral which is given, including cosmological expansion of the universe, by (Takahashi & Nakamura, 2003)

$$F(f) = \frac{D_{OS}\xi_0^2(1+z_L)}{D_{OL}D_{LS}}\frac{f}{i}\int \exp\left(2\pi i f t_d(\theta,\beta)\right) d^2\vec{x}, \tag{5.41}$$

where each symbol retains its meanings from the previous discussions. We may convert this to the same dimensionless form that we have done for other quantities to yield (Nakamura & Deguchi, 1999)

$$F(w,\vec{y}) = \frac{w}{2\pi i}\int \exp[iwT(\vec{x},\vec{y})]d^2\vec{x}, \tag{5.42}$$

where we denote that $T(x,y) = \phi(x,y)+\phi_m$ where ϕ_m is the constant from Equation 5.39 which is chosen so as to yield a minimal time delay induced from the lensing of zero. We have also introduced the *dimensionless frequency* which is given by

$$w = \frac{D_{OS}}{D_{OL}D_{LS}}\xi_0^2(1+z_L)\omega \tag{5.43}$$

The simplest wave optics lensing would be the case of axially symmetric lenses. In such a case, Equation 5.42 may be rewritten as

$$F(w,y) = iwe^{iwy^2/2}\int xJ_0(wxy)\exp\left[iwT(x,y)\right]dx, \tag{5.44}$$

where J_0 is the Bessel function of the first kind. As may be noted this is, in general, a highly oscillatory integral and given the definition of $T(x, y)$ is dependent upon the lens mass density profile. We noted that in the case where the frequency of the gravitational waves is significantly higher than one this returns to the purely geometric case—the *geometric optics approximation*—and all of our previous discussions hold. In this case, the diffraction integral (Equation 5.42) has non-zero contributions only from the stationary points of T(x,y)—which correspond to the geometrical images produced and so the amplification factor may be given by (Nakamura & Deguchi, 1999)

$$F_{\text{geo}} = \sum_j \left|\mu_j\right|^{1/2} \exp\left[iwT(\vec{x}_j, \vec{y}) - i\pi n_j\right], \tag{5.45}$$

where we introduce the parameter n_j which is called the Morse index and may take only three values, 0, 0.5, or 1 depending upon whether the stationary point for the image corresponds to a minima, saddle, or maxima of the Fermat potential, $\phi(x, y)$. These images are also noted as being Type I, II, or III respectively and relate with the previously noted discussion of parity, with Type I and Type III being images of positive parity, and Type II being images of negative parity (Schneider et al., 1992). The physical implication of the Morse index term is to introduce a phase shift to the GW of either 0, 90°or 180°, again, respectively (Nakamura & Deguchi, 1999).

From the definition of the amplification factor mentioned at the end of section 5.2 and the fact that in both regimes it is purely dependent upon properties of the lens rather than those of the source, it may be noted that the relationship between the strain of the lensed signal and that from the source is simply

$$h^L(f) = F(w, y) \times h(f) \tag{5.46}$$

meaning that importantly, models of lensed GW waveforms, may be easily computed from the standard GW waveform models discussed in Section 4.7 once the amplification factor is computed.

One important note that one may see examining both Equation 5.46 and 5.45 is that where the geometric optics approximation is valid, individual images of the signal will have no frequency-dependent effects, meaning that their frequency evolution will be unaffected. This may be contrasted with the wave optics case where the frequency dependency of the amplification is always present.

5.8 Scales of Lensing

As a gravitationally induced process, the lensing object may be almost anything in the universe from individual compact objects to galactic clusters. Different scales of lensing produce a differing level of effect. For GW lensing, the mass scale determines whether or not the geometric optics approximation is valid. The scales of lensing are typically divided into several subdivisions; we here define these scales of lensing.

Strong Lensing Strong lensing is produced by the largest scales of lensing object such as galaxies or galactic clusters and as the name implies, produces the most dramatic effects of lensing. Figure 5.2 discussed earlier is an example of strong lensing. It is characterised by the images being spatially resolvable in their separation from each other and, in the EM case, significant smearing of the image into arcs around the Einstein ring. In GW lensing, the geometric optics approximation is valid and from our previous discussions strong lensing results in the emission of multiple copies of the signal that are fully separated in time of arrival, and that each experience a particular magnification and phase shift based on the lens properties and the image type respectively.

Weak Lensing We noted in Section 5.3 that for rays passing by the lens plane far from the centre of the projected distribution that the effect will be that of only a single image with some small deflection. This effect is the domain of weak lensing and for any given light ray or GW arriving it will likely experience this several times due to the cumulative matter distribution between the source and the detector/observer. Weak lensing is typically not individually detectable and is instead detected statistically from the background.

Millilensing Decreasing the scale of the lensing object from an entire foreground galaxy to that of galactic sub-structure will in turn decrease the separation of the images from each other. This regime is known as millilensing due to in EM, the millilarcsecond scale separation of the images and in GW, the millisecond scale time delays between the image. At this level of time delay, whilst the geometric optics approximation remains valid for GW signals, the time delay is sufficiently small that the copies of the signal overlap which will introduce some interference between the images and induce a beating pattern in the detected signal.

Microlensing Decreasing the scale of the lensing object even further such that it is now that of individual compact objects, fields of stars, or even an individual star reaches the scale of microlensing. In both the EM and GW are no longer resolvable as separate. In the EM case this is detected as a change in apparent brightness. In the GW case however, there are still the beating patterns similar to the millilensing scale, but the geometric optics approximation is no longer valid and wave optics effects will appear in the signal particularly at low frequency.

PART II

DETERMINATION OF LENS PARAMETERS AND MASS DENSITY PROFILE FOR LENSED GRAVITATIONAL WAVES

6

Development of an Analysis Framework for Gravitational Wave Microlensing

> *Brothers, he who dies here dies in the radiance of the future, and we are entering a tomb all flooded with the dawn*
>
> —Enjolras, *Les Misérables*
> Victor Hugo

Disclaimer

The following chapter is based on the work Gravelamps: *Gravitational Wave Lensing Mass Profile Model Selection* which was co-authored by Martin Hendry and published in the Astrophysical Journal. The resulting framework is publicly available—at time of writing—on GitLab.

Armed with the knowledge of the previous chapters which has led us to the topic of gravitational lensing and specifically to the lensing of GW signals, we now turn to the question of finding and understanding lensed GW signals. The detection of GW150914 (Abbott et al., 2016a) represented the culmination of a century's effort from the first predictions of GWs by Einstein (Einstein, 1916). From that initial detection, others have followed to reach the current state of GW astronomy with the 90 detections considered in the most recent catalogue, Abbott et al. (2023a).

The shifting of the detection of GW signals from in and of themselves exceptional towards being more routine has also meant a shift towards the many new opportunities for scientific development that the observation and analysis of GW signals presents us with and one of these is the search for lensed GW signals both from the perspective of LVK data analysis (Hannuksela et al., 2019; Abbott et al., 2021f, 2023d; Janquart et al., 2023b) and outside of it by others interested (Broadhurst et al., 2019).

Whilst the searches are a scientific goal in and of themselves, there has also been significant interest in what GW lensing could provide in terms of further experiments, as a parallel to the detection of GWs opening these new avenues in the first place. Some of the avenues that GW lensing may open are significant improvements to the localisation of GWs (Hannuksela et al., 2020) and improvements to the characterisation of the source (Lai et al., 2018; Diego, 2020), making measurements of the cosmological parameters in a distinct manner from other GW-based approaches (Sereno et al., 2011; Cao et al., 2019), and providing continuing tests of GR (Collett & Bacon, 2017; Fan et al., 2017; Goyal et al., 2023).

The question that we will focus on in this chapter, and indeed through many of the remaining chapters is that of the lens itself. The most obvious question following the detection of GW lensing would be, "*what is the lens*", and indeed lens reconstruction is a widely used technique in EM observations of lensing providing an invaluable indirect probe of dark matter (Schneider, 1996). Prior work to that discussed here, demonstrated that differing mass density profiles of the lens would impart different properties on to the signal (Takahashi & Nakamura, 2003; Cao et al., 2014) and had sought to constrain the parameters of the lens from the signal (Herrera-Martín et al., 2019; Mishra et al., 2021).

The work presented in this chapter would build upon these foundations to construct a platform to perform template-based parameter estimation analyses using a number of differing lens models. It will focus primarily on the microlensing regime where wave-optics effects may not be neglected, work to analyse GW signals for signatures of microlensing had been previously undertaken in Hannuksela et al. (2019) and Abbott et al. (2021f). However, these had been restricted to the isolated point mass only case due to the computational cost of computing the amplification factor for other models. The resulting successful platform is a package termed GRAVELAMPS written in a combination of C++ (ISO, 2020) and PYTHON (Van Rossum & Drake, 2009) capable of rapidly computing the amplification factor in both the wave and geometric optics regimes allowing deployment in a large number of use cases for, at launch, a number of mass density profiles.

6.1 Lens Mass Density Profiles

We first describe some of the commonly used lens mass density profiles and in particular the computation of the amplification factor under each of these models.

6.1.1 Isolated Point Mass

As we have discussed, the simplest mass density profile for a lensing object is that of the isolated point mass. It is particularly applicable in the microlensing case as a profile for individual stars or black holes. It may however, also be used for extended objects, through the Birkhoff Theorem which notes that the exterior solution to the vacuum form (where the energy-momentum tensor is zero) of any spherically symmetric object must be given by the Schwarzschild metric (Birkhoff & Langer, 1923).

We have in the previous sections discussed the profile at length. The simplicity of the profile means that it is one of the only profiles which has an analytic solution to Equation 5.44. For this profile, the scale length chosen for the lens plane, ξ_0, is chosen to correspond to the Einstein radius given by Equation 5.13 and so is given by

$$\xi_0 = \left(\frac{4M_L D_{OL} D_{LS}}{D_{OS}}\right)^{1/2}. \tag{6.1}$$

Inserting this normalisation length into the definition of the dimensionless frequency, Equation 5.43, means that for this profile the dimensionless frequency may be given by

$$w = 4M_{lz}\omega, \tag{6.2}$$

where M_{lz} is the *redshifted lens mass*. We finally note that the lensing potential of the isolated point mass is given by $\psi(x) = \log x$. The combination of these ultimately yields that the amplification factor will be given by (Peters, 1974; Takahashi & Nakamura, 2003)

$$F(w, y) = \exp\left(\frac{\pi w}{4} + i\frac{w}{2}\left\{\log\left(\frac{w}{2} - 2\phi_m(y)\right)\right\}\right)\Gamma\left(1 - \frac{i}{2}w\right){}_1\mathcal{F}_1\left(\frac{i}{2}w, 1; \frac{i}{2}wy^2\right), \tag{6.3}$$

where ${}_1\mathcal{F}_1$ is the confluent hypergeometric function of the first kind, also known as Kummer's function, and Γ represents the Gamma function. For the isolated point mass the phase shift required for a minimal time delay of zero is given by $\phi_m(y) = (x_m - y)^2/2 - \log x_m$ for an image position value of $x_m = y + \sqrt{y^2 + 4}$.

For the geometric optics case of this profile, we noted in the previous chapter that this simple profile violates the Burke theorem and produces only two images. Specifically it produces one image of positive parity and one of negative, i.e. a Type I and a Type II, and thus Equation 5.45 for this profile becomes

$$F_{\text{geo}}(w, y) = \left|\mu_+\right|^{1/2} - \left|\mu_-\right|^{1/2} e^{iw\Delta T}, \tag{6.4}$$

where the magnifications for the images are given by (Schneider et al., 1992)

$$\mu_\pm = \frac{1}{2} \pm \frac{y^2 + 2}{2y\sqrt{y^2 + 4}}, \tag{6.5}$$

and the time delay between the images is given by (Schneider et al., 1992)

$$\Delta T = \frac{1}{2}y\sqrt{y^2 + 4} + \log\frac{\sqrt{y^2 + 4} + y}{\sqrt{y^2 + 4} - y}. \tag{6.6}$$

6.1.2 Singular Isothermal Sphere

A step up in complexity but remaining relatively simple, the next profile we discuss is the SIS. This profile is the simplest one that replicates key observed galactic behaviour—namely the flat rotation curve. It does this by modelling the large, extended object as a dark matter halo with embedded luminous matter. Whilst it has the strength of replicating the flat rotation curve, it suffers from a non-physical central singularity.

The profile arises from considering the Lane-Emden equation relating the pressure and density of a polytropic gas sphere in the limit of high n (Hunter, 2001). This results in the full three dimensional density profile given by (Binney & Tremaine, 2008)

$$\rho_{\mathrm{SIS}}(r) = \frac{\sigma^2}{2\pi G r^2}, \tag{6.7}$$

where σ is the one-dimensional velocity dispersion. Projecting this to the lens plane, the surface mass density is therefore given by

$$\Sigma(\vec{\xi}) = \frac{\sigma^2}{2G\xi}. \tag{6.8}$$

Integrating this, we may find that the mass enclosed within a circle of radius ξ on the projected lens plane will be given by

$$\begin{aligned} M(\xi) &\equiv 2\pi \int_0^{\xi} \xi' \Sigma(\xi') d\xi' \\ &= \frac{\pi\sigma^2}{G}\xi. \end{aligned} \tag{6.9}$$

The scale length for ξ_0 that we choose is, in line with the Einstein radius which will be given by (Takahashi & Nakamura, 2003)

$$\xi_0 = 4\pi\sigma^2 \frac{D_{OL}D_{LS}}{D_{OS}}, \tag{6.10}$$

which may be combined with the enclosed mass to yield a redshifted lens mass of

$$M_{lz} = 4\pi\sigma^4(1+z_L)\frac{D_{OL}D_{LS}}{D_{OS}}. \tag{6.11}$$

We may see that this will again lead to Equation 5.43 as the relationship between the dimensionful and dimensionless frequencies.

The deflection potential may be given by the simple relationship $\psi(\vec{x}) = x$, from which it may be evaluated that the phase shift required for a minimal time delay of zero will be given by $\phi_m(y) = y + 1/2$. These may be inserted into Equation 5.44. To solve the resulting expression, we first expand part of the exponential term to yield

$$F(w, y) = -iwe^{\frac{i}{2}wy^2 + iw\phi_m(y)} \sum_{n=0}^{\infty} \frac{(-iw)^n}{n!} \int_0^{\infty} x^{1+n} J_0(wxy) e^{iwx/2}. \tag{6.12}$$

Using the identity for the confluent hypergeometric function that $e^z {}_1\mathcal{F}_1(a, b; z) = {}_1\mathcal{F}_1(a, b; z)$ (Abramowitz & Stegun, 1964), the work of Matsunaga & Yamamoto (2006) showed that this will eventually yield

$$F(w,y) = e^{\frac{i}{2}w(y^2+2\phi_m(y)} \sum_{n=0}^{\infty} \frac{\Gamma(1+n/2)}{n!} \left(2we^{\frac{3\pi i}{2}}\right)_1^{n/2} \mathcal{F}_1\left(1+\frac{n}{2}, 1; -\frac{i}{2}wy^2\right). \tag{6.13}$$

In the geometric optics regime, at low source position the picture remains much the same as for the isolated point mass case, two images produced—one positive parity Type I, and one negative parity Type II. However, the SIS has a caustic at $y = 1$, and as briefly mentioned in Section 5.3 outside the final caustic, only a single image is produced. This marks a difference from the isolated point mass case in which two images are *always* produced. The single image produced is naturally the Type I, and so from Equation 5.45 we can see that for the SIS case,

$$F_{\text{geo}}(w,y) = \begin{cases} \left|\mu_+\right|^{1/2} - i\left|\mu_-\right|^{1/2} e^{iw\Delta T} & \text{for } y < 1 \\ \left|\mu_+\right|^{1/2} & \text{for } y \geq 1 \end{cases}, \tag{6.14}$$

where the magnification for each image is given by $\mu_\pm = \pm 1 + \frac{1}{y}$ and the dimensionless time delay between the images is given by $\Delta T = 2y$.

6.1.3 Navarro Frenk White

The current cosmological model of ΛCDM is a model of a universe consisting of luminous matter, dark matter, and a non-zero cosmological constant that represents dark energy—see e.g. Carroll (2001) for additional information about the ΛCDM model. The CDM stands for *cold dark matter*, i.e. the belief in this model is that dark matter is both cold and collisionless. One method from cosmological models to provide information on the distribution of that dark matter component of the universe is to perform N-body simulations, these are simulations of the behaviour of a large number of particles to simulate for instance the development of galaxies.

From such simulations, the work Julio Navarro, Carlos Frenk, and Simon White (1995) concluded that the spherically averaged profile of galactic halos in a CDM model may be given by scaling a universal profile which now, as may be expected, bears the name of the NFW profile. The profile, as will become clear, is another step up in complexity from the SIS profile but does not remove the major weakness of that profile, i.e. the central singularity. The success of the NFW model therefore contributes to the outstanding core-cusp problem i.e. that this success is in conflict with the rotation curve observations that galaxies should have relatively flat dark matter cores—see e.g. de Blok (2010) for further information.

The profile is given by (Navarro et al., 1996)

$$\rho_{\text{NFW}}(r) = \frac{\rho_s}{r/r_s\,(1+r/r_s)^2}, \tag{6.15}$$

where r_s is the characteristic scale of the profile and ρ_s is the scale density of the profile. The characteristic scale replaces the Einstein radius as the most convenient scale length for ξ_0 in this profile. The surface mass density oft the profile is thus given by (Bartelmann, 1996)

$$\Sigma(x) = \frac{2\rho_s r_s}{x^2 - 1} f(x), \tag{6.16}$$

where

$$f(x) = \begin{cases} 1 - \frac{2}{\sqrt{x^2-1}} \arctan\sqrt{\frac{x-1}{x+1}} & \text{for } x > 1 \\ 1 - \frac{2}{\sqrt{1-x^2}} \operatorname{arctanh}\sqrt{\frac{1-x}{1+x}} & \text{for } x < 1 \\ 0 & \text{for } x = 1 \end{cases} . \tag{6.17}$$

This increased complexity leads to a similarly piecewise form for the deflection potential which is given by

$$\psi(x) = \frac{k_s}{2} g(x), \tag{6.18}$$

with $k_s = 16\pi\rho_s(D_{OL}D_{LS}/D_{OS})r_s$ and the function $g(x)$ defined as

$$g(x) = \begin{cases} \left(\log\frac{x}{2}\right)^2 - 4\left(\operatorname{arctanh}\sqrt{\frac{1-x}{1+x}}\right)^2 & \text{for } x \leq 1 \\ \left(\log\frac{x}{2}\right)^2 + 4\left(\arctan\sqrt{\frac{x-1}{1+x}}\right)^2 & \text{for } x > 1 \end{cases} . \tag{6.19}$$

These do not allow analytical solutions to Equation 5.44 meaning that for the NFW profile, it must be evaluated numerically. Similarly in the geometric optics regime, numerical evaluation must be deployed to compute the image positions—representing a significant increase in complexity compared with the SIS or the point mass cases.

The NFW profile has two caustics, a radial and tangent caustic with the number of images produced depending on the former caustic. In cases where the source is inside of the radial caustic, i.e. $|y| < y_{\text{crit}}$, the profile produces three images and outside of it will produce only the single image case. This therefore marks an improvement upon the two previous models given that it follows the Burke theorem and adheres to observations of the number of images observed from galactic lensing.

6.2 Design Philosophy

Having established a selection of models that it would be desirable to have implemented, we turn our discussion to the practical development of the analysis framework that would come to be known as Gravelamps. There are the obvious requirements of such a framework, i.e. that it must be accurate and efficient. However, there are also philosophical considerations in approaching the development of large pieces of software, particularly those aimed not just at performing analysis for the author but being a platform for community usage and development. The following are the design principles that were decided upon for the development of Gravelamps.

Openness As may be noted in the previous section, the computation of the amplification factor from even simple profiles involves the computation of special functions and the integrals thereof, high value factorials, etc. This is obviously a complex process and it is naturally tempting to consider languages such as Wolfram's MATHEMATICA (Wolfram Research, Inc., 2024) which are purpose-built for such mathematical tasks. Such languages are proprietary, however, and come with associated financial costs and license restrictions that may negatively impact the ability of the community at large to either use the GRAVELAMPS framework in the first place, or restrict how it may be deployed.

Consequently, GRAVELAMPS was designed to be free open-source software—both in the 'free' and 'libre' contexts of open-source software developments. It has been made available under the permissive MIT license and uses libraries and packages that adhere to this general ethos allowing users to modify and deploy GRAVELAMPS in whichever manner they see fit.

Simplicity An important requirement for frameworks to be used by more than just the author are those of accessibility and simplicity. The readability and understandability of the code accepted into the GRAVELAMPS codebase is paramount and should be able to be understood by anyone with sufficient familiarity with the C++ and PYTHON programming languages.

Extensibility Frameworks expected to be used by the community cannot remain static. As an analysis of multiple models, GRAVELAMPS must be extensible to additional models of lens—the three that are discussed here are far from the only models available. For instance, attempts to address the central singularity in these profiles have resulted in the Burkert profile (Burkert, 1995). GRAVELAMPS has therefore been designed in modular fashion to allow users to contribute new profiles in keeping with the previous two philosophies.

6.3 Computation of the Amplification Factor

GRAVELAMPS' primary focus is the implementation of lens mass density profiles in both the wave and geometric optics regimes allowing the user to efficiently construct lensed GW signals. In geometric optics these calculations are practical to do on-the-fly and are thus available to the end user within the GRAVELAMPS PYTHON modules. However, as has been noted in Section 6.1, computation of the amplification factor for models in the wave optics regime is computationally challenging due to the highly oscillatory nature of Equation 5.44 and the requirement for high precision calculation of special functions in the cases of analytic solutions (e.g. point mass and SIS).

For these cases, Gravelamps contains C++ libraries implementing each of the models that are included with the wave optics calculations being done using C arbitrary precision library arb (Johansson, 2017) which is made available through the FLINT package (The FLINT team, 2023). These libraries are employed the command line program `gravelamps_generate_lens` which is designed to produce a grid of dimensionless frequency and source position, i.e. w and y over which the amplification factor will be calculated and stored in files. These files may then be used in a scipy-based interpolator (Virtanen et al., 2020) to allow efficient calculation of the amplification factor for use in the inference process for GW signals that will be discussed in the following sections.

Figure 6.1 illustrates the processes undertaken by the `gravelamps_generate_lens` program. To allow the program to be employed in as wide a number of use case possible, it allows the configuration of a number of aspects of the lens generation beyond simply the model to use. These include

- The dimensionless frequency and source position ranges which form the grid for the calculation of the amplification factor.
- The number of grid points in each of these ranges. By default Gravelamps will generate a linear spacing, however, it is capable of accepting any arbitrary list of grid points—though interpolation is possible only for sorted lists.
- The arbitrary precision to use in wave optics calculations. This widens the use cases of Gravelamps to those where some accuracy may be sacrificed for the benefit of the speed of the calculations.
- The upper limit of the infinite summation in the SIS case and the diffraction integral in the NFW case. Again, this grants the user the capability to decide precisely how much precision is necessary for their use case.
- The point at which the geometric optics regime is considered to be valid. This again improves the flexibility for users to decide which frequency regions must be investigated for wave optics effects.

Figure 6.2 shows the results of using the lens generation program to compute the amplification factors for the isolated point mass, SIS, and NFW profiles. Included are both the wave and geometric optics regimes for a number of source position values. These values span both the regimes where multiple and single images are produced for the latter two profiles—recalling that the point mass case always produces multiple images.

Whilst in a realistic deployment, it is likely that these cases would be mixed at a specified dimensionless frequency, deployment in this manner serves to demonstrate the differences between the two cases and justify why this choice was given to the user. As may be seen, in the region where multiple images would be produced, the wave optics and geometric optics converge relatively quickly—see Figure 6.3 which shows the residual for the SIS case in this region. It is noted that the convergence between the

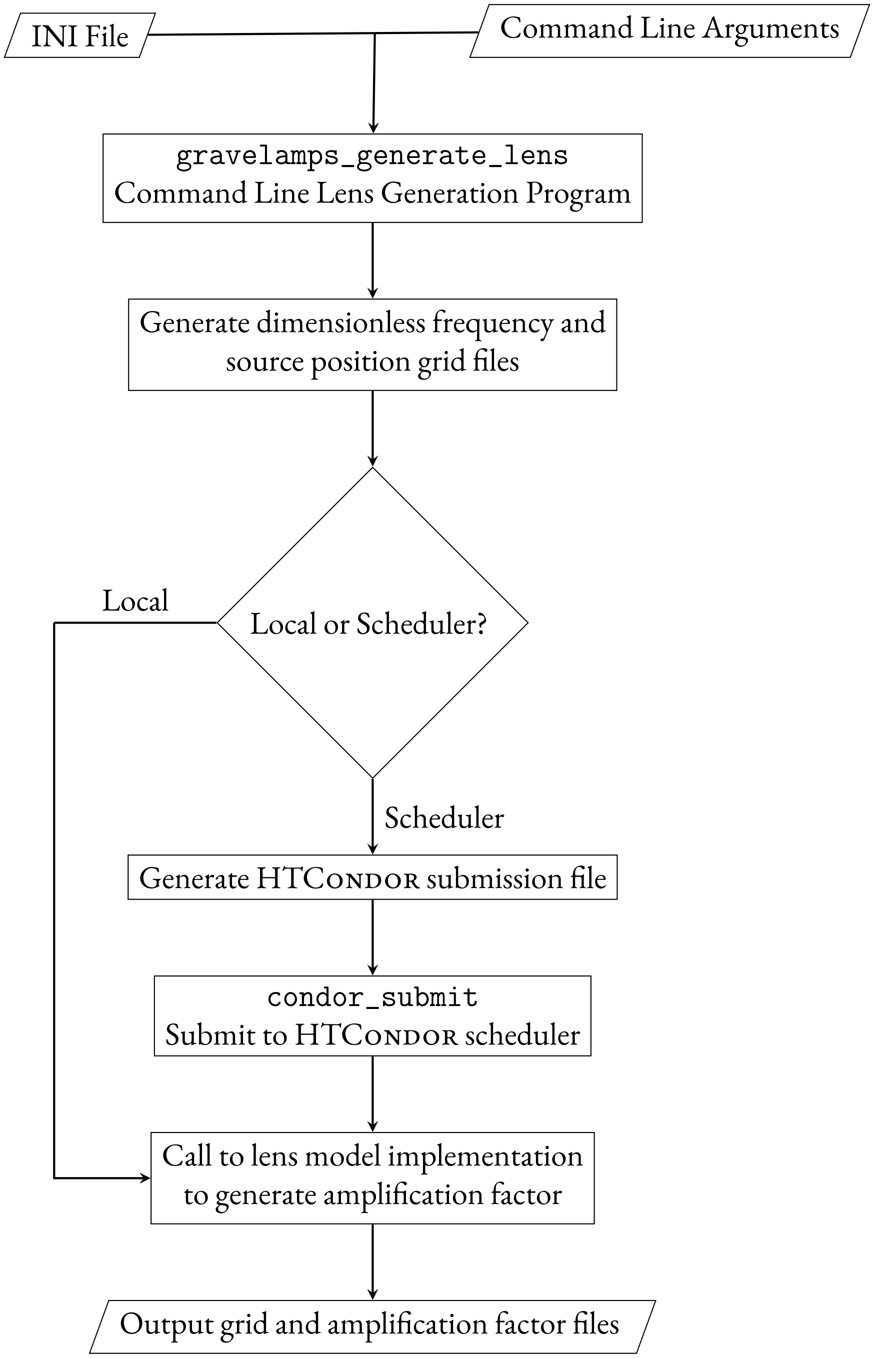

Figure 6.1: Flowchart depicting the Gravelamps lens generation procedures. From the user specified options in the configuration, it will ultimately produce four files containing the dimensionless frequency and source position grids and those containing the real and imaginary components of the amplification factor in the space corresponding to the grid.

wave optics and geometric optics regimes for the NFW case is noticeably slower than that for the point and SIS models.

In the scenario where only a single image is produced in the geometric optics regime, there is a more significant difference between the behaviours of the two calculations of the amplification factor. In this case, the wave optics amplification factors have a damped oscillatory behaviour which tends

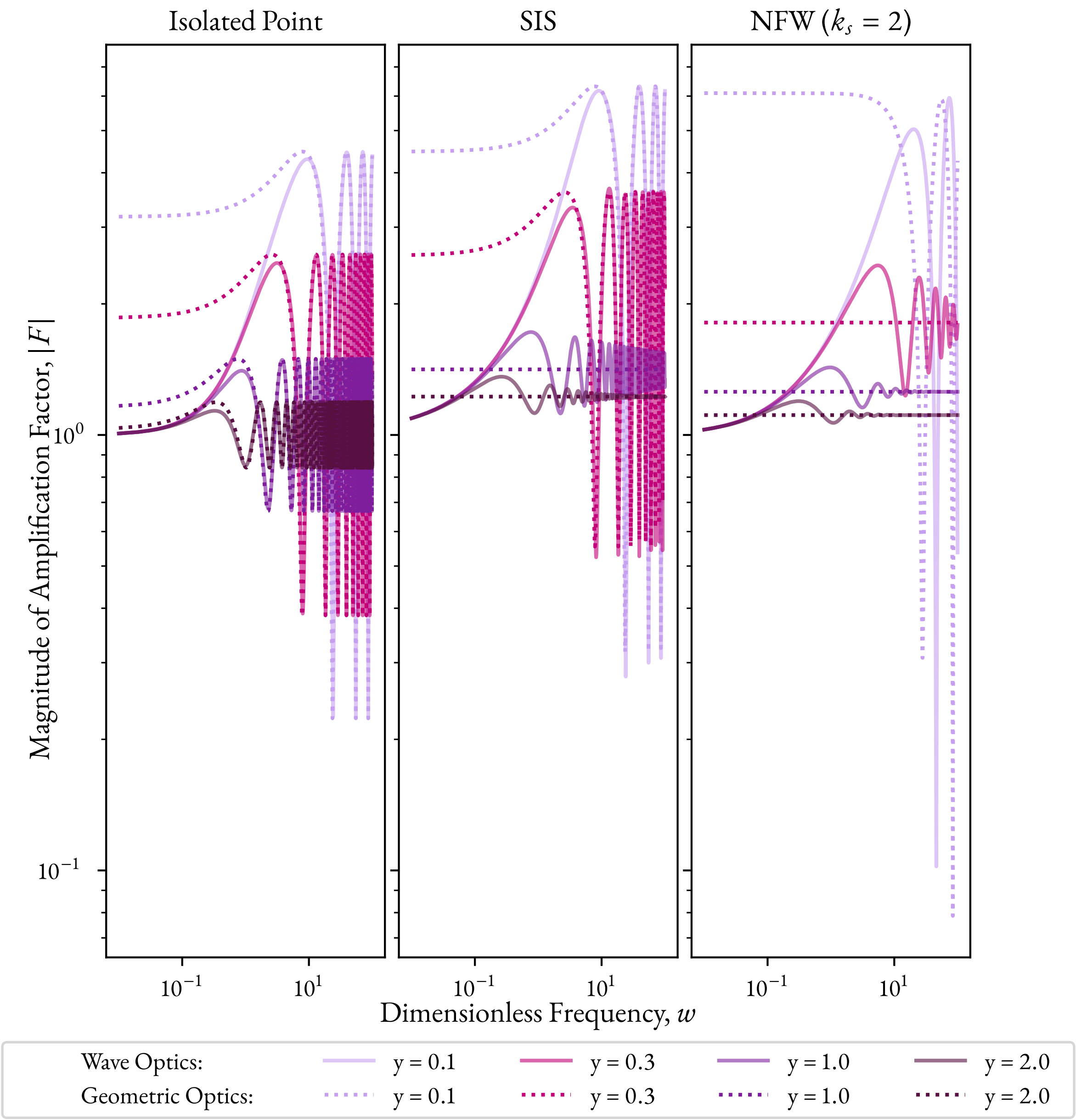

Figure 6.2: The amplification factor for the isolated point mass, SIS, and NFW mass density profiles as computed by Gravelamps' lens generation program. The dotted lines indicate geometric optics only calculation, whilst the solid lines indicate wave optics only calculation. Gravelamps may operate in either regime, or indeed switch at a specified dimensionless frequency value to maximise utility.

towards the geometric optics value. How quickly this damping occurs depends on the closeness of the source position to the caustic—see Figure 6.4 for the residual for the SIS case in this region. Therefore, one must decide how close to the caustic one would wish to include the majority of this oscillatory behaviour counter balanced with the increasing computational cost of including higher frequency wave optics calculations.

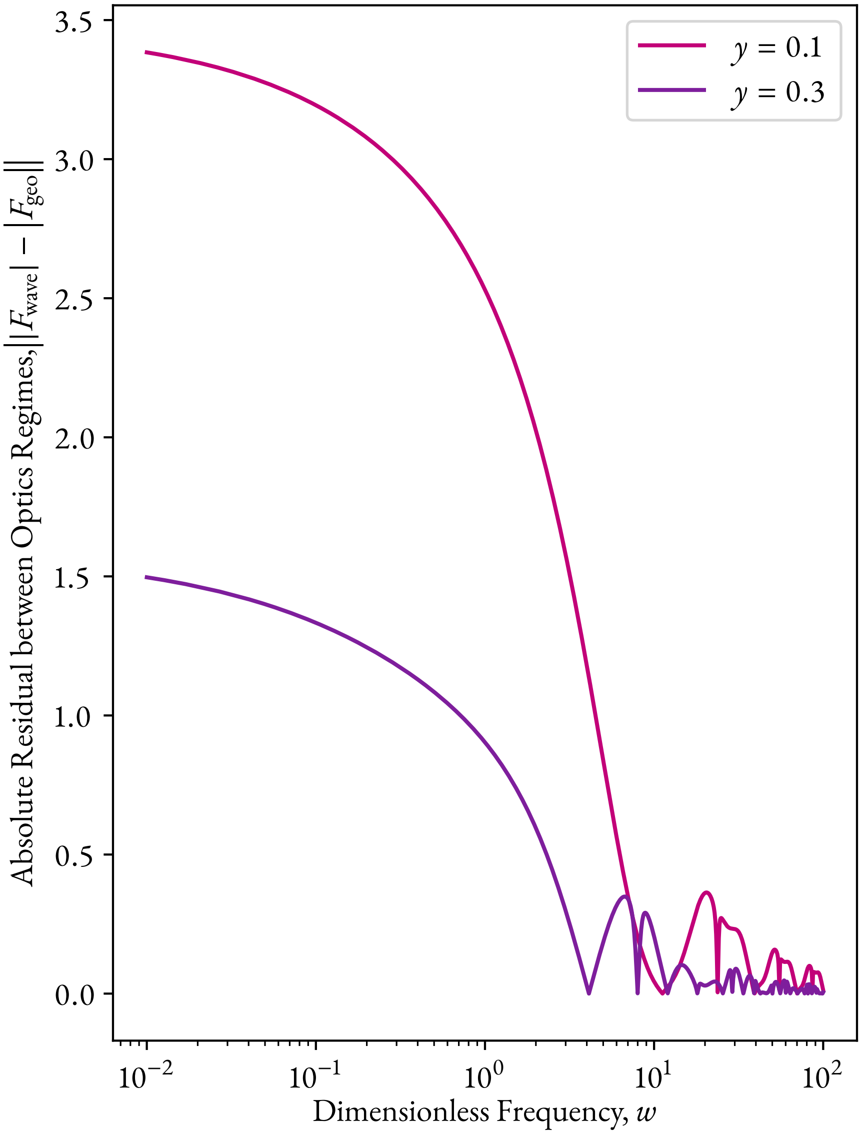

Figure 6.3: The absolute residual between the wave optics and geometric optics calculations of the amplification factor for the SIS model in the region where multiple images are produced, i.e. below $y = 1.0$. As may be seen, the residual significantly declines before $w = 1$ with the overall oscillation decreasing as w increases indicating that the geometric optics and wave optics agree relatively quickly.

6.4 Inference of Lens Model Parameters

We turn to the second program that exposes the Gravelamps functionality to the end user; this is the gravelamps_inference program. A schematic flowchart of this program is provided in Figure 6.5. To explore it the program first acquires the necessary data for analysis. This may be done in two ways

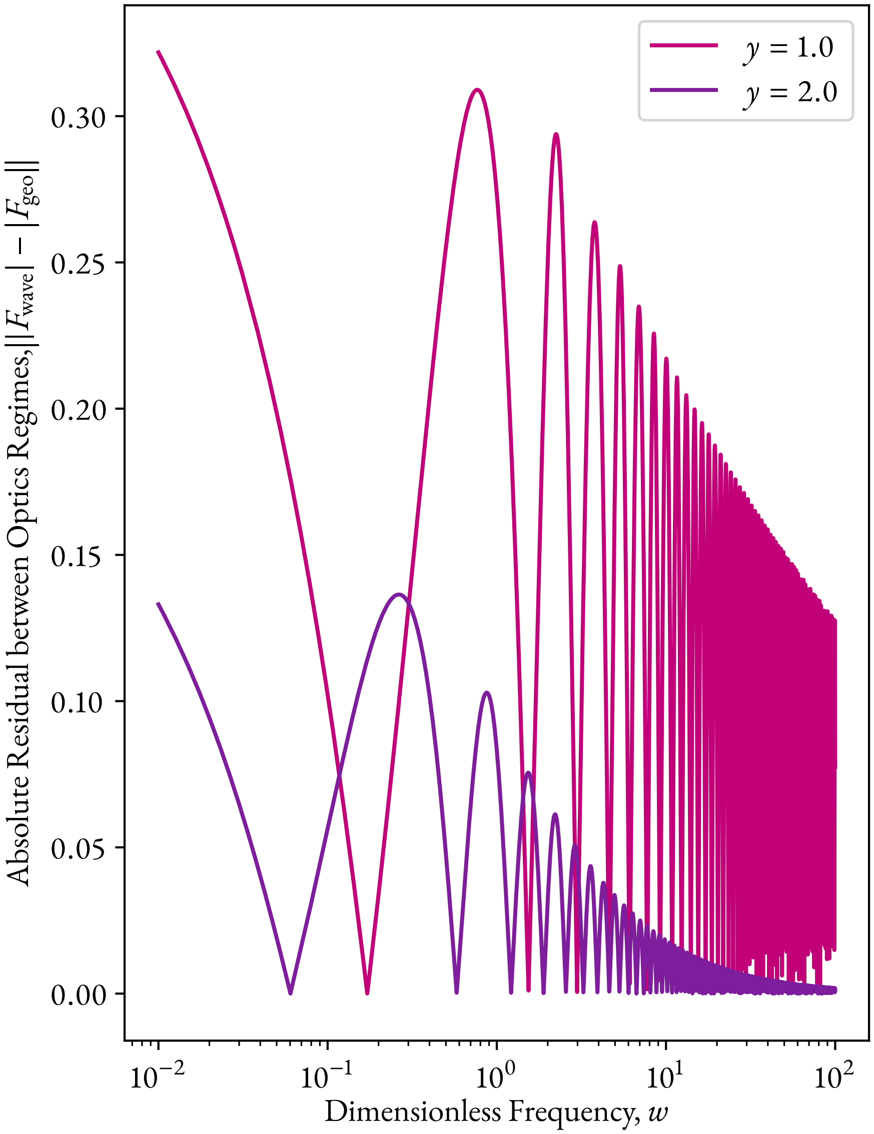

Figure 6.4: The absolute residual between the wave optics and geometric optics calculations of the amplification factor for the SIS model in the region where single images are produced. The residual follows the damping of the oscillation in the wave optics regime.

depending on whether it must retrieve GW data from the interferometers themselves or the inclusion of a set of parameters to create a simulated injection. These then may be analysed using a nested sampling implementation to retrieve posteriors on the source and the evidence for the selected lens model. Repeating this process multiple times then allows the calculation of the Bayes factors between these different models to determine which is the most likely.

The first step in the process of the data analysis is the generation of the lensed waveform. This

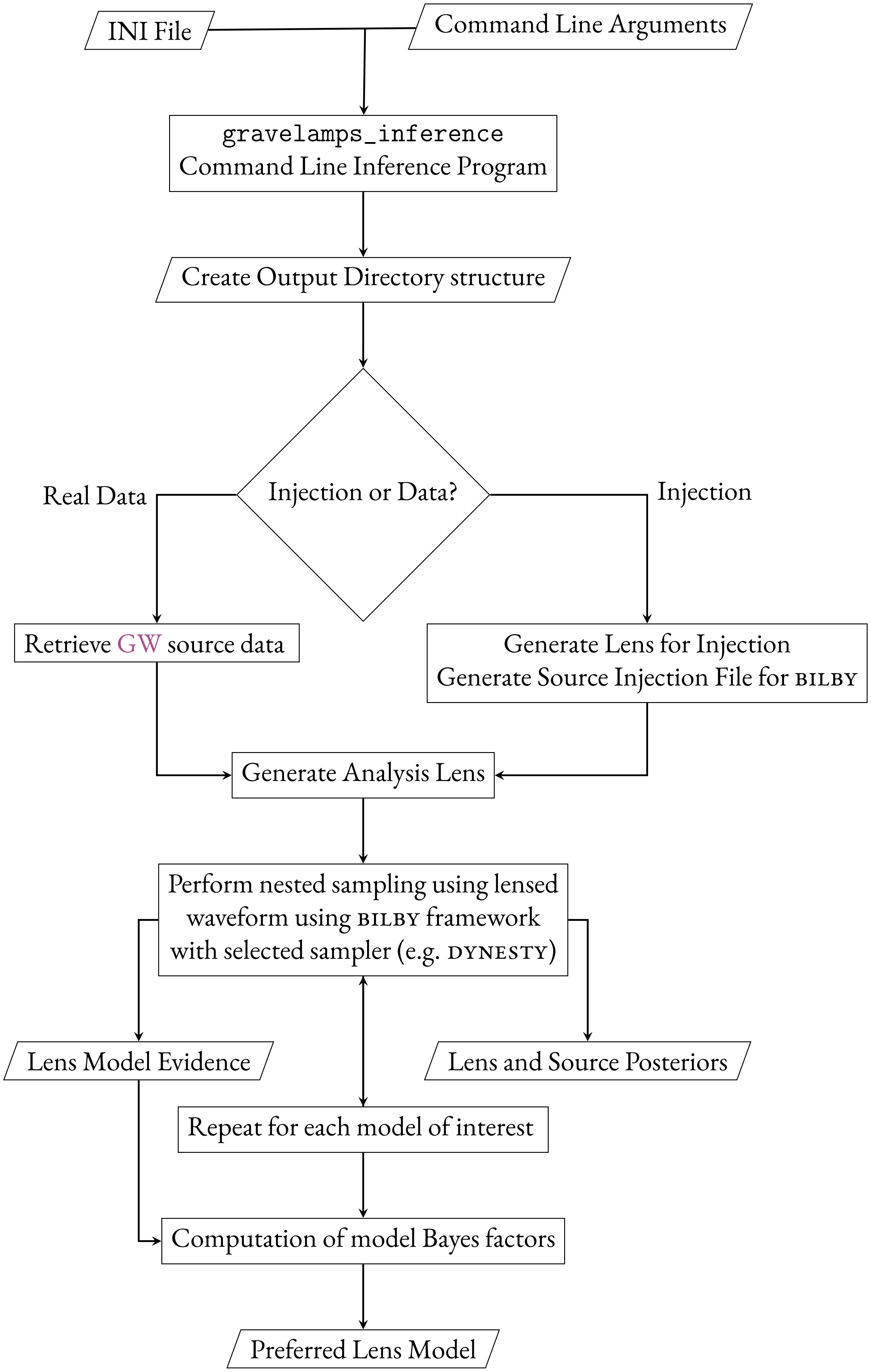

Figure 6.5: Flowchart depicting the procedures followed by the GRAVELAMPS inference program. The repetitions may be run in parallel or sequentially as additional runs of the program to arrive at a lensed model.

is done in GRAVELAMPS by first calling out to the relevant waveform approximants as discussed in Section 4.7.2; these implementations are made available as part of the LALSUITE package (LIGO Scientific Collaboration et al., 2018) and exposed in PYTHON through the BILBY package (Ashton et al., 2019). GRAVELAMPS will then use the generated amplification factor to lens the source waveform for use in the analysis. This may be done either by directly calling the amplification factor calculations or by using the output of `gravelamps_generate_lens` to construct an interpolator.

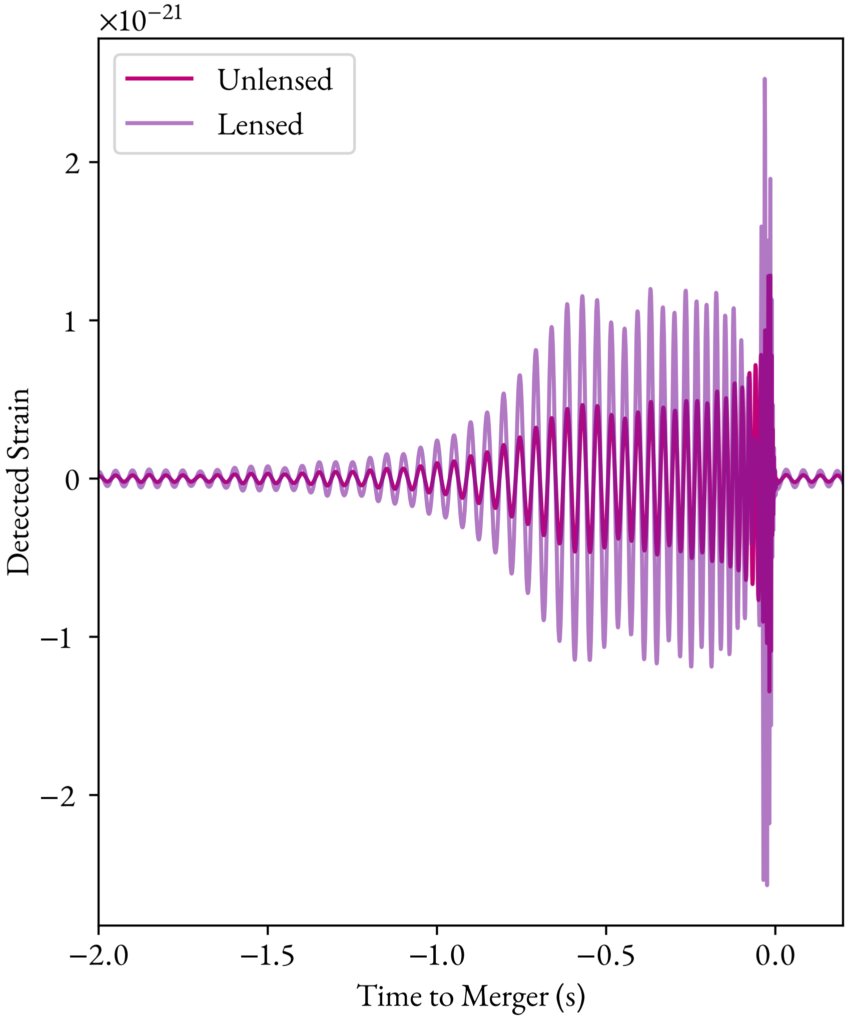

Figure 6.6: An example of a lensed waveform generated by GRAVELAMPS. In this case, this waveform is a binary black hole—the parameters of which are listed in full in Table 6.1—lensed by a $500M_\odot$ isolated point mass with a dimensionless source position of 0.1 that is located halfway between the source and the observer.

Figure 6.6 shows the comparison between the unlensed waveform generated for a BBH with the parameters listed in Table 6.1 using the IMRPHENOMXPHM waveform approximant (Pratten et al., 2021) and the same waveform lensed by a $1000M_\odot$ isolated point mass lens at a dimensionless source position of 0.3 located halfway between the source binary and the observer. In addition to the obvious amplification, one may also see the characteristic beating pattern that is the main observational signature of microlensing.

The next stage of the analysis is performing the nested sampling procedure outlined in detail in Section 3.8. Here again, Gravelamps employs the use of the bilby framework to gain access to a number of nested sampling algorithms—in particular the bilby_pipe package (Romero-Shaw et al., 2020) is used to create an integration with the HTCondor scheduler to deploy Gravelamps efficiently at scale. In particular, two will be used in the remainder of this thesis, those being dynesty (Speagle, 2020) and nessai (Williams et al., 2021).

Source Parameter	Value
Primary object mass, $m_1(M_\odot)$	36
Secondary object mass, $m_2(M_\odot)$	29
Luminosity distance, d_L(Mpc)	410
Dimensionless primary spin magnitude, a_1	0.4
Dimensionless secondary spin magnitude, a_2	0.3
Primary tilt angle, θ_1	0.5
Secondary tilt angle, θ_2	1.0
Azimuthal angle between component spins, ϕ_{12},	1.7
Azimuthal angle between total binary angular and orbital momenta, ϕ_{jl}	0.3
Angle between total binary angular momentum and line-of-sight, θ_{jn}	0.4
Polarisation angle, ψ	2.659
Phase at reference frequency, ϕ	1.3
Right Ascension, α	1.375
Declination, δ	1.2108
Coalesence Time, t_c	1125259642.413

Table 6.1: GW150914-like parameters used in the the example Gravelamps inference investigation

We now examine the results of such a nested sampling investigation of a lensed signal under the lensing hypothesis. For this, we examine a GW150914-like BBH signal—the parameters of which are given in Table 6.1—that has, again, been lensed by a $1000M_\odot$ isolated point mass at a dimensionless source position of 0.3 that is placed halfway between the binary and the observer. The choice of this parameter set was made to allow the lensing to be easily detectable.

The simulated signal from these parameters, again using the IMRPhenomXPHM waveform approximant, was then injected into simulated noise based upon the projected power spectral densities for the LVK detectors for O4. The resultant data was analysed using Gravelamps under the assumption of the isolated point mass lensing hypothesis with the dynesty nested sampler.

A subset of the resultant posteriors is shown in Figure 6.7. The subset shown are the firstly source parameters that will be most affected by the presence of microlensing—i.e. the chirp mass, $\mathcal{M}$, the mass ratio, q, the luminosity distance, d_L, followed by the lens model parameters. Overlaid on all of the plots are the injected values, and on the 1-dimensional posteriors the 1-σ boundaries which are used to form the headings of each column, alongside the median of the posterior. For four of the shown

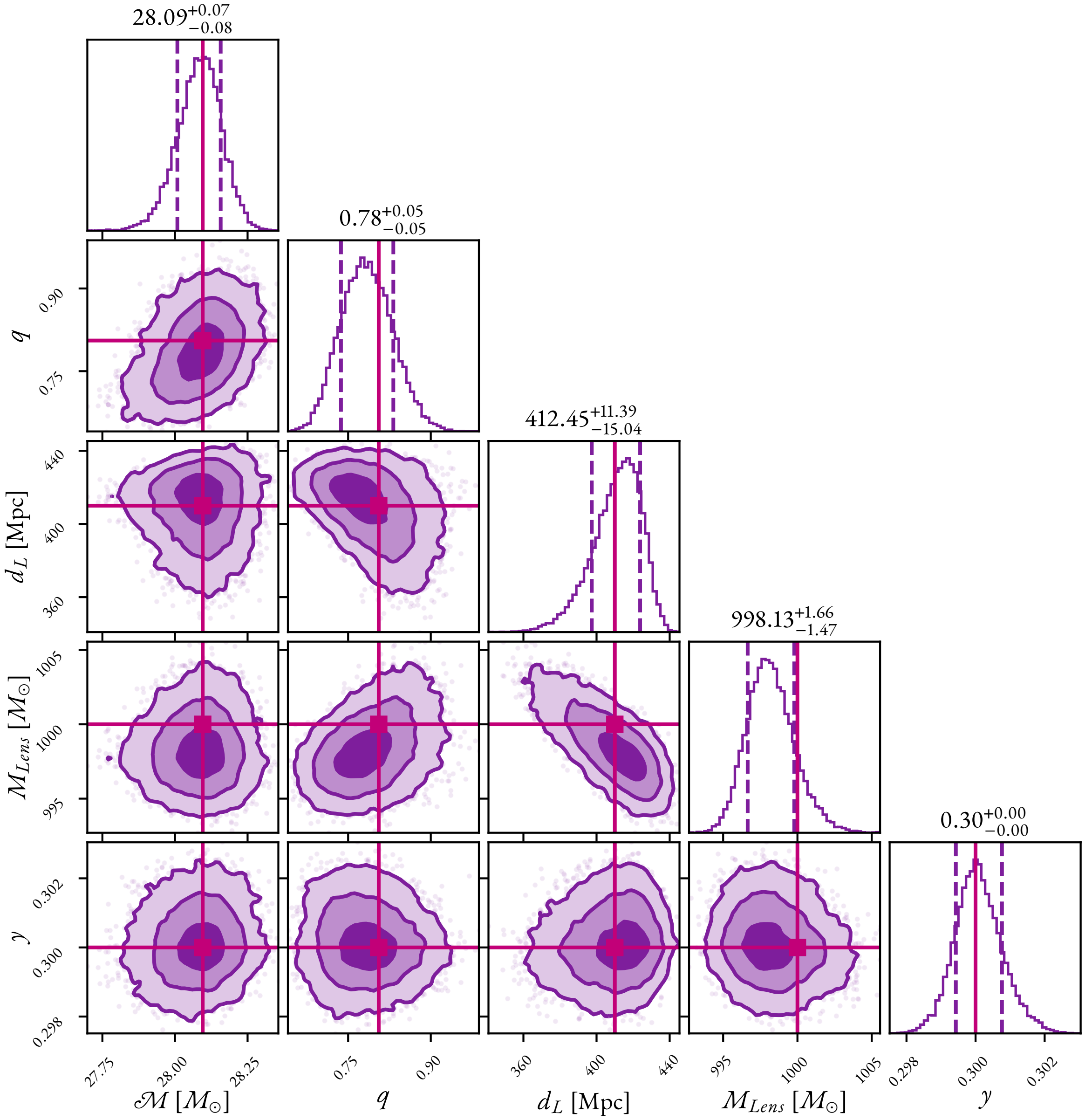

Figure 6.7: Subset of the parameter estimation results obtained using the DYNESTY nested sampler for a lensed GW150914-like BBH GW event analysed as such. Parameters shown are from left-to-right: the chirp mass, $\mathcal{M}$, the mass ratio, q, the luminosity distance, d_L, the lens frame lens mass, M_{Lens}, and the dimensionless source position, y.

parameters the injected value is within this 1-σ bound, and in the final case—that of the lens mass—is above the upper bound by $0.21 M_\odot$ and may be seen from the contours to be well within the 2-σ interval. This indicates a successful recovery providing a basis to continue to investigate whether the lens model may be retrieved following multiple such analyses using differing lens models.

6.5 Model Selection for Microlensing

We have presented a first proof-of-concept in the determination of lens parameters when performing a nested sampling investigation of a lensed signal as that model of lensing system. We now replicate the investigation of the point mass lensing injection using the unlensed, SIS, and NFW with $k_s = 2$ cases. We show the equivalent Figures to Figure 6.7 for each of these respective models in Figures 6.8, 6.9, and 6.10. We then continue and perform each of the combinations using the same set of parameters. The calculated $\log_{10}$ Bayes factors from this investigation are shown in Table 6.2.

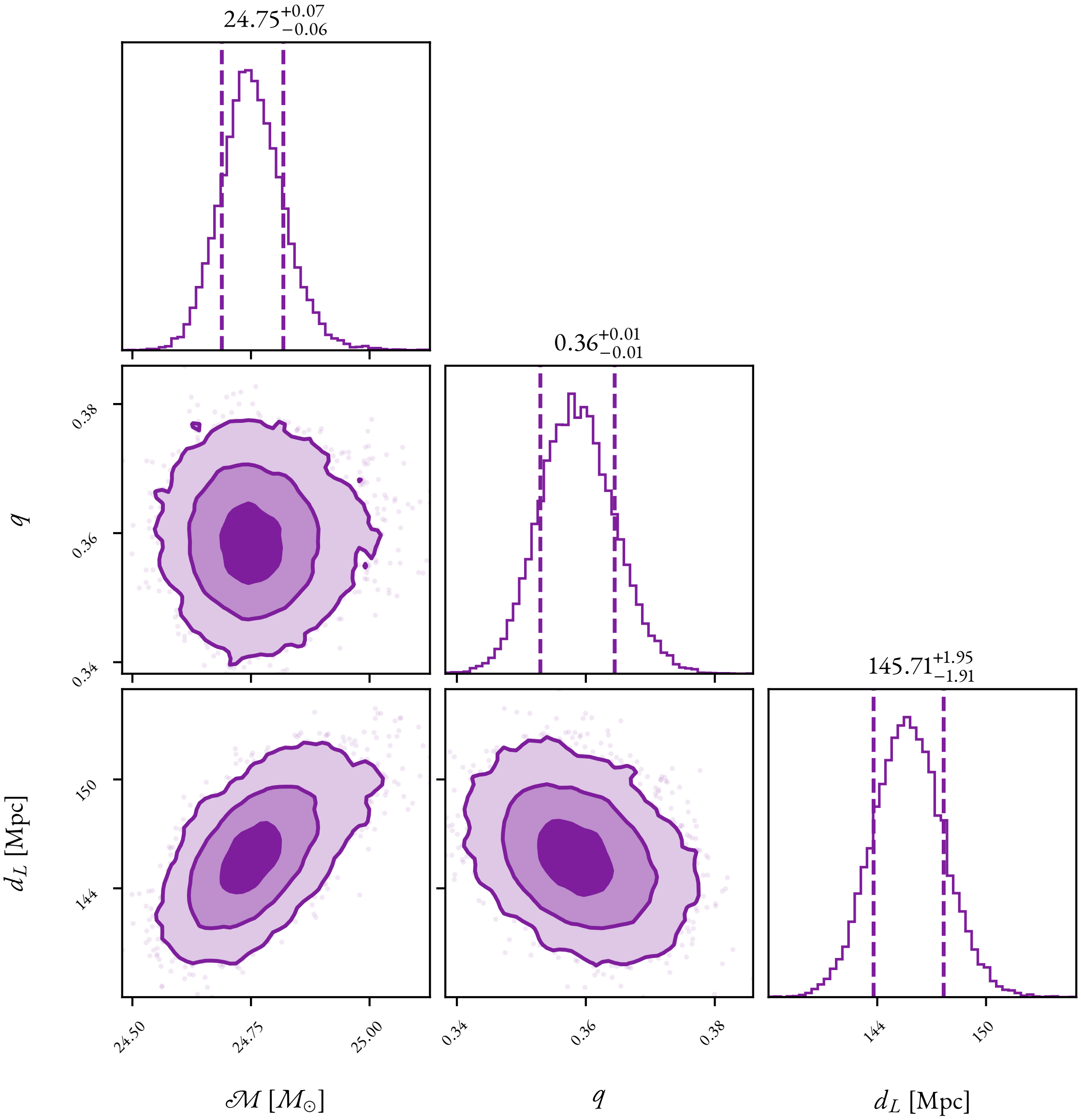

Figure 6.8: Subset of the parameter estimation results obtained using the DYNESTY nested sampler for a GW150914-like BBH GW event lensed by an isolated point mass analysed under the unlensed hypothesis. Format of the plot is the same as Figure 6.7.

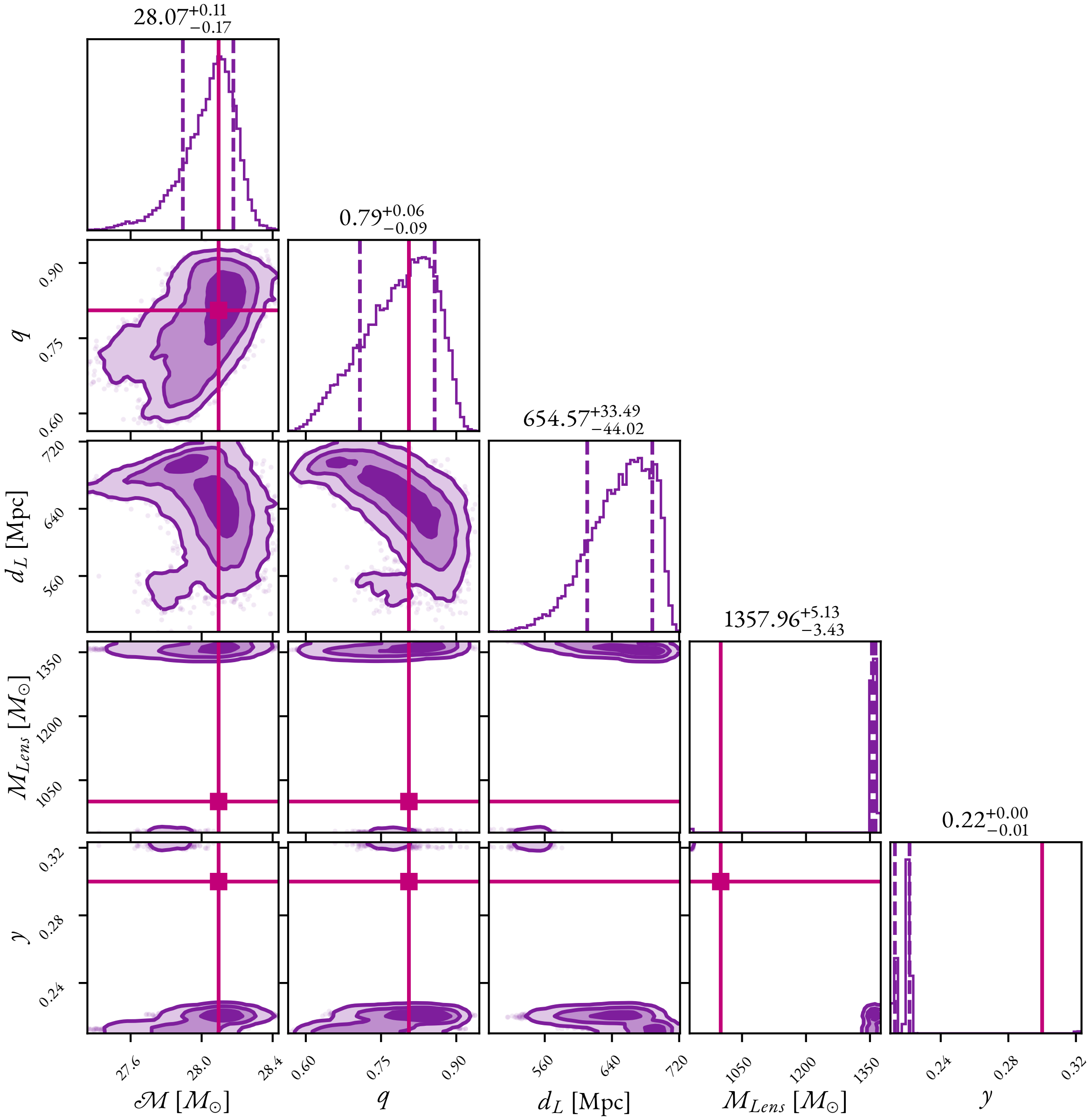

Figure 6.9: Subset of the parameter estimation results obtained using the DYNESTY nested sampler for a GW150914-like BBH GW event lensed by an isolated point mass analysed under the SIS microlensing hypothesis. Format of the plot is the same as Figure 6.7.

Model	Unlensed	Isolated Point Mass	SIS	NFW
Unlensed	0.00	6.06	−0.43	−0.82
Isolated Point Mass	3729.28	0.00	13.25	49.26
SIS	4016.60	49.93	0.00	476.14
NFW	113.80	37.01	27.00	0.00

Table 6.2: $\log_{10}$ Bayes Factors resulting from the parameter estimation investigations of signals generated using the model specified in the row label. The column header indicates which model the recovery was performed with.

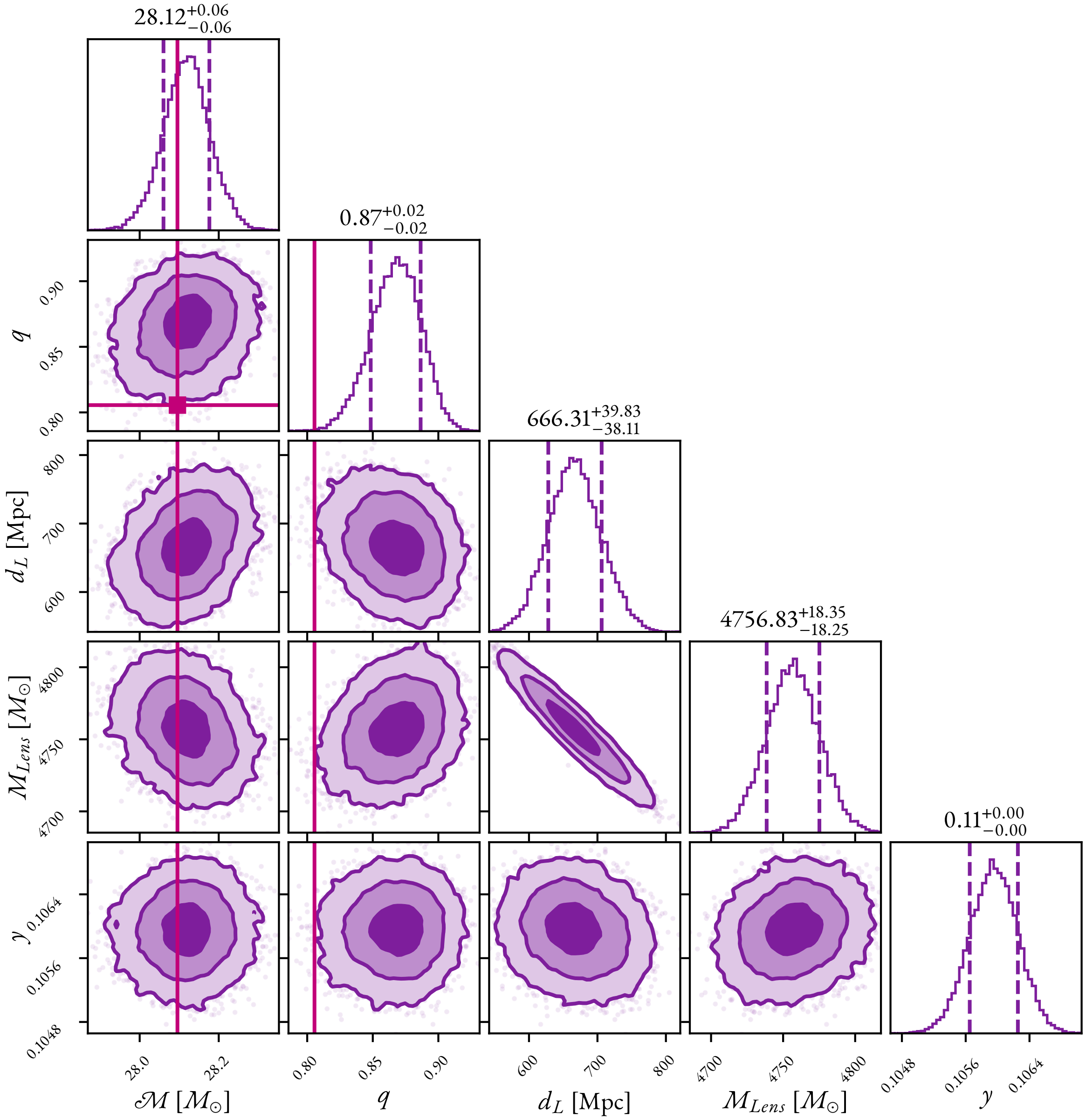

Figure 6.10: Subset of the parameter estimation results obtained using the DYNESTY nested sampler for a GW150914-like BBH GW event lensed by an isolated point mass analysed under the NFW microlensing hypothesis. Format of the plot is the same as Figure 6.7.

One may immediately note from Table 6.2 that each lens model is significantly favoured over the unlensed hypothesis, indicating that this approach may be used to identify microlensing signals. However, it is noted that the only misidentified cases from this investigation are those of the SIS and NFW investigations of an unlensed signal.

To illustrate why this is the case, the posteriors from these investigations are shown in Figures 6.11 and 6.12 for the models respectively. As might be expected, the lens mass and source position posteriors reflect the priors used for these analyses. In both cases, however, the binary mass parameters are well recovered. The luminosity distance parameters are recovered with less success, though are within the tails of the posterior. Examining again Figure 6.2, the combination of high lens mass and source

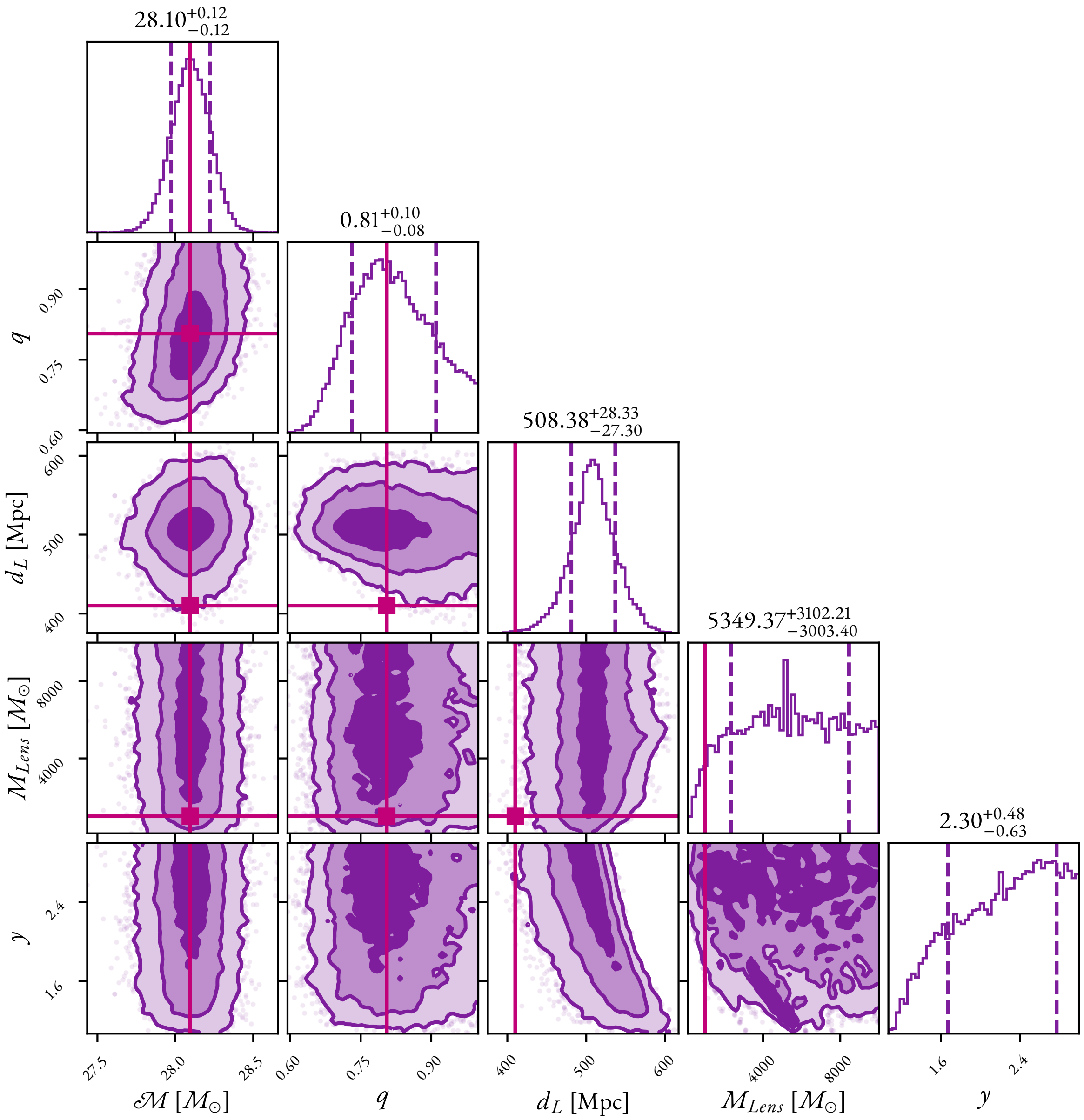

Figure 6.11: Subset of the parameter estimation results obtained using the DYNESTY nested sampler for a GW150914-like BBH GW event analysed as lensed by an SIS lens. Format of the plot is the same as Figure 6.7.

position results in a flat amplification factor meaning that much of this parameter space will return the same morphology as an unlensed signal with the extra degrees of freedom which is likely why these are lightly—but not conclusively—favoured over the true unlensed models.

Between lens models, the true lens model is favoured in all cases, conclusively so with the caveat that these parameters are such that the lensing effect is relatively large, giving support to the notion of using this parameter estimation framework to identify the lensing model. Isolated point mass analysis, given the greater distinction between itself across the parameter space and the unlensed case, is also given support for being an initial search method.

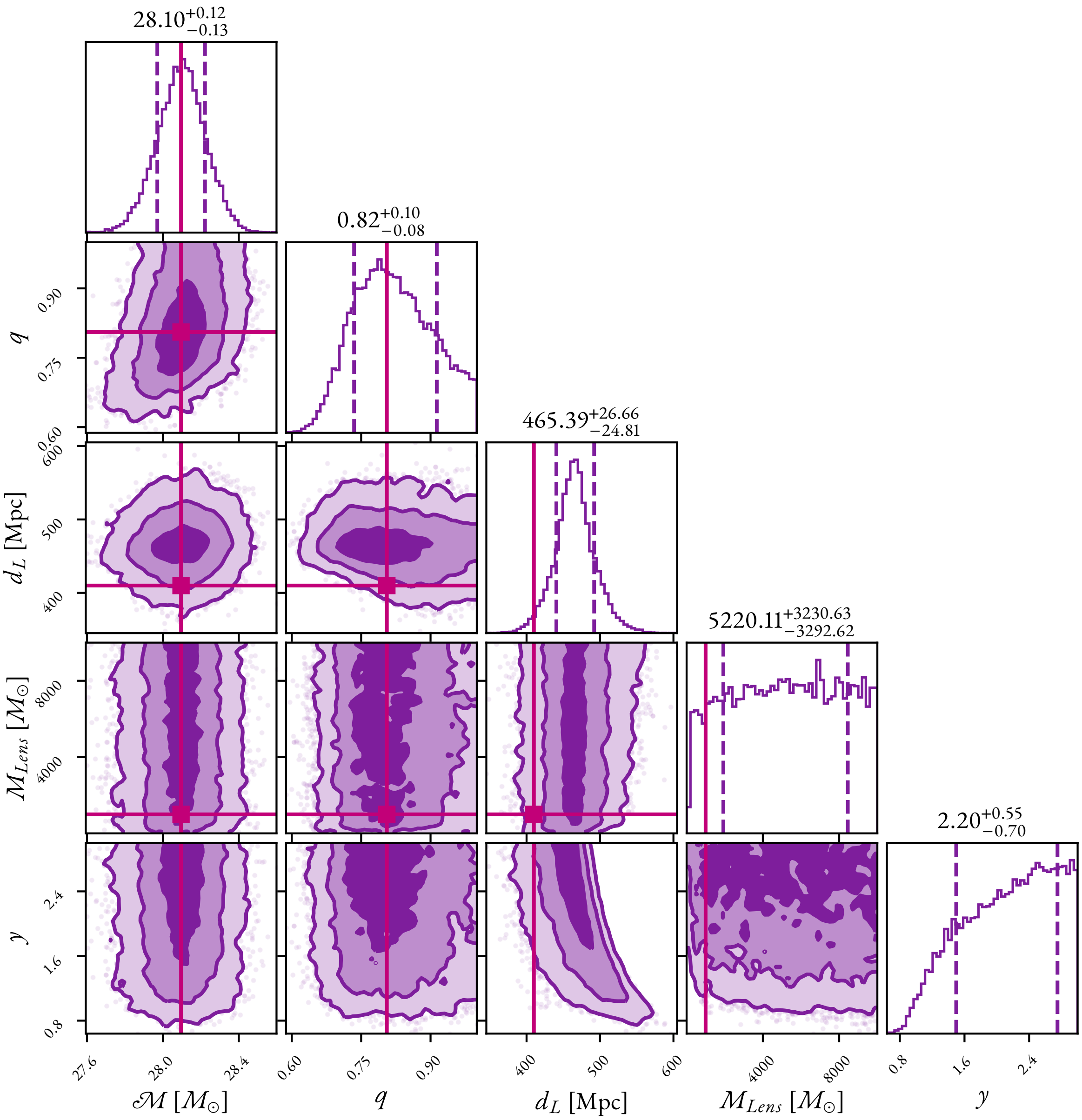

Figure 6.12: Subset of the parameter estimation results obtained using the DYNESTY nested sampler for a GW150914-like BBH GW event analysed as lensed by an NFW lens. Format of the plot is the same as Figure 6.7.

6.6 Limitations of Single Image Analysis

Given the success of this methodology in identifying the lens model in the microlensing regime, and the ability of the GRAVELAMPS implementations of the lensing models, it is tempting to ask the question about strong lensing and whether it may be identified in single GW event parameter estimation. To illustrate such an investigation, Figures 6.13 and 6.14 show a subset of the posteriors obtained from an SIS and NFW investigation of the same GW150914-like source parameters lensed by a $4.4\times10^7 M_\odot$ SIS lens, i.e. something appropriate to galactic scale strong lensing with a dimensionless source position of 1.0.

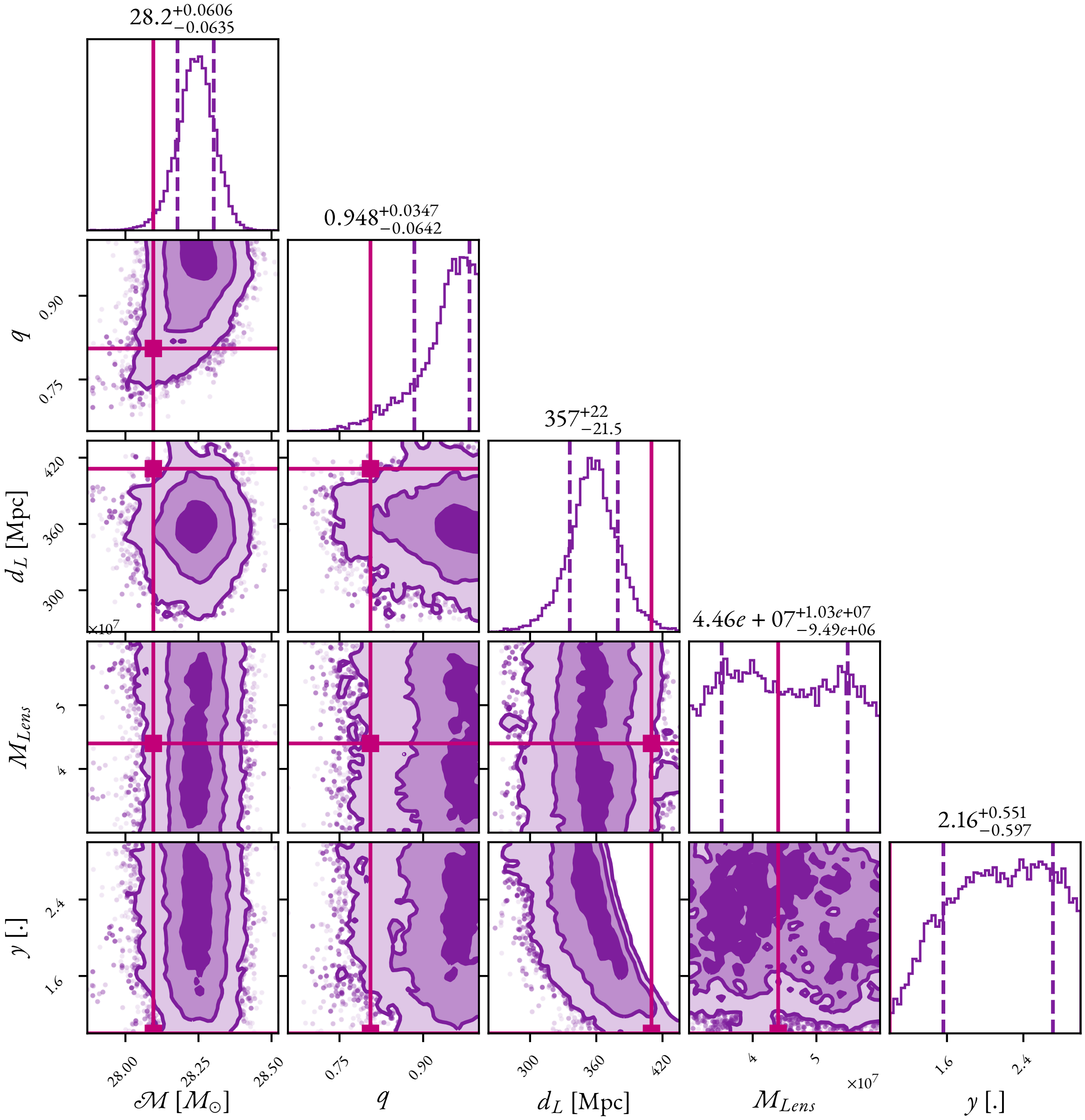

Figure 6.13: Subset of the parameter estimation results obtained using the DYNESTY nested sampler for a GW150914-like BBH GW event lensed by a galactic scale SIS lens and analysed as such. Format of the plot is the same as Figure 6.7.

In these cases neither the lens nor binary parameters are well recovered and indeed the two recoveries are consistent with each other. This is reflected in the comparison between the evidences for these models which yields a $\log_{10}$ Bayes factor of -0.05 indicating an inability to distinguish between the two models. This is again the result of the flattening of the amplification factor for these two models at geometric optics scales which results in the same morphology as the unlensed signal providing no additional information on the amplification parameters signalling that this approach on single images is insufficient for the strong lensing case.

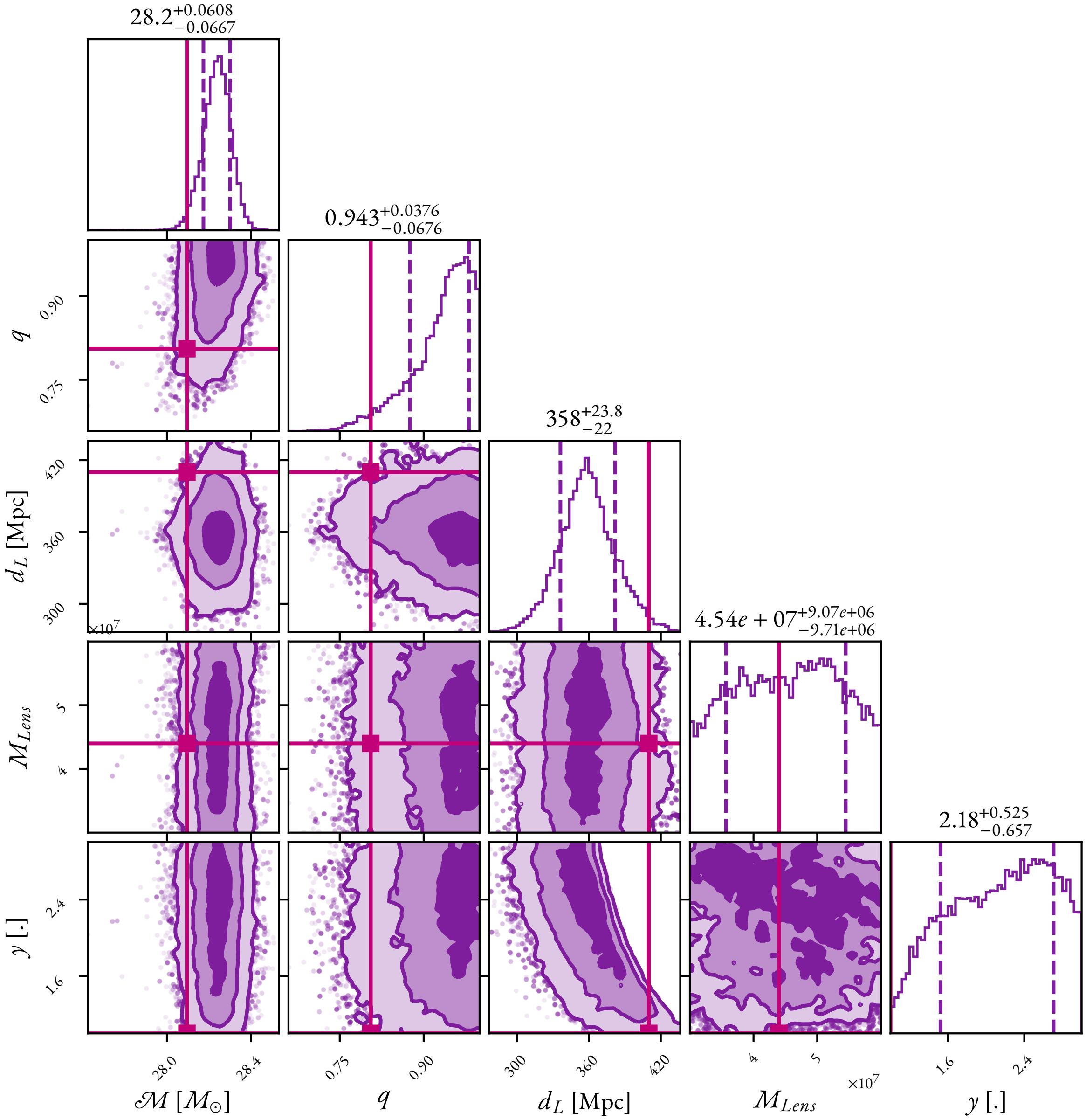

Figure 6.14: Subset of the parameter estimation results obtained using the DYNESTY nested sampler for a GW150914-like BBH GW event lensed by a galactic scale SIS lens and analysed as lensed by an NFW lens. Format of the plot is the same as Figure 6.7.

6.7 Conclusion

In this chapter, we have presented GRAVELAMPS, a framework that is built to perform template-based parameter estimation investigations of GW signals to determine both the presence of GW microlensing and in the affirmative case to assess the most likely lens model and the parameters thereof. The framework is a combination of PYTHON and C++ which enables the rapid computation of the amplification factors resulting from a variety of lensing models whilst being open and extensible for any additional models that are integrated in the future.

Using a simulated GW150914-like signal we have given an initial proof-of-concept that both the correct-model analysis will accurately recover the parameters of the source accounting for the lensing effect and the lensing parameters and that the correct-model will be preferred over both the unlensed hypothesis and other models of lensing. In so doing, we have also presented an initial justification for a primary model search using the isolated point mass model to efficiently scan through GW data for candidates for follow-up investigation.

Additionally, we have shown the limitations of this form of investigation on single GW events which is that larger lenses which would produce strong lensing may not be identified using this format for which another methodology needs to be identified—which will be discussed further in Chapter 8.

Adhering to the principles of free, open source software, Gravelamps is made available to the public with the permissive MIT License.

7

Deployments of the Gravelamps Pipeline

> *The Universe is a mess, I've got plenty of things to keep me busy*
>
> —Trance Gemini, *Andromeda*
>
> Created by Gene Roddenberry and Robert Hewitt Wolfe

Disclaimer

The following chapter is partially based on the work I performed for *Follow-up analyses to the O3 LIGO-Virgo-KAGRA lensing searches* which was co-authored by Justin Janquart, Srashti Goyal, and 29 others. It was published in the Monthly Notices of the Royal Astronomical Society.

The following chapter is also partially based on work performed for an in-preparation paper that will be co-authored by Justin Janquart, Paolo Cremonese, Alvin Li, and Juno C. L. Chan, as well as others.

By the end of O3, the Gravelamps package had reached a sufficiently mature stage that it could be deployed to investigate real GW events. The lensing analyses at that time had concluded that no confident detections of lensing in either the strong lensing or microlensing regimes had been found (Abbott et al., 2023d). However, it had identified a number of candidates that were worthy of additional scrutiny, and in this chapter we present the Gravelamps analyses that were performed on these candidates as well as two initial candidates from the currently ongoing O4 on which lensing interest has been identified.

This chapter will also discuss upgrades to the Gravelamps package and strategies developed from these initial small-scale deployments designed to allow for much larger deployment during the full O4 lensing analyses in which Gravelamps is expected to be a participant pipeline.

7.1 Searches for Millilensing using Phenomenological Approach

As discussed in Section 6.2, Gravelamps was designed to be an extensible platform that may be added to by the wider GW lensing community to incorporate additional lensing models. The first major addition of such a lensing model is a phenomenological approach for the millilensing scale of lensing that was first developed in Liu et al. (2023). We will here briefly summarise this model and provide an initial demonstration of its operation within the Gravelamps package as was done for the first models in Chapter 6.

Recalling Section 5.8, millilensing corresponds to the domain of sub-galactic structure which is sufficient to produce time delays on the scale of milliseconds, from which the name arises. At this scale, the geometric optics approximation is valid as is the case with strong lensing, but the produced images will overlap resulting in beating patterns similar to that of microlensing. The temporal closeness of the resulting images also allows continued examination as a single signal as compared with the strong lensing case.

That the geometric optics is valid means that the amplification factor may be calculated using Equation 5.45, i.e. the summation of the magnification, time delay, and Morse phase shift for each of the produced signals which are termed *millisignals*. It may be noted however, that the magnification is degenerate with the luminosity distance to the source, such that for the j^{th} produced millisignal the effective luminosity distance is given by (Liu et al., 2023)

$$d_j^{\text{eff}} = \frac{d_L}{\sqrt{\mu_j}}. \tag{7.1}$$

Time-ordering the signals, we may choose a time delay of zero, such that the time delays of the other signals are relative to the first signal. Combining this choice with Equation 7.1, we may therefore see that the amplification factor for this millilensing case is given by

$$F(f, d_j^{\text{eff}}, t_j, n_j) = d_L \left(\frac{1}{d_1^{\text{eff}}} \exp\left[-i\pi n_1\right] + \frac{1}{d_2^{\text{eff}}} \exp\left[2\pi f t_2 - i\pi n_2\right] + \ldots \right). \tag{7.2}$$

This approach has been implemented into Gravelamps by means of a python module that may be deployed with either a static number of millisignals or with that number as a free parameter. Liu et al. (2023) presents the testing of validity for this method, but we here present the results of its operation within the Gravelamps framework as an illustration before its deployment in later sections.

Figure 7.1 shows the example waveform used in the test case. The unlensed waveform uses the same GW150914-like parameters as outlined in Table 6.1 with the exception of increasing the luminosity distance to 1200Mpc. The millilensed waveform has been generated such that the first image has a Morse index of 0, i.e. is a Type I image. A second image has also been generated with a time delay of 0.058s and magnified such that it has an apparent luminosity distance of 410Mpc and has a Morse index of 0.5, i.e. is a Type II image.

This waveform was subject to three analyses—as a millilensed waveform with the number of images

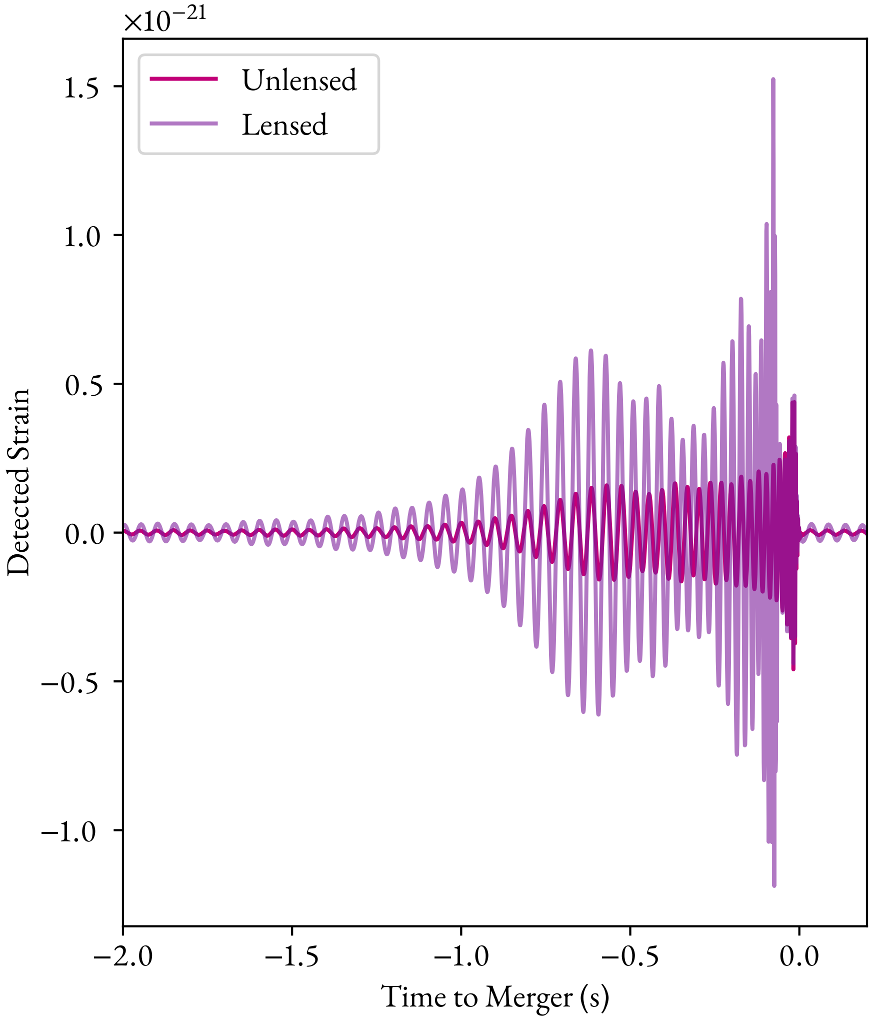

Figure 7.1: An example of a millilensed waveform generated by Gravelamps with the original source waveform for comparison. In this case a GW150914-like signal has been lensed by a millilens such that two images have been produced with an apparent luminosity distance of 1200 and 410Mpc with a time delay of $0.058s$ and Morse indices of 0 and 0.5 respectively.

produced fixed to two, as a point mass microlensing waveform, and as an unlensed waveform. These yielded a $\log_{10}$ Bayes factor preference for millilensing of 157 over the microlensing model and 189 over the unlensed model. Consequently the microlensing model presents a $\log_{10}$ Bayes factor of 32 over the unlensed model. This again would present an intial justification for using the point mass microlensing search as an initial sweep for further investigation before deploying the millilensing model.

Turning to the recovery of the lensing observable parameters, these are presented in Figure 7.2. The luminosity distances of the two images as well as the time delay is well recovered, as has been the case with the microlensing results in the previous searches.

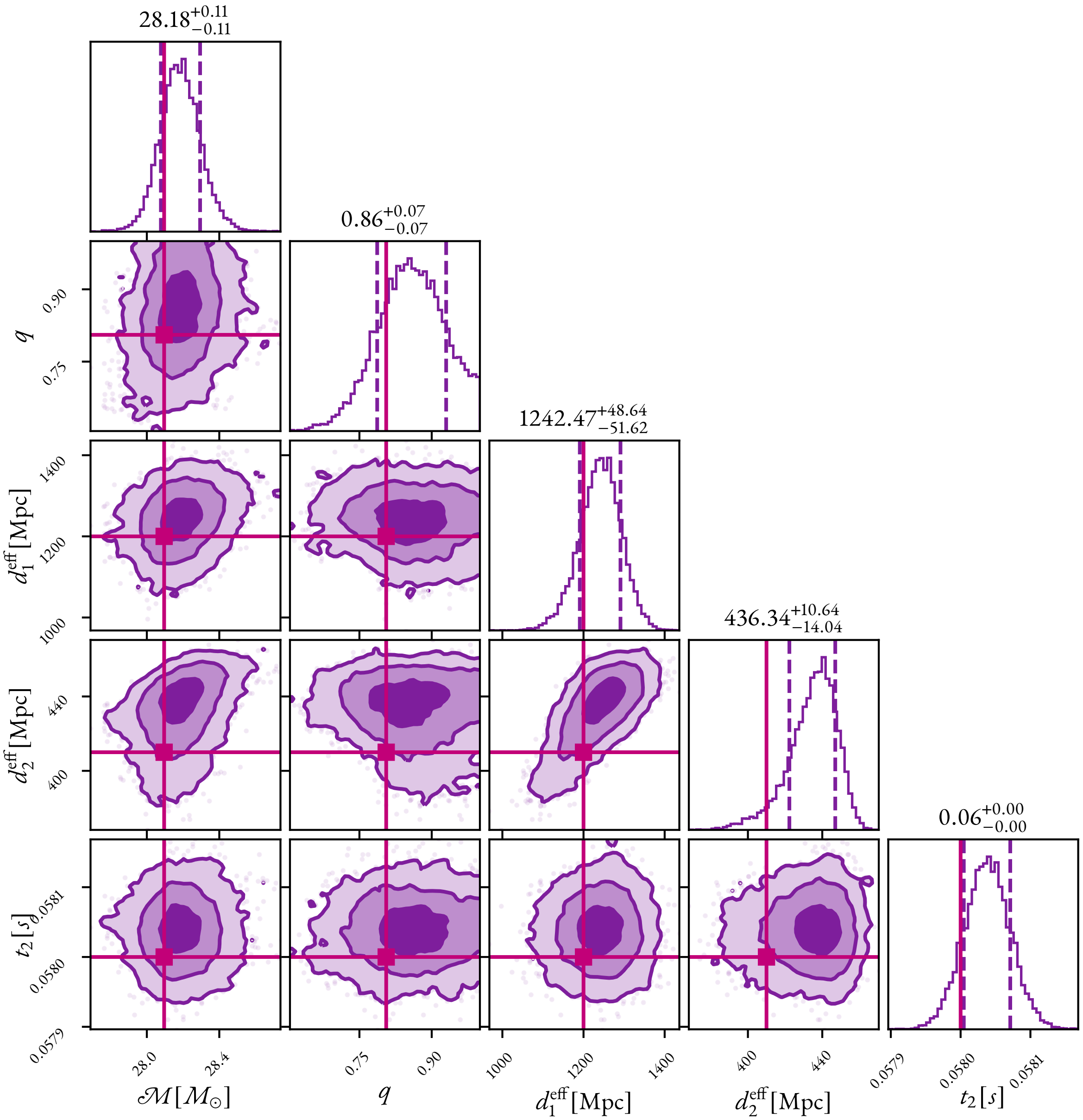

Figure 7.2: Subset of the parameter estimation results analysing a millilensed GW150914-like event analysed as such with the number of images fixed to two.

7.2 GW190412

GW190412 was detected during O3 and was identified as a BBH coalescence with a $30M_\odot$ primary and $8M_\odot$ secondary. It is notable for being alongside GW190814 one of the two events detected during that observing run that contained significant HOM content (Abbott et al., 2020c; Abbott et al., 2020a). This significant HOM content made it of particular interest for lensing searches as its presence would allow the identification of Type II strongly lensed images from a single signal—see Janquart et al. (2021) for further details.

Investigations of this event that were conducted for Type II signals revealed a marginal preference for a Type II signal with $\log_{10}$ Bayes factors of 0.61 and 0.30 over Type I and Type III respectively (Abbott et al., 2023d). It was therefore followed up with additional scrutiny which revealed that the apparent support was dependent upon waveform choice and is thus likely the consequence of a noise artefact.

As the main feature of Type II lensing would be apparent de-phasing, it was also investigated whether or not this may be the result of the misidentification of a microlensed signal. As such GW190412 was subject to investigation by GRAVELAMPS with both the isolated point mass and SIS lensing models. These yielded marginal support for the microlensing hypothesis in both cases with $\log_{10}$ Bayes factors of 0.6 and 0.4 respectively.

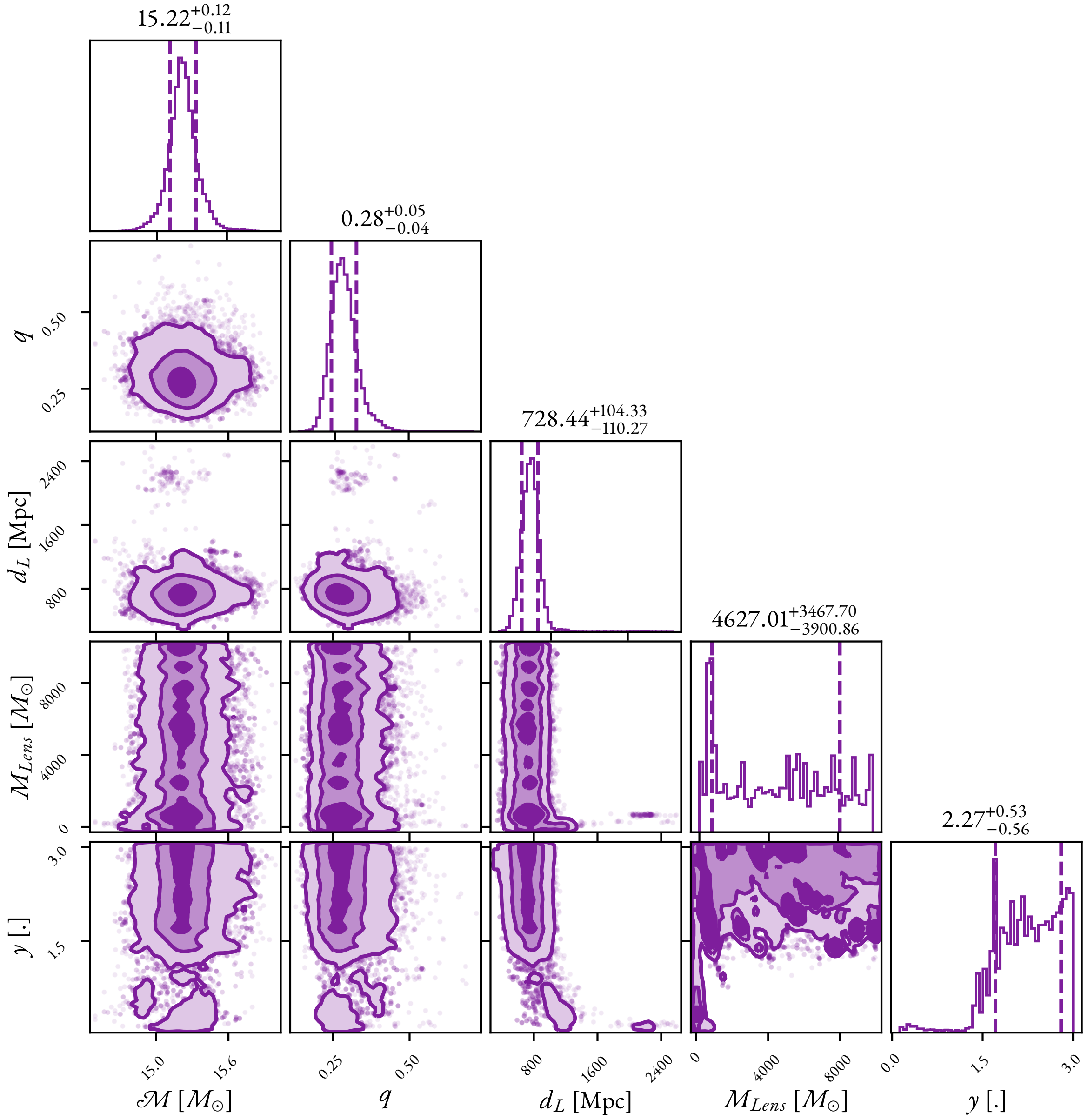

Figure 7.3: Subset of parameter estimation results from analysing GW190412 under the isolated point mass microlensing hypothesis. Format of the plot is the same as Figure 6.7.

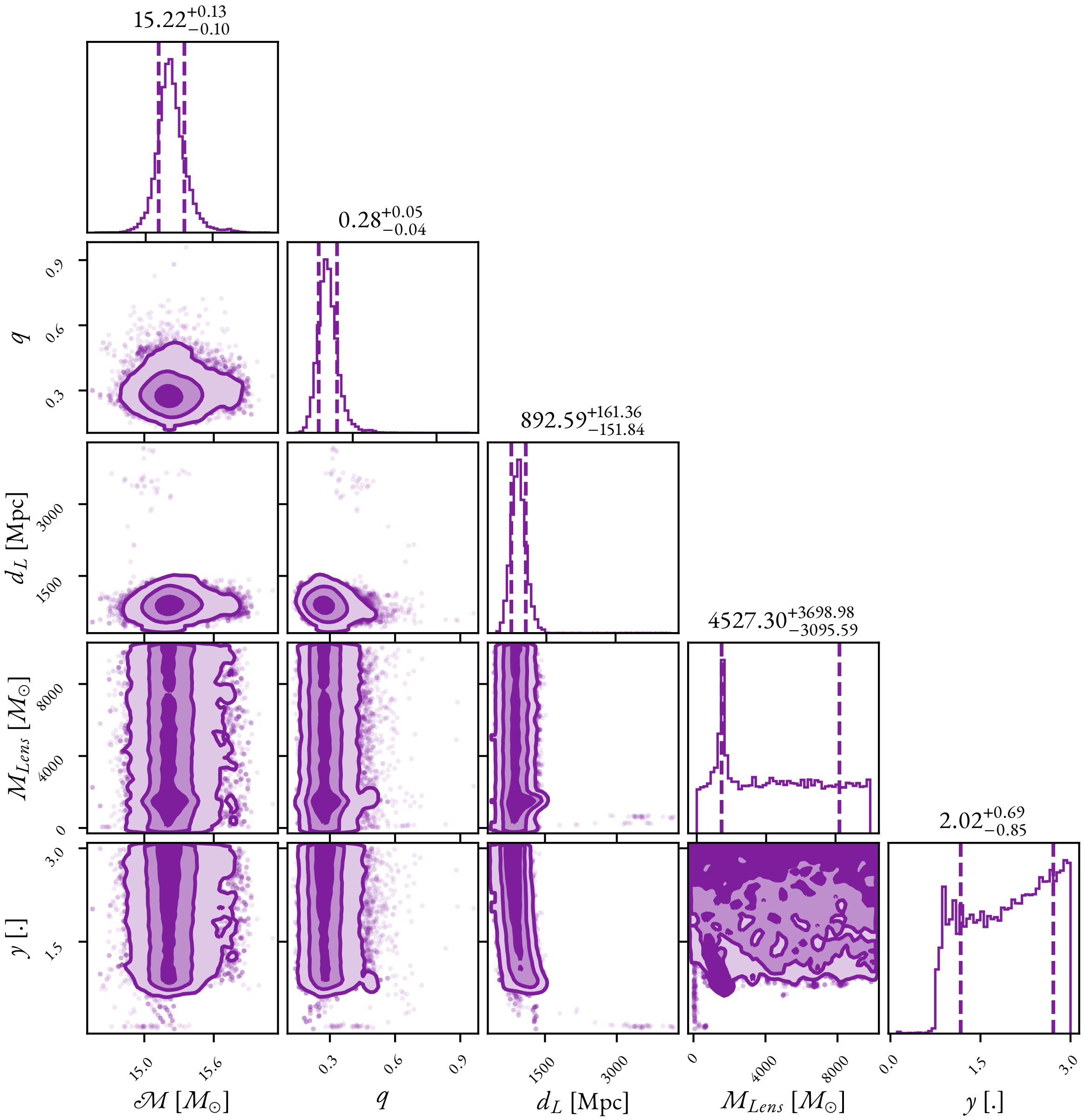

Figure 7.4: Subset of parameter estimation results from analysing GW190412 under the SIS microlensing hypothesis. Format of the plot is the same as Figure 6.7.

Examinations of the resultant posteriors as shown in Figures 7.3 and 7.4, however, do not indicate significant constraint of the lensing parameters. The preference for the high source position indicates the region of parameter space resulting in a relatively small amplification factor. We notice also in the SIS case, the preference for high mass also indicates a preference for a flat amplification factor. Comparing the source posteriors with those for an equivalent investigation using an unlensed model, shown in Figure 7.5 yield similar results. Combined with the relatively low Bayes factor, these indicate that the slender support is likely the result of a noise artefact, inline with the expectations from the Type II analyses.

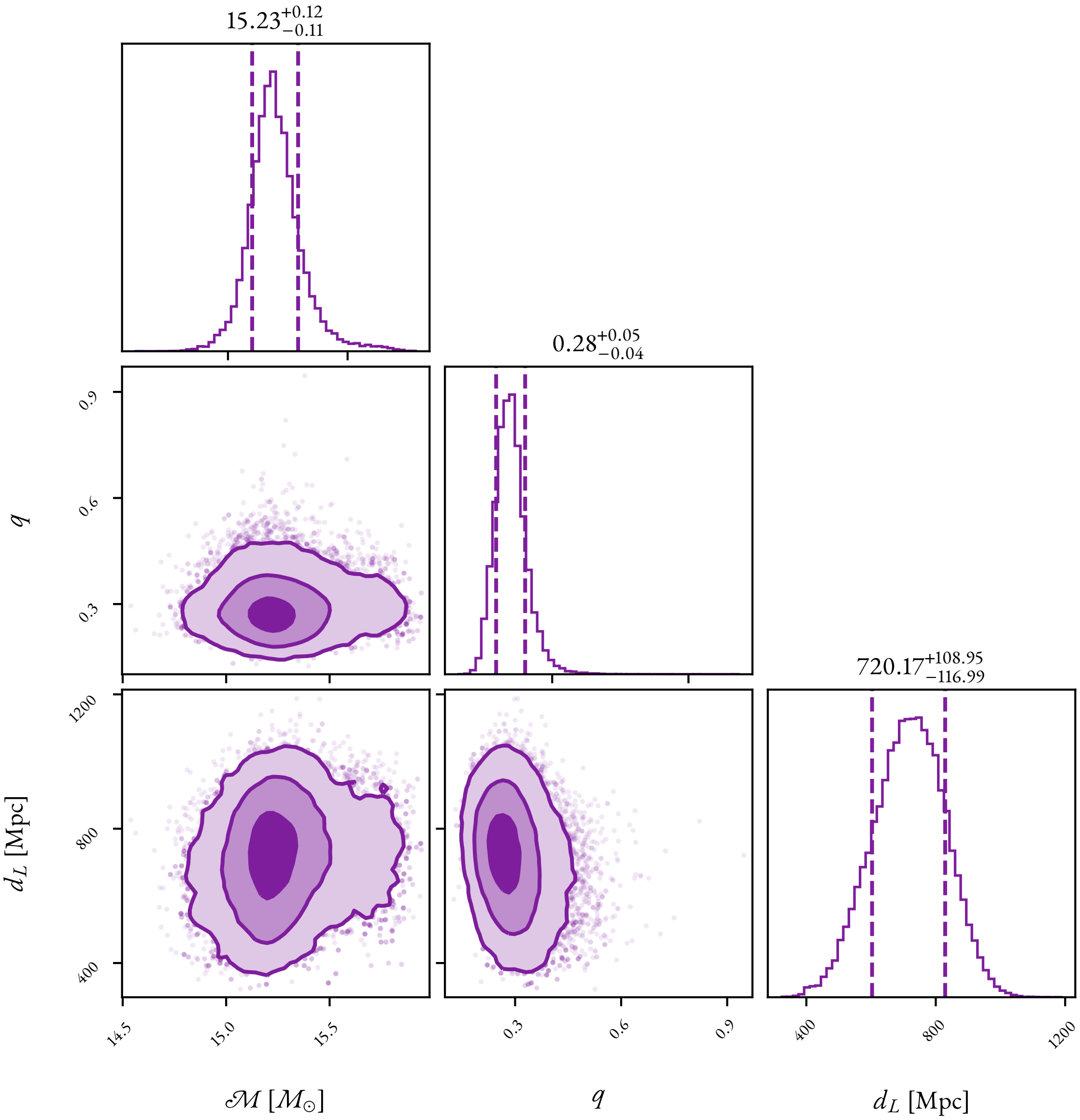

Figure 7.5: Subset of parameter estimation results from analysing GW190412 under the unlensed hypothesis. Format of this plot is the same as the first three columns of Figure 6.7.

7.3 GW191103 and GW191105

GW191103 and GW191105 are both BBH signals that were detected during O3 (Abbott et al., 2023a). From the perspective of standard BBH analyses, these events did not display any noteworthy features. However, lensing analyses generated some interest in this pair as a potential candidate for strong lensing. This was due to notable overlap between the sky location and masses for this pair (Abbott et al., 2023d)—see Figures 7.6 and 7.7. The two day time delay between the mergers also meant it would be consistent with the expectations for galaxy scale lenses (Wierda et al., 2021b). However, LVK analyses ultimately discarded the pair after a full consideration of the data, selection effects, and astrophysical expectations (Abbott et al., 2023d).

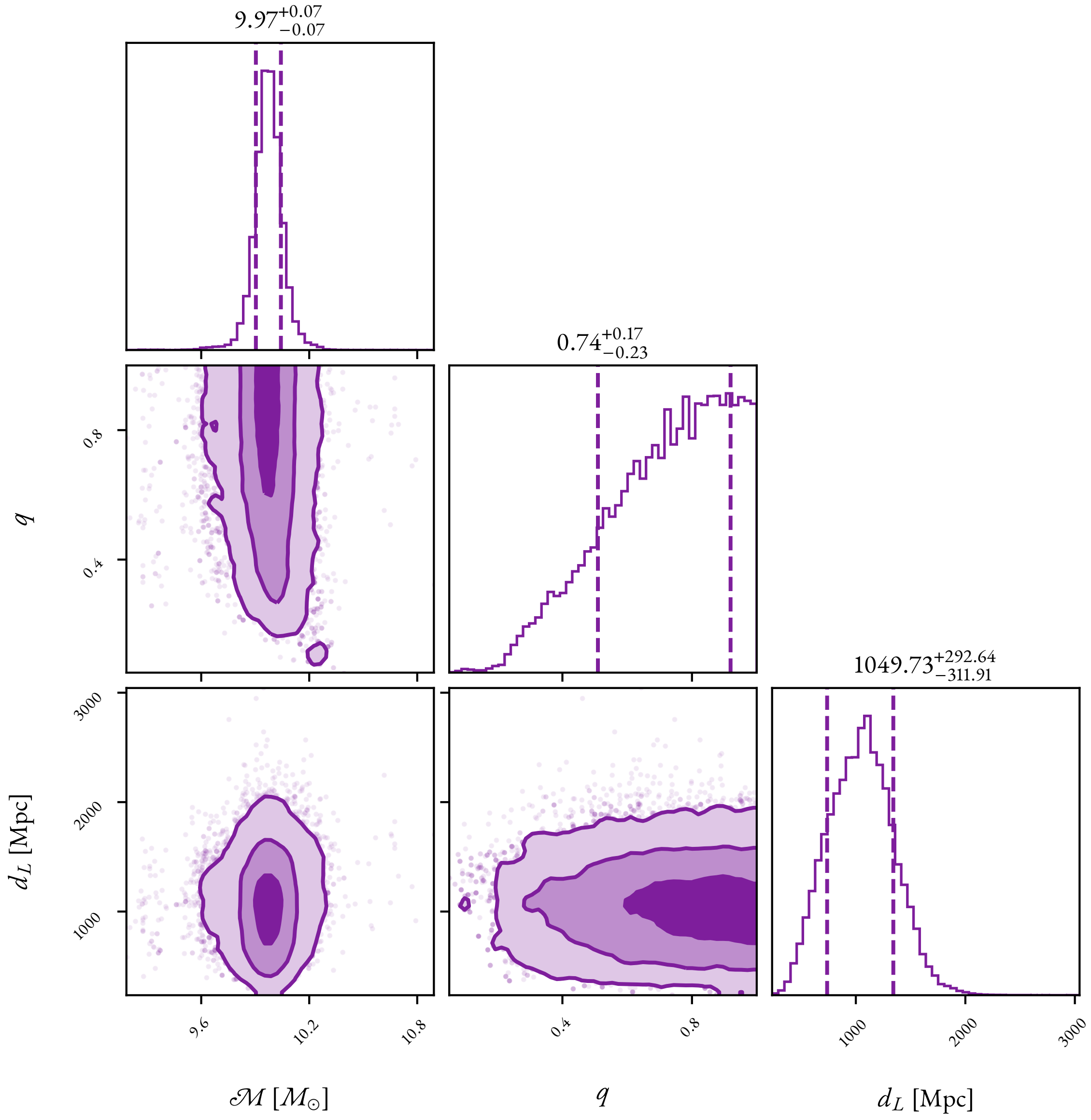

Figure 7.6: Subset of parameter estimation results from analysing GW191103 under the unlensed hypothesis. Format of this plot is the same as the first three columns of Figure 6.7.

However, given the relative initial preference for the pair, these events were examined in greater detail in Janquart et al. (2023b). This included an investigation of whether either of these events display any indications of microlensing signatures. The reason for this interest in particular is that the most likely scenario for microlensing events is the case of a microlens embedded within a larger lens (Seo et al., 2022).

Analyses of these two events under both the isolated point mass and SIS microlensing hypotheses do not yield significant support. The most optimistic of these analyses is that of GW191103 under the isolated point mass hypothesis which gives a $\log_{10}$ Bayes factor comparison with the unlensed hypothesis of 0.38. The most pessimistic is that of GW191105 under the same hypothesis which gives a $\log_{10}$

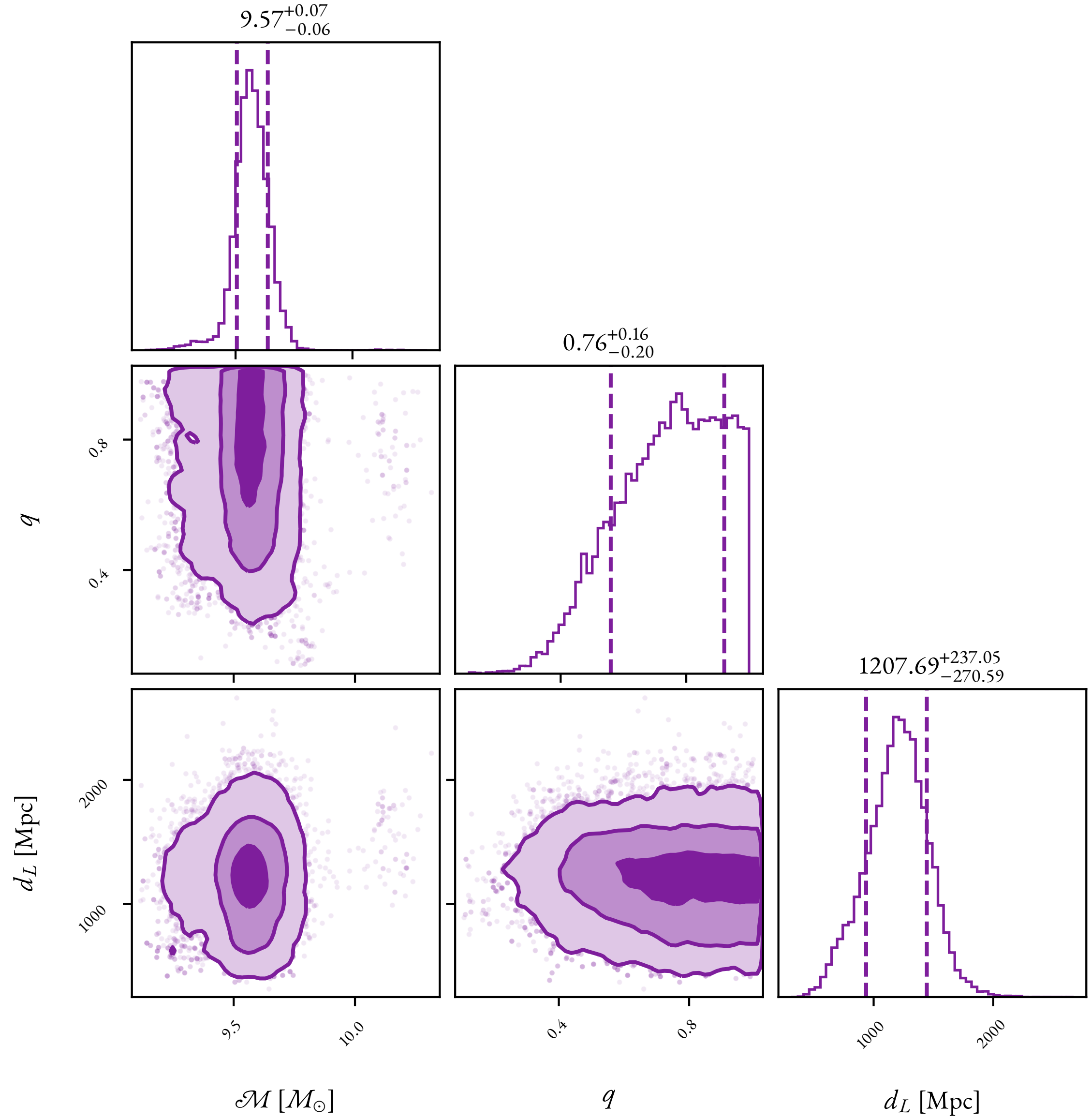

Figure 7.7: Subset of parameter estimation results from analysing GW191105 under the unlensed hypothesis. Format of this plot is the same as the first three columns of Figure 6.7.

Bayes factor comparison with the unlensed hypothesis of -0.35.

Figures 7.8–7.11 present the posteriors for these investigations. Similarly to for GW190412, they do not demonstrate significant constraint for the lensing parameters which again supports the unlensed hypothesis, leading the overall conclusion of the microlensing analysis of this pair to be that neither displays any real support for signatures of microlensing.

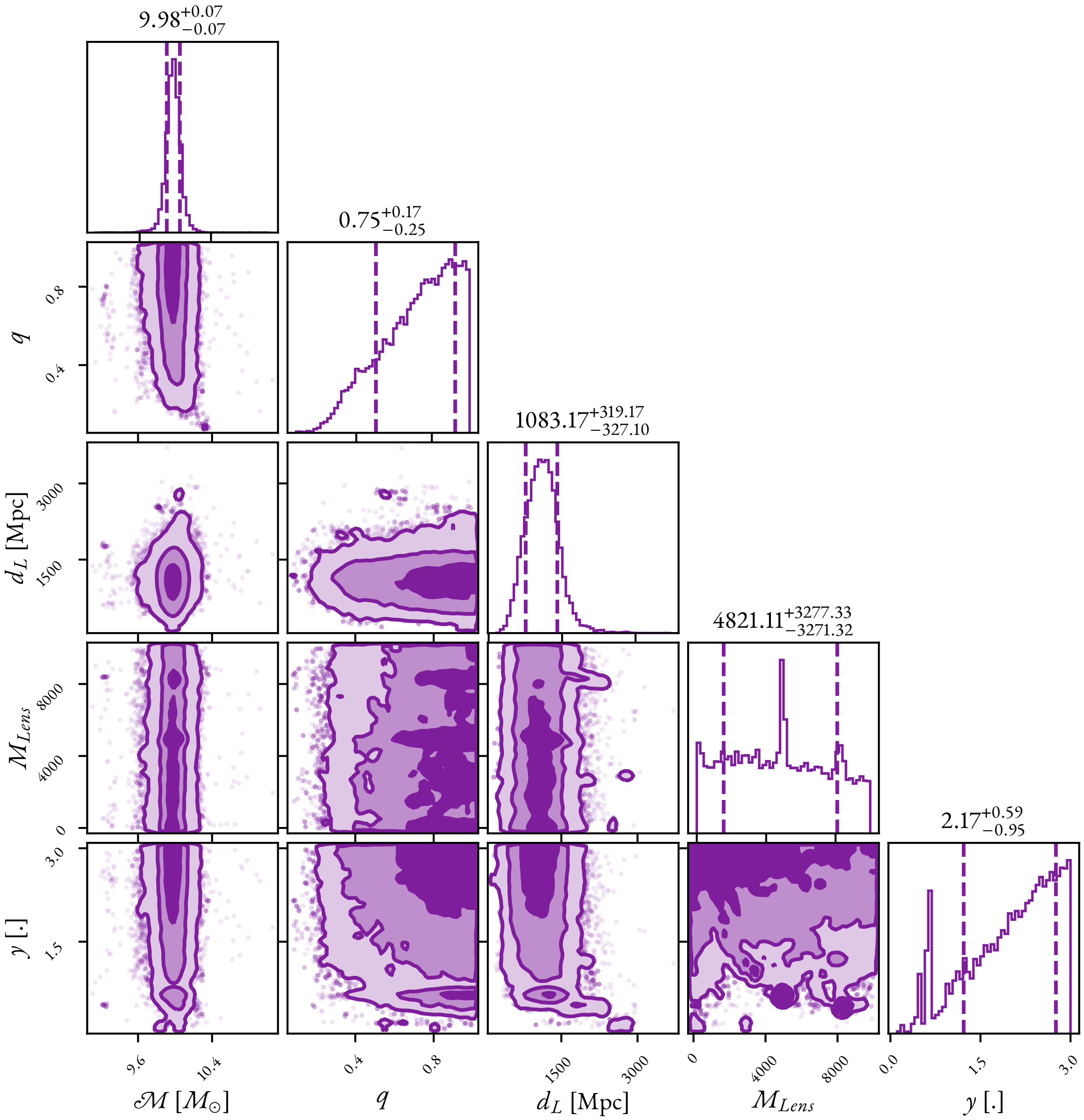

Figure 7.8: Subset of parameter estimation results from analysing GW191103 under the isolated point mass microlensing hypothesis. Format of the plot is the same as Figure 6.7.

7.4 GW200208

GW200208 was, during the O3 primary lensing search (Abbott et al., 2023d), the event that had the highest preference for microlensing of those investigated, with a $\log_{10} \mathcal{B}^{\mathrm{L}}_{\mathrm{U}}$—the Bayes factor comparing the microlensed and unlensed hypotheses—of 0.8. This value whilst relatively high, did remain within the boundary of expectation for unlensed events based off of the background study performed however. An additional reason for further scrutiny however, was the constraint of the detector frame lens mass which as we have shown in the consideration of the other events in this chapter is atypical

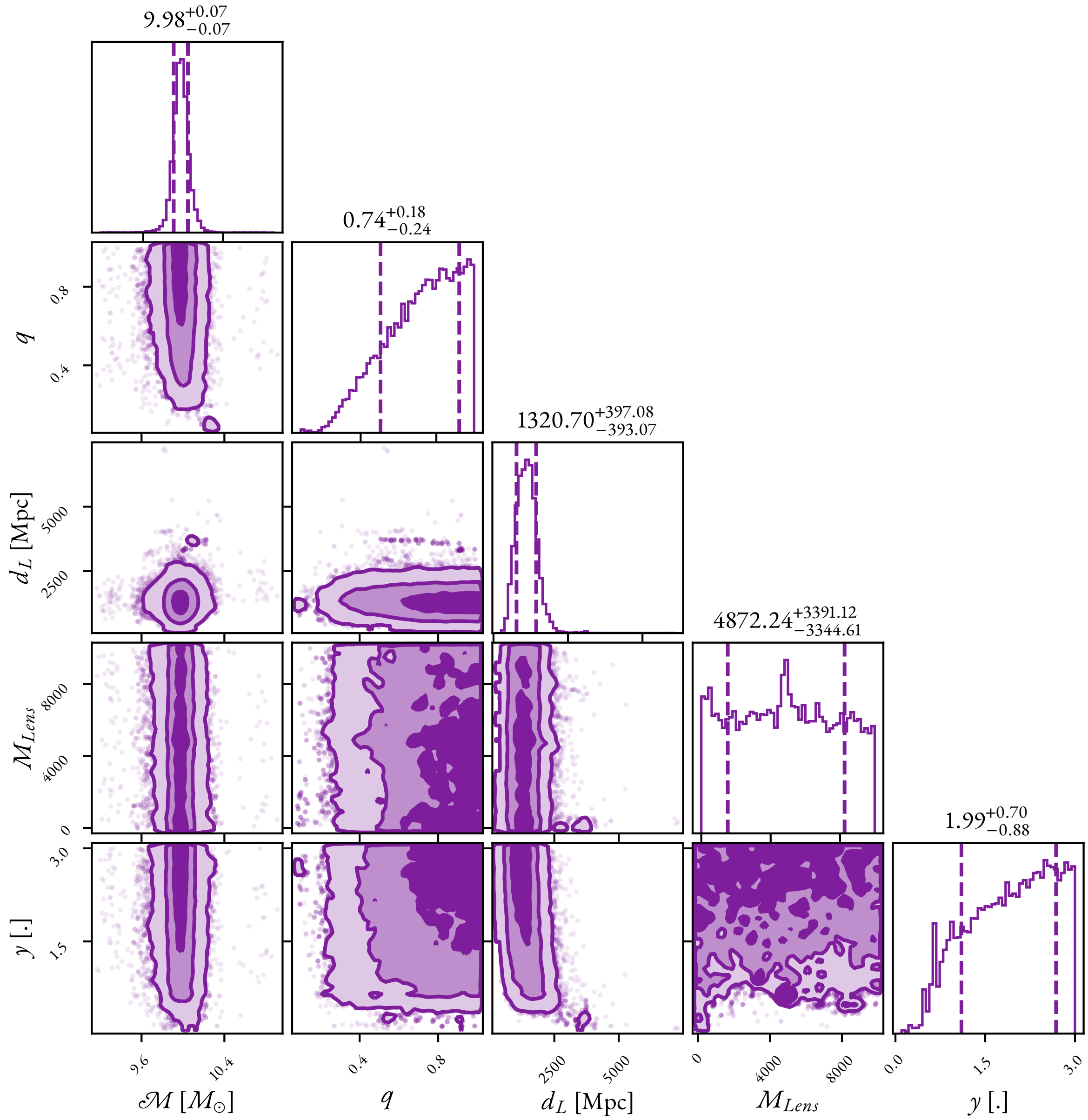

Figure 7.9: Subset of parameter estimation results from analysing GW191103 under the SIS microlensing hypothesis. Format of the plot is the same as Figure 6.7.

for unlensed events. Primary LVK analysis whilst deeming it worthy of additional scrutiny, concluded that the cause for the apparent favouring was likely the result of a short duration noise fluctuation causing a mimic of the beating pattern of microlensing (Abbott et al., 2023d).

A reanalysis of this event using the Gravelamps isolated point mass and SIS models confirmed the results of the initial investigation that the event required scrutiny, with a $\log_{10} \mathcal{B}^{\mathrm{L}}_{\mathrm{U}}$ of 1.20 for the isolated point mass case and 1.77 for the SIS case—i.e. marginal support for an SIS model.

Figures 7.13 and 7.14 show the posteriors from these investigations. As may be seen, unlike the other O3 candidates, the posteriors for these display constraint towards particular values of lensing parameters—in both cases approximately a $2000 M_\odot$ lens at a dimensionless source position of 0.6. It may be noted that the 3-σ confidence interval for these parameters does display a similar level of broad-

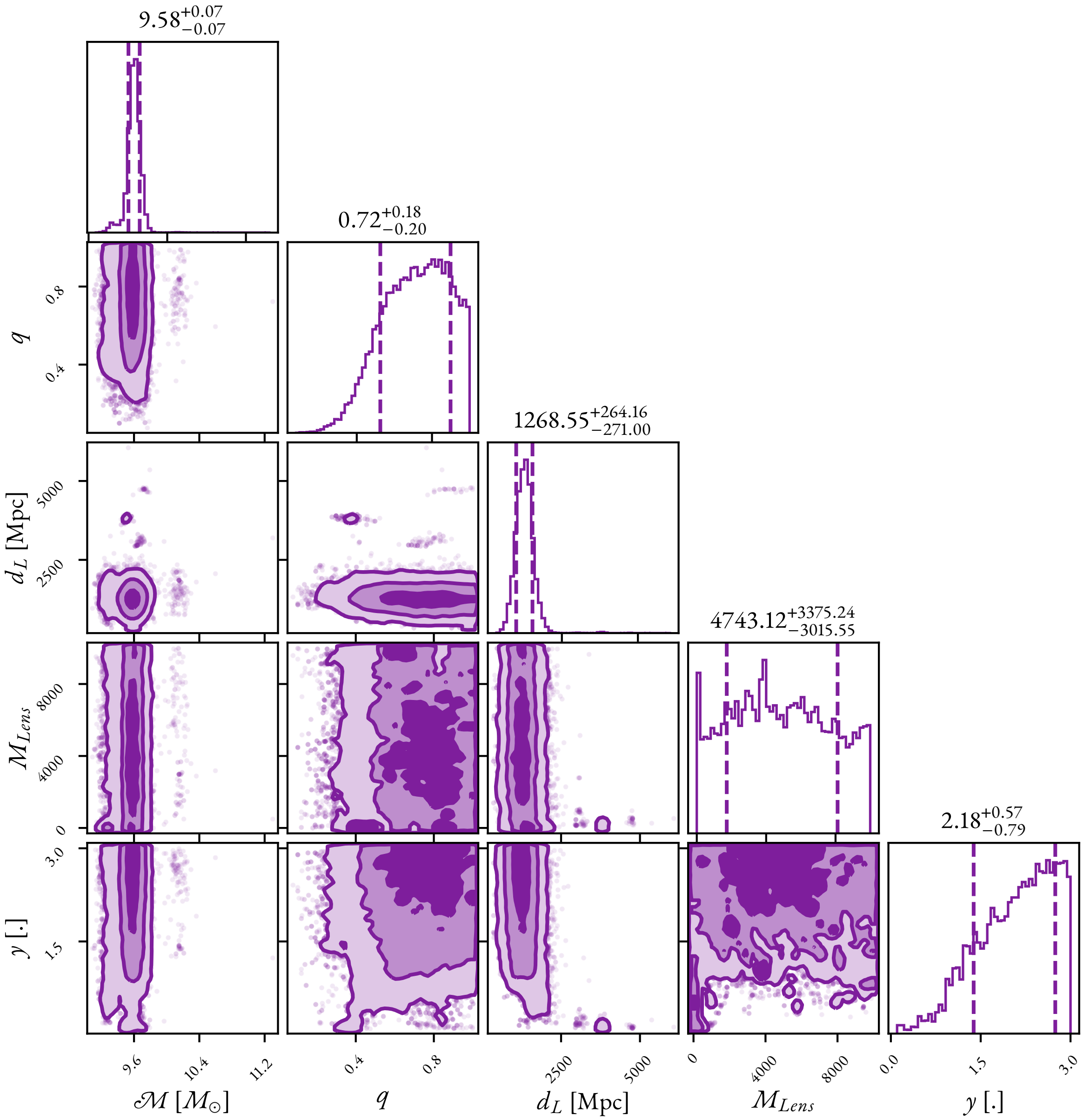

Figure 7.10: Subset of parameter estimation results from analysing GW191105 under the isolated point mass microlensing hypothesis. Format of the plot is the same of Figure 6.7.

ness to the other candidates, but the peaks of these posteriors are clear. Combined with the slender support for the microlensing hypothesis meant that this signal required additional investigation.

One additional investigation that was carried out, under the scenario that GW200208 was a genuine microlensing event, was a reanalysis of GW200208 under the isolated point mass microlensing assumption with the location of the lens along the line of sight as a free parameter. The expectation for the wave optics influenced regime of microlensing is that this may be identifiable rather than completely degenerate as is the case with strong lensing given the so called *mass-sheet degeneracy* (Cremonese et al., 2021). Figure 7.15 shows the updated posteriors when examining for this parameter also which yields only a slender increase in support for placing the lens nearer the observer than the source.

To further scrutinise whether GW200208 was a genuine microlensing event, we investigate whether

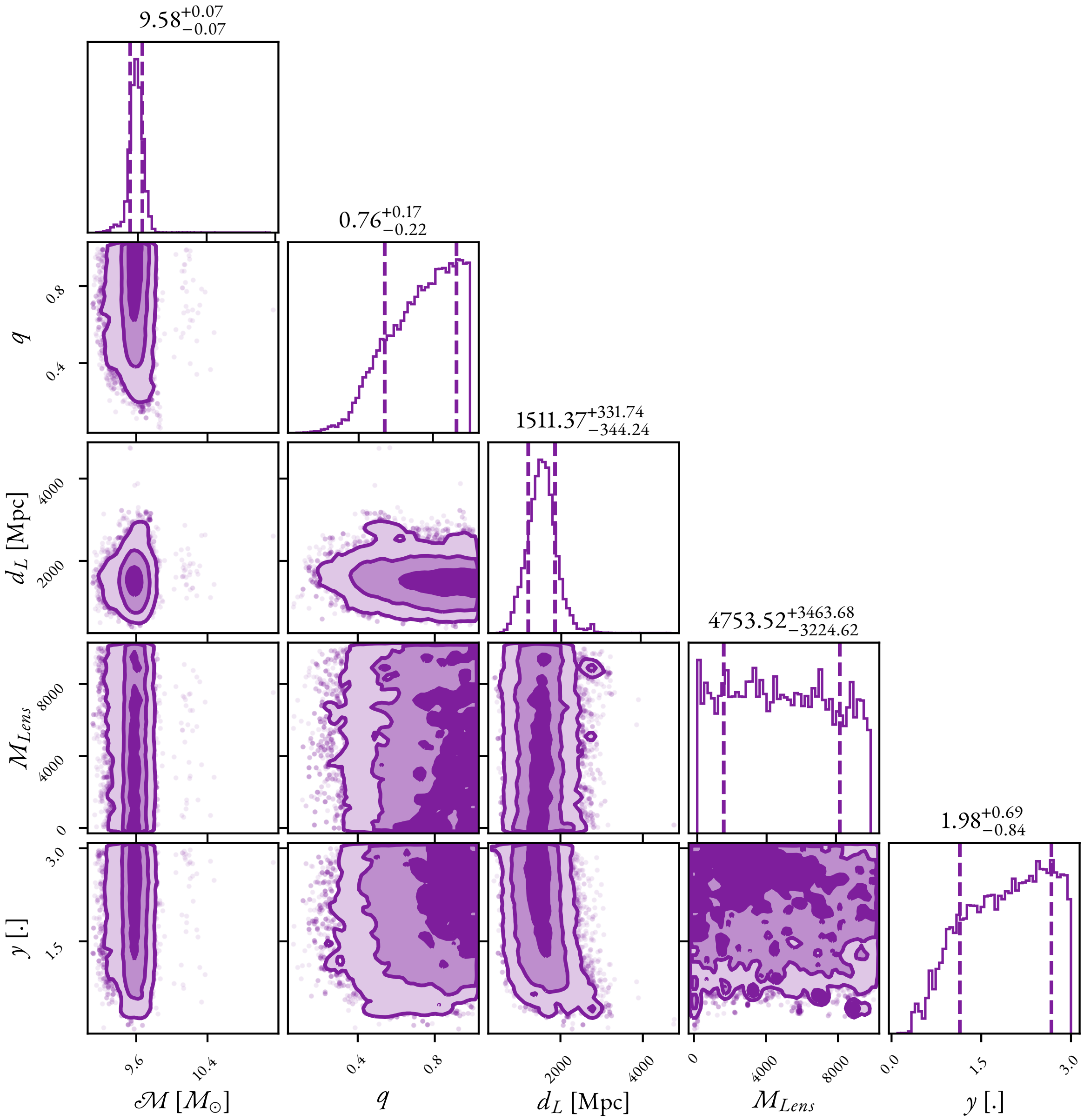

Figure 7.11: Subset of parameter estimation results from analysing GW191105 under the SIS microlensing hypothesis. Format of the plot is the same as Figure 6.7.

an event with the suggested parameters from the microlensing analysis of GW200208 would be detected and with what significance, so as to ascertain whether the slender support for GW200208 that was observed was realistic. To gain insight into this, the maximum likelihood parameters from the microlensing analysis—which are given in Table 7.1—were used to create a simulated lensed signal which used the SIS model as it was the most preferred. This was then added to a realisation of Gaussian noise assuming a representative PSD for the noise around the time of the detection of GW200208. Analysis of this injection yielded a $\log_{10} \mathcal{B}^{\mathrm{L}}_{\mathrm{U}}$ of 0.37 and 0.79 for the isolated point mass and SIS lens models respectively. It is notable that these are *lower* than that for GW200208, indicating that at current sensitivity an event with these parameters would not be confidently identified leading this analysis to be inconclusive for the status of GW200208.

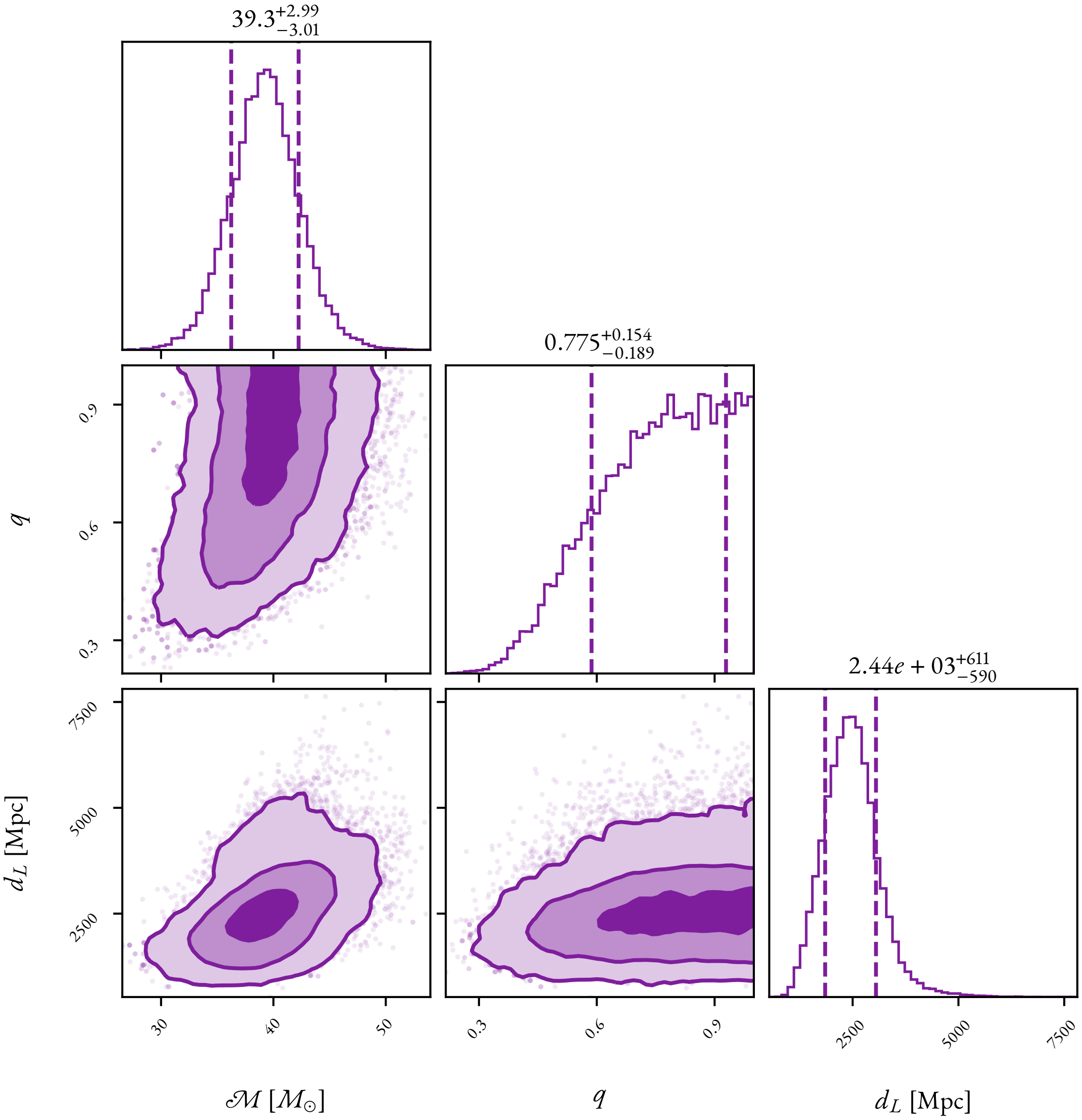

Figure 7.12: Subset of parameter estimation results from analysing GW200208 under the unlensed hypothesis. Format of the plot is the same as the first three columns of Figure 6.7.

Examination of the resultant posteriors from the injection analysis—shown in Figures 7.16, 7.17, and 7.18, does indicate a weaker recovery than the posteriors from the actual event which could indicate the impact of the actual detector noise compared with the Gaussian noise realisation being mistaken for additional support for the lensing hypothesis, however further investigation of the noise would be needed to draw a conclusion.

To further examine GW200208's status as a microlensing candidate, we turn to the residual power left when the maximum-likelihood waveform fit from the unlensed parameter estimation is removed from the data. In the case of a genuine microlensing event, one would expect to see coherent oscillatory power remaining across the frequencies of detection in each of the detectors due to the unaccounted for oscillatory behaviour of the amplification factor alongside the other fluctuations which are typical

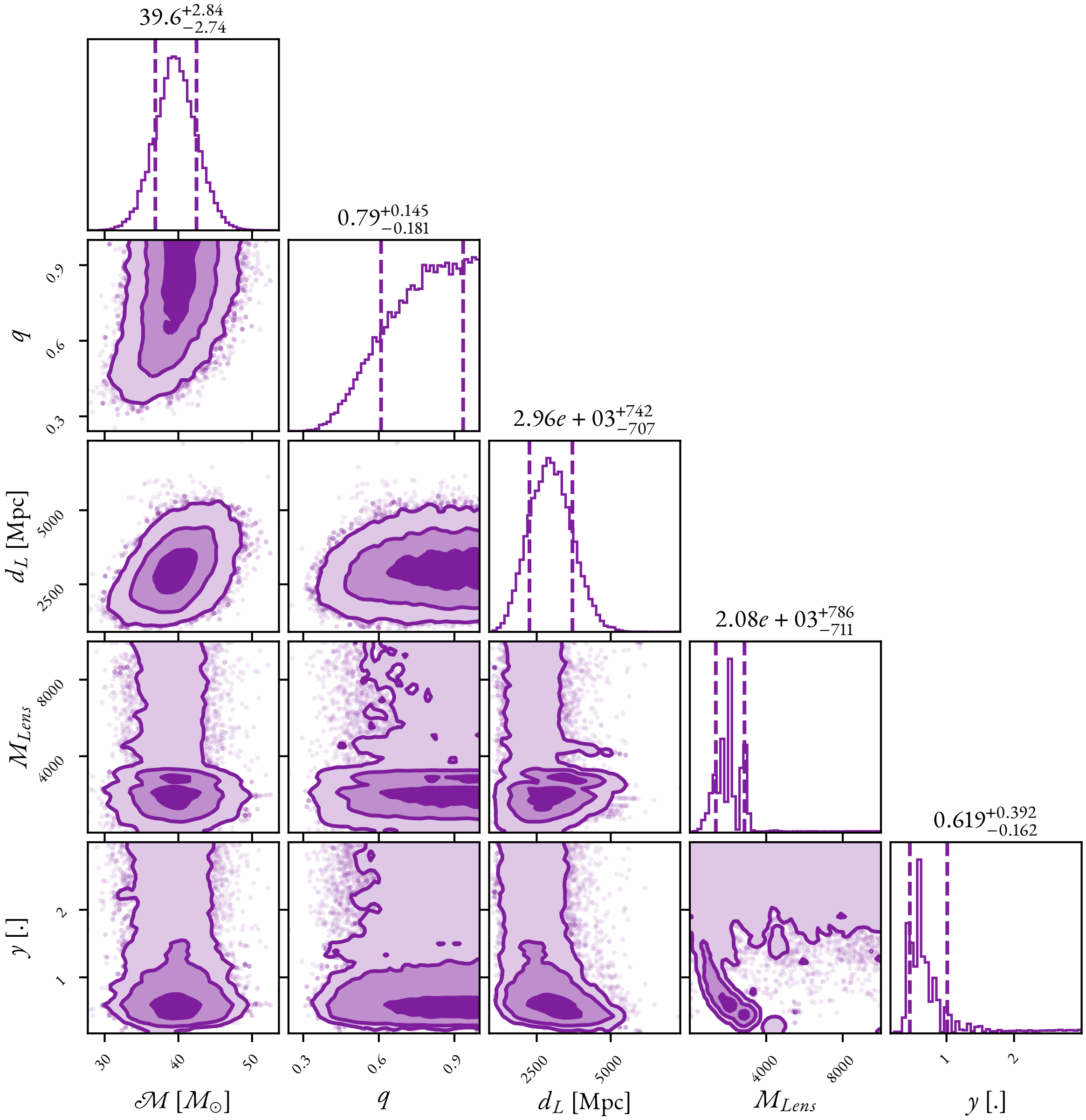

Figure 7.13: Subset of parameter estimation results from analysing GW200208 under the isolated point mass microlensing hypothesis. Format of the plot is the same as Figure 6.7.

of the detectors. An examination of residual power for GW200208 was conducted in Abbott et al. (2021e) which was searching for residual power which might indicate a deviation from GR. This analysis calculated a p-value corresponding to the probability of a background event with residual power greater than that for GW200208 was 0.97 suggesting that the residual power is well within expectations for residual noise.

Figure 7.19 shows the residuals from performing this subtraction for a subset of the total frequency range in which no obvious oscillatory behaviour may be coherently seen between the three detectors. This, despite the increase in support for the microlesing hypothesis seen with the SIS model, leads to support for the conclusion from Abbott et al. (2023d) that the apparent preference for microlensed waveforms for this event is most likely driven by detector noise mimicking the amplification factor

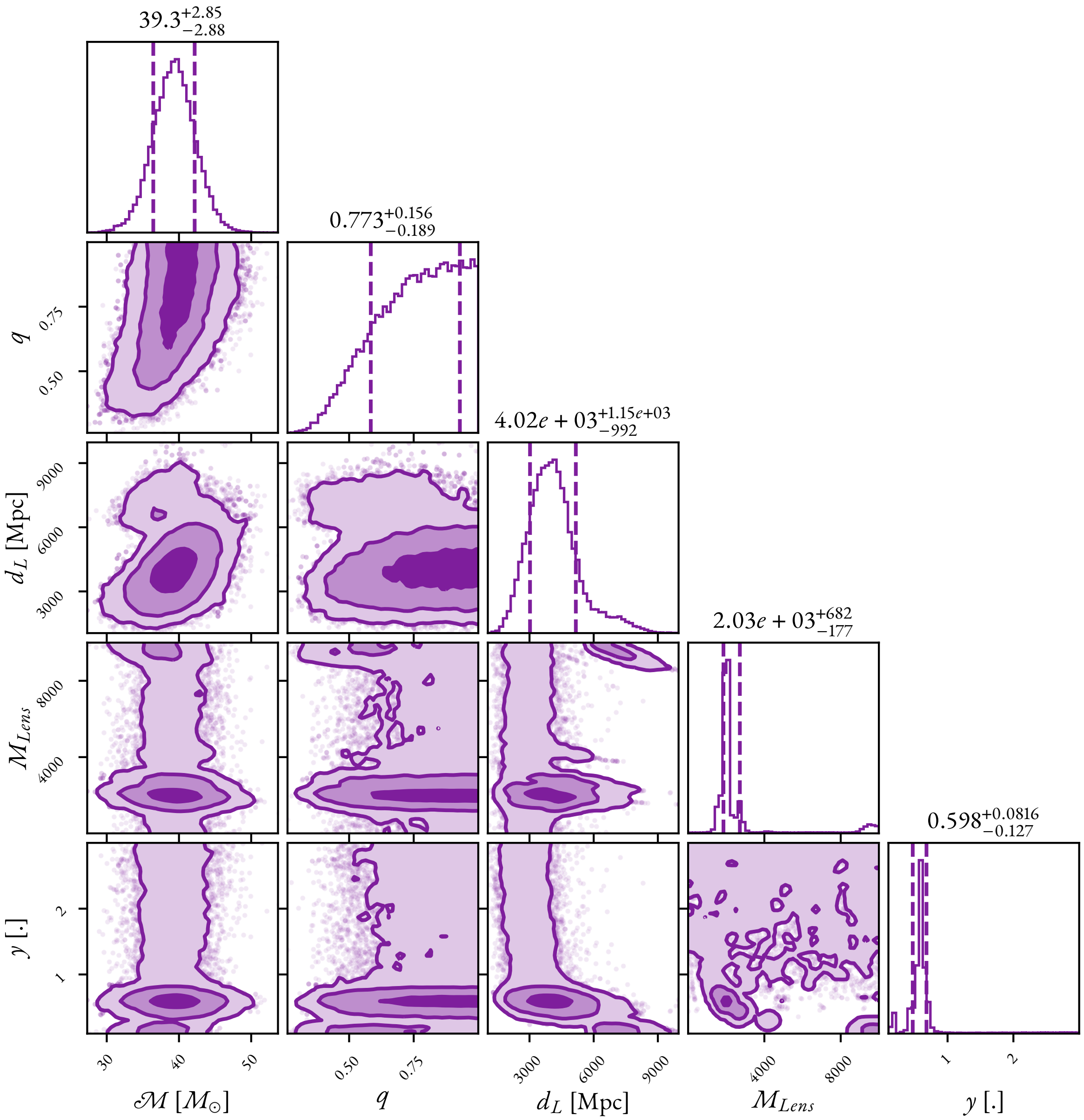

Figure 7.14: Subset of parameter estimation results from analysing GW200208 under the SIS microlensing hypothesis. Format of the plot is the same as Figure 6.7.

behaviour.

7.5 GW230529

GW230529 was the first exceptional GW event detected during O4. It is an NSBH which has been determined to have component masses of $3.6^{+0.8}_{-1.2} M_\odot$ and $1.4^{+0.6}_{-0.2} M_\odot$ (The LIGO Scientific Collaboration et al., 2024). The primary mass is therefore inside of the so-called *lower mass gap*—an apparent lack of compact objects between the population of neutron stars and stellar mass black holes which arises from observations of mass measurements from X-ray binary systems (Bailyn et al., 1998).

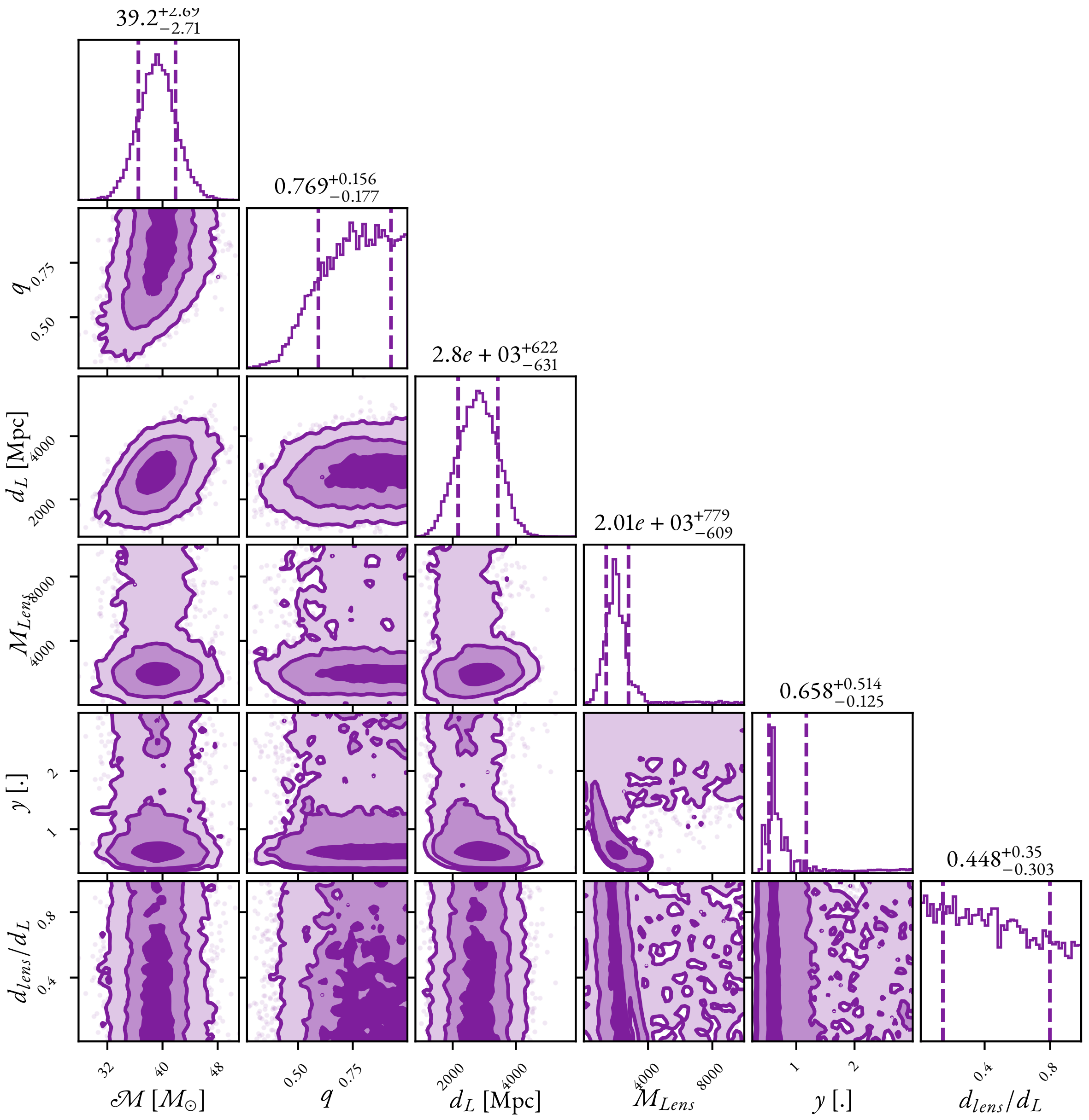

Figure 7.15: Subset of parameter estimation results from analysing GW200208 under the isolated point mass microlensing hypothesis with a varying lens distance. Format is the same as Figure 6.7 with the additional column showing the fractional distance of the lens compared with the source.

Whilst this gap has thus far been empirical, and the observation of GW230529 may show that it is not astrophysical, under the assumption that it were truly a gap then GW230529 would therefore be a strong a prior candidate for lensing which would have the potential to make a BNS appear heavier and thus have the observed component masses when analysed under the unlensed hypothesis.

To investigate the potential for GW230529 to be a microlensing candidate, Gravelamps analyses have been conducted for this event for each of three waveform models covering the three potential system configurations: IMRPhenomXPHM (Pratten et al., 2021) which represents the BBH case, IMRPhenomPv2_NRTidalv2 (Dietrich et al., 2019) which represents the BNS case, and IMRPhenomNSBH (Thompson et al., 2020) which represents the NSBH case.

Injected Parameter	Value
Chirp mass, $\mathcal{M}_c (M_\odot)$	34.85
Mass ratio, q	0.59
Luminosity distance, d_L (Mpc)	2592.72
Dimensionless primary spin magnitude, a_1	0.46
Dimensionless secondary spin magnitude, a_2	0.08
Primary tilt angle, θ_1	2.78
Secondary tilt angle, θ_2	1.38
Azimuthal angle between component spins, ϕ_{12}	2.20
Azimuthal angle between total binary angular and orbital momenta, ϕ_{jl}	1.12
Angle between total binary angular momentum and line-of-sight, θ_{jn}	2.29
Polarisation angle, ψ	1.18
Phase at reference frequency, ϕ	4.87
Right ascension, α	2.43
Declination, δ	−0.60
Coalesence time, $t_c (s)$	1265202095.94
Lens Mass, $M_{\text{Lens}} (M_\odot)$	2200.61
Dimensionless source position, y	0.61

Table 7.1: Maximum likelihood parameters from the SIS investigation of GW200208 used to create the injection.

None of these cases yielded support for the microlensing hypothesis, with $\log_{10} \mathcal{B}^{\text{PM}}_{\text{U}}$ values of -0.014, 0.098, and -0.019 respectively. Only the BNS case is positive, but is well below the threshold for further investigation let alone identification. This investigation would therefore conclude that GW230529 is not a microlensing candidate and maintains support for the LVK conclusion of the primary mass being within the lower mass gap.

7.6 Deployment Strategies for GRAVELAMPS in O4

With the increasing sensitivity and continued development of analysis frameworks, each observing run has yielded considerably more detections than the previous. This pattern is expected to continue in O4 with an expectation of $O(100\text{s})$ of GW signals being detected during this time. This represents a significant increase in the computational costs of deployment of GRAVELAMPS during O4 and we must therefore consider how the pipeline may be deployed.

The first of these considerations is simply how to launch the significant number of expected analyses. Whilst manual construction of each run is possible this relies on the gathering of sufficient information about each event in order to determine valid prior regions, etc. At any stage of this process errors may be induced requiring further intervention and cross-checking. So to minimise this, GRAVELAMPS has developed an integration to the large scale analysis deployment framework ASIMOV (Williams et al., 2023). This framework allows the automated construction of analyses based on a YAML ledger of information about each event, allowing automated centralisation of this data and appropriate handling

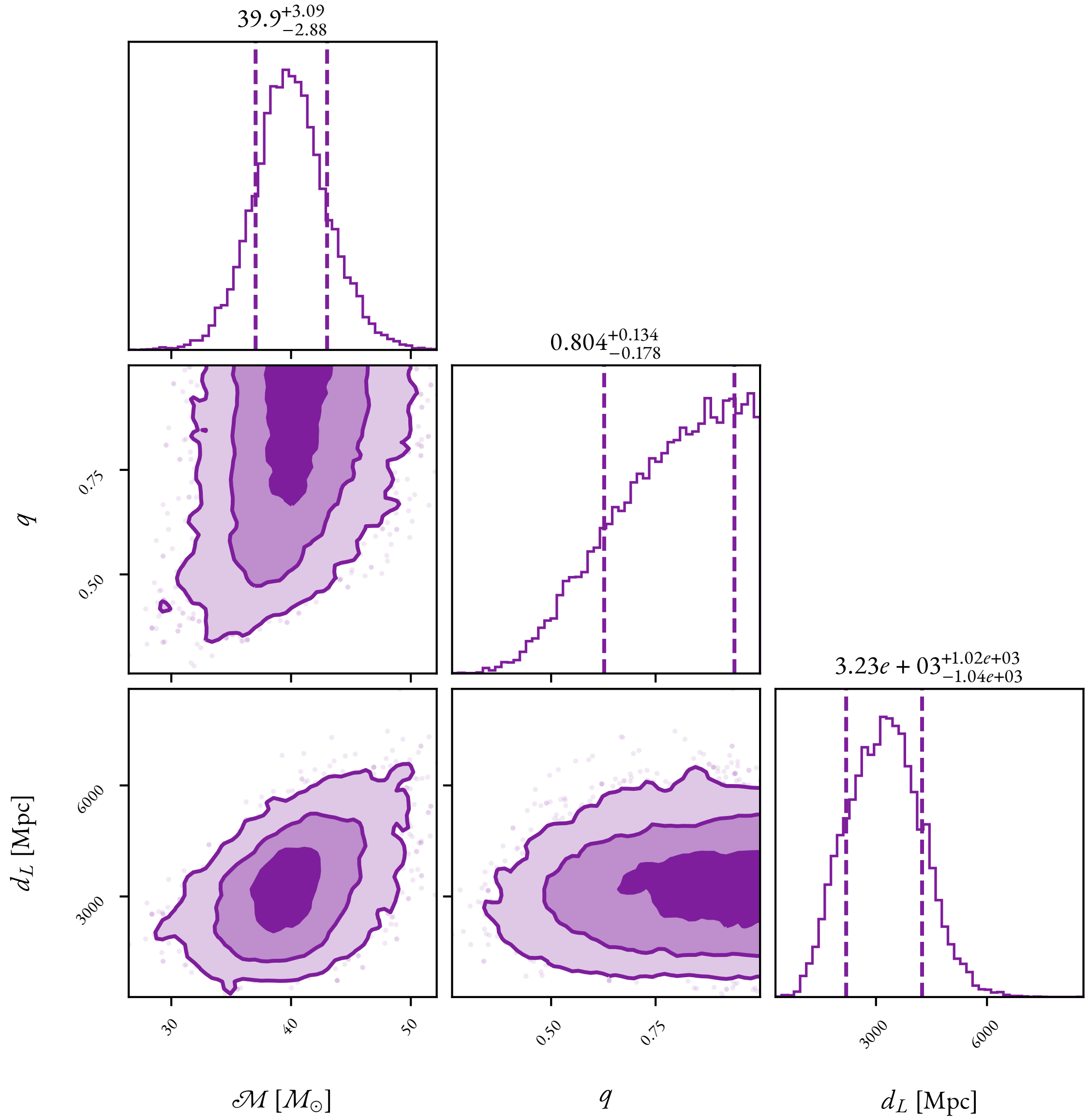

Figure 7.16: Subset of parameter estimation results from analysing the GW200208-like injection generated from the maximum likelihood sample of the SIS investigation under the unlensed hypothesis. Format of the plot is the same as the first three columns of Figure 6.7.

of both the analysis and any dependencies.

This dependency handling also allows control of launching automated follow-up for events for potential candidates. Whilst the most complete analysis of the data would be to deploy each of the implemented lens models on it, this multiplies the computational cost of analysing an event. We have demonstrated initially in the previous chapters that the isolated point mass microlensing model is preferred over the unlensed model in the case of lensing by other microlensing models and the phenomenological millilensing model. The isolated point mass model therefore may be used as a single individual model to sweep over all of the data, with candidates that display significant preference for the microlensing model to then be investigated by the other analyses.

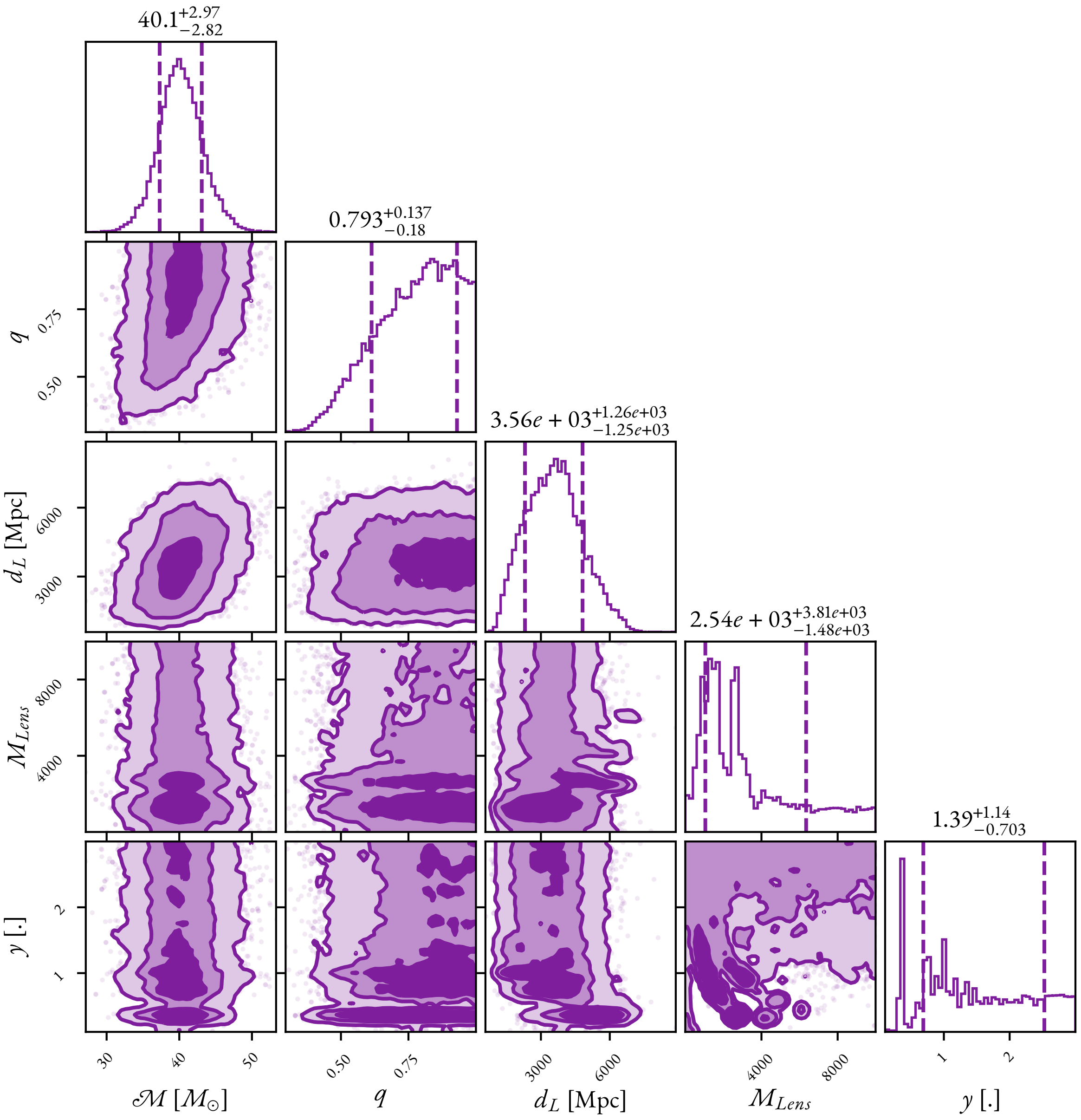

Figure 7.17: Subset of parameter estimation results from analysing the GW200208-like injection generated from the maximum likelihood sample of the SIS investigation under the isolated point mass microlensing hypothesis. Format of the plot is the same as Figure 6.7.

An additional step that could also be taken through the use of ASIMOV dependency handling would be the prioritisation of these follow-up investigations where the scale of the Bayes factor between the lensed and unlensed models determining a priority factor for the follow-up investigations. This priority could be continuously updated as the follow-up investigations conclude to ensure highest priority is given to those candidates that continue to favour the microlensing or millilensing hypothesis through multiple models. However, follow-up investigation is not currently expected to be necessary on a sufficiently high number of runs to justify this step at this time.

A second consideration for large scale deployment is the handling of the resultant metadata that such a large volume of analyses will generate. This includes the configurations and result files from each

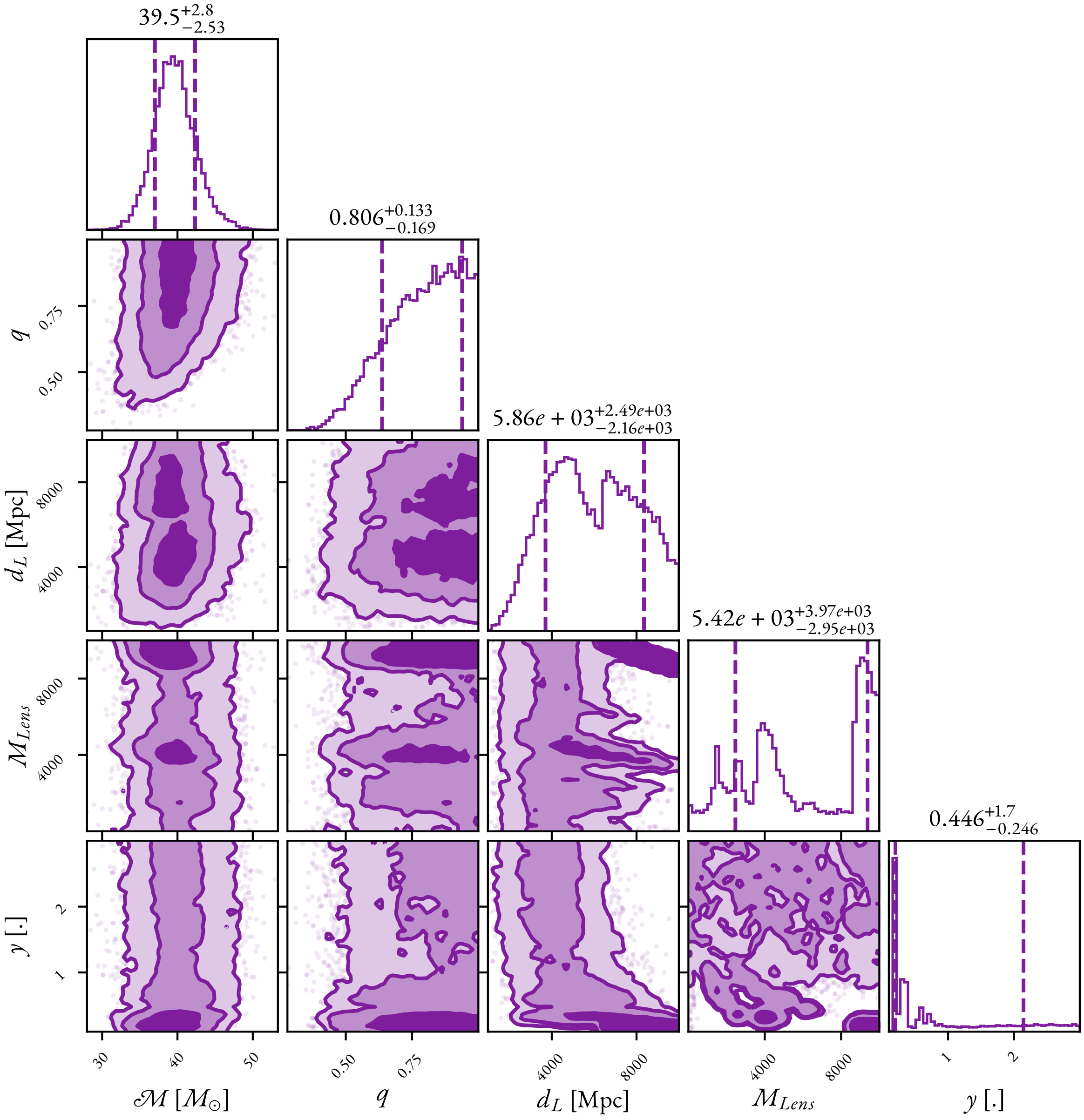

Figure 7.18: Subset of parameter estimation results from analysing the GW200208-like injection generated from the maximum likelihood sample of the SIS investigation under the SIS microlensing hypothesis. Format of the plot is the same as Figure 6.7.

run as well keeping track of relevant analysts and other contacts, etc. To this end, Gravelamps has also been made compatible with the CBCFlow metadata handling package for the analysis of CBC signals (Udall et al., 2022).

Both of these integrations have been made both with the aim of ensuring that deployment of Gravelamps itself may be smooth at such large scale, but also to allow interoperability with other lensing analyses that will take place under the auspices of a larger automation project currently—at time of writing—under development. This project is termed LensingFlow.

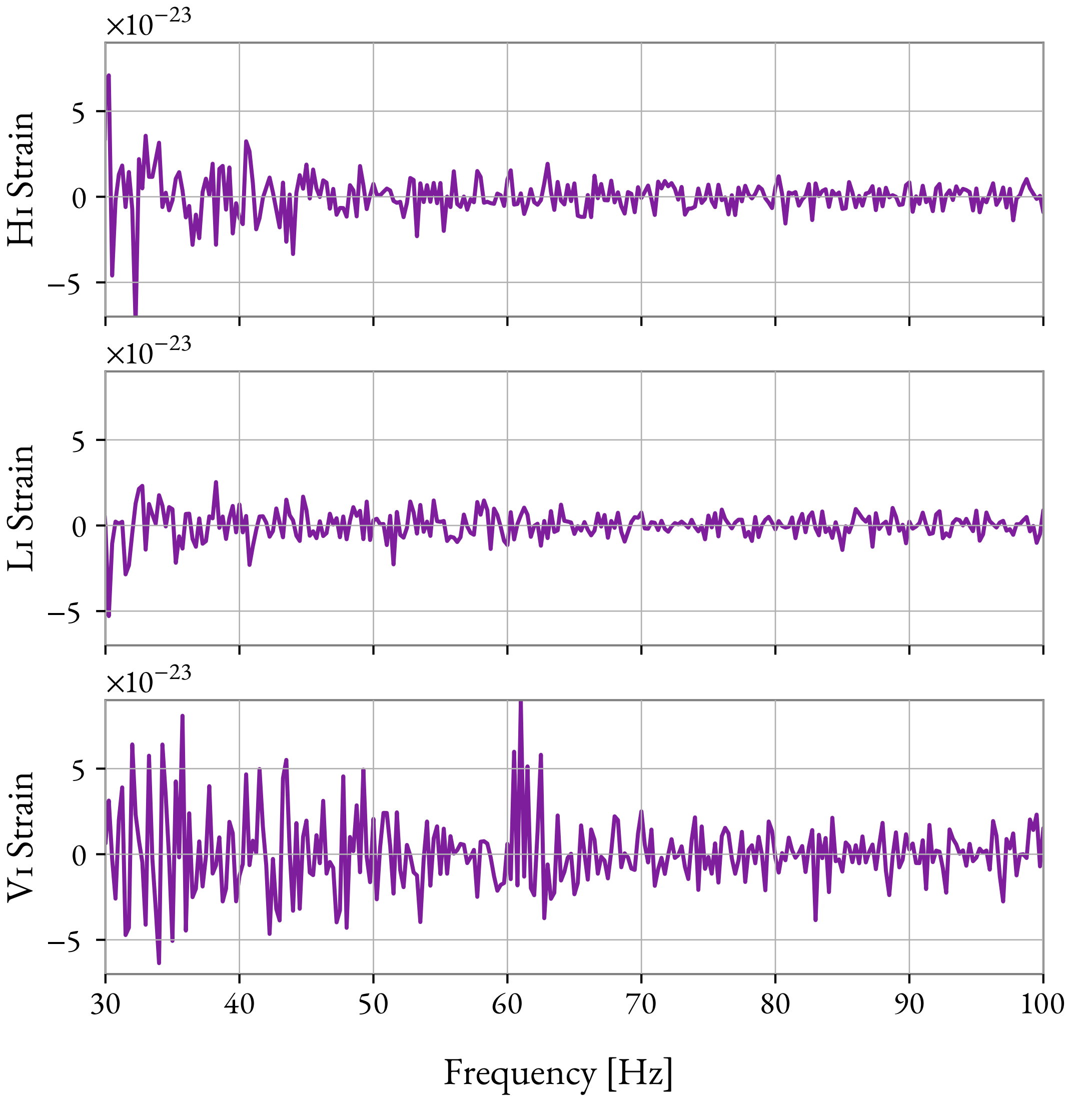

Figure 7.19: The residual power remaining in each of the LIGO Hanford, LIGO Livingston, and the Virgo detectors when subtracting the best fit unlensed waveform from the data.

7.7 Conclusion

In this chapter, we have presented some of the initial developments and deployments of the Gravelamps pipeline since its initial creation.

The first development was the introduction of the phenomenological millilensing model developed by Liu et al. (2023) expanding the use cases of Gravelamps outside of the purely microlensing realm and demonstrating that additional waveforms may be folded in, in the manner that was aimed for in the development of the framework.

This was followed by the first deployments on real GW signals, specifically those candidates found by the O3 lensing searches (Abbott et al., 2023d; Janquart et al., 2023b). Three of these candidates, GW190412, GW191103, and GW191105 displayed no support for the microlensing hypothesis both in terms of low Bayes factor as well as a lack of constraint for any proposed lensing parameters upon the conclusion of the parameter estimation investigations.

The final candidate from these O3 investigations was GW200208 which generated more interest from the perspective of microlensing searches with some Bayes factor support for the isolated point mass and SIS microlensing models. To further investigate this event, an injection was carried out with the maximum proposed likelihood parameters which revealed that such an event would not be well recovered. However, the candidate was ruled out after examination of the residuals when subtracting the maximum likelihood unlensed waveform do not yield any coherent oscillatory behaviour that would be expected supporting the initial conclusions of the LVK analysis that support is likely caused by a transient noise feature.

We then presented an investigation into the O4 event GW230529 which generated interest from the lensing community due to being within the so-called lower mass gap. If it is the case that the lower mass gap has an astrophysical cause then this signal would therefore be quite likely to be the result of lensing. However, investigation of this event did not yield any support for the microlensing hypothesis.

Finally, we discussed the strategies for the deployment of Gravelamps at the significantly higher scales that will be required for full O4 analysis. This involved integration of deployment within the automation framework Asimov (Williams et al., 2023) and within the metadata handling framework CBCFlow (Udall et al., 2022). We also discussed that this is the initial stages of inclusion in a wider lensing automation effort termed LensingFlow that is currently under development.

8

Lens Model Selection for Strongly Lensed Gravitational Wave Signals

---

You can use logic to justify almost anything. That's its power—and its flaw.
Kathryn Janeway, *Star Trek: Voyager*
Based on *Star Trek* Created by Gene Rodenberry.

Disclaimer

The following chapter is based on the work *Determination of Lens Mass Density Profile from Strongly Lensed Gravitational-Wave Signals* which was co-authored by Justin Janquart and Martin Hendry and published in the Astrophysical Journal.

8.1 Identification of Strong Gravitational Wave Lensing

Turning our discussion now to the strong lensing of GW signals, we have noted strong lensing produces multiple wholly resolvable signals. The time separation is dependent upon the exact scale of the lens but may be as low as minutes or as high as months for galaxy scale lenses (Ng et al., 2018) and up to years for galactic cluster scale lenses (Smith et al., 2018). These signals by Equation 5.45 experience their own individual magnification, time delay, and Morse phase shift but do not have their overall frequency evolution affected. Therefore, identifying strong lensing may be done by searching for this repetition of evolution. We here describe some of the methods used to search for these lensed images in GW data used in Abbott et al. (2023d) and Janquart et al. (2023b) to provide context for the following discussions.

Searches for strong lensing have typically focused on *pairs* of events given the exponentially increasing number of investigations that must be performed when searching for higher multiplets. This discussion will abide by that convention; however, in the majority of cases note that each described method may be subsequently applied to higher multiplets in an analogous fashion.

Upon first receiving new GW signals, some of the first pieces of information that are made available are *time frequency* plots and *sky-maps*. The former describe the energy for a given frequency at a given time within the detector, with GW events having a particular shape associated with the frequency evolution. We would therefore expect that a lensed pair would produce similarly shaped curves with differing intensity. The initial sky-maps are plots of the initial localisation of the GW event based on the matched-filtering processes done to identify the event. Currently these posteriors are broader than the expected change in the position of the two images due to the lensing distortion, and so we would expect that a lensed pair would have compatible sky localisation posteriors. These two similarity criteria are the basis for the low latency search LENSID (Goyal et al., 2021a) which uses a machine learning classifier to rapidly identify candidate lensing pairs by examination of these two rapidly generated pieces of information.

Another investigation that may take place after the first parameter estimation based analyses of GW signals takes a similar basis is that of investigation into the posterior overlap between differing events. Lensed pairs of events would be expected to have significant overlap in the estimated source parameters aside from those that are strongly affected by the lensing. This may be quantified into a Bayes factor as (Haris et al., 2018a)

$$\mathcal{B}^{\mathrm{L}}_{\mathrm{U}} = \int \frac{P(\theta|d_1)P(\theta|d_2)}{P(\theta)} d\theta, \tag{8.1}$$

where θ represents the binary parameters of the GW.

It is important to note that whilst both of the above discussed searches—alongside other such methods which adopt a similar strategy of looking for consistency between pairs of events—are extremely rapid, at this stage of candidate identification these cannot rule out astrophysical co-incidence. For this purpose, more computationally intensive joint parameter estimation must be carried out to fully calculate the likelihoods under the lensed and unlensed hypotheses. However, these searches do significantly narrow the number of pairs that need to be investigated saving significant computational resources compared to the deployments of full parameter estimation investigations.

We will now briefly summarise how these parameter estimation approaches work whilst referring the reader to Janquart et al. (2021) and Lo & Magana Hernandez (2023) for a fuller discussion of the topic. As we have noted, in geometric optics, lensed images may be described in terms of the binary parameters, θ, and the lensed parameters $\mathbf{\Lambda}_j$ of the j^{th} image. Under the lensed hypothesis, $\mathcal{H}_{\mathrm{L}}$, the binary parameters will be identical, and the joint evidence—neglecting any selection effects—will be given by (Lo & Magana Hernandez, 2023)

$$p(d_1, d_2|\mathcal{H}_{\mathrm{L}}) = \int p(d_1|\theta, \mathbf{\Lambda}_1)\, p(d_2|\theta, \mathbf{\Lambda}_2)\, p(\theta, \mathbf{\Lambda}_1, \mathbf{\Lambda}_2)\, d\theta\, d\mathbf{\Lambda}_1 d\mathbf{\Lambda}_2, \tag{8.2}$$

where the latter term is the prior on the binary and image lensing parameters and the former two terms are the individual likelihoods for each signal as described in Veitch & Vecchio (2010). In the unlensed hypothesis, $\mathcal{H}_{\mathrm{U}}$, the events are independent of one another and thus the joint likelihood is simply the product of the two individual likelihoods, i.e. $p(d_1, d_2|\mathcal{H}_\mathrm{U}) = p(d_1|\theta)p(d_2|\theta)$.

Comparing these two joint evidences provides an estimate of which hypothesis is more likely; however, due to the neglect of selection effects in Equation 8.2 it is important to note that this is not a complete Bayes factor as it remains sensitive to the BBH population. The ratio of these two evidences is thus given the name *Coherence ratio*,

$$C^\mathrm{L}_\mathrm{U} = \frac{p(d_1, d_2|\mathcal{H}_\mathrm{L})}{p(d_1|\mathcal{H}_\mathrm{U})p(d_2|\mathcal{H}_\mathrm{U})}. \tag{8.3}$$

The process to go from this value to the full Bayes factor between the two hypotheses including the selection effects is outlined in Lo & Magana Hernandez (2023).

Calculation of the joint likelihood necessary for the calculation of the coherence ratio is a computationally intensive process, but may be sped up by instead considering the *conditional evidence* alongside the individual evidences which allows acceleration of the computation through importance sampling and look-up tables. The full details of this are described in Janquart et al. (2021, 2023a), but we will briefly outline this here.

As discussed in Chapter 3, the conditional and joint evidences are related as

$$p(d_1, d_2|\mathcal{H}_\mathrm{L}) = p(d_1|\mathcal{H}_\mathrm{L})p(d_2|d_1, \mathcal{H}_\mathrm{L}). \tag{8.4}$$

This may be expanded by considering instead of the individual lensing parameters of the images the *relative lensing parameters*, $\mathbf{\Phi}$— i.e. the relative magnification, time delay, and Morse difference between the two images—and the *effective parameters*, $\mathbf{\Theta}$ of the first image where the magnification has been absorbed into the observed luminosity distance, and the time delay has been absorbed into the observed coalescence time, leaving only the Morse index of the first image not absorbed into the observed source parameters, meaning the effective parameters are described as

$$\begin{aligned} t_c^{\mathrm{obs},2} &= t_c^{\mathrm{obs},1} + t_{21} \\ d_L^{\mathrm{obs},2} &= \sqrt{\mu_\mathrm{rel}}\, d_L^{\mathrm{obs},1} \\ n_2 &= n_1 + n_{21}. \end{aligned} \tag{8.5}$$

Using these, the conditional evidence of Equation 8.4 may be evaluated as a "marginalised" likelihood of the form (Janquart et al., 2021)

$$p(d_2|d_1, \mathcal{H}_\mathrm{L}) = \int \left\langle p(d_2|\mathbf{\Theta}, \mathbf{\Phi}) \right\rangle_{p(\mathbf{\Theta}|d_1)} p(\mathbf{\Phi}) d\mathbf{\Phi}. \tag{8.6}$$

The first term of the integrand is the likelihood of the second event averaged over the posterior samples of the first event. This already is cheaper to compute than directly computing the joint evidence, but may be further computationally sped up by the recycling of the samples from the parameter estimation investigation of the first event to create a look-up table for use in calculating Equation 8.6.

Both direct calculation of the joint evidence as well as this conditional approach have been deployed on GW data and are incorporated into the HANABI (Lo & Magana Hernandez, 2023) and GOLUM pipelines respectively (Janquart et al., 2021). The following sections will use the GOLUM pipeline for its strong lensing workflows.

8.2 Model Selection of Lensed Gravitational Wave Signals

The above approaches for strong lensing identification, alongside others, have largely created a framework to answer the question of: "*for a given pair of images, are these images lensed?*" whilst sidestepping the question of "*by what?*". In large part, this has been to the benefit of answering the former question whilst avoiding misidentification of lensed pairs due to application of the wrong model. However, this is not to say that no effort has been taken to answering the latter question, with some initial steps taken such as in Janquart et al. (2022) where it was suggested to reweight the detection statistics using model information from various catalogs built from differing lens models such as those found in Haris et al. (2018b); Wierda et al. (2021a), or More & More (2022). Similarly, given that Lo & Magana Hernandez (2023) describes the inclusion of the model for the calculation of the selection effects to achieve a more complete Bayes factor for the context of answering the first question, the process could simply be repeated multiple times to account for different lens profiles.

However, there are notable downsides to performing both methods. In the former, whilst it is capable of handling realistic and complex lens models, the downside is the generation of an extended catalog of sources to explore. These sources must be drawn from particular source and lens populations which means that this approach is more affected by systematic biases than the direct application of a lens model. However, in the second approach where the model is directly applied it requires an analytic formulation for the magnification probability distribution. This limits its applicability to simpler lens models. Mitigations to this weakness of the Lo & Magana Hernandez (2023) approach can be made by including the same catalog information as in the first approach but again, this opens it to the systematics problems. Efforts to use both of these approaches on candidate lensed signals are discussed in greater detail in Janquart et al. (2023b).

An additional complication for model selection of strongly lensed GW signals is the need for the identification of the multiplets. As we have noted in Chapter 6, single image analysis is insufficient to be able to extract lensing information due to the degeneracy between the source and lensing parameters in this case.

We therefore seek an approach, based on the outputs of the model agnostic detection pipelines, that includes the multiple images and that does not require computationally expensive resampling of the parameter space or the construction of the extended catalogs which opens the method up to additional impact from systematic biases in the source and lens populations. If the former can be avoided, this is of benefit to the lensing community as a rapid follow-up investigation for identified strong lensing candidates—for instance one may imagine the scenario where, if lensing information may be identified from a pair quickly enough, then additional images may be predicted.

The goal of such a methodology is to find the evidence for a given lens model, which will here be termed $\mathcal{H}_{\rm m}$, which consists of a set of lens parameters, $\mathbf{\Upsilon}$. By direct application of Bayes' theorem (Equation 3.5), this evidence is given by:

$$p(d_1, d_2|\mathcal{H}_{\rm m}) = \frac{p(d_1, d_2|\mathbf{\Theta}, \mathbf{\Phi}, \mathbf{\Upsilon}, \mathcal{H}_{\rm m})\,p(\mathbf{\Theta}, \mathbf{\Phi}, \mathbf{\Upsilon}|\mathcal{H}_{\rm m})}{p(\mathbf{\Theta}, \mathbf{\Phi}, \mathbf{\Upsilon}|d_1, d_2, \mathcal{H}_{\rm m})}, \tag{8.7}$$

where $\mathbf{\Theta}$ and $\mathbf{\Phi}$ represent the effective binary parameters and the relative lensing observable parameters as discussed in the previous section. To simplify the discussion of these terms going forward, we define the evidence for a chosen model as $\mathcal{Z}_{\rm m} = p(d_1, d_2|\mathcal{H}_{\rm m})$ and the model likelihood as $\mathcal{L}(\mathcal{H}_{\rm m}) = p(d_1, d_2|\mathbf{\Theta}, \mathbf{\Phi}, \mathbf{\Upsilon}, \mathcal{H}_{\rm m})$. We will, in the following discussion, actually aim for the inverse of the evidence as it will be shown to be easier to calculate. Once calculated, it is obviously trivial to invert this back to the evidence. The inverse of the evidence is given from the above as

$$\frac{1}{\mathcal{Z}_{\rm m}} = \frac{p(\mathbf{\Theta}, \mathbf{\Phi}, \mathbf{\Upsilon}|d_1, d_2, \mathcal{H}_{\rm m})}{\mathcal{L}(\mathcal{H}_{\rm m})\,p(\mathbf{\Theta}, \mathbf{\Phi}, \mathbf{\Upsilon}|\mathcal{H}_{\rm m})}. \tag{8.8}$$

The posterior that forms the numerator of Equation 8.8 may be expanded further to yield

$$p(\mathbf{\Theta}, \mathbf{\Phi}, \mathbf{\Upsilon}|d_1, d_2, \mathcal{H}_{\rm m}) = p(\mathbf{\Upsilon}|\mathbf{\Theta}, \mathbf{\Phi}, d_1, d_2, \mathcal{H}_{\rm m})\,p(\mathbf{\Theta}, \mathbf{\Phi}|d_1, d_2, \mathcal{H}_{\rm m}). \tag{8.9}$$

We note that the lattermost term of Equation 8.9 is, in fact, insensitive to the lens model since the apparent lensing parameters and the effective binary parameters may be fully determined from the data, and as such it becomes simply $p(\mathbf{\Theta}, \mathbf{\Phi}|d_1, d_2)$. Inserting this back into Equation 8.8 yields

$$\frac{1}{\mathcal{Z}_{\rm m}} = \frac{p(\mathbf{\Upsilon}|\mathbf{\Theta}, \mathbf{\Phi}, d_1, d_2, \mathcal{H}_{\rm m})\,p(\mathbf{\Theta}, \mathbf{\Phi}|d_1, d_2)}{\mathcal{L}(\mathcal{H}_{\rm m})\,p(\mathbf{\Theta}, \mathbf{\Phi}, \mathbf{\Upsilon}|\mathcal{H}_{\rm m})} \tag{8.10}$$

This may be solved using a similar approach to Equation 8.6, i.e. by sampling $p(\mathbf{\Theta}, \mathbf{\Phi}|d_1, d_2)$, computing the remaining terms of Equation 8.10 and averaging the ratio over all of the taken samples, i.e.

$$\frac{1}{\mathcal{Z}_{\rm m}} = \left\langle \frac{p(\mathbf{\Upsilon}|\mathbf{\Theta}, \mathbf{\Phi}, d_1, d_2, \mathcal{H}_{\rm m})}{\mathcal{L}(\mathcal{H}_{\rm m})\,p(\mathbf{\Theta}, \mathbf{\Phi}, \mathbf{\Upsilon}|\mathcal{H}_{\rm m})} \right\rangle_{p(\mathbf{\Theta}, \mathbf{\Phi}|d_1, d_2)} \tag{8.11}$$

The sampled quantity, $p(\mathbf{\Theta}, \mathbf{\Phi}|d_1, d_2)$, is the posterior on the effective binary and relative lensing parameters from the data, i.e. the output of a model-agnostic joint parameter estimation pipeline which can be arrived at from either a full joint parameter estimation or a conditional approach. Both the prior and the likelihood are known and easily calculable—the prior obviously so, and the likelihood being the joint likelihood using an implementation discussed in more detail in Janquart et al. (2023a) with the produced lensed waveform from the sampled parameters. Finally, the numerator—the conditional probability of the lens parameters given the model—may be computed in a number of ways. For simpler lens models, it may be computed directly using analytic relationships between the model parameters and the lensing observables—some of which are discussed in Section 6.1. For more complex models, other approaches may be undertaken such as numerically evaluating the lens equations for the given points.

Equation 8.11 therefore achieves the goals for a lens model selection method for strong lensing from the output of the model agnostic searches which bypasses the needed for resampling of an extended parameter space. This means that it may be used for the discussed rapid follow-up of identified candidates. It has been implemented within the Gravelamps package (Wright et al., 2022) for the isolated point mass and SIS models—both of which contain analytic relationships between the redshifted lens mass, M_{lz}, and dimensionless source position, y and the observable lensing parameters. Whilst these models are relatively simple compared with the state-of-the-art for strong lensing, they allow testing of the methodology within a more well known environment to allow for proof-of-concept testing. This may then in future work, be expanded to these more complex models.

8.3 Investigations of Methodological Performance

To perform initial testing of the methodology's validity, it was subjected to a number of test applications. The primary source of these investigations was the application of the methodology to a set of seventy five simulated GW signals with known binary and lens parameters. This allowed investigation of the ability of the method to identify the appropriate lensing model as well as the reconstruction of the lens model's specific parameter posteriors. The stability of this evidence calculation could also be examined as a function of the inclusion of a varying number of samples to identify when a preliminary result would be considered robust for the highest possible speed of deployment. Finally, whilst a real lensing event has not yet been detected, the performance of the methodology on real-world data was examined by considering the event pair GW191230–LGW200104; this is the event pair within Janquart et al. (2023b) which had the highest significance from the lensing searches of the ultimately discarded candidates.

8.3.1 Injection Set Investigation

The main test of the methodological performance was to investigate the results of subjecting a series of simulated lensing events to the method to see if both the model can be recovered as well as whether lens parameter posteriors consistent with the true values are constructed. To ensure a realistic testing set, the mass, spin, and redshift parameters for these were chosen to reflect the inferred population from the O3 population investigations, i.e. Abbott et al. (2023c) with the other parameters distributed across their possible states. The events were chosen to be lensed by SIS lenses with a uniform prior on the redshifted lens mass between $10^6 M_\odot$ and $10^9 M_\odot$ and a power-law prior distribution on the dimensionless source position with $\alpha = 1$ between values of 0 and 1 (exclusive of the endpoints)—i.e. reflecting the cases for SIS lensing that produce multiple images whilst avoiding the direct hit and caustic cases.

Once the sample binary and lens parameters were drawn, the lensed pair of signals were generated using the IMRPhenomXPHM (Pratten et al., 2021) waveform approximant and each image was lensed using the relevant contribution to Equation 5.45. These signals were injected into a simulated detector network consisting of LIGO's Livingston and Hanford detectors as well as the Virgo detector using a noise realisation representative of the expectations for noise during O4 allowing a realistic short-term projection of the abilities of the method. These simulated injections were then subjected to joint parameter estimation using the GOLUM pipeline (Janquart et al., 2021, 2023a) which uses the conditional approach discussed in Section 8.1. This analysis was performed with the Nessai machine learning-based nested sampler (Williams et al., 2021). The following priors were used on the model agnostic lensing observables:

Relative Magnification:	Uniform between 0.01 and 50
Time Delay:	Uniform over the range of the injected time delay ±0.2 seconds
Morse Index:	Uniform on the discrete values of 0, 0.5, and 1.0

Once concluded, the resulting samples from the joint parameter estimation were then used to evaluate Equation 8.11 under the assumption of both models to reconstruct posteriors on the lensing parameters for each model and then compare the evidence for each model to determine the most likely. In this main injection set, this was done for each sample that was produced by the joint parameter estimation.

Figure 8.1 shows the distribution of the recovered Bayes factors comparing the SIS and isolated point mass lensing models in the form of both the raw histogram of the values as well as the inferred distribution constructed using a kernel density estimator (KDE). All of the events considered demonstrate a positive log Bayes factor, indicating a consistent preference for the true SIS model. As can also be seen, the raw histogram does not overlap with zero, yielding sufficient consistent support for identification. The minimum log Bayes factor of the considered events was 1.44, the maximum was 7.98 and the mean across the events was 3.44.

Turning now to the construction of the posteriors on the model specific lens parameters, Figure 8.2 shows the reconstructed posteriors on the lens model parameters for the true SIS model both in the form of the raw histogram and the constructed KDE. Overlaid is the true value of the parameter for both cases. As can be seen in this example, the posterior displays constraint around the true value indicating a successful recovery of the parameter.

In a more broad look, the parameters were typically recovered, with the accuracy and constraint dependent upon the joint parameter estimation recovery of the relative lensing observables. A selection of these recoveries which demonstrates this is shown in Figure 8.3 which shows the comparison between the posterior for the relative magnification from the GOLUM joint parameter estimation compared with the model specific dimensionless source position for the SIS model obtained from the methodology. As can be seen, in the first rows where the relative magnification has a tight constraint, so

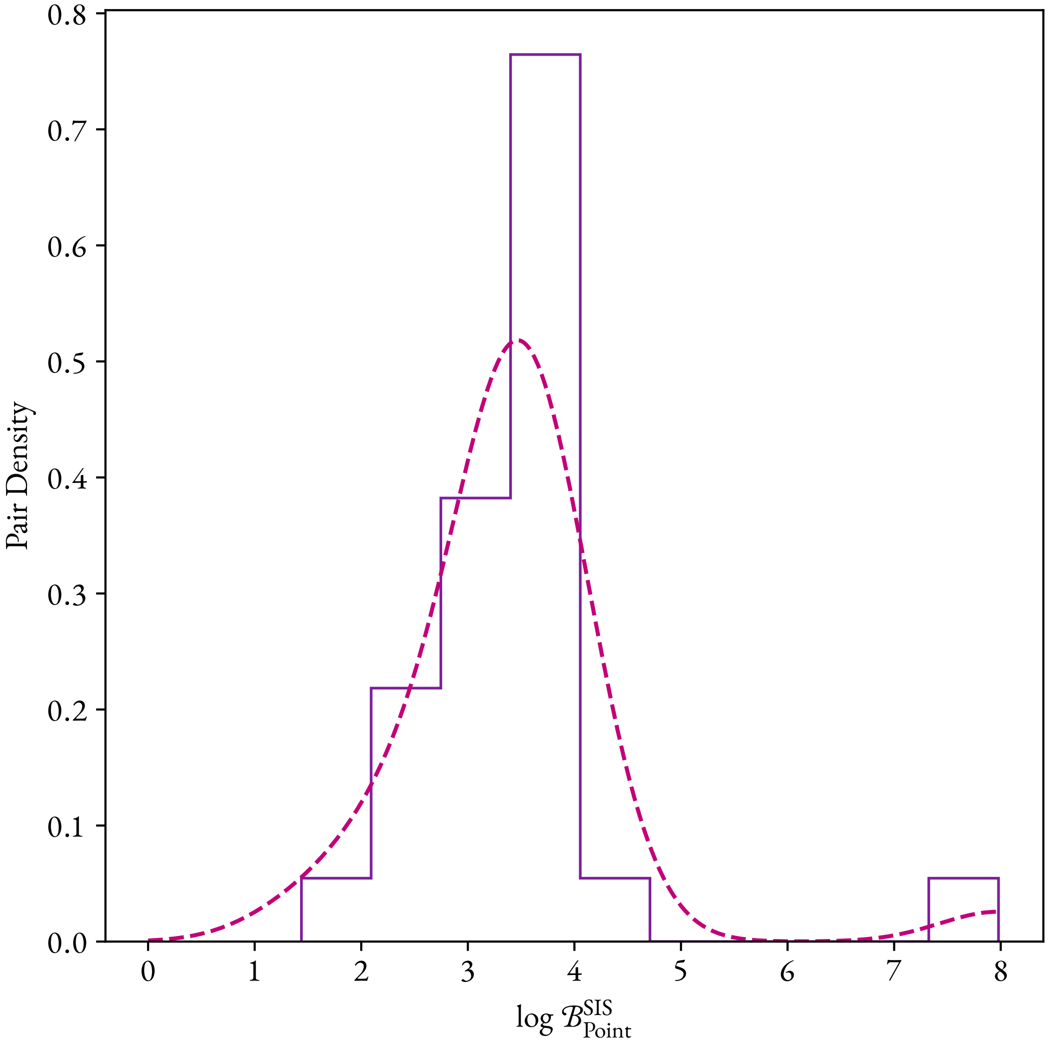

Figure 8.1: Distribution of the log Bayes factors comparing the SIS and isolated point mass lensing models for the set of 75 simulated GW signals. The solid purple line indicates the raw histogram of these Bayes factors, with the dashed line showing the inferred distribution from a KDE. All events analysed show a positive Bayes factor indicating that the SIS model was correctly preferred in all cases.

too does the source position. Oppositely, in the case of row five, where joint parameter estimation has failed to recover the relative magnification, this remains the case in the source position reconstruction.

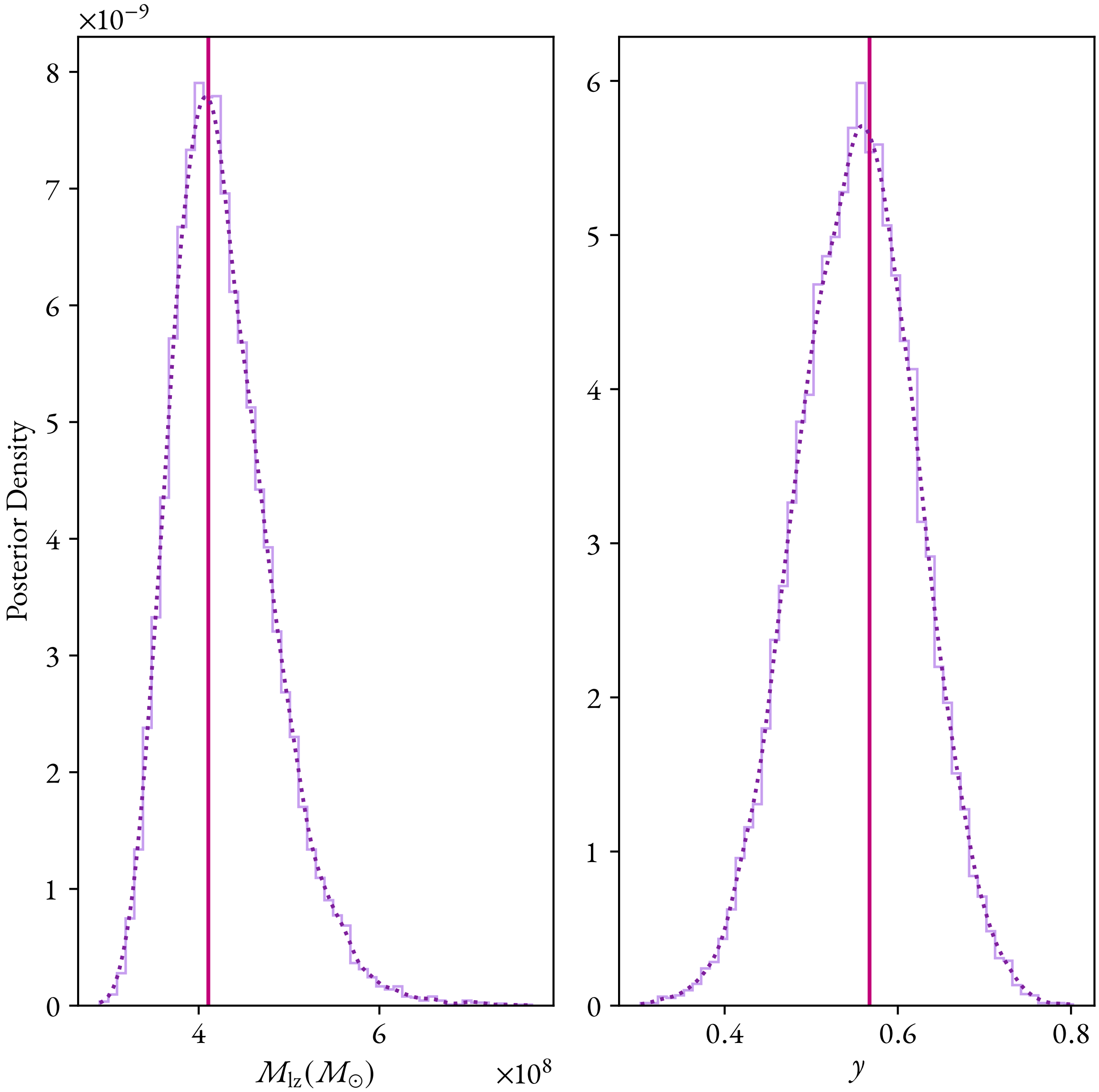

Figure 8.2: Reconstructed posteriors for the lens parameters—the redshifted lens mass and dimensionless source position—for an example event from the 75 simulated GW signals under the assumption of the true model. Plotted are the raw histogram with a KDE overlaid in the dotted line. The solid vertical line indicates the position of the true value. As can be seen, in both cases, these posteriors are constrained around the true value indicating a successful recovery of these parameters.

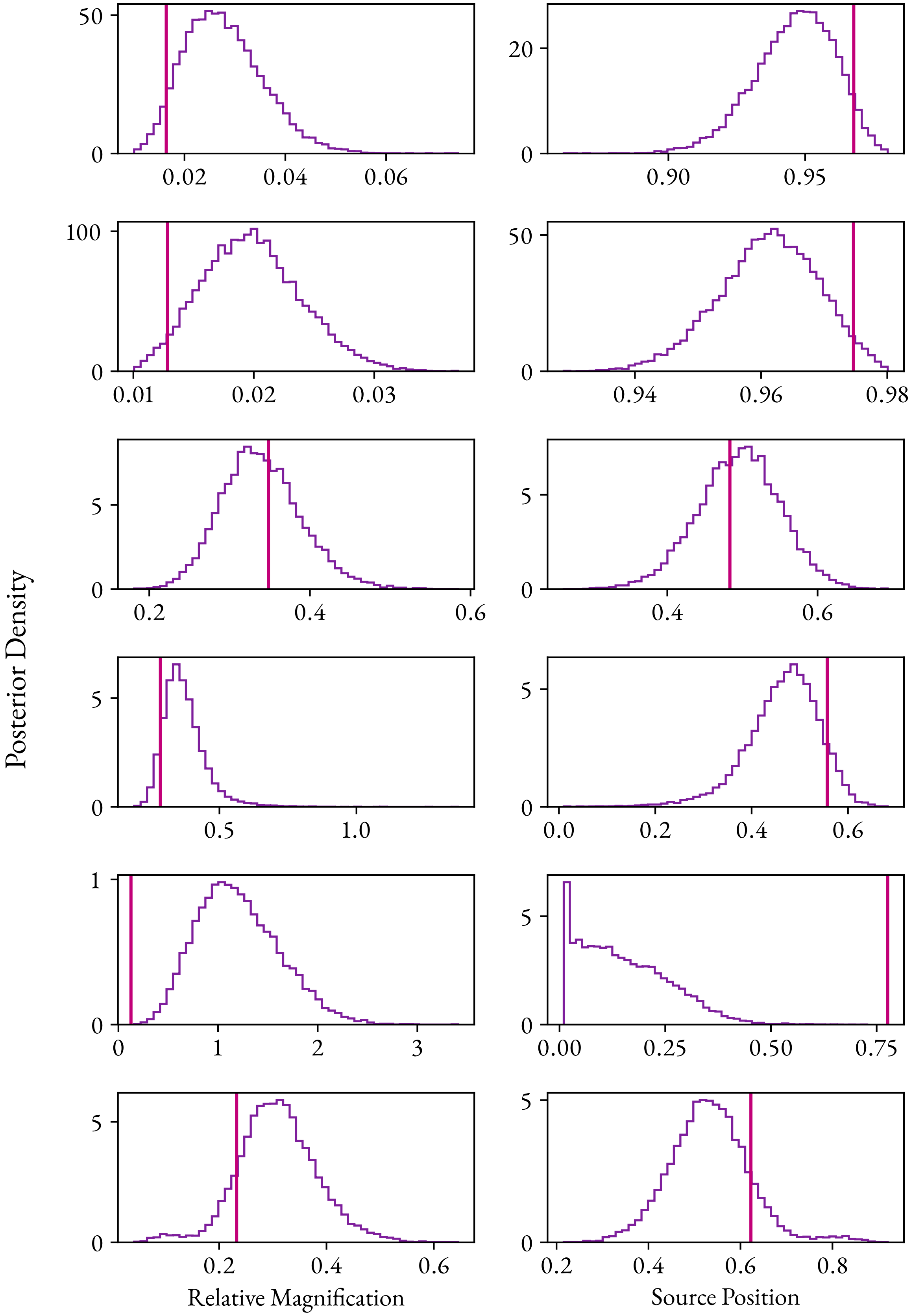

Figure 8.3: Comparison of the recoveries of the observable relative magnification from the GOLUM joint parameter estimation analysis with the reconstructed dimensionless source position for the SIS model from the presented methodology. As can be seen, the recovery of the parameter is strongly related to the recovery of the observable, with the case of the fifth row showing a failure to recover in both cases. This is in line with expectations for the methodology.

8.3.2 Stability of Methodological Result

Whilst the methodology may already be deployed at speed, an additional investigation was carried out into the stability of the result using fewer samples. This serves two functions—both showing that the result progressively stabilises towards a robust final result as well as indicating the point at which a preliminary result may be considered sufficiently robust for use should a scenario requiring the utmost speed arise—such as the aforementioned notion of predicting later images from earlier ones.

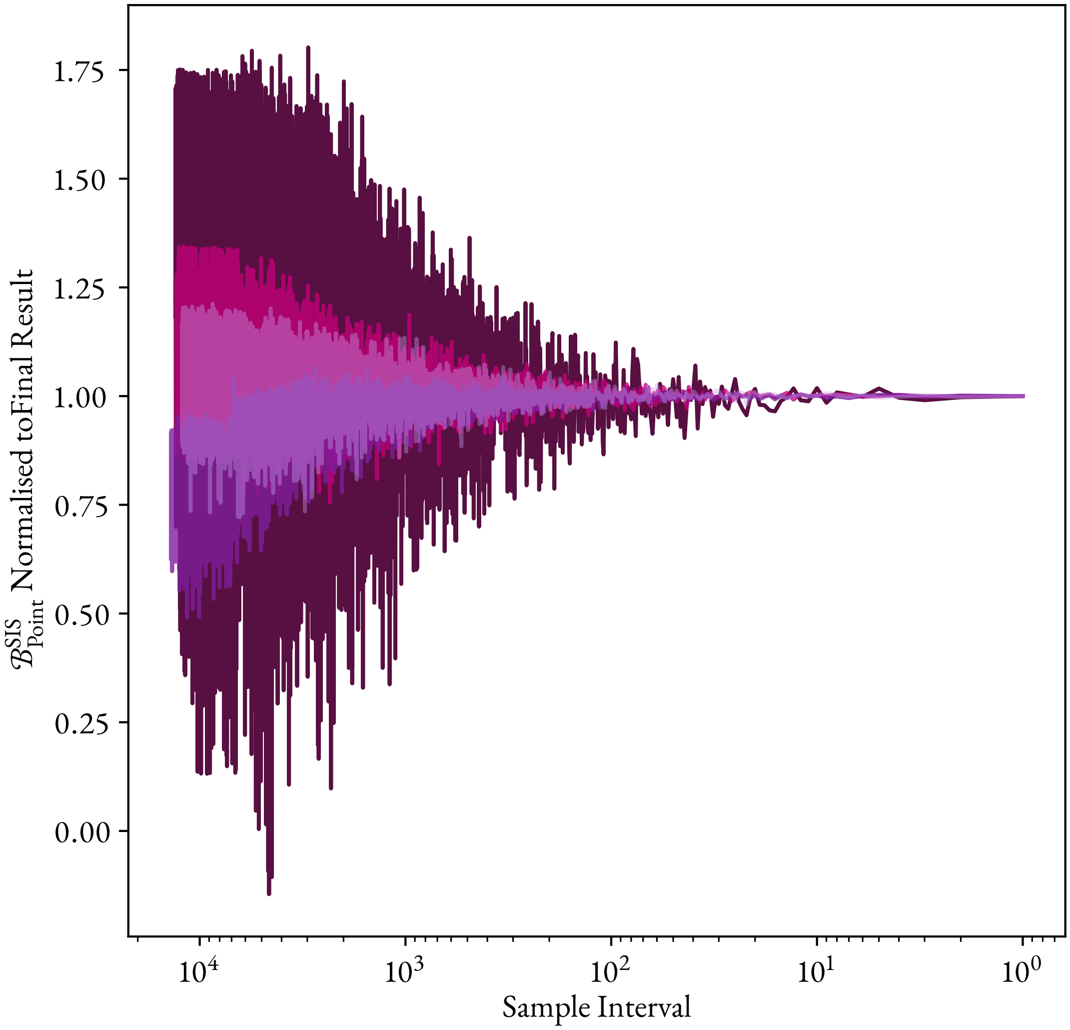

Figure 8.4: The resulting value of the method as a function of including every n samples for four of the simulated GW signals. This value is normalised to the final result to allow the comparison between multiple investigations. As can be seen, increasing the number of samples obviously tends the result towards a more stable value. A prelimninary result would be representative of the final result at approximately the inclusion of every 100^{th} sample.

Figure 8.4 shows the evolution of the result of the Bayes factor calculation from four of the simulated events as progressively more samples are included. This was done by taking an interval n from an ever decreasing value of n towards 1. The values shown are also normalised to the final result to allow the comparison between the different investigations. As can be seen from the figure, all cases trend towards a final value as more samples are included. Whilst the rate of stabilisation varies between the four events, in all cases the point at which a preliminary result may be considered representative of the final result occurs at the inclusion of approximately 1% of samples which allows extremely rapid deployment on the conclusion of the joint parameter estimation investigation.

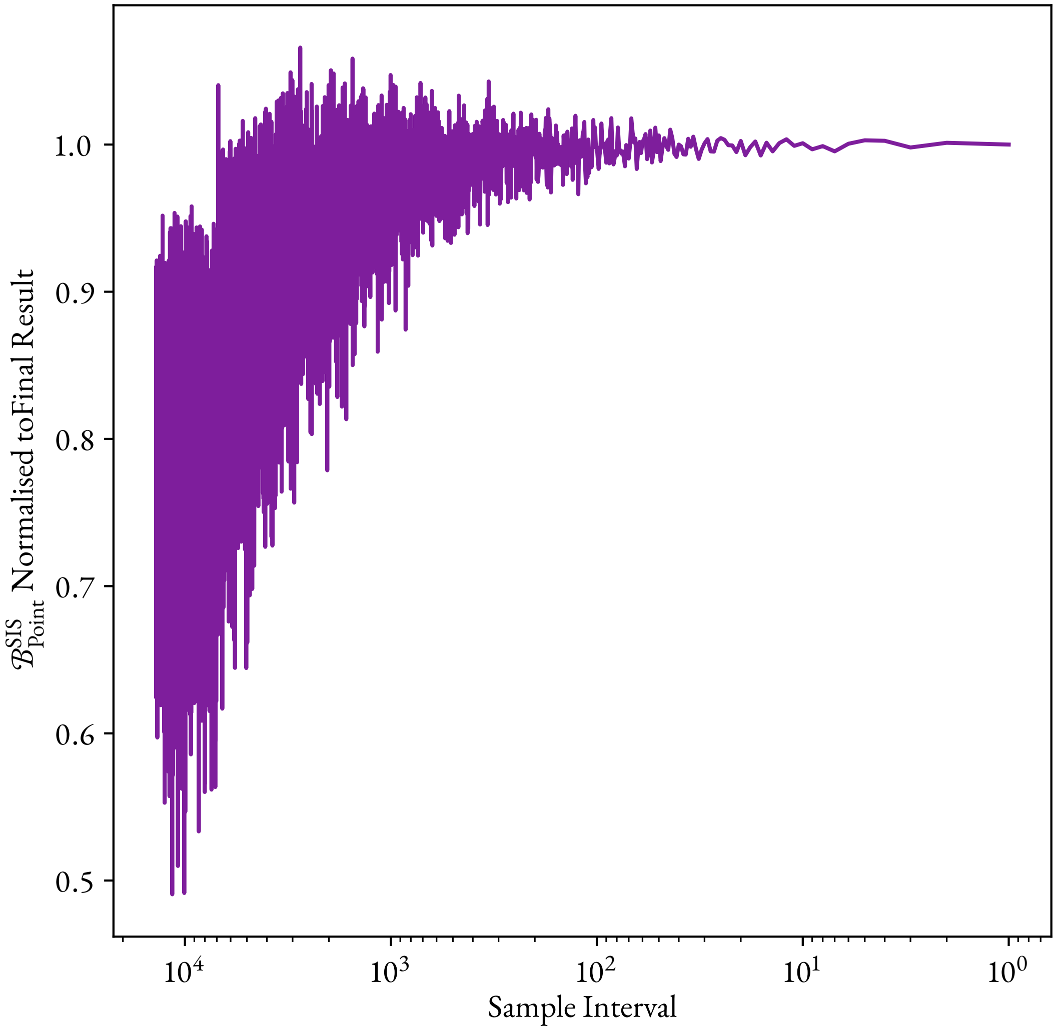

Figure 8.5: An example of the progression of stability from the model selection method as more samples are included for a case which initially centres on a deviated value from the final result. Again by the inclusion of every 100^{th} sample, this reaches a point at which a preliminary result would be representative of the final result.

One notable feature of certain events is that the initial oscillation of the results may not centre on the final result. This is visible in one of the cases shown in Figure 8.4 but is isolated in Figure 8.5 for clarity. However, in this instance it remains the case that by the inclusion of 1% of samples, the preliminary result is representative of the final result.

8.3.3 Example Deployment on GW191230–LGW200104

As we have noted throughout this work, as of the end of O3, the LVK has not yet found any significant evidence of lensing signatures in the currently detected signals (Abbott et al., 2021f, 2023d). However, as was discussed extensively in the previous chapter, there have been signals that have displayed features similar to those expected of lensed signals that have been analysed in greater detail—see Janquart et al. (2023b). These signals represent the current best opportunities to test lensing analyses on realistic data. Therefore, to test the methodology discussed in this chapter in a realistic setting it was also deployed on the pair GW191230–LGW200104 which is the pair that of those analysed in Janquart et al. (2023b) was found to have the highest Bayes factor in favour of lensing though it was ultimately discarded upon full consideration and in particular given the low probability of astrophysical origin of LGW200104. In the following analysis, these were treated as both a real and lensed event for the purposes of demonstration.

The pair was reanalysed using GOLUM (Janquart et al., 2021, 2023a) and the Nessai nested sampler (Williams et al., 2021) to bring analysis of this pair into line with the simulated set discussed in the previous sections. These results were then placed through the methodology. This yielded support for the SIS lensing model with a $\log_{10} \mathcal{B}^{\mathrm{SIS}}_{\mathrm{Point}}$ of 3.65. This was consistent with the finding of Janquart et al. (2023b) that consideration of the SIS model did improve preference for the pair as compared with the model agnostic data. It should be noted that Janquart et al. (2023b) would ultimately conclude that the singular isothermal ellipsoid (SIE) model was the *most* preferred.

Figure 8.6 shows both the posteriors on the lensing parameters reconstructed by this method for the SIS model as well as the original recovered posteriors on the relative lensing observable parameters from the GOLUM joint parameter estimation, as well as the median of these posteriors. The reconstruction of the lens posteriors is notably very broad, with the dimensionless source posterior railing against the direct hit case. This may be an indicative of the fact it has been deployed on a pair that is believed to not be lensed, and thus the results do not necessarily have to indicate something sensible. However, taking for a moment that this were both a pair of genuine GW signals as well as genuinely lensed, then the analysis here would indicate that an SIS lens with a detector frame lens mass of $5.08^{+0.94}_{-2.09} \times 10^{10} M_{\odot}$ and a dimensionless source position of $0.23^{+0.15}_{-0.14}$. However, it must be stressed that this analysis does not make any claims about the reality of the pair being lensed.

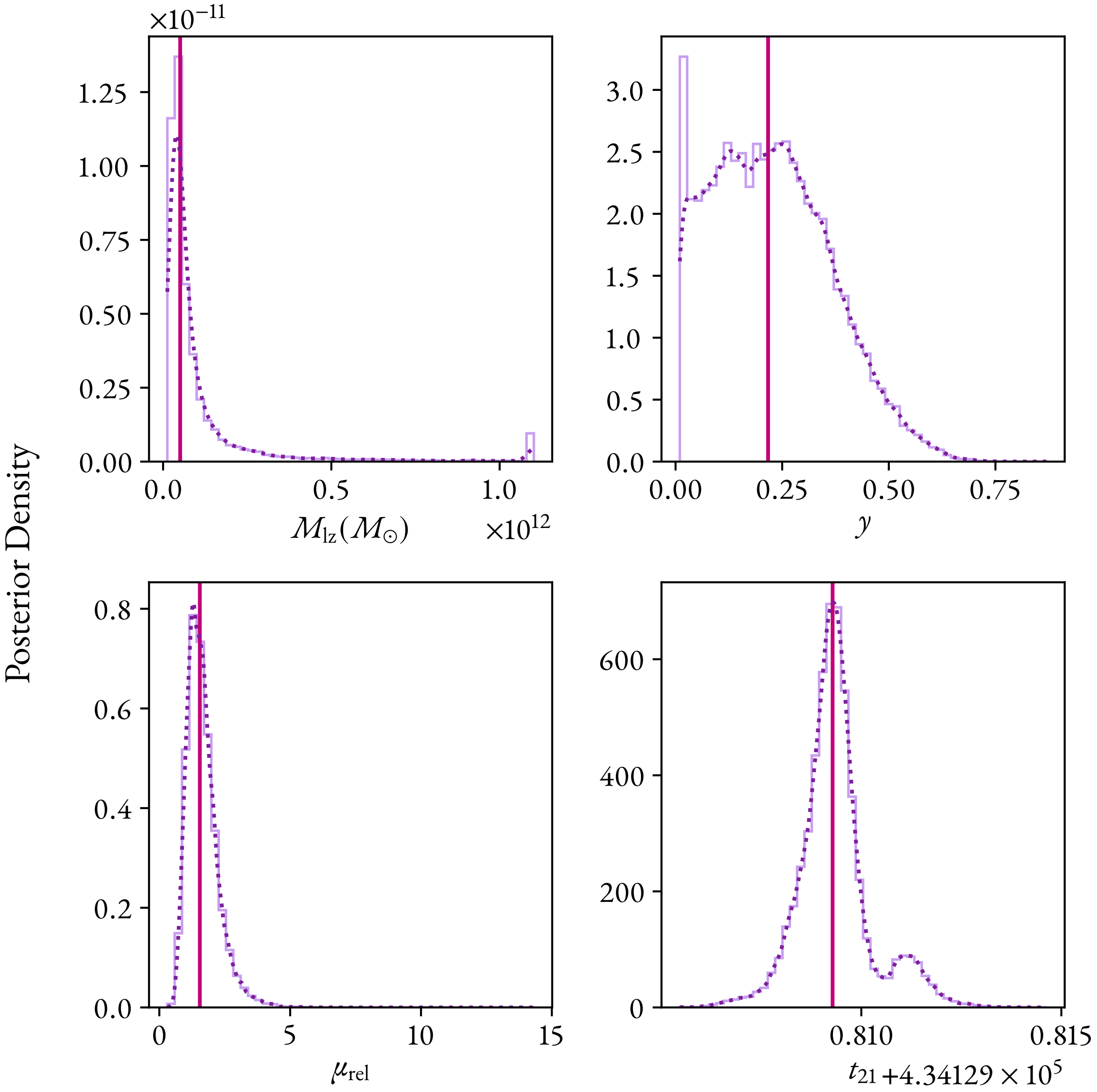

Figure 8.6: *Top:* Reconstructed posteriors on the model specific lens parameters for the SIS model. *Bottom:* Recovered posteriors from the GOLUM joint parameter estimation on GW191230–LGW200104. In both, the solid histograms are the raw posterior histograms. The dotted lines indicate fitted KDEs to the posteriors, and the solid vertical line indicates the median of the posterior.

8.4 Conclusion

In this chapter, we have presented a method to overcome one of the challenges identified in Chapter 6, i.e. a methodology for performing model selection on strongly lensed GW signals. This has been done in the form of a rapid postprocessing method that can be deployed on the output of the model agnostic joint parameter estimation analyses which avoids the need to resample multiple times which would vastly increase the computational cost of multiple signal analyses.

To demonstrate the efficacy of the method using the relatively simple isolated point and SIS models, a set of 75 simulated SIS-lensed pairs of GW signals were created following the observed population of BBHs based on the O3 observations, analysed using the GOLUM joint parameter estimation package and then subject to the methodology. In all cases, the correct lensing model was identified with the reconstruction of the model specific parameters falling in line with the recovery of the model agnostic lensing observable parameters.

It was further shown that the method stabilises with the inclusion of an increasing number of samples from the joint parameter estimation results to identify that a preliminary result would be robustly representative of the final result from the inclusion of approximately 1% of the total number of samples. This allows an already rapid process to be deployed at even greater speed in the case where such an analysis would be beneficial such as for the prediction of future images based on the arrival of the first pair.

Finally, whilst there remain no real lensed GW signals on which to test the method, to gain an understanding of the results of the method when deployed on actual GW data, it was deployed on GW191230–LGW200104, the candidate pair from O3 that displayed the highest Bayes factor for lensing before being ultimately discarded. The analysis indicated a preference for the SIS model; however, it must again be stressed that this is only under the likely false assumption of lensing for the pair.

9

Effect of Deviations from General Relativity on Searches for Gravitational Wave Microlensing and Millilensing

> *We must agree on what is real. Because of this, we are the only animal on Earth that goes mad*
>
> The Narrator, *Legion*
> created for TV by Noah Hawley

Disclaimer

The following chapter is based on the work *Effect of Deviations from General Relativity on Searches for Gravitational Wave Microlensing and Type II Strong Lensing* which was co-authored by Justin Janquart and Nathan Johnson-McDaniel and has been submitted for publication in the Astrophysical Journal.

In Chapter 1, our discussion presented GR as the current pinnacle of thought on an explanation for gravity. We also discussed the development of gravitational theory from the origins of Aristolean thought through to the development and testing of GR. In particular, we noted that GR has passed every laboratory (Berti et al., 2015) and astrophysical test (Will, 2014) that has been deployed on it so far.

GW signals offer the ability to further test GR in the dynamical, highly non-linear regime. In general, these tests have focused on placing limits on any potential deviations from GR rather than affirmative testing of alternative theories of gravity. This has largely been due to the fact that the development of accurate waveform models for the inspiral, merger, and ringdown (IMR) of GWs in non-GR theories is in its infancy.

Modifications to the theory of gravity will broadly affect three areas of the GW:

Generation	Such as differing post-Newtonian coefficients (for further detail see e.g. Tahura & Yagi (2018); Bernard et al. (2022), or Shiralilou et al. (2022)) as well as differences in the merger-ringdown phase (see e.g. Okounkova et al. (2020) or Corman et al. (2023) and the quasinormal mode (QNM) spectrum of the final black hole (see e.g. Srivastava et al. (2021); Wagle et al. (2022) or Cano et al. (2023)).
Propagation	For further detail, see e.g. Mirshekari et al. (2012); Kostelecký & Mewes (2016); Mewes (2019) or Zhu et al. (2023).
Polarisation Modes	As we discussed in Chapter 4, GW signals contain two tensorial (the *plus* and *cross*) polarisation modes. In addition to these, general theories of gravitation may allow up to six modes—two additional scalar modes and two vectorial modes—see e.g. Eardley et al. (1973b) and Eardley et al. (1973a).

Some of the specific examples of additional effects on GWs that modifications to the theory of gravitation would yield include dispersion (Mirshekari et al., 2012) due to the existence of a massive graviton or Lorentz violations, amplitude birefrigence (Okounkova et al., 2022)—the explicit enhancement or suppression of the left or right circular polarisation modes of the GW—, or amplitude dampening (Nishizawa, 2018; Belgacem et al., 2018).

As of the end of O3, investigations by the LVK into the detected GW events had not found any significant support for physics beyond that contained within GR (Abbott et al., 2019f, 2021d,e). However, as the detectors improve in sensitivity and the number of events increase, this will lead to an increase in the sensitivity to ever smaller deviations from GR.

As we have noted briefly above, and will do in more detail in the remainder of this chapter, deviations from GR—like gravitational lensing—produce modifications to the GW waveform. Additionally, gravitational lensing of GW has also been proposed as a means of further testing deviations from GR. Specifically, it has been proposed to allow probing of extra polarisations (Goyal et al., 2021b; Magaña Hernandez, 2022), birefringence (Ezquiaga & Zumalacárregui, 2020; Goyal et al., 2023), or modifications to dispersion induced by massive gravitons (Finke et al., 2021; Narola et al., 2023). Because of both this overlap in effect as well as the potential to leverage lensing to test for deviations from GR, it is therefore vital in the individual searches for each of these phenomena to be aware of the effect that one may have on the other, and in particular to understand whether false positives may arise in either search due to the presence of the other.

This chapter will focus on whether phenomenological deviations from GR or proxies for signals from exotic objects that may mimic black hole mergers have an effect on searches for microlensing and millilensing. For a fuller examination of the effects also on searches for Type II strong lensing, see Wright et al. (2024). The complimentary investigations into whether microlensing may induce false positives in searches for deviations from GR was explored in Mishra et al. (2023) where it was found that such false positives can occur in some circumstances.

9.1 Deviations from General Relativity and the Generation of Modified Waveforms

As we have noted, in general, alternative theories of gravitation affect three aspects of GW signals—generation, propagation, or polarisation. In the following, we will consider phenomenological modifications to all of these. We will also consider the case of proxies for waveforms from exotic objects that may exist in such alternate theories of gravitation that may mimic BBH mergers. Specifically, we will consider

- dispersion due to a massive graviton;
- self-consistent modifications to the energy flux and the QNM spectrum as proxies for general modifications arising from non-GR theories;
- the addition of a scalar polarisation mode;
- scaled waveforms from a BNS system as proxies for an exotic object binary mimicking a BBH.

The philosophy of choosing a single one of these deviations for the construction of non-GR waveforms is to include an interesting non-GR effect in a controlled environment. This is not intended to replicate specific alternate theories of gravitation—aside, technically, from the massive graviton case though we note that this is just the phenomenological introduction of dispersive propagation. The waveform generation methods described here are also being employed by the LVK Testing General Relativity (TGR) working group in a mock data challenge.

The starting point for the generation of a GW signal in a modified theory of gravity is a waveform model within GR. Many such models exist and were discussed briefly in Section 4.7.2. Here, the baseline waveform chosen was that of the EOB family, specifically the waveform model TEOBResumS-v3-GIOTTO (Damour & Nagar, 2014; Nagar et al., 2016, 2018, 2020a; Akçay et al., 2021; Riemenschneider et al., 2021; Gamba et al., 2022). This waveform was used as a model for precessing BBHs on quasicircular orbits. It contains the dominant (2, ±2) modes as well as the subdominant (2, ±1), (3, ±3), (3± 2), (4, ±4), and (5, ±5) modes (in the co-processing frame) with a robust merger-ringdown model (Nagar et al., 2020b). The injections that will be investigated here will contain all of these modes.

We now turn our discussion to briefly detail each of the considered phenomenological modifications to GR that were outlined above.

9.1.1 Dispersion and Massive Gravitons

In GR, the propagation of GWs is non-dispersive and consequently follows the relation $E^2 = p^2c^2$ between the energy, E, and the momentum, p of the wave. In alternative theories of gravitation, however, this need not be the case and the propagation may be dispersive. One particular example of this would be a massive graviton which being massive would necessarily travel below the speed of light and would also have the speed dependent upon their energy. Given the chirp like nature of a CBC merger would mean that gravitons emitted nearer the merger would be faster than those emitted earlier. A generalised parametric relation may be employed to describe the leading effects of dispersion for a number of these non-GR scenarios (Mirshekari et al., 2012)

$$E^2 = p^2c^2 + A_\alpha p^\alpha c^\alpha, \tag{9.1}$$

where we introduce the Lorentz-violating phenomenological parameters A and α to describe the dispersion.

In the specific case of a graviton with mass, m_g, and a theory that contains no other deviations from GR that result in dispersive propagation, special relativity predicts that Equation 9.1 may also be given by (Will, 1998)

$$E^2 = p^2c^2 + m_g^2c^4, \tag{9.2}$$

i.e. the case of $\alpha = 0$ and $\sqrt{A_0} = m_gc^2 > 0$. The effect of this dispersion is to introduce a dephasing of the entire signal in the frequency domain compared with the GR prediction. This dephasing may be given by (Will, 1998)

$$\delta\psi(f) = \frac{\pi c D_0}{\lambda_g^2 f}, \tag{9.3}$$

where $\lambda_g = h/(m_gc)$ is the Compton wavelength of the graviton and D_0 is a distance measure given as (Mirshekari et al., 2012)

$$D_0 = \frac{1+z}{H_0}\int_0^z \frac{dz'}{(1+z')^2\sqrt{\Omega_M(1+z')^3 + \Omega_\Lambda}}, \tag{9.4}$$

where z is the redshift of the binary, $H_0 = 67.9\mathrm{km\,s^{-1}Mpc^{-1}}$ is the Hubble constant, $\Omega_M = 0.3065$ is the matter contribution to universal density, and $\Omega_\Lambda = 0.6935$ is the dark energy contribution to universal density. We have here used the TT+lowP+lensing+ext results from Ade et al. (2016) for the values given above.

As we have noted, the LVK have conducted investigations into potential deviations from GR through each of the observing runs. Examination of the high significance BBH detections through O3 allowed placed a bound on the upper limit of the mass of the graviton by constraining the existence of the dispersive effects discussed above. At 90% credibility, this investigation yielded a constraint of

$m_g \leq 1.27{\times}10^{-23}\text{eV}/c^2$ (Abbott et al., 2021e). This was further improved to $m_g \leq 9.6{\times}10^{-24}\text{eV}/c^2$ by Payne et al. (2023) in which simultaneous modelling of the astrophysical population of compact binaries was performed.

Figure 9.1 shows an illustration of the effect that a massive graviton would have on a waveform as compared with the standard GR waveform produced for the same parameters. The mass of the graviton chosen is larger than the constraints discussed above to make the effect obvious. The waveforms as shown are aligned at 20Hz.

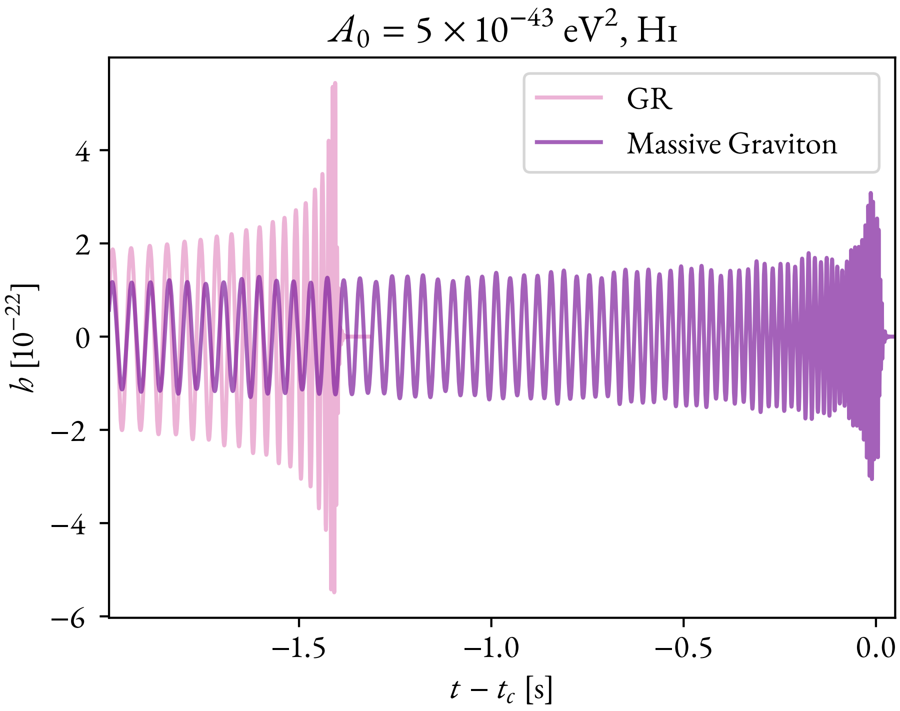

Figure 9.1: Comparison between a standard GR waveform and the same waveform produced under the assumption of a graviton with mass $m_g \simeq 7.07 \times 10^{22}\text{eV}/c^2$ corresponding to $A_0 = 5 \times 10^{-43}$. These waveforms are aligned at 20Hz and are shown from the perspective of the LIGO Hanford detector.

9.1.2 Modifications to Energy Flux and QNM Spectrum

Alternative theories of gravitation often lead to differences in all of the GW energy and angular and linear momenta fluxes as well as the binary's binding energy and the QNM spectrum of the final black hole. However, as discussed above, in these investigations we will consider only the case of isolated modifications to GR without consideration of specific theories of gravity. In particular, we will separately consider modifications to the energy flux and the QNM spectrum. In both of these modifications, we have set the mass and spin of the resulting final black hole used to obtain the QNM frequencies iteratively. This means that they will satisfy the balance of energy and angular momentum since the carriage of both away from the system by the GW are modified compared with the GR case.

We will begin our discussion with that of the modification to energy and angular momentum fluxes. We, here, follow the lead of Ghosh et al. (2016, 2017) and Johnson-McDaniel et al. (2022) in their construction. In these cases, it was applied to an older non-spinning which was here generalised to the more modern TEOBResumS-v3-GIOTTO model. Specifically, we modify the energy flux by multiplying those waveform modes which enter at the second post-Newtonian (2PN) order by a factor of $a_2^{1/2}$, so their contribution to the energy and angular momentum fluxes is multiplied by a factor of a_2. This will result in the modifications to the GW phasing at all of the post-Newtonian orders including and higher than 2PN. This modification is similar to that which one expects in some of the non-GR theories—for instance dynamical Chern-Simons theory in which the GW phasing differs from GR at 2PN Yagi et al. (2012).

The modes that first enter at 2PN are the $(3, \pm 2)$, $(4, \pm 4)$, and the $(4, \pm 2)$ modes. Of these, we only modify the former two as these the ones that first enter the energy flux specifically at 2PN and have a robust merger-ringdown model in TEOBResumS-v3-GIOTTO. The omitted modes have a significantly smaller contribution than that from the include modes—specifically only $\approx 5 \times 10^{-4}$ of the total Newtonian energy flux comes from this set of modes.

We consider both the cases where the (3 ± 2) and (4 ± 4) modes of the GW signal are multiplied by $a_2^{1/2}$ and the case where they are not—which corresponds to the case where the additional energy and angular momentum is radiated in a field that does not couple to the GW detectors—which will be referred to as with and without waveform scaling respectively. The latter case is considered in order to investigate larger deviations in the PN coefficients—resulting in larger differences in the length of the waveform from a given frequency and in the final mass and spin since these larger deviations were found to be necessary to obtain a detectable GR deviation in earlier studies which merely analysed the dominant modes—without having the significantly non-GR waveform features caused by significantly increasing the amplitude of the HOMs.

Figure 9.2 shows an illustration of the effect that modifications to the energy flux will cause to the waveform in both the cases of waveform scaling and no waveform scaling—corresponding to the top and bottom figures respectively—compared with the standard GR waveform produced for the same parameters. The modifications to the energy flux depicted are both the largest deviations considered within this chapter to make the effect as obvious as possible. The waveforms depicted are aligned at 20Hz as in Figure 9.1.

To proxy the complete modification to the QNM spectrum that one may expect in alternative theories of gravitation, we modify the QNM spectrum from the standard Kerr spectrum to that of Kerr-Newman. This modification includes a charge parameter in addition to the mass and spin parameters used in Kerr. To make this modification, we begin from the results for the $(2, 2, 0)$ and $(3, 3, 0)$ QNMs computed in Dias et al. (2022b), where the (ℓ, m, n) notation also includes the overtone index, n, in addition to the ℓ and m multipolar indices. We also note that Dias et al. (2022a) computed additional QNMs; however, these were unavailable when these waveforms were initially constructed and thus have not been used.

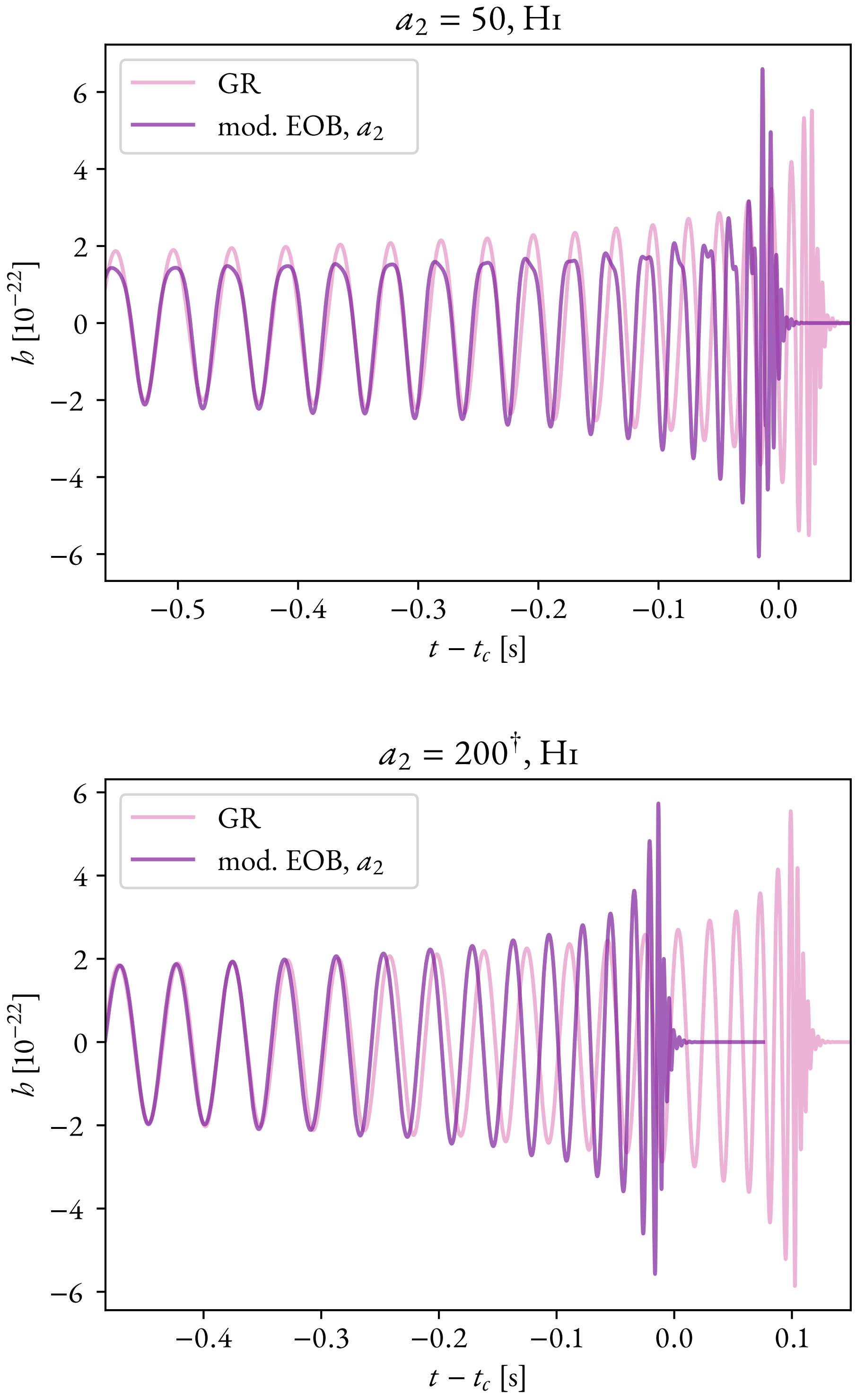

Figure 9.2: Comparison between a standard GR waveform and the same waveform produced under the assumption of modifications to the energy flux both with (top) and without (bottom) waveform scaling. The two waveforms on each plot are aligned at 20Hz and are shown from the perspective of the LIGO Hanford detector.

Instead, for computing the necessary additional QNMs needed for the TEOBResumS-v3-GIOTTO ringdown model—specifically the $n = 0, 1$ QNMs for each included mode—we began from the eikonal approximation for the complex frequencies—valid for large ℓ—using specifically the version from Yang et al. (2012) and Li et al. (2021):

$$\omega^{\text{eik}}_{\ell mn} = \left(\ell + \frac{1}{2}\right)\omega_{\text{orb}} + m\omega_{\text{prec}} - i\left(n + \frac{1}{2}\right)\gamma_L, \tag{9.5}$$

where ω_{orb} and ω_{prec} are frequencies which correspond to the spherical photon orbit and γ_L is the Lyapunov exponent of the orbit. These are all taken to be free parameters, so we will refer to the final results as a *tuned eikonal* expression. The frequency parameters are determined using the real parts of the $(2, 2, 0)$ and $(3, 3, 0)$ QNMs as

$$\begin{aligned} \omega_{\text{orb}} &= 6\omega^{\text{Re}}_{220} - 4\omega^{\text{Re}}_{330} \\ \omega_{\text{prec}} &= -7\omega^{\text{Re}}_{220} + 5\omega^{\text{Re}}_{330}. \end{aligned} \tag{9.6}$$

This expression may be applied to obtain the real parts for the $(4, 4, 0)$ and $(5, 5, 0)$ QNMs where it will give good accuracy for Kerr, particularly at larger spins. To make the modification to Kerr-Newman, these expressions are computed for both regimes and this is used to scale the Kerr QNM frequencies in the TEOBResumS-v3-GIOTTO model so that in the limit of zero charge, this reduces to the Kerr expressions.

For the $(2, 1, 0)$ and $(3, 2, 0)$ QNMs, however, we found that the tuned eikonal expression was less accurate than the following expression

$$\omega^{\text{Re, spinning}}_{\ell,\ell-1,0} \approxeq \omega^{\text{Re, non-spinning}}_{\ell\ell 0} + \frac{\ell - 1}{\ell}\left(\omega^{\text{Re, spinning}}_{\ell\ell 0} - \omega^{\text{Re, non-spinning}}_{\ell\ell 0}\right). \tag{9.7}$$

This expression may be obtained by noting that the difference between QNM frequencies for the m modes is due to spin and so one may use the scaling of the frequency with m from the eikonal expression—which is the same as that for the linear-in-spin corrections (see e.g. Pani et al. (2013) for further detail). This expression is therefore referred to as a *spin expansion-like* expression. To make the modifications for these modes, again, we follow the ratio computation as above.

For the imaginary components of each of the modes, we take $\gamma_L/2$ to be given by the $(2, 2, 0)$ inverse damping time for the $\ell = 2$ modes and by the $(3, 3, 0)$ inverse damping time for all other modes. For the values of the final spins and charges that are considered within this chapter, the difference between the values of γ_L inferred from either set is minimal ($\sim 3\%$). We then scale the Kerr values of the damping times used in TEOBResumS-v3-GIOTTO by the ratio of the Kerr-Newman and Kerr values of γ_L.

Figure 9.3 shows the comparison between a waveform produced using standard GR with the Kerr QNM spectrum and our modifications to using the Kerr-Newman QNMs calculated using the above method. These waveforms are aligned at 20Hz and shown from the perspective of the LIGO Hanford detector as done for the other comparisons within this section; however, the plot has been zoomed

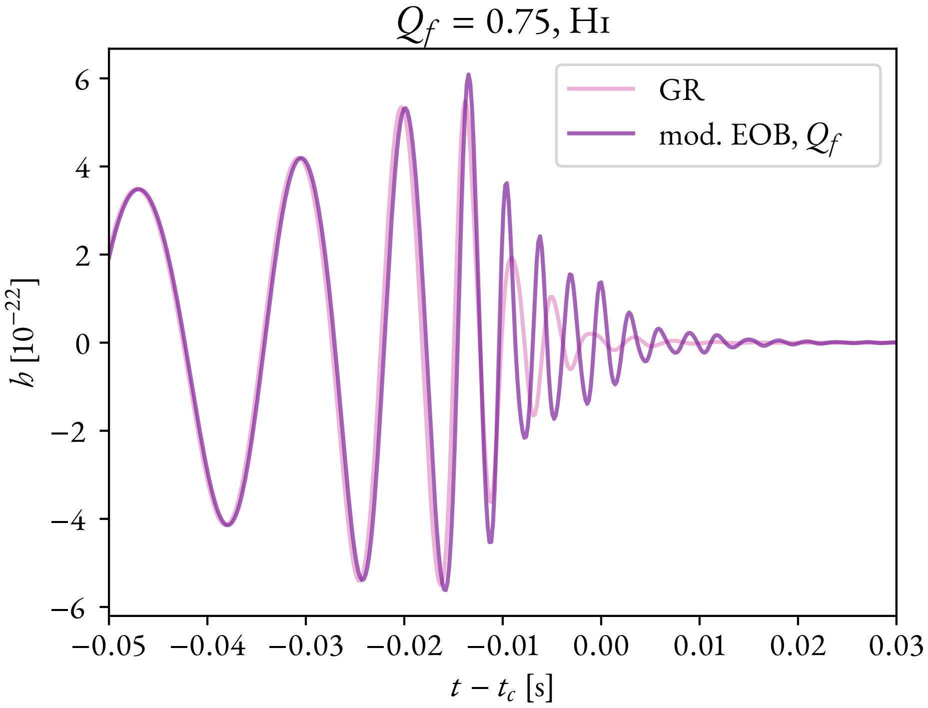

Figure 9.3: Comparison between a standard GR waveform and the same waveform produced under the assumption of a modification to the QNM spectrum from that of Kerr to that of Kerr-Newman with a dimensionless charge of 0.75. The two waveforms are aligned at 20Hz but the plot zooms in on the merger and ringdown to show the differences between the waveforms. The waveforms are shown from the perspective of the LIGO Hanford detector.

in to focus on the merger and ringdown to show the effects of the modification. Once again, the modification shown is the largest considered within this chapter so the effect is at its most visible.

In Johnson-McDaniel et al. (2022), it was shown that a number of the standard tests of GR that are deployed by the LVK—such as those in Abbott et al. (2021e)—are able to detect sufficiently large modifications to the energy flux. Similarly, a number of tests in Abbott et al. (2021e) are sensitive to modifications to the QNM spectrum such as the dedicated ringdown analyses. The current lack of evidence for deviations from GR found by these analyses, however, do not straightforwardly place constraints on possible values of a_2 or on the charge of the final black holes considered in these waveforms.

9.1.3 Addition of a Scalar Mode of Polarisation

We here consider the addition of a scalar mode of polarisation to a standard GW waveform. In any actual theory of gravitation that would result in radiation in additional polarisations, we would expect that this would lead to a different tensorial waveform than in GR given, for instance, the change in phasing resulting from the extra energy radiated in these additional modes. However, in the investigations within this chapter, we leave the tensor modes unchanged to isolate purely the effects of the additional polarisation.

To create these waveforms, we will use the leading tensor-scalar waveform results from Bernard et al. (2022) to scale the tensor polarisations, specialising to the case where the sensitivities of the two objects are equal, i.e. the $\mathcal{S}_- = 0$ case in Bernard et al. (2022), which yields no dipole radiation which is consistent with the tensor polarisation modes that we have used which also contain no dipole radiation. In this case, the amplitude of the scalar waveform depends on the following combination of scalar-tensor theory parameters

$$a_{\text{scalar}} = \frac{\sqrt{\alpha}\zeta\mathcal{S}_+}{1-\zeta}, \tag{9.8}$$

where the parameters in this expression are defined in full in Table I of Bernard et al. (2022). Considering only the leading order, we may use Equation 9.8 to write the scalar waveform modes to be written in terms of their tensor waveform counterparts. Absorbing all of the constant quantities into $\bar{a}_{\text{scalar}}$, this relation is given by

$$h^s_{\ell m} = \begin{cases} -\bar{a}_{\text{scalar}}\sqrt{\frac{\ell(\ell-1)}{(\ell+1)(\ell+2)}}h_{\ell m} & \text{for } \ell+m \text{ even,} \\ 0 & \text{otherwise.} \end{cases} \tag{9.9}$$

This leads to the overall contribution to the detector strain from the scalar modes being given by

$$h^{\text{scalar}} = F_S \sum_{\ell,m} h^s_{\ell m}\,{}^0Y_{\ell m}(\iota,\phi_0), \tag{9.10}$$

where $F_S = -\frac{1}{2}\sin^2\theta\cos 2\phi$ is the antenna response pattern for the scalar breathing mode—see e.g. Will (2014) and noting that θ and ϕ are the spherical co-ordinates of the source in the detector frame), and ${}^0Y_{\ell m}$ are the standard zero spin spherical harmonics where ι and ϕ_0 are the binary inclination and phase at the time of coalescence respectively. The calculation of the antenna response pattern in this chapter will be done by using the implementation within the PyCBC software package (Nitz et al., 2023).

The value of the quantity, $\bar{a}_{\text{scalar}}$ is set in terms of the relative amplitude of the $(2,\pm2)$ scalarial and tensorial mode contributions to the response of the detector with the largest SNR for the tensor signal—which in this case is the LIGO Hanford detector—which means we must therefore include the spherical harmonics and detector antenna pattern. Specifically, we will fix the amplitude ratio given by

$$\mathcal{A} = \frac{\bar{a}_{\text{scalar}}}{\sqrt{6}}\frac{|F_S|}{\sqrt{F_+^2+F_\times^2}}\frac{2\cdot{}^0Y_{22}(\iota,0)}{{}^{-2}Y_{2,2}(\iota,0)+{}^{-2}Y_{2,-2}(\iota,0)}, \tag{9.11}$$

where F_+ and $F_\times$ are the antenna response patterns for the plus and cross tensorial polarisations respectively and ${}^{-2}Y_{2,\pm2}$ are the $(2,\pm2)$ spin-(-2) weighted spherical harmonics.

We will still apply this scaling to only the modes where $\ell+m$ is even in the intertial frame even for the precessing systems that we consider here. This is a simplification of the behaviour one would expect in a precessing system, where in actuality all of the scalar modes in the inertial frame for such a system would be non-zero due to the precession. However, only the even $\ell + m$ modes would be non-zero in the coprecessing frame. This simplification was made in keeping with the philosophy of the work in this chapter of considering relatively simple modifications to GR to investigate their effects on the lensing investigations whilst retaining some physical motivation.

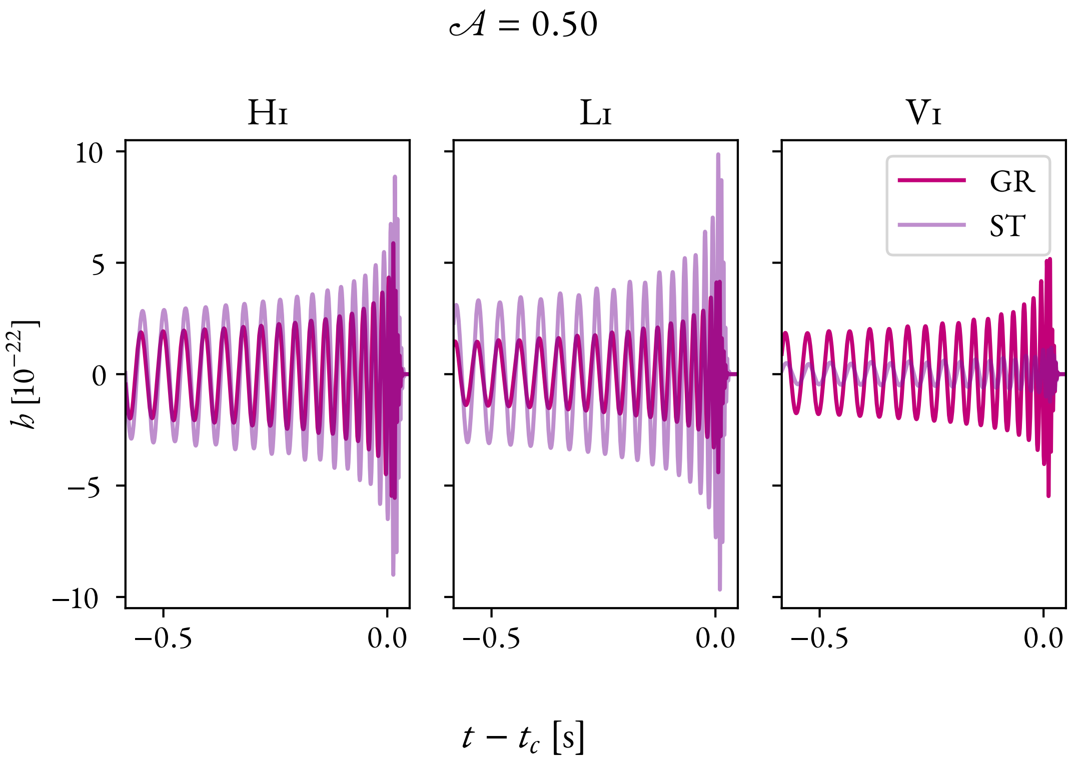

Figure 9.4: Illustration of comparisons between a standard GR waveform and the same waveform produced with an additional scalar mode of polarisation with fixed amplitude ratio, $\mathcal{A} = 0.5$. These waveforms are aligned at 20Hz and are shown from the perspectives of each of the three currently operational GW detectors.

An example of the resultant waveform from the addition of the scalar polarisation in shown in Figure 9.4 shown from the perspective of each of the detectors and aligned at 20Hz. This, as has been the case with the other such illustrations, is that of the largest deviation considered within this chapter to result in the most visible distortions to the waveforms.

Similarly to the previous discussion, searches by the LVK have been performed for additional modes of polarisations. As of Abbott et al. (2021e) there has been no support for these additional modes. However, this has not been translated into specific constraints on scalar-tensor waveforms as depicted here.

9.1.4 Black Hole Mimickers

The final deviations from GR that we will discuss here are waveforms from black hole mimickers such as exotic objects permitted by alternative theories of gravitation that for instance provide additional fields that are not present in standard GR. Examples of these objects include—but are not limited to—boson stars (Liebling & Palenzuela, 2023) or more general dark matter stars (Giudice et al., 2016). Black hole mimickers may also be caused by more exotic non-GR phenomena such as firewalls (Almheiri et al., 2013) or gravastars (Mazur & Mottola, 2004). A more complete review of potential sources of black hole mimickers may be found in Cardoso & Pani (2019).

To investigate the response of searches for lensing to these waveforms, it would be ideal to conduct testing on modelled waveforms from these individual phenomena. Unfortunately, even for the best modelled of the above examples, boson stars—see Siemonsen & East (2023) for some of the most recent efforts—modelling has yet to reach the level of sophistication as simulations used to provide waveforms for BBHs, BNSs, or NSBHs. To proxy these, we will instead consider BNS waveforms which are scaled to BBH-like masses. This approach has been previously taken in Johnson-McDaniel et al. (2020) and is justified in that waveforms from such objects are expected to have both the effects of non-zero tidal deformability (Cardoso et al., 2017), as well as non-Kerr spin-induced multipole moments (Uchikata et al., 2016; Adam et al., 2022) in the inspiral. Finally, they may also have a post-merger signal that differs from the standard GR black hole ringdown (Siemonsen & East, 2023).

We will, specifically, consider two particular waveforms, which are both from the CoRe catalogue (Dietrich et al., 2018b; Gonzalez et al., 2023) and will include all of the spherical harmonic modes through $\ell = 4$:

BHM-P The numerical relativity simulation of a precessing BNS with masses of $1.35M_\odot$ and $1.11M_\odot$ and dimensionless spin vectors of $(-0.077, -0.077, -0.077)$ and $(-0.090, -0.090, -0.90)$ at a dimensionless frequency of $GMf/c^3 = 4.76 \times 10^{-3}$ from (Dietrich et al., 2018a, CoRe ID BAM:0110). This simulation used the SLy (Douchin & Haensel, 2001) equation of state for neutron stars. These stars have dimensionless dtidal deformabilites of 392 and 1291 resulting in an effective tidal deformability, $\tilde{\Lambda}$ (Wade et al., 2014), of 724.

BHM-NS The numerical relativity simulation of a non-spinning BNS from Ujevic et al. (2022) with masses of $1.72M_\odot$ and $0.98M_\odot$ (CoRe ID BAM:0131). This simulation also uses the SLy equation of state giving the stars dimensionless tidal deformabilities of 66 and 2569 respectively yielding an effective tidal deformability of 509. This case was chosen given that it has a more BBH-like post-merger signal than the precessing case. This is illustrated in Figure 9.5.

Examples of scaled versions of both of these waveforms are illustrated in Figure 9.5 and compared with BBH waveforms with similar parameters aligned at 20Hz and shown form the perspective of the Hanford detector as with the other figures in this section.

One of the approaches used to look for exotic objects in CBCs such as those described at the start of this section is to search for so-called *echoes*. These are repeated signals due to the signal reflecting multiple times off radial potential barriers. As of Abbott et al. (2021e), no such echoes have been found,

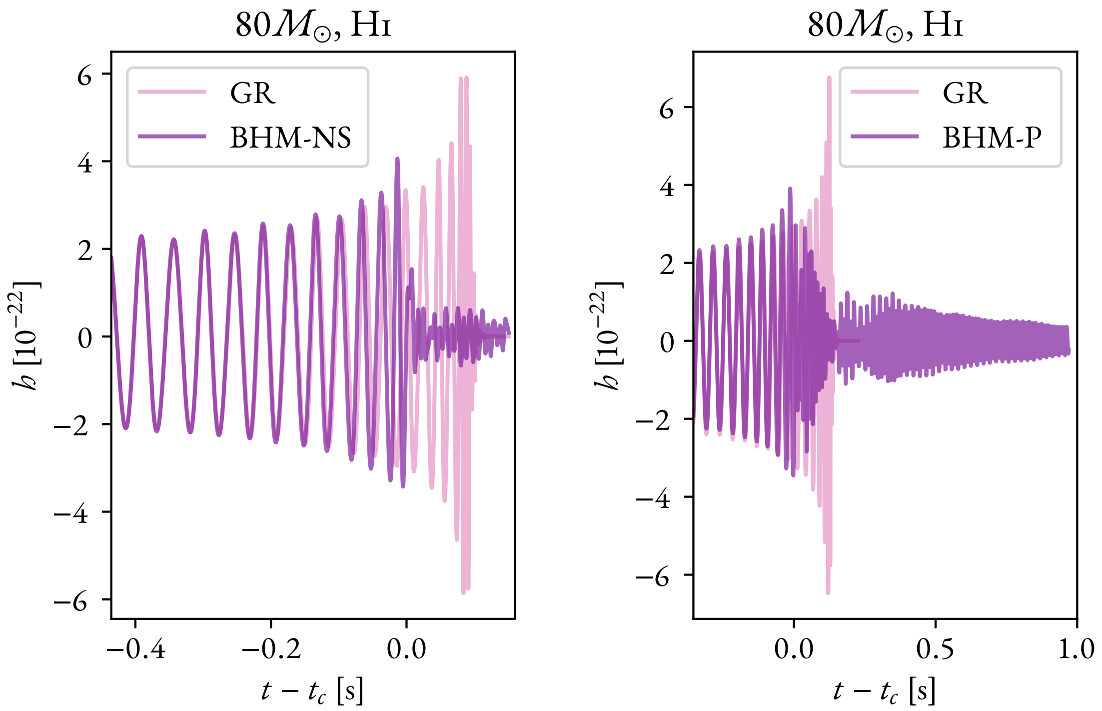

Figure 9.5: Comparisons between the two BNS waveforms scaled to a total mass of $80M_\odot$ discussed above and BBH waveforms with similar parameters. These waveforms are aligned at 20Hz and shown from the perspective of the Hanford detector.

though we note that echoes will only be present for a subset of possible black hole mimickers, so objects such as mergers of binary boson stars or the scaled BNS waveforms discussed here will not produce such echoes and their existence could not be ruled out by such an investigation.

Additional investigatory methods have been employed for specific object types for specific GW signals, however. For instance, GW190521—a high mass event (Abbott et al., 2020b)—was investigated using waveforms for head-on Proca star collisions and found a slight preference for such waveforms compared with the BBH waveforms (Calderón Bustillo et al., 2021). Such investigations were expanded to other high-mass events in Calderón Bustillo et al. (2023) but did not find these waveforms favoured for any firm detection.

9.2 Investigation Setup

To investigate how each of the deviations from either GR or the BBH hypothesis discussed in the previous section would impact the searches for microlensing and millilensing, a series of simulated signals using as its basis GW150914-like parameters (Abbott et al., 2016a)—which are detailed in Table 9.1 was constructed for each deviation spanning the parameter space of the deviation in question as follows:

Source Parameter	Value
Total mass, $M_{\text{tot}}(M_\odot)$	72
Mass ratio, q	0.8
Luminosity distance, $d_L(\text{MPc})$	452
Inclination, ι	1.59
Right ascension, α	1.68
Declination, δ	-1.27
Polarisation angle, ψ	3.93
Coalescence time, $t_c(s)$	1126259462
Primary dimensionless spin vector, χ_1	$(-0.1, -0.1, -0.1)$
Secondary dimensionless spin vector, χ_2	$(-0.1, 0.0, 0.1)$

Table 9.1: GW150914-like parameters used as the basis for the generation of non-GR waveforms.

Massive Graviton	Twenty logarithmically space values of A_0 from $5\times10^{-45}\text{eV}^2$ to $5\times10^{-43}\text{eV}^2$ which corresponds to a graviton mass range of $m_g \simeq 7.07\times10^{-23}\text{eV}^2/\text{c}^2$ to $m_g \simeq 7.07\times10^{-22}\text{eV}^2/\text{c}^2$ respectively.
Modified Energy Flux	The following values of a_2 with waveform scaling: $2, 5, 10, 20$, and 50. The following values of a_2 without waveform scaling: $20, 50, 75, 100, 125, 150, 175$, and 200.
Modified QNM Spectrum	Values of the final dimensionless charge, Q_f, from 0.50 to 0.75 in steps of 0.05.
Additional Scalar Polarisation	Values of the fixed amplitude ratio, $\mathcal{A}$, from 0.05 to 0.50 in steps of 0.05.
BHM-P	Scaling the total mass from $90M_\odot$ to $150M_\odot$ in steps of $10M_\odot$.
BHM-NS	Scaling the total mass from $80M_\odot$ to $160M_\odot$ in steps of $10M_\odot$.

The choices for the non-GR parameter space were made to reflect cases where one expects the deviations from GR to be easily detectable by at least some of the analyses searching for deviations as well as some cases which will be less easily detectable. In particular, it must be noted that the values for the graviton mass are significantly above the constraints sets by the LVK since these constraints are the result of combining the analysis of multiple events whereas we will here only be analysing single events. For the black hole mimicker cases, the lower bound on the total mass was chosen to ensure sufficient higher mode content is within the LVK detectable band (i.e. from 20Hz)—with the choice here ensuring that the $|m| \leq 3$ modes are within band whilst the upper bound was chosen to retain a sufficient number of inspiral cycles in band for the analysis.

Each simulated signal was then subjected to the Gravelamps microlensing and millilensing analyses, as discussed in Chapters 6 and 7. These analyses were conducted with the dynesty (Speagle, 2020) nested sampler using the IMRPhenomXPHM (Pratten et al., 2021) waveform model for precessing

BBHs implemented within LALSuite (LIGO Scientific Collaboration et al., 2018). IMRPhenomXPHM includes the same HOMs as the TEOBResumS-v3-GIOTTO model aside from the $(5, \pm 5)$ modes.

The resultant frames from the generation process described in Section 9.1 were made without noise and were analysed under the assumption of the predicted noise curves for the current LIGO-Virgo detector network during O4, using specifically the noise curve for LIGO with a 190Mpc horizon (Abbott et al., 2020a). This yielded SNRs for the individual injections between 21.81 and 65.88 which is high enough for obvious detection with the used sensitivities. The configuration of the analyses was chosen to conform to those deployed in Abbott et al. (2023d) and Janquart et al. (2023b)—i.e. reflective of actual lensing investigations.

9.2.1 General Relativity Baseline

Prior to the investigation of the non-GR waveforms, we will first examine an investigation of a standard GR waveform constructed using the GW150914-like parameters outlined in Table 9.1 in order to set a baseline from which the non-GR waveforms may be compared. The results of this investigation will be briefly summarised here, but the more detailed interpretations of results will be given in the following section with the results from the testing set.

Microlensing Investigation *(Isolated Point Mass)*	This investigation yielded a $\log_{10} \mathcal{B}^{\mathrm{PM}}_{\mathrm{U}}$ of -2.5, i.e. giving support for the unlensed hypothesis. Under the strategy for the deployment of such a search in O4 outlined in Section 7.6 such a result would preclude further analysis.
Microlensing Investigation *(SIS)*	This investigation was more closely aligned with the unlensed case yielding a $\log_{10} \mathcal{B}^{\mathrm{SIS}}_{\mathrm{U}}$ of 0.0, i.e. indistinguishability. An examination of the resultant posteriors for this case mirroring such investigations done in Chapter 7 revealed that the lens mass posterior reflects the prior, and the dimensionless source position is entirely above the $y = 1$ caustic, which mirrors the expectations for an unlensed event.
Millilensing Investigation	This investigation did not find any support for additional millisignals in the posteriors nor in terms of the Bayes factor support with a $\log_{10} \mathcal{B}^{\mathrm{MiL}}_{\mathrm{U}}$ of -0.4.

It can thus be seen that the overall conclusion of these investigations would be that the event does not by itself lend support to the microlensing or millilensing hypotheses. One would, therefore, expect that any suggestion of false positivity from investigations into the non-GR waveforms based upon this baseline would be as a result of the deviation from GR rather than the source parameter combination or the effect of waveform systematics.

9.3 Investigation of non-GR Signals

9.3.1 Isolated Point Mass

Table 9.2: Results of performing isolated point mass microlensing analysis using Gravelamps on the simulated modified GR events. Highlighted cells indicate the cases that breach the $\log_{10}\mathcal{B}^{\mathrm{PM}}_{\mathrm{U}}$ threshold that would flag these events for further investigation as microlensing candidates. As can be seen, the modified energy flux cases with no waveform scaling, the modified QNM spectrum cases, and those cases with an additional scalar mode of polarisation all display no examples where false positives are identified. In all other cases, in at least one investigation a false positive is identified.

Massive Graviton		Modified Energy Flux		Modified QNM Spectrum		BHM-P	
$A_0(\mathrm{eV}^2)$	$\log_{10}\mathcal{B}^{\mathrm{PM}}_{\mathrm{U}}$	a_2	$\log_{10}\mathcal{B}^{\mathrm{PM}}_{\mathrm{U}}$	Q_f	$\log_{10}\mathcal{B}^{\mathrm{PM}}_{\mathrm{U}}$	$M_{\mathrm{tot}}(M_\odot)$	$\log_{10}\mathcal{B}^{\mathrm{PM}}_{\mathrm{U}}$
5.00×10^{-45}	-2.3	2	-2.4	0.50	-2.4	80	15.1
6.37×10^{-45}	-2.0	5	-2.2	0.55	-2.4	90	18.8
8.11×10^{-45}	-2.1	10	-1.6	0.60	-2.3	100	26.8
1.03×10^{-44}	-2.3	20	0.9	0.65	-2.3	110	31.2
1.32×10^{-44}	-2.4	50	8.6	0.70	-2.0	120	24.3
1.68×10^{-44}	-2.3	20†	-2.4	0.75	-2.1	130	41.2
2.14×10^{-44}	-2.3	50†	-2.2			140	47.4
2.73×10^{-44}	-2.2	75†	-2.1			150	34.3
3.48×10^{-44}	-2.3	100†	-2.2	Scalar Polarisation		BHM-NS	
4.43×10^{-44}	-2.2	125†	-2.3	$\mathcal{A}$	$\log_{10}\mathcal{B}^{\mathrm{PM}}_{\mathrm{U}}$	$M_{\mathrm{tot}}(M_\odot)$	$\log_{10}\mathcal{B}^{\mathrm{PM}}_{\mathrm{U}}$
5.64×10^{-44}	-2.2	150†	-2.2	0.05	-2.6	80	-0.7
7.19×10^{-44}	-2.0	175†	-2.1	0.10	-2.5	90	0.1
9.16×10^{-44}	-2.2	200†	-1.8	0.15	-2.7	100	1.3
1.17×10^{-43}	-2.2			0.20	-2.4	110	3.2
1.49×10^{-43}	-0.5			0.25	-2.6	120	5.9
1.90×10^{-43}	9.6			0.30	-3.1	130	7.3
2.42×10^{-43}	27.3			0.35	-3.0	140	7.4
3.08×10^{-43}	28.1			0.40	-3.1	150	9.2
3.92×10^{-43}	15.6			0.45	-3.2	160	11.3
5.00×10^{-43}	24.6			0.50	-3.1		

Note— Cells denoted with a †are the no waveform scaling cases.

Table 9.2 provides the complete results for the isolated point mass investigation, with the highlighted cells indicating those with a Bayes factor comparing the isolated point mass and unlensed hypotheses, $\mathcal{B}^{\mathrm{PM}}_{\mathrm{U}}$, indicating sufficiently high support for the microlensing hypothesis that they would be flagged for additional follow-up investigations in the manner of Janquart et al. (2023b) that were discussed in more detail in Chapter 7. This threshold has been placed at $\mathcal{B}^{\mathrm{PM}}_{\mathrm{U}} > 1.0$ which is based upon the background microlensing analysis that was done in Abbott et al. (2021f). The errors on the Bayes factors are expected to be of $O(0.1)$ in both this and the subsequent analyses.

As may be seen within the table, the modifications to QNM spectrum, the additional of a scalar mode of polarisation and the non-waveform-scaling modifications to the energy flux do not yield any scenarios in the space tested in which a false positive for the isolated point mass microlensing model is obtained. The remaining cases, however, do demonstrate in at least one scenario in which not only is a false preference for the microlensing model obtained but that false preference is strong—particularly in the cases of the highest graviton masses tested and the BHM-P set in which *all* of the investigations yield this preference.

The BHM-P investigations yield two additional points of note. The first is that the prior on the luminosity distance needed to be extended from an upper limit of 2Gpc to an upper limit of 5Gpc in order to ensure full enclosure of the posterior reflecting the relatively low values of y supported—as shown in Figure 9.6. The constraint in these injections seen at higher masses is typical of microlensing candidates; however, at the lower mass injections, multimodal behaviour is seen in the posteriors which is not expected of true candidates and would raise additional concerns about the veracity of these investigations as candidates.

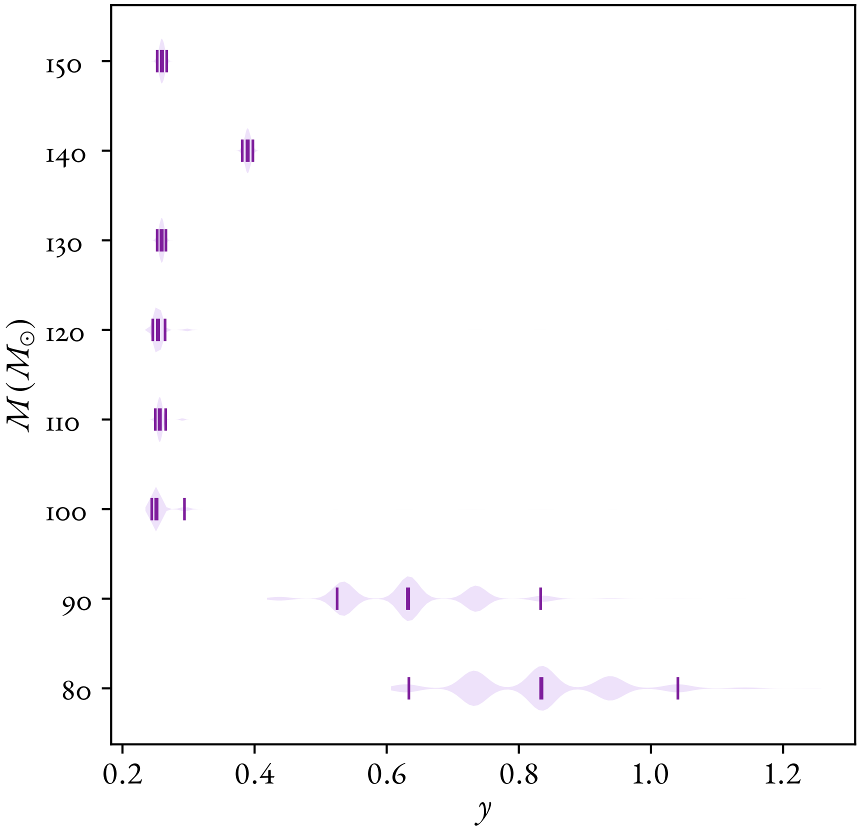

Figure 9.6: Posteriors on the dimensionless source position recovered from the investigation of the precessing black hole injection set. The vertical lines indicate the median and the boundaries of the 90% confidence interval. As may be seen, there is constraint towards low values of the source position in the majority of cases which reflects the apparent preference for high magnification. However, the multimodal behaviour at low mass is not expected for true microlensing candidates.

The second point of note in regards the BHM-P investigations is that investigation of the individual chains of the parameter estimation run revealed a weaker local maximum likelihood point in the parameter space. Chains that found this local maximum could remain stuck within it which would lead to significant intra-chain disagreement in the final results of the investigation. The combination of the chains given here reflects those with the highest preference from the investigation. This behaviour is seen in both the lensed and unlensed investigation of these injections.

One of the first stage checks in evaluating potential candidates for microlensing identified by the Bayes factor that may be performed—as was the case in the investigations in Chapter 7 from Janquart et al. (2023b)—is the checking of the lens parameter posteriors. True lensing candidates are obviously expected to have some constraint towards a particular value of the lensing parameters. In unlensed events, one may expect to see either uninformative posteriors or preference towards zero lens mass and high source position reflecting the parts of the lensing parameter space that yield the smallest distortions from the source waveform. Therefore, seeing constraint to particular values is a sign that further investigations would be required and that a signal may be identified as microlensed.

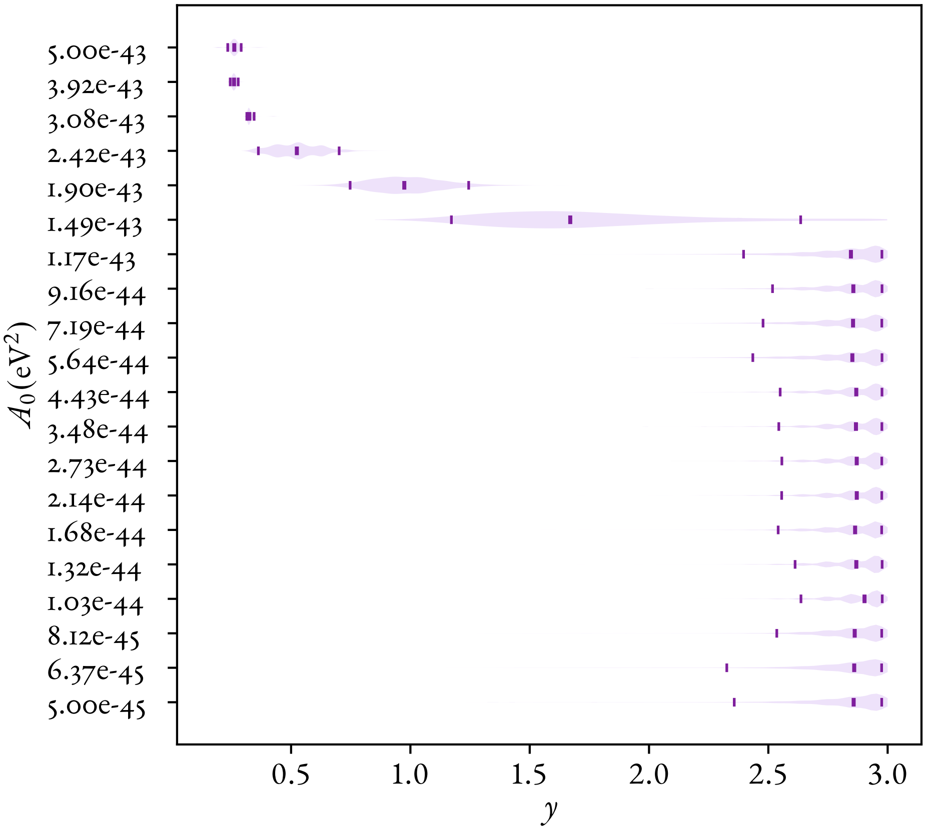

Figure 9.7: Posteriors on the dimensionless source position recovered from the massive graviton injection set. The vertical lines indicate the median and boundaries of the 90% confidence interval. As may be seen, those cases that result in preference for the unlensed case rail against the upper limit of the prior which is the expectation for unlensed events. However, the higher mass graviton cases that do yield support for the microlensing case display constraint towards progressively lower values of the source position, which would be the expectation for microlensing candidates.

Figure 9.7 demonstrates both of these possibilities. The lower mass graviton injections which favour the unlensed hypothesis rail against the upper limit of the prior space as is expected for unlensed events. However, beginning with the injection with $A_0 = 1.49 \times 10^{-43}$, constraint is displayed towards values within the posterior space, demonstrating a trend towards lower source position with higher mass. In the first such case, there is still sufficient support at higher source position to explain the preference for the unlensed hypothesis—though also noting why it is much reduced compared to the injections before it. Consequently the high mass graviton injections with their high Bayes factors and lens parameter constraint would be considered as sufficiently interesting to warrant additional investigations. However, it is worth noting that the lowest deviations that would lead to false positivity already correspond to a graviton mass scenario that is above the limits set by current analyses such as those from Abbott et al. (2021e).

The remaining investigations of the other injections sets were largely similar to that of the massive graviton investigation in terms of investigation of the posteriors, with the unlensed expectations reflected in those investigations that have no support for the microlensing hypothesis and constraint to specific values in those cases that do display support for the microlensing hypothesis. This significant constraint also reinforces the large values of Bayes factor shown in those cases. The BHM-NS results are similar to the BHM-P results in that these also in some of the cases display the same multimodal behaviour that is seen in the latter case. This is, again something that would shed some doubt on these cases given that this is outwith the expectations for a true microlensing candidate.

9.3.2 SIS

The follow-up analysis performed both in Chapter 7 and in Janquart et al. (2023b) on microlensing candidates was to investigate an additional microlensing mass density profile; specifically that of the SIS profile. In those investigations, it was noted that the one microlensing candidate investigated displayed increased support for the SIS model as compared with the isolated point mass model. However, the primary purpose of such a follow-up would be to gain information about the lensing object from an actual lensed event rather than to identify potential microlensing candidates. Nevertheless, we proceed with this analysis here in order to ascertain whether the false positive status shown in the point mass model is restricted to that model or would be preserved/increased by this additional model. We will also deploy this investigation on all of the injection sets rather than merely those that are considered interesting by the isolated point mass microlensing search to investigate if additional false positives could occur dependent upon model choice.

The results of this investigation showing the Bayes factor comparing the isolated point mass and SIS models are shown in Table 9.3. The cells highlighted in light pink are those that displayed a preference for the isolated point mass model over the unlensed model that retain that preference compared with the SIS model. Those highlighted in dark purple are those that again displayed preference the isolated point mass over the unlensed hypothesis which display a preference for the SIS model over the point mass model. This latter scenario represents a minority of the cases that display preference for the microlensing hypothesis—specifically the highest mass graviton cases as well as some of the BHM-NS cases. It is worth noting for the BHM-NS cases that the majority of all of this set are also compatible with being indistinguishable between the two models.

Table 9.3: Results of performing SIS microlensing analysis using Gravelamps on the simulated modified GR events. Cells highlighted in light pink are those that a $\log_{10}$ Bayes factor in favour of the point mass microlesning case that continue to prefer that model. The darker highlighted cells are those that display a preference for the SIS model.

Massive Graviton		Modified Energy Flux	
$A_0(\mathrm{eV}^2)$	$\log_{10}\mathcal{B}^{\mathrm{SIS}}_{\mathrm{PM}}$	a_2	$\log_{10}\mathcal{B}^{\mathrm{SIS}}_{\mathrm{PM}}$
5.00×10^{-45}	2.4	2	2.5
6.37×10^{-45}	2.2	5	2.3
8.11×10^{-45}	2.3	10	1.8
1.03×10^{-44}	2.3	20	−0.7
1.32×10^{-44}	2.4	50	−2.3
1.68×10^{-44}	2.4	$20^{\dagger}$	2.5
2.14×10^{-44}	2.3	$50^{\dagger}$	2.4
2.73×10^{-44}	2.4	$75^{\dagger}$	2.2
3.48×10^{-44}	2.4	$100^{\dagger}$	2.3
4.43×10^{-44}	2.4	$125^{\dagger}$	2.3
5.64×10^{-44}	2.3	$150^{\dagger}$	2.4
7.19×10^{-44}	2.2	$175^{\dagger}$	2.3
9.16×10^{-44}	2.3	$200^{\dagger}$	2.0
1.17×10^{-43}	2.3		
1.49×10^{-43}	0.9		
1.90×10^{-43}	−1.3		
2.42×10^{-43}	−3.8		
3.08×10^{-43}	−8.0		
3.92×10^{-43}	4.0		
5.00×10^{-43}	1.3		

Modified QNM Spectrum		BHM-P	
Q_f	$\log_{10}\mathcal{B}^{\mathrm{SIS}}_{\mathrm{PM}}$	$M_{\mathrm{tot}}(M_\odot)$	$\log_{10}\mathcal{B}^{\mathrm{SIS}}_{\mathrm{PM}}$
0.50	2.5	80	−14.3
0.55	2.6	90	−1.3
0.60	2.4	100	−0.8
0.65	2.4	110	−4.3
0.70	2.2	120	−1.2
0.75	2.1	130	−7.6
		140	−85.8
		150	−5.4

Scalar Polarisation		BHM-NS	
$\mathcal{A}$	$\log_{10}\mathcal{B}^{\mathrm{SIS}}_{\mathrm{PM}}$	$M(M_\odot)$	$\log_{10}\mathcal{B}^{\mathrm{SIS}}_{\mathrm{PM}}$
0.05	2.7	80	−0.1
0.10	2.8	90	0.0
0.15	3.0	100	0.7
0.20	2.6	110	−0.3
0.25	2.8	120	0.2
0.30	3.4	130	0.2
0.35	3.3	140	0.2
0.40	3.1	150	−0.9
0.45	3.4	160	−0.2
0.50	3.1		

Note— Cells denoted with a †are the no waveform scaling cases.

In all but one case—that of the $140M_\odot$ BHM-P waveform—the support for the SIS microlensing hypothesis despite being lower than that for the isolated point mass microlensing hypothesis would still be above the support for the unlensed hypothesis—though it should be noted that the $80M_\odot$ BHM-P result would be just below the $\mathcal{B}^{\mathrm{L}}_{\mathrm{U}}$ threshold of interest. Examining the $140M_\odot$ BHM-P case further, the source parameter posterior estimates do not reflect the primary or secondary likelihood maxima found in the point mass and unlensed analyses and are instead between the source parameter values corresponding to these maxima which may have resulted in the substantially weaker support for this model. Similarly to the point mass case, the BHM-P investigations required extending the luminosity distance prior to 5Gpc.

As before, one may investigate candidates of interest by looking at the posteriors of the lensing parameters. In this case, there is a slight difference in the expectations for unlensed events as compared with the isolated point mass case. In the SIS model, one expects support to spread out across the $y > 1$ space given that in the geometric optics approximation, i.e. high lens mass, the amplification factor in this range is flat, yielding a resulting waveform similar to the unlensed case—an example of posteriors showing this behaviour is shown within Figure 9.8. This is also the most probable reason that support for the SIS is almost universally higher than that for the isolated point mass model in those events that would be discarded by the isolated point mass support and brings the SIS and unlensed searches into the regions of indistinguishability. This is also another reason to perform the isolated point mass microlensing search in order to identify candidates before performing analyses with additional models.

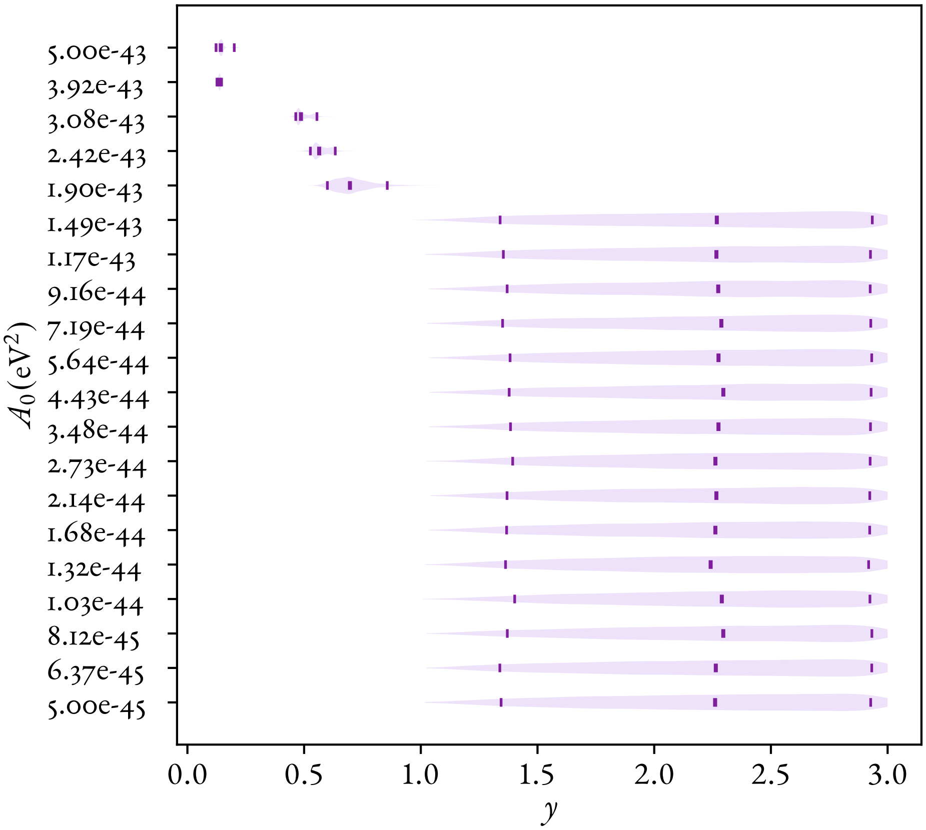

Figure 9.8: Posteriors on the dimensionless source position recovered from the massive graviton injection set when investigated with the SIS model. The vertical lines indicate the median and the boundaries of the 90% confidence interval. As may be seen, those cases that result in preference for the unlensed case display broad recoveries above the $y = 1$ threshold that results in a flat amplification factor across much of the mass space which is the expectation for unlensed events. However, again, the higher mass graviton cases that yield support for the microlensing hypothesis display constraint towards lower values of the source position which is the expectation for true microlensing candidates.

9.3.3 Millilensing

In addition to the secondary microlensing model, the investigations from Janquart et al. (2023b) and that were discussed in Chapter 7 investigated the potential for a microlensing candidate to be instead a millilensing candidate. As we have discussed in Chapter 5, in this scenario the lens is sufficiently large that the geometric optics applies but that the images are still separated in time such that they overlap resulting in beating patterns similar to microlensing. This analysis is performed using the phenomenological millelensing model introduced in Liu et al. (2023) and implemented within Gravelamps. In

Table 9.4: Results of performing the phenomenological millilensing analysis using the Gravelamps on the simulated modified GR events. Highlighted cells indicate those events that a $\log_{10}$ Bayes factor in favour of the millilensing case over the unlensed case. The colour of the highlighted cell indicates the number of millisignals favoured—dark blue corresponds to a single image, light blue to two, pink to three, and purple to four.

Massive Graviton		Modified Energy Flux		Modified QNM Spectrum		BHM-P	
$A_0(\mathrm{eV}^2)$	$\log_{10}\mathcal{B}^{\mathrm{MiL}}_{\mathrm{U}}$	a_2	$\log_{10}\mathcal{B}^{\mathrm{MiL}}_{\mathrm{U}}$	Q_f	$\log_{10}\mathcal{B}^{\mathrm{MiL}}_{\mathrm{U}}$	$M_{\mathrm{tot}}(M_\odot)$	$\log_{10}\mathcal{B}^{\mathrm{MiL}}_{\mathrm{U}}$
5.00×10^{-45}	−0.5	2	−0.5	0.50	−0.5	80	23.1
6.37×10^{-45}	−0.1	5	−0.3	0.55	−0.3	90	46.6
8.11×10^{-45}	−0.3	10	−0.4	0.60	−0.4	100	69.4
1.03×10^{-44}	−0.3	20	1.3	0.65	−0.3	110	72.1
1.32×10^{-44}	−0.1	50	22.5	0.70	0.1	120	28.5
1.68×10^{-44}	−0.4	20†	−0.3	0.75	−0.3	130	50.3
2.14×10^{-44}	−0.4	50†	−0.3			140	−4.9
2.73×10^{-44}	−0.3	75†	−0.4			150	60.2
3.48×10^{-44}	−0.3	100†	−0.5	Scalar Polarisation		BHM-NS	
4.43×10^{-44}	−0.4	125†	−0.6	$\mathcal{A}$	$\log_{10}\mathcal{B}^{\mathrm{MiL}}_{\mathrm{U}}$	$M(M_\odot)$	$\log_{10}\mathcal{B}^{\mathrm{MiL}}_{\mathrm{U}}$
5.64×10^{-44}	−0.1	150†	−0.3	0.05	−0.6	80	1.1
7.19×10^{-44}	−0.2	175†	−0.4	0.10	−0.1	90	1.0
9.16×10^{-44}	−0.3	200†	0.0	0.15	−0.1	100	4.1
1.17×10^{-43}	−0.3			0.20	1.3	110	9.8
1.49×10^{-43}	0.0			0.25	1.7	120	15.9
1.90×10^{-43}	11.6			0.30	−0.2	130	17.6
2.42×10^{-43}	32.0			0.35	−0.0	140	18.8
3.08×10^{-43}	39.7			0.40	−0.3	150	17.7
3.92×10^{-43}	74.7			0.45	−0.2	160	17.9
5.00×10^{-43}	76.6			0.50	−0.1		

Note— Cells denoted with a †are the no waveform scaling cases.

this analysis, we allow for up to four signals to be present within the overall signal. This is sufficient to give an indication of whether there is support for additional images but remains tractable for performing a large number of analyses.

Table 9.4 gives the results of the millilensing analysis showing the $\log_{10}$ Bayes factor between the millilensing and the unlensed waveforms. The cell highlight color indicates the recovered number of images from the posterior from one to four. As can be seen, all of the potential cases are present. Table 9.4 indicates that in addition ot all candidates that are flagged for investigation by the microlensing analysis, the millilensing analysis also flags two of the injections with an additional scalar mode of polarisation as false positives with preference for a single image. Examining the posterior for the first image for the $\mathcal{A} = 0.20$ case, the one with the smaller GR deviation—shown in Figure 9.9–indicates a preference for being a type II image, which is consistent with the type II specific analysis performed in Wright et al. (2024). The lowest two mass BHM-NS injections are additionally now found to have sufficient support for follow-up consideration in this case, with one and two image recoveries respectively. This would be in line with the slender support for the $M = 90M_\odot$ case in the microlensing analysis, and the slender disfavouring for the $M = 80M_\odot$ case.

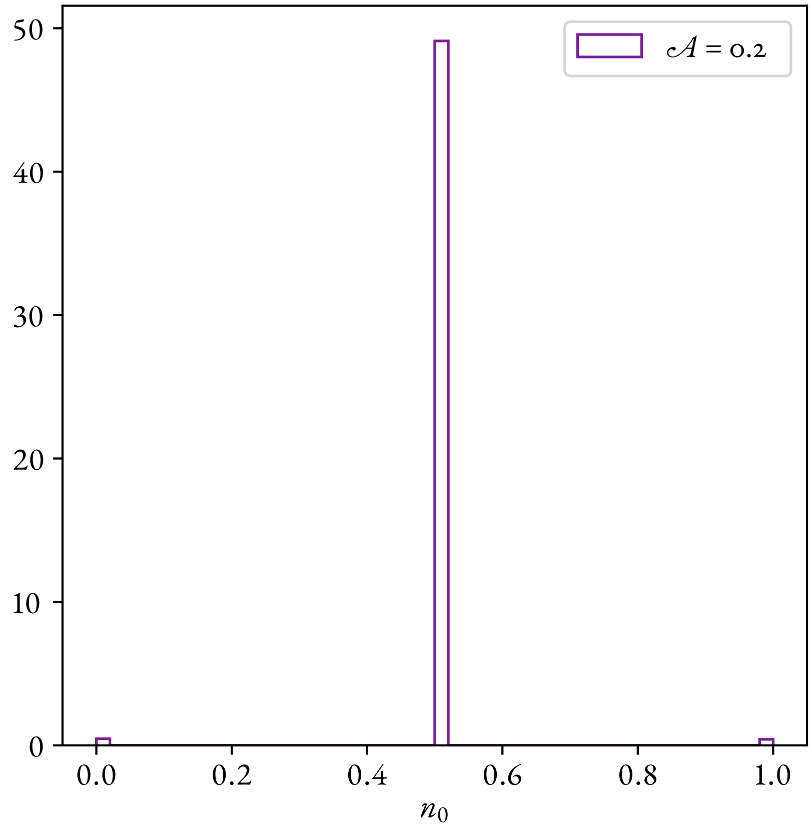

Figure 9.9: Recovered posterior on the Morse index of the $\mathcal{A} = 0.20$ injection—one of the two cases for this injection set that returned a favouring for a single millilensing image. As can be seen, support is significant for $n = 0.5$, i.e. a type II image, which is consistent with the result found by the Type II investigation in Wright et al. (2024), and the event would be flagged for further investigations.

We performed a similar posterior consistency check to the one that was performed for the microlesning analysis. For unlensed events, the posterior space for the lensing observables should reflect the respective priors, all of which were simply uniform. For lensed events, the posteriors should demonstrate constraint for each of the parameter sets corresponding to images that have support and reflecting the priors for those images that do not. Such behaviour is illustrated in Figure 9.10 in the recovered posteriors on the effective luminosity distance of a proposed second image for the massive graviton series of injections which displays broad uniform posteriors indicative of no support for the additional signal up until the $A_0 = 1.90 \times 10^{-43}\mathrm{eV}^2$ at which point the posteriors display constraint towards a particular value reflecting the point at which the Bayes factor support additional millisignals.

Similarly to the SIS analysis, the $140 M_\odot$ BHM-P waveform does not yield support for the millilensing hypothesis despite posterior support for a four millisignal millilensing hypothesis support for the $130 M_\odot$ and $150 M_\odot$ cases. In this instance, the source posteriors in all chains more closely resembled the local maximum found for the point mass and unlensed analyses, and this was the case with a re-

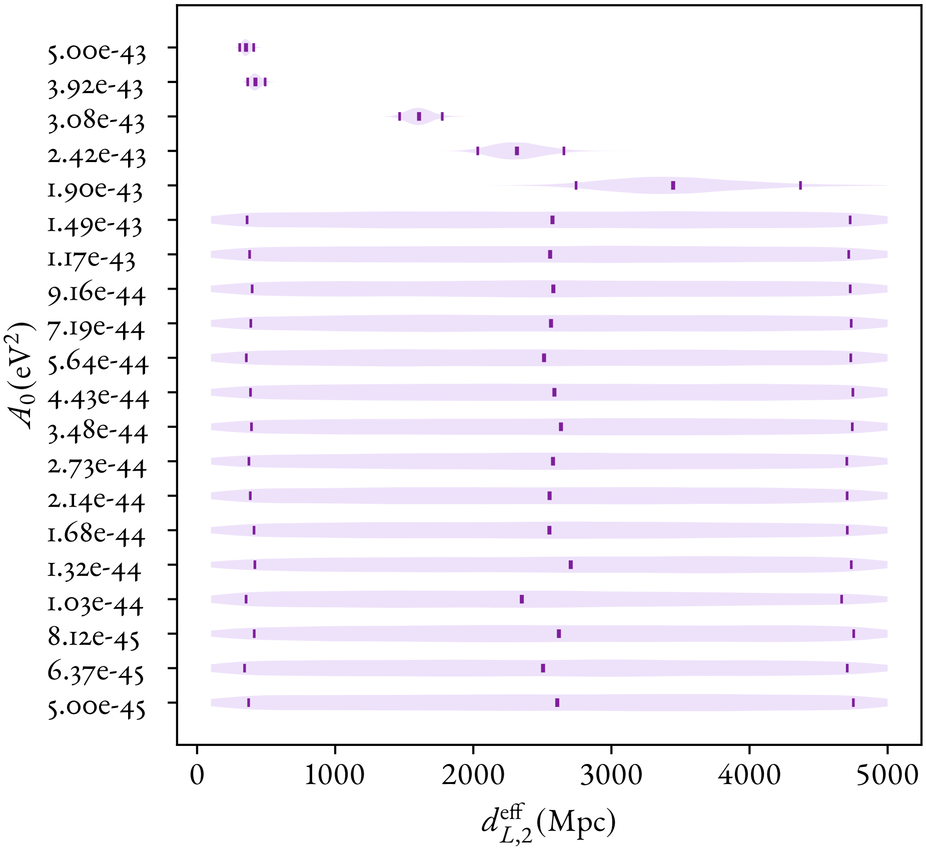

Figure 9.10: Recovered posteriors on the luminosity distance of a proposed second millisignal for the massive graviton series of injections analysed using the phenomenological millilensing model. The vertical lines indicate the median and 90% confidence interval. Lower graviton mass injections display broad posteriors across the entire space which is an indication of a lack of support for a second image. The higher mass graviton mass injections, however, display constraint towards a value which is an indication of support for a number of images greater than or equal to two following the expectation for the presence of a millisignal.

peated analysis of this waveform. This may be an indication that all of the analysis are untrustworthy in the case of this waveform.

With the exception of the two additional scalar mode of polarisation investigations, the Morse index posteriors do not display a consistent constraint to a single value for those images that are supported, varying between support for a particular value, two of the values, or all three. This is not necessarily unexpected for true lensing candidates and so whilst it does not add support for the lensing hypothesis, neither does it allow for these candidates to be discarded.

In the microlensing investigations of the BHM-P injections, we noted the requirement to increase the maximum of the luminosity distance posterior from 2Gpc to 5Gpc. In the millilensing investigations, the maximum effective luminosity distance of the prior was allowed to reach 100Gpc in these cases. The estimates for the median effective luminosity distance for these injections varied between 5Gpc to 12Gpc. This reinforces the suggestion from the microlensing analyses that these waveforms would demonstrate the apparent highest magnifications. While this level of magnification may shed some doubt on these events due to it being unlikely, it is difficult to infer the absolute magnification of an unknown signal. Rather, it is only possible to infer the relative magnification between the images, which in these cases was between 1 and 10, and would not be in and of itself disqualifying when compared to expected values from current models—see e.g. More & More (2022).

9.3.4 Potential for Additional Biases

The primary focus of the investigations carried out within this Chapter and within Wright et al. (2024) was to investigate whether deviations from GR would impact the searches for microlensing and millilensing (as well as Type II strong lensing in the case of Wright et al. (2024)), and as we have shown there are cases where such a deviation may provoke a false positive from these investigations. If such a false positive were actually identified in a realistic analysis, one question that one may pose, is to what extent does this misidentification degrade the estimation of the source parameters as compared to the already degraded estimates from the standard GR investigation.

Table 9.5 displays the comparison of the median and 90% confidence interval boundaries between the lensed and unlensed estimates for the chirp mass, mass ratio, and luminosity distance for the isolated point mass microlensing and unlensed investigations. These are the parameters that are most likely to be affected in the microlensing analysis by false support for the microlensing hypothesis.

The chirp mass and mass ratio estimates in the massive graviton and modified energy flux cases do not display significant signs of consistent bias as a result of the microlensing investigation—though there are obviously significant limitations on the conclusions one may draw from the single example of the modified energy flux case. In the black hole mimicker cases, the lensed investigations are typically larger—though there are one or two exceptions to this—particularly in the $M = 140M_{\odot}$ BHM-NS case which is inline with the peculiarities that have been discussed about analysis of this event.

The luminosity distance estimates are significantly more affected, as would be expected, given that the posteriors demonstrate constraints in the lens parameter posteriors. In all cases, the lensed estimate is significantly higher than the unlensed estimate, with the estimates for the BHM-P cases comparatively higher than those of the other deviation types—again an indication that these have the highest apparent magnification.

The preliminary conclusion of this limited exercise in the microlensing analysis would therefore be that in addition to the false identification of the signal as a lensed signal, estimations of the source parameters under this false hypothesis are likely to be degraded compared with the already incorrect results obtained when analysing under the standard unlensed GR waveforms.

9.4 Conclusion

In the coming years, given the expected continued improvements to the sensitivity of the current ground-based detector network (Abbott et al., 2020a), in addition to the greater likelihood of the ob-

Table 9.5: Estimates on the chirp mass, $\mathcal{M}_c$, the mass ratio, q, and the luminosity distance, d_L, for the point mass and standard GR analyses of those events that would be identified as false positives under the point mass microlensing hypothesis. Estimates given are the median of the posterior, with the error bars indicating the boundaries of the 90% confidence interval. For easy reference, the true values are $\mathcal{M}_c = 31.11 M_\odot$, and $q = 0.8$ for the massive graviton and modified energy injections, $M_c = 0.4328M, q = 0.82$ for the BHM-P injections, and $M_c = 0.4154M, q = 0.57$ for the BHM-NS injections. The true value of d_L was 452Mpc for all injections.

	GR Estimate			Lensed Estimate		
Injection	$\mathcal{M}_c(M_\odot)$	q	d_L(Mpc)	$\mathcal{M}_c(M_\odot)$	q	d_L(Mpc)
			Massive Graviton			
$A_0 = 1.90 \times 10^{-43}\text{eV}^2$	$26.31^{+0.23}_{-0.23}$	$0.166^{+0.004}_{-0.003}$	1118^{+59}_{-51}	$26.29^{+0.20}_{-0.20}$	$0.167^{+0.007}_{-0.003}$	1338^{+137}_{-101}
$A_0 = 2.42 \times 10^{-43}\text{eV}^2$	$23.81^{+0.49}_{-0.12}$	$0.182^{+0.008}_{-0.038}$	1134^{+64}_{-67}	$24.25^{+0.12}_{-0.14}$	$0.144^{+0.004}_{-0.002}$	1644^{+279}_{-194}
$A_0 = 3.08 \times 10^{-43}\text{eV}^2$	$21.74^{+0.12}_{-0.13}$	$0.139^{+0.008}_{-0.005}$	1101^{+77}_{-62}	$21.65^{+0.09}_{-0.10}$	$0.137^{+0.004}_{-0.002}$	1930^{+62}_{-104}
$A_0 = 3.92 \times 10^{-43}\text{eV}^2$	$16.97^{+0.16}_{-0.19}$	$0.25^{+0.02}_{-0.01}$	279^{+37}_{-31}	$16.23^{+0.32}_{-0.25}$	$0.83^{+0.01}_{-0.01}$	544^{+84}_{-69}
$A_0 = 5.00 \times 10^{-43}\text{eV}^2$	$14.10^{+0.17}_{-0.17}$	$0.85^{+0.02}_{-0.02}$	255^{+43}_{-33}	$14.08^{+0.17}_{-0.18}$	$0.83^{+0.02}_{-0.02}$	463^{+79}_{-63}
			Modified Energy Flux			
$a_2 = 50$	$31.25^{+0.76}_{-0.88}$	$0.51^{+0.07}_{-0.06}$	502^{+53}_{-56}	$31.89^{+0.73}_{-0.90}$	$0.50^{+0.06}_{-0.05}$	536^{+49}_{-48}
			BHM-P			
$M = 80M_\odot$	$35.62^{+2.53}_{-1.64}$	$0.31^{+0.09}_{-0.04}$	923^{+135}_{-136}	$35.46^{+2.44}_{-1.61}$	$0.31^{+0.08}_{-0.04}$	926^{+734}_{-167}
$M = 90M_\odot$	$41.91^{+2.99}_{-2.40}$	$0.40^{+0.08}_{-0.05}$	945^{+140}_{-136}	$41.02^{+3.05}_{-2.21}$	$0.39^{+0.07}_{-0.05}$	1342^{+850}_{-487}
$M = 100M_\odot$	$47.73^{+3.02}_{-2.34}$	$0.50^{+0.07}_{-0.05}$	927^{+149}_{-151}	$50.62^{+7.25}_{-5.06}$	$0.57^{+0.19}_{-0.11}$	2152^{+796}_{-918}
$M = 110M_\odot$	$52.63^{+4.05}_{-2.71}$	$0.60^{+0.10}_{-0.06}$	841^{+170}_{-163}	$60.22^{+6.61}_{-7.89}$	$0.79^{+0.18}_{-0.20}$	2342^{+903}_{-661}
$M = 120M_\odot$	$57.37^{+11.40}_{-4.72}$	$0.70^{+0.29}_{-0.11}$	863^{+283}_{-176}	$65.67^{+3.11}_{-5.89}$	$0.93^{+0.07}_{-0.17}$	2566^{+949}_{-796}
$M = 130M_\odot$	$55.94^{+6.92}_{-4.04}$	$0.68^{+0.17}_{-0.10}$	994^{+223}_{-253}	$66.85^{+2.15}_{-3.81}$	$0.96^{+0.03}_{-0.09}$	2537^{+757}_{-713}
$M = 140M_\odot$	$54.80^{+4.86}_{-3.41}$	$0.65^{+0.10}_{-0.08}$	1073^{+226}_{-218}	$67.07^{+2.00}_{9.87}$	$0.97^{+0.03}_{-0.20}$	2400^{+598}_{-918}
$M = 150M_\odot$	$53.72^{+4.03}_{-3.52}$	$0.62^{+0.10}_{-0.08}$	1100^{+277}_{-237}	$59.47^{+6.16}_{-5.05}$	$0.86^{+0.13}_{-0.19}$	2347^{+561}_{-650}
$M = 160M_\odot$	$50.52^{+4.63}_{-3.53}$	$0.55^{+0.11}_{-0.18}$	1053^{+287}_{-215}	$60.24^{+6.29}_{-6.34}$	$0.85^{+0.13}_{-0.20}$	2585^{+649}_{-561}
			BHM-NS			
$M = 100M_\odot$	$48.02^{+1.97}_{-1.76}$	$0.50^{+0.04}_{-0.03}$	1021^{+90}_{-77}	$48.78^{+2.41}_{-2.52}$	$0.54^{+0.07}_{-0.06}$	1735^{+158}_{-331}
$M = 110M_\odot$	$47.74^{+1.77}_{-1.72}$	$0.50^{+0.04}_{-0.03}$	950^{+80}_{-72}	$48.78^{+1.89}_{-2.06}$	$0.54^{+0.06}_{-0.05}$	1612^{+136}_{-164}
$M = 120M_\odot$	$49.76^{+1.80}_{-1.70}$	$0.54^{+0.04}_{-0.04}$	944^{+85}_{-74}	$51.79^{+2.20}_{-2.06}$	$0.60^{+0.08}_{-0.05}$	1658^{+154}_{-165}
$M = 130M_\odot$	$49.63^{+1.60}_{-1.55}$	$0.53^{+0.04}_{-0.03}$	799^{+70}_{-60}	$51.58^{+1.80}_{-1.69}$	$0.58^{+0.05}_{-0.04}$	1395^{+112}_{-102}
$M = 140M_\odot$	$33.54^{+0.18}_{-0.46}$	$0.255^{+0.003}_{-0.004}$	294^{+26}_{-23}	$33.45^{+0.13}_{-0.20}$	$0.253^{+0.001}_{-0.003}$	397^{+33}_{-29}
$M = 150M_\odot$	$35.10^{+0.62}_{-0.78}$	$0.28^{+0.01}_{-0.01}$	376^{+46}_{-38}	$45.67^{+1.84}_{-1.46}$	$0.45^{+0.04}_{-0.03}$	761^{+108}_{-94}

servation of a lensed event we will also be able to investigate potential deviations from GR with greater precision. Should candidates for a lensed detection be identified, it is important to understand any potential sources of false positivity that may mimic the signatures of lesning. In this chapter, we have analysed phenomenological deviations from GR to understand if any such deviations would in and of themselves cause such false positivity in searches for microlensing and millilensing.

To perform this investigation, we have taken several possible deviations from GR—specifically a massive graviton, modifications to the energy flux and the QNM spectrum, and an additional scalar mode of polarisation—as well as the possibility of exotic compact objects and subjected them to the forms of microlensing and millilenisng analysis that have been discussed both within this thesis as well as deployed specifically in Janquart et al. (2023b) to determine to what extent any false positive candidates could be identified and if any could be ruled out by the follow-up analyses. We have here used the predicted noise curves for O4 to present a reasonably realistic scenario for current performance and our results indicate that there are a number of scenarios that could result in a false positive.

In the initial isolated point mass microlensing analysis, a graviton with mass $\geq 4.36 \times 10^{-22} \mathrm{eV}/c^2$, would cause a sufficient preference for the microlensing hypothesis to warrant further follow-up investigation. This further investigation in the form of the SIS and millilensing analyses would similarly find significant support for the respective models meaning that these would be identified as lensing candidates. However, gravitational wave observations place constraints on the mass of the graviton to well below this threshold ($< 1.27 \times 10^{-23} \mathrm{eV}/c^2$ at 90% credibility). Beneath this threshold, support for the unlensed waveform was consistent.

Modifications to the energy flux with $a_2 = 50$ were able to produce a false positive in both the initial point mass microlensing and the follow-up SIS microlensing analysis. The follow-up millilensing analysis would also identify the modification with $a_2 = 20$ as a slenderly favoured candidates.

Neither modifications to the QNM spectrum nor the addition of a scalar mode of polarisation yielded any situations in which the initial microlensing investigation would yield a sufficiently confident false positive to warrant additional investigation. However, should such investigations be carried out, the $\mathcal{A} = 0.20$ and $\mathcal{A} = 0.25$ additional scalar mode cases slenderly preferred a single type II millilensed image—consistent with the findings of the type II specific investigation that was performed in Wright et al. (2024) on these waveforms.

Binaries of exotic compact objects, which were here proxied by scaling BNS waveforms to BBH masses resulted in significant false positivity in both the precessing and non-spinning cases. These waveforms displayed preference for all three of the isolated point mass, SIS, and millilensing models as compared with the unlensed model in the majority of the analyses performed. As such objects have not been conclusively ruled out, microlensing and millilensing candidates would need to be examined for signatures of such objects before claims of lensing would be able to be made. One particular indicator in the case of the non-spinning analysis may be significant chain disagreement when parameter estimation was performed on these waveforms.

Additionally, we examined the recovered posteriors of the lensed waveforms compared with the unlensed waveforms to note whether such false identification as a lensed waveform would further degrade the source parameter estimates compared with the already incorrect GR recoveries. IN the case of the microlensing analysis, this would have significant consequences on the luminosity distance estimates, which with very few exceptions were considerably worse than the unlensed estimates.

Ultimately, therefore, this examination concludes that there are scenarios in which deviations from GR would be the source of a false positive result in the searches for microlensing and millilensing and therefore potential lensing candidates should be subject to some scrutiny for searches for such deviations as part of the identification process for lensed events. Should a misidentification occur, it is likely that the ultimately estimated source parameters will be degraded compared to the misidentification of GR.

10

Conclusions and Future Prospects

> *This place is the end of all things.*
> *And the beginning.*
>
> The Heart of a Living Thing, *Dishonored*
> Developed by Arkane Studios

Finally, reader, our discussion turns towards its conclusions and to the question of how this discussion could continue in the future were we to return to it. Our discussion began with a simple statement—that should you drop it, this thesis will fall down. From there, we explored the development of the theory of gravitation from its beginnings in Greece with Aristotle through to the work of Isaac Newton and to the current best theory that we have for gravity, General Relativity. From that point, we were on the path to understanding the context of the true question that this thesis desires to answer: should a gravitational wave signal be gravitationally lensed, can we determine the mass density profile of the object that has served as the lens?

Our discussion separated into four sections discussing answering this question that we will summarise here at the end.

The Development of Gravelamps

Chapter 6 discussed the development of Gravelamps, a piece of free and open source software developed to answer the question of what can we determine about the lens when investigating potentially microlensed GW signals. In particular, it takes a parameter estimation based approach implementing three models of microlensing as a base—the isolated point mass, the SIS, and the NFW—but with the capacity to be easily extended to further models as required.

The true strength of Gravelamps compared with other similar approaches that had been employed previously is its ability to rapidly compute the amplification factor for each of these models even in the complicated wave optics regime—for which it employs the C-language arbitrary precision library arb (Johansson, 2017). It then switches to python in order to gain access to the standard parameter estimation framework, bilby (Ashton et al., 2019), bringing it into line with other parameter estimation based analyses for GWs.

We demonstrated examples of the production of the amplification factor for each of the implemented models, as well as a test simulation to demonstrate that, when examining with multiple models including the unlensed model, it is possible to determine both the question of is a GW signal lensed and our main question of "*by what*"?

We also discussed the design philosophy of the Gravelamps platform as one that values readability and accessibility of its codebase, and expansibility to be a truly useful framework for the GW lensing community as a whole should they wish to use it.

Microlensing and Millilensing Searches

Chapter 7 would build upon the foundational framework provided by Chapter 6 to discuss some of the initial deployments of and expansions to the Gravelamps framework. We firstly discussed those candidate events that were determined by Abbott et al. (2023d) to be those that most closely matched the expectations for lensing—albeit that they would be ultimately discarded. These candidates were analysed in conjunction with the other analyses performed on these candidates in Janquart et al. (2023b). Three of these candidates—GW191103, GW191105, and GW190412 displayed no particular interest from the microlensing perspective.

However, the candidate GW200208 would display some support for the microlensing hypothesis when examined in the isolated point mass microlensing model. This support was increased upon consideration of the SIS model, which meant that we needed to investigate this event in more detail to give an indication of its ultimate status. For this we examined a simulation of an event with the same parameters as those estimated by analysis of GW200208 injected into representative noise from around the time of the event—this yielded that the expected support for microlensing from such an event would be lower than that recovered for this event.

Ultimately the status of GW200208 would be determined by investigation of the residual power from the detectors when the maximal likelihood unlensed signal was removed. There was a lack of the expected coherent oscillatory power between the detectors leading to support for the conclusion of Abbott et al. (2023d) that the apparent support is the result of transient noise effects.

Following on from the investigation of the O3 candidates, we examined the O4 event GW230529, which is believed to contain one member of the binary within the lower mass gap. If this lower mass gap is astrophysically motivated and such black holes do not exist, then one such way this support could result would be the effect of lensing causing an error in the estimated mass when not accounted for. Examinations of this pair using the isolated point mass microlensing model for the BBH, BNS, and NSBH models did not find any support for microlensing, however.

We also showed the first major extension to Gravelamps—the incorporation of the phenomenological millilensing model developed by Liu et al. (2023). We as well proposed strategies for deployment of Gravelamps in future observing runs—in particular to minimise the resource usage of such a computationally intensive search and how Gravelamps may be incorporated with a more sophisticated automation and prioritisation framework.

A Methodology for Strong Lensing

Our discussions in Chapter 6 provided us with a means to answer the questions of a lens in the microlensing regime—expanded to the millilensing regime also in Chapter 7. However, they also revealed that the approach taken by Gravelamps was unable to provide answers when examining signals for signatures of strong lensing individually—we instead needed to find a different approach for this regime that would account for the multiple resolvable images produced by strong lensing. This was the focus of our discussions in Chapter 8.

We first considered the means by which strong lensing of GWs may be identified—in particular, we focus on the joint parameter estimation approaches undertaken by such pipelines as GOLUM (Janquart et al., 2021, 2023a) or hanab (Lo & Magana Hernandez, 2023). These provide a model agnostic framework for detection using observable parameters rather than model specific parameter sets. We therefore set our sights on identifying a means to translate these already estimated posteriors rather than trying a significantly more expensive resampling of the parameter space.

We identified a mathematical formalism by which to perform this translation and to ultimately arrive at the evidence for a given lensing model that could be easily replicated for multiple models to ascertain the most likely model of lensing. In so doing, we needed to reconstruct posteriors on the model specific parameters allowing us to also receive estimates of these giving us access to the same information as expected for the microlensing and millilensing regimes.

With the framework identified, we then demonstrated that it performed well using a series of 75 simulated pairs of signals and subjecting them to the methodology finding a consistent preference for the correct model and with posterior recoveries in line with those received from the model agnostic joint parameter estimation. Finally, we showed an example of a real deployment of this framework on the pair GW191230–LGW200104—the lensing candidate from Janquart et al. (2023b) that had the highest support but that was ultimately discarded after consideration of the fuller picture and the uncertainty regarding the potential non-astrophysical origins of LGW200104.

Moving Beyond GR Prior to Chapter 9, our discussions had presented an endpoint in the development of the theory of gravitation with GR. However, as we reached the end of our discussions, it is also important to remember that development of gravitational theory remains ongoing and alternative explanations may be provided. Given that modifications to the theory of gravitation may have significant effects on the production and propagation of GW signals—and indeed on the nature of lensing—it is important to understand if these signals by themselves would yield any false positivity in searches for lensing and this was the focus of Chapter 9.

For this investigation, we created a series of injections each based on a GR baseline resembling GW150914 and each with an isolated modification to GR from the inclusion of massive gravitons, modifications to the energy flux, modifications to the QNM spectra, and the inclusion of additional modes of polarisation. We also examined two sets of signals based on BNS signals scaled to BBH-like masses as a proxy for exotic compact objects. These injections were then analysed using the GRAVELAMPS framework for potential support for microlensing and/or millilensing.

We found that there are a number of cases in which such a signal would produce a false positive result in the microlensing and millilensing analyses—particularly with high massive gravitons or exotic compact objects. Whilst scenarios of the former are unlikely based on the constraints set by, for instance, Abbott et al. (2021e)—exotic compact objects have not yet been ruled out. This provides us with motivation to examine microlensing candidate effects for any potential signatures of, for instance, tidal deformability that would indicate that the candidate was instead not a vanilla BBH.

We also examined the question of, should such a false positive be made, would this degrade the already incorrect GR estimates of the parameters of the binary and found that this is likely to be the case—though we note that with limited numbers of such injections, a stronger statement cannot be made at this time.

We, therefore, have provided a framework to answer questions both of identifying and interrogating lensed GW signals in the future. Whilst at the end of O3 such a signal has not yet been detected, we know that with the increasing sensitivity of the detector network, with the increasing numbers of events being detected, and in the longer term, with the increasing number of detectors online, the detection of lensing is a matter of when. It is therefore vital to have such frameworks in place for when that detection does occur so that we may answer the most obvious of the follow-up questions quickly and accurately.

That is, reader, not to say that such questions are simply ready to be answered and there are a number of places in which future work may be identified from the discussions that we have had here. For instance, GRAVELAMPS as an extensible framework may draw upon the latest literature to examine additional possible microlensing models and move beyond both a single lens to a field of microlenses—or indeed to multiplanar lensing should a single signal encounter multiple objects between the source and observation.

It will also be critical to expand the available models for the strong lensing methodology in which only the simplest models with analytic relations between the lens model parameters and the observables were tested. More complex models must be examined and methods to rapidly transfer between the observables and the model parameters must be identified to ensure that this approach may be deployed at high speed.

We also identified ongoing work, such as the integration of GRAVELAMPS within large scale metadata handling and automation frameworks to meet the demands of analysis of GW data in the future as the number of signals increases. Such work will become increasingly vital given that the rate of detections will only ever increase and will become unmanageable for manual deployment in short order.

The final example that will be provided here—though this is of course very much a non-exhaustive set—of work that could be carried through to the future would be that whilst we have investigated the effect deviations from GR would have on the searches for lensing under the assumption of investigation within a lensed GR context, it is important to ask the question of what would a lensed signal actually look like in alternative thoeries of gravitation. Would such a signal be detectable as lensed within the GR context and would there be particularly effects that could be examined for in current analyses for instance.

Our work therefore, reader, is only beginning—at this time before we have detected any lensed signals. Whilst the work, in this moment, has been exclusively developmental, it shall not remain so for much longer. Thus, whilst this discussion concludes, the topic will remain open going onwards.

> *And I was warm. And I was loved. And I was finished.*
>
> Buffy Summers, *Buffy the Vampire Slayer*
> Created by Joss Whedon

Bibliography

Aasi, J., Abbott, B., Abbott, R., et al. 2014, Physical Review Letters, 113, doi: 10.1103/physrevlett.113.011102

Aasi, J., Abbott, B. P., Abbott, R., et al. 2015, Classical and Quantum Gravity, 32, 074001, doi: 10.1088/0264-9381/32/7/074001

Abadie, J., Abbott, B. P., Abbott, R., et al. 2011, Phys. Rev. D, 83, 042001, doi: 10.1103/PhysRevD.83.042001

Abbott, B., Abbott, R., Abbott, T., et al. 2017a, Physical Review D, 95, doi: 10.1103/physrevd.95.042003

—. 2019a, Physical Review D, 100, doi: 10.1103/physrevd.100.024017

—. 2019b, Physical Review D, 100, doi: 10.1103/physrevd.100.062001

—. 2019c, Physical Review D, 100, doi: 10.1103/physrevd.100.061101

Abbott, B. P., Abbott, R., Abbott, T. D., et al. 2020a, LRR, 23, 3, doi: 10.1007/s41114-020-00026-9

—. 2016a, Phys. Rev. Lett., 116, 061102, doi: 10.1103/PhysRevLett.116.061102

—. 2016b, Phys. Rev. Lett., 116, 221101, doi: 10.1103/PhysRevLett.116.221101

—. 2017b, Phys. Rev. Lett., 119, 161101, doi: 10.1103/PhysRevLett.119.161101

—. 2017c, The Astrophysical Journal Letters, 848, L12, doi: 10.3847/2041-8213/aa91c9

Abbott, B. P., Abbott, R., Abbott, T. D., et al. 2017a, Nature, 551, 85, doi: 10.1038/nature24471

—. 2017b, Physical Review Letters, 118, 121101, doi: 10.1103/PhysRevLett.118.121101

Abbott, B. P., Abbott, R., Abbott, T. D., et al. 2019d, The Astrophysical Journal Letters, 882, L24, doi: 10.3847/2041-8213/ab3800

—. 2019e, Phys. Rev. Lett., 123, 011102, doi: 10.1103/PhysRevLett.123.011102

—. 2019f, Phys. Rev. D, 100, 104036, doi: 10.1103/PhysRevD.100.104036

—. 2019g, The Astrophysical Journal, 874, 163, doi: 10.3847/1538-4357/ab0e15

—. 2020b, Phys. Rev. D, 101, 084002, doi: 10.1103/PhysRevD.101.084002

—. 2021a, The Astrophysical Journal, 909, 218, doi: 10.3847/1538-4357/abdcb7

Abbott, R., Abbott, T. D., Abraham, S., et al. 2020c, Phys. Rev. D, 102, 043015, doi: 10.1103/PhysRevD.102.043015

Abbott, R., Abbott, T. D., Abraham, S., et al. 2020a, The Astrophysical Journal Letters, 896, L44, doi: 10.3847/2041-8213/ab960f

—. 2020b, Phys. Rev. Lett., 125, 101102, doi: 10.1103/PhysRevLett.125.101102

Abbott, R., Abbott, T. D., Abraham, S., et al. 2021b, The Astrophysical Journal Letters, 915, L5, doi: 10.3847/2041-8213/ac082e

—. 2021c, The Astrophysical Journal Letters, 913, L7, doi: 10.3847/2041-8213/abe949

—. 2021d, Phys. Rev. D, 103, 122002, doi: 10.1103/PhysRevD.103.122002

Abbott, R., Abe, H., Acernese, F., et al. 2021e, Tests of General Relativity with GWTC-3. https://arxiv.org/abs/2112.06861

Abbott, R., Abbott, T. D., Abraham, S., et al. 2021f, The Astrophysical Journal, 923, 14, doi: 10.3847/1538-4357/ac23db

Abbott, R., Abbott, T., Acernese, F., et al. 2021g, Physical Review D, 104, doi: 10.1103/physrevd.104.122004

Abbott, R., Abbott, T. D., Abraham, S., et al. 2021h, Phys. Rev. Lett., 126, 241102, doi: 10.1103/PhysRevLett.126.241102

—. 2021i, The Astrophysical Journal, 921, 80, doi: 10.3847/1538-4357/ac17ea

Abbott, R., Abbott, T., Abraham, S., et al. 2021j, Physical Review D, 104, doi: 10.1103/physrevd.104.082004

—. 2021k, Physical Review D, 104, doi: 10.1103/physrevd.104.022004

Abbott, R., Abbott, T. D., Acernese, F., et al. 2022a, Phys. Rev. D, 105, 082005, doi: 10.1103/PhysRevD.105.082005

Abbott, R., Abe, H., Acernese, F., et al. 2022b, Phys. Rev. D, 106, 042003, doi: 10.1103/PhysRevD.106.042003

—. 2022c, Phys. Rev. D, 105, 102001, doi: 10.1103/PhysRevD.105.102001

Abbott, R., Abbott, T. D., Acernese, F., et al. 2023a, Phys. Rev. X, 13, 041039, doi: 10.1103/PhysRevX.13.041039

Abbott, R., Abe, H., Acernese, F., et al. 2023b, The Astrophysical Journal, 949, 76, doi: 10.3847/1538-4357/ac74bb

Abbott, R., Abbott, T. D., Acernese, F., et al. 2023c, Phys. Rev. X, 13, 011048, doi: 10.1103/PhysRevX.13.011048

Abbott, R., Abe, H., Acernese, F., et al. 2023d, Search for gravitational-lensing signatures in the full third observing run of the LIGO-Virgo network. https://arxiv.org/abs/2304.08393

Abramowitz, M., & Stegun, I. A. 1964, Handbook of Mathematical Functions With Formulas, Graphs and Mathematical Tables (National Bureau of Standards Applied Mathematics Series No. 55) (National Bureau of Standards (NBS), United States Department of Commerce)

Acernese, F., Agathos, M., Agatsuma, K., et al. 2014, Classical and Quantum Gravity, 32, 024001, doi: 10.1088/0264-9381/32/2/024001

Adam, C., Castelo, J., García Martín-Caro, A., et al. 2022, Phys. Rev. D, 106, 123022, doi: 10.1103/PhysRevD.106.123022

Ade, P. A. R., Aghanim, N., Arnaud, M., et al. 2016, A&A, 594, A13, doi: 10.1051/0004-6361/201525830

Akçay, S., Gamba, R., & Bernuzzi, S. 2021, Phys. Rev. D, 103, 024014, doi: 10.1103/PhysRevD.103.024014

Akutsu, T., Ando, M., Arai, K., et al. 2020, Progress of Theoretical and Experimental Physics, 2021, 05A101, doi: 10.1093/ptep/ptaa125

Almheiri, A., Marolf, D., Polchinski, J., & Sully, J. 2013, JHEP, 2013, doi: 10.1007/jhep02(2013)062

Anderson, M., Hirschmann, E. W., Lehner, L., et al. 2008, Phys. Rev. D, 77, 024006, doi: 10.1103/PhysRevD.77.024006

Aristotle. 1930a, in The Works of Aristotle, Volume 2, ed. W. D. Ross & translated by J. L Stocks (Oxford Clarendon Press)

Aristotle, a. 1930b, in The Works of Aristotle, Volume 2, ed. W. D. Ross, translated by R. P. Hardie, & R. K. Gaye (Oxford Clarendon Press)

Ashton, G., Hübner, M., Lasky, P. D., et al. 2019, The Astrophysical Journal Supplement Series, 241, 27, doi: 10.3847/1538-4365/ab06fc

Aston, S. M., Barton, M. A., Bell, A. S., et al. 2012, Classical and Quantum Gravity, 29, 235004, doi: 10.1088/0264-9381/29/23/235004

Babak, S., Hewitson, M., & Petiteau, A. 2021, LISA Sensitivity and SNR Calculations. https://arxiv.org/abs/2108.01167

Bailyn, C. D., Jain, R. K., Coppi, P., & Orosz, J. A. 1998, Astrophys. J., 499, 367, doi: 10.1086/305614

Bartelmann, M. 1996, A&A, 313, 697, doi: 10.48550/arXiv.astro-ph/9602053

Bayes, R. T. 1763, Philosophical Transactions of the Royal Society, 53, 370, doi: https://doi.org/10.1098/rstl.1763.0053

Belgacem, E., Dirian, Y., Foffa, S., & Maggiore, M. 2018, Phys. Rev. D, 97, 104066, doi: 10.1103/PhysRevD.97.104066

Bernard, L., Blanchet, L., & Trestini, D. 2022, J. Cosmology Astropart. Phys., 2022, 008, doi: 10.1088/1475-7516/2022/08/008

Berti, E., Barausse, E., Cardoso, V., et al. 2015, Classical and Quantum Gravity, 32, 243001, doi: 10.1088/0264-9381/32/24/243001

Betancourt, M. 2018, A Conceptual Introduction to Hamiltonian Monte Carlo. https://arxiv.org/abs/1701.02434

Binney, J., & Tremaine, S. 2008, Galactic Dynamics, 2nd edn. (Princeton University Press), 885

Birkhoff, G. D., & Langer, R. E. 1923, Relativity and modern physics

Boole, G. 1847, The Mathematical Analysis of Logic
Being an Essay Towards a Calculus of Deductive Reasoning (Barclay & Macmillan)

Broadhurst, T., Diego, J. M., & au2, G. F. S. I. 2019, Twin LIGO/Virgo Detections of a Viable Gravitationally-Lensed Black Hole Merger. https://arxiv.org/abs/1901.03190

Brucato, R., & Kristian, J. 1973, ApJ, 179, L129, doi: 10.1086/181133

Buonanno, A., & Chen, Y. 2001, Phys. Rev. D, 64, 042006, doi: 10.1103/PhysRevD.64.042006

Buonanno, A., Iyer, B. R., Ochsner, E., Pan, Y., & Sathyaprakash, B. S. 2009, Physical Review D, 80, doi: 10.1103/physrevd.80.084043

Burke, W. L. 1981, ApJ, 244, L1, doi: 10.1086/183466

Burkert, A. 1995, The Astrophysical Journal, 447, doi: 10.1086/309560

Calderón Bustillo, J., Sanchis-Gual, N., Torres-Forné, A., et al. 2021, Phys. Rev. Lett., 126, 081101, doi: 10.1103/PhysRevLett.126.081101

Calderón Bustillo, J., Sanchis-Gual, N., Leong, S. H. W., et al. 2023, Phys. Rev. D, 108, 123020, doi: 10.1103/PhysRevD.108.123020

Cano, P. A., Fransen, K., Hertog, T., & Maenaut, S. 2023, Phys. Rev. D, 108, 024040, doi: 10.1103/PhysRevD.108.024040

Cao, S., Qi, J., Cao, Z., et al. 2019, Sci. Rep., 9, 11608, doi: 10.1038/s41598-019-47616-4

Cao, Z., Li, L.-F., & Wang, Y. 2014, Phys. Rev. D, 90, 062003, doi: 10.1103/PhysRevD.90.062003

Cardoso, V., Franzin, E., Maselli, A., Pani, P., & Raposo, G. 2017, Phys. Rev. D, 95, 084014, doi: 10.1103/PhysRevD.95.084014

Cardoso, V., & Pani, P. 2019, LRR, 22, 4, doi: 10.1007/s41114-019-0020-4

Carroll, S. 2013, Spacetime and Geometry: An Introduction to General Relativity; International ed (Pearson Educational)

Carroll, S. M. 2001, Living Reviews in Relativity, 4, doi: 10.12942/lrr-2001-1

Cho, G., Gopakumar, A., Haney, M., & Lee, H. M. 2018, Physical Review D, 98, doi: 10.1103/physrevd.98.024039

Collett, T. E., & Bacon, D. 2017, Physical Review Letters, 118, doi: 10.1103/physrevlett.118.091101

Copernicus, N. 1543, De revolutionibus orbium coelestium (Johannes Petreius)

Corman, M., Ripley, J. L., & East, W. E. 2023, Phys. Rev. D, 107, 024014, doi: 10.1103/PhysRevD.107.024014

Crabb, G. 1843, Universal Technical Dictionary (Baldwin, Craddock, and Joy)

Cremonese, P., Ezquiaga, J., & Salzano, V. 2021, Physical Review D, 104, doi: 10.1103/physrevd.104.023503

Damour, T., & Nagar, A. 2014, Phys. Rev. D, 90, 044018, doi: 10.1103/PhysRevD.90.044018

de Blok, W. J. G. 2010, Advances in Astronomy, 2010, 1–14, doi: 10.1155/2010/789293

Dias, Ó. J. C., Godazgar, M., & Santos, J. E. 2022a, JHEP, 07, 076, doi: 10.1007/JHEP07(2022)076

Dias, Ó. J. C., Godazgar, M., Santos, J. E., et al. 2022b, Phys. Rev. D, 105, doi: 10.1103/physrevd.105.084044

Diego, J. M. 2020, Phys. Rev. D, 101, 123512, doi: 10.1103/PhysRevD.101.123512

Dietrich, T., Bernuzzi, S., Brügmann, B., Ujevic, M., & Tichy, W. 2018a, Phys. Rev. D, 97, 064002, doi: 10.1103/PhysRevD.97.064002

Dietrich, T., Samajdar, A., Khan, S., et al. 2019, Physical Review D, 100, doi: 10.1103/physrevd.100.044003

Dietrich, T., Radice, D., Bernuzzi, S., et al. 2018b, CQGra, 35, 24LT01, doi: 10.1088/1361-6382/aaebc0

Douchin, F., & Haensel, P. 2001, A&A, 380, 151, doi: 10.1051/0004-6361:20011402

Duane, S., Kennedy, A., Pendleton, B. J., & Roweth, D. 1987, Physics Letters B, 195, 216, doi: https://doi.org/10.1016/0370-2693(87)91197-X

Dyson, F. W., Eddington, A. S., & Davidson, C. 1920, Philosophical Transactions of the Royal Society of London. Series A, Containing Papers of a Mathematical or Physical Character, 220, 291, doi: 10.1098/rsta.1920.0009

Eardley, D. M., Lee, D. L., & Lightman, A. P. 1973a, Phys. Rev. D, 8, 3308, doi: 10.1103/PhysRevD.8.3308

Eardley, D. M., Lee, D. L., Lightman, A. P., Wagoner, R. V., & Will, C. M. 1973b, Phys. Rev. Lett., 30, 884, doi: 10.1103/PhysRevLett.30.884

Easther, R., Giblin, J. T., & Lim, E. A. 2007, Phys. Rev. Lett., 99, 221301, doi: 10.1103/PhysRevLett.99.221301

Ebersold, M., & Tiwari, S. 2020, Phys. Rev. D, 101, 104041, doi: 10.1103/PhysRevD.101.104041

Einstein, A. 1905, Annalen der Physik, 322, 891, doi: 10.1002/andp.19053221004

—. 1908, Jahrbuch der Radioaktivität und Elektronik, 4, 411

—. 1911, Annalen der Physik, 340, 898, doi: 10.1002/andp.19113401005

—. 1915a, Sitzungsberichte der Königlich Preussischen Akademie der Wissenschaften, 778

—. 1915b, Sitzungsberichte der Königlich Preussischen Akademie der Wissenschaften, 799

—. 1915c, Sitzungsberichte der Königlich Preussischen Akademie der Wissenschaften, 831

—. 1915d, Sitzungsberichte der Königlich Preussischen Akademie der Wissenschaften, 844

—. 1916, Sitzungsberichte der Königlich Preussischen Akademie der Wissenschaften, 688

Ezquiaga, J. M., & Zumalacárregui, M. 2020, Phys. Rev. D, 102, 124048, doi: 10.1103/PhysRevD.102.124048

Fan, X.-L., Liao, K., Biesiada, M., Piórkowska-Kurpas, A., & Zhu, Z.-H. 2017, Phys. Rev. Lett., 118, 091102, doi: 10.1103/PhysRevLett.118.091102

Finke, A., Foffa, S., Iacovelli, F., Maggiore, M., & Mancarella, M. 2021, Phys. Rev. D, 104, 084057, doi: 10.1103/PhysRevD.104.084057

Friel, N., & Pettitt, A. N. 2008, Journal of the Royal Statistical Society. Series B (Statistical Methodology), 70, 589. http://www.jstor.org/stable/20203843

Galilei, G. 1954, Dialogues Concerning Two New Sciences, ed. & translated by Alfonso de Salvio & Henry Crew (Dover Publications)

—. 1967, in Dialogue Concerning the Two Chief World Systems: Ptolemaic & Copernican, ed. & translated by Stillman Drake (Univeristy of California Press)

Gamba, R., Akçay, S., Bernuzzi, S., & Williams, J. 2022, Phys. Rev. D, 106, 024020, doi: 10.1103/PhysRevD.106.024020

Gelfand, A. E., & Smith, A. F. M. 1990, Journal of the American Statistical Association, 85, 398. http://www.jstor.org/stable/2289776

Geman, S., & Geman, D. 1984, IEEE Trans. Pattern Anal. Machine Intell., PAMI-6, 721, doi: 10.1109/TPAMI.1984.4767596

Ghosh, A., Ghosh, A., Johnson-McDaniel, N. K., et al. 2016, Phys. Rev. D, 94, 021101, doi: 10.1103/physrevd.94.021101

Ghosh, A., Johnson-McDaniel, N. K., Ghosh, A., et al. 2017, CQGra, 35, 014002, doi: 10.1088/1361-6382/aa972e

Gigerenzer, G., Swijitink, Z., Porter, T., et al. 1989, The Empire of Chance: How Probability Changed Science and Everyday Life (Cambridge University Press)

Giudice, G. F., McCullough, M., & Urbano, A. 2016, J. Cosmology Astropart. Phys., 2016, 001, doi: 10.1088/1475-7516/2016/10/001

Goggans, P. M., & Chi, Y. 2004, in American Institute of Physics Conference Series, Vol. 707, Bayesian Inference and Maximum Entropy Methods in Science and Engineering, ed. G. J. Erickson & Y. Zhai, 59–66, doi: 10.1063/1.1751356

Gonzalez, A., et al. 2023, CQGra, 40, 085011, doi: 10.1088/1361-6382/acc231

Goyal, S., D., H., Kapadia, S. J., & Ajith, P. 2021a, Physical Review D, 104, doi: 10.1103/physrevd.104.124057

Goyal, S., Haris, K., Mehta, A. K., & Ajith, P. 2021b, Phys. Rev. D, 103, 024038, doi: 10.1103/PhysRevD.103.024038

Goyal, S., Vijaykumar, A., Ezquiaga, J. M., & Zumalacárregui, M. 2023, Physical Review D, 108, doi: 10.1103/physrevd.108.024052

Green, P. J. 1995, Biometrika, 82, 711, doi: 10.1093/biomet/82.4.711

Gregory, P. 2005, Bayesian Logical Data Analysis for the Physical Sciences (Cambridge University Press)

Hannuksela, O. A., Collett, T. E., Çalışkan, M., & Li, T. G. F. 2020, Monthly Notices of the Royal Astronomical Society, 498, 3395, doi: 10.1093/mnras/staa2577

Hannuksela, O. A., Haris, K., Ng, K. K. Y., et al. 2019, The Astrophysical Journal Letters, 874, L2, doi: 10.3847/2041-8213/ab0c0f

Haris, K., Mehta, A. K., Kumar, S., Venumadhav, T., & Ajith, P. 2018a, Identifying strongly lensed gravitational wave signals from binary black hole mergers. https://arxiv.org/abs/1807.07062

—. 2018b, Identifying strongly lensed gravitational wave signals from binary black hole mergers. https://arxiv.org/abs/1807.07062

Hastings, W. K. 1970, Biometrika, 57, 97, doi: 10.1093/biomet/57.1.97

Herrera-Martín, A., Hendry, M., Gonzalez-Morales, A. X., & Ureña-López, L. A. 2019, The Astrophysical Journal, 872, 11, doi: 10.3847/1538-4357/aafaf0

Hubble, E. 1929a, Proceedings of the National Academy of Science, 15, 168, doi: 10.1073/pnas.15.3.168

Hubble, E. P. 1929b, ApJ, 69, 103, doi: 10.1086/143167

Hulse, R. A., & Taylor, J. H. 1975, ApJ, 195, L51, doi: 10.1086/181708

Hunter, C. 2001, Monthly Notices of the Royal Astronomical Society, 328, 839, doi: 10.1046/j.1365-8711.2001.04914.x

ISO. 2020, ISO/IEC 14882:2020: Programming languages — C++ (Geneva, Switzerland: International Organization for Standardization (ISO)), 1853

Iyer, B., Souradeep, T., Unnikrishnan, C. S., et al. 2011, LIGO-India: Proposal for an Interferometric Gravitational-Wave Observatory. https://dcc.ligo.org/LIGO-M1100296/public

Janquart, J., Hannuksela, O. A., K., H., & Van Den Broeck, C. 2021, Monthly Notices of the Royal Astronomical Society, 506, 5430, doi: 10.1093/mnras/stab1991

Janquart, J., Haris, K., Hannuksela, O. A., & Van Den Broeck, C. 2023a, Monthly Notices of the Royal Astronomical Society, 526, 3088–3098, doi: 10.1093/mnras/stad2838

Janquart, J., More, A., & Van Den Broeck, C. 2022, Mon. Not. Roy. Astron. Soc., 519, 2046, doi: 10.1093/mnras/stac3660

Janquart, J., Seo, E., Hannuksela, O. A., Li, T. G. F., & Van Den Broeck, C. 2021, The Astrophysical Journal Letters, 923, L1, doi: 10.3847/2041-8213/ac3bcf

Janquart, J., Wright, M., Goyal, S., et al. 2023b, Monthly Notices of the Royal Astronomical Society, 526, 3832, doi: 10.1093/mnras/stad2909

Jeffreys, H. 1946, Proceedings of the Royal Society of London Series A, 186, 453, doi: 10.1098/rspa.1946.0056

Johansson, F. 2017, IEEE Transactions on Computers, 66, 1281, doi: 10.1109/TC.2017.2690633

Johnson-McDaniel, N. K., Ghosh, A., Ghonge, S., et al. 2022, Phys. Rev. D, 105, doi: 10.1103/physrevd.105.044020

Johnson-McDaniel, N. K., Mukherjee, A., Kashyap, R., et al. 2020, Phys. Rev. D, 102, 123010, doi: 10.1103/PhysRevD.102.123010

Kant, I. 1981, Universal natural history and theory of the heavens, ed. & translated by Stanley L. Jaki (Scottish Academic Press)

Kepler, J. 1609, Astronomia Nova (Prague)

—. 1619, Harmonice Mundi (Linz)

Khan, S., Husa, S., Hannam, M., et al. 2016, Physical Review D, 93, doi: 10.1103/physrevd.93.044007

Kidder, L. E. 2008, Phys. Rev. D, 77, 044016, doi: 10.1103/PhysRevD.77.044016

Kostelecký, V. A., & Mewes, M. 2016, PhLB, 757, 510, doi: 10.1016/j.physletb.2016.04.040

Lai, K.-H., Hannuksela, O. A., Herrera-Martín, A., et al. 2018, Physical Review D, 98, doi: 10.1103/physrevd.98.083005

Laplace, P.-S. 1812, Théorie analytique des probabiltiés (Mme. Ve Courcier)

Li, P.-C., Lee, T.-C., Guo, M., & Chen, B. 2021, Phys. Rev. D, 104, 084044, doi: 10.1103/PhysRevD.104.084044

Liebling, S. L., & Palenzuela, C. 2023, LRR, 26, 1, doi: 10.1007/s41114-023-00043-4

LIGO Scientific Collaboration, Virgo Collaboration, & KAGRA Collaboration. 2018, LVK Algorithm Library - LALSuite, Free software (GPL), doi: 10.7935/GT1W-FZ16

Liu, A., Wong, I. C. F., Leong, S. H. W., et al. 2023, Monthly Notices of the Royal Astronomical Society, 525, 4149–4160, doi: 10.1093/mnras/stad1302

Lo, R. K. L., & Magana Hernandez, I. 2023, Phys. Rev. D, 107, 123015, doi: 10.1103/PhysRevD.107.123015

Lucey, J. R., Schechter, P. L., Smith, R. J., & Anguita, T. 2018, Monthly Notices of the Royal Astronomical Society, 476, 927, doi: 10.1093/mnras/sty243

Luo, J., Chen, L.-S., Duan, H.-Z., et al. 2016, Classical and Quantum Gravity, 33, 035010, doi: 10.1088/0264-9381/33/3/035010

Magaña Hernandez, I. 2022. https://arxiv.org/abs/2211.01272

Maggiore, M. 2008, Gravitational Waves Volume I: Theory and Experiments (Oxford University Press)

Martynov, D., Hall, E., Abbott, B., et al. 2016, Physical Review D, 93, doi: 10.1103/physrevd.93.112004

Marzola, L., Racioppi, A., & Vaskonen, V. 2017, The European Physical Journal C, 77, doi: 10.1140/epjc/s10052-017-4996-1

Matsunaga, N., & Yamamoto, K. 2006, Journal of Cosmology and Astroparticle Physics, 2006, 023–023, doi: 10.1088/1475-7516/2006/01/023

Mazur, P. O., & Mottola, E. 2004, PNAS, 101, 9545, doi: 10.1073/pnas.0402717101

Metropolis, N., Rosenbluth, A. W., Rosenbluth, M. N., Teller, A. H., & Teller, E. 1953, J. Chem. Phys., 21, 1087, doi: 10.1063/1.1699114

Mewes, M. 2019, Phys. Rev. D, 99, 104062, doi: 10.1103/physrevd.99.104062

Michelson, A. A., & Morley, E. W. 1887, American Journal of Science, 34, 333, doi: 10.2475/ajs.s3-34.203.333

Mirshekari, S., Yunes, N., & Will, C. M. 2012, Phys. Rev. D, 85, doi: 10.1103/physrevd.85.024041

Mishra, A., Krishnendu, N. V., & Ganguly, A. 2023. https://arxiv.org/abs/2311.08446

Mishra, A., Meena, A. K., More, A., Bose, S., & Bagla, J. S. 2021, Monthly Notices of the Royal Astronomical Society, 508, 4869–4886, doi: 10.1093/mnras/stab2875

Misner, C. W., Thorne, K. S., & Wheeler, J. A. 2017, Gravitation (Princeton University Press)

Mollerach, S., & Roulet, E. 2002, Gravitational Lensing and Microlensing (World Scientific), doi: 10.1142/4890

Moore, C. J., Cole, R. H., & Berry, C. P. L. 2014, Classical and Quantum Gravity, 32, 015014, doi: 10.1088/0264-9381/32/1/015014

More, A., & More, S. 2022, Mon. Not. Roy. Astron. Soc., 515, 1044, doi: 10.1093/mnras/stac1704

Nagar, A., Damour, T., Reisswig, C., & Pollney, D. 2016, Phys. Rev. D, 93, 044046, doi: 10.1103/PhysRevD.93.044046

Nagar, A., Pratten, G., Riemenschneider, G., & Gamba, R. 2020a, Phys. Rev. D, 101, 024041, doi: 10.1103/PhysRevD.101.024041

Nagar, A., Riemenschneider, G., Pratten, G., Rettegno, P., & Messina, F. 2020b, Phys. Rev. D, 102, 024077, doi: 10.1103/PhysRevD.102.024077

Nagar, A., Bernuzzi, S., Del Pozzo, W., et al. 2018, Phys. Rev. D, 98, 104052, doi: 10.1103/physrevd.98.104052

Nakamura, T. T., & Deguchi, S. 1999, Prog. Theor. Phys. Suppl., 133, 137, doi: 10.1143/ptps.133.137

Narola, H., Janquart, J., Haegel, L., et al. 2023. https://arxiv.org/abs/2308.01709

Navarro, J. F., Frenk, C. S., & White, S. D. M. 1996, The Astrophysical Journal, 462, 563, doi: 10.1086/177173

Newton, I. 1972, Philisophiæ naturalis principia mathematica, ed. Alexandre Koyré, Bernard Cohen, & Anne Whitman (Cambridge University Press)

Ng, K. K. Y., Wong, K. W. K., Broadhurst, T., & Li, T. G. F. 2018, Phys. Rev. D, 97, 023012, doi: 10.1103/PhysRevD.97.023012

Nishizawa, A. 2018, Phys. Rev. D, 97, 104037, doi: 10.1103/physrevd.97.104037

Nitz, A., Harry, I., Brown, D., et al. 2023, gwastro/pycbc: v2.2.2 release of PyCBC, v2.2.2, Zenodo, doi: 10.5281/zenodo.8340277

Okounkova, M., Farr, W. M., Isi, M., & Stein, L. C. 2022, Phys. Rev. D, 106, 044067, doi: 10.1103/physrevd.106.044067

Okounkova, M., Stein, L. C., Moxon, J., Scheel, M. A., & Teukolsky, S. A. 2020, Phys. Rev. D, 101, 104016, doi: 10.1103/PhysRevD.101.104016

Pani, P., Berti, E., & Gualtieri, L. 2013, Phys. Rev. Lett., 110, 241103, doi: 10.1103/PhysRevLett.110.241103

Payne, E., Isi, M., Chatziioannou, K., & Farr, W. M. 2023, Phys. Rev. D, 108, 124060, doi: 10.1103/PhysRevD.108.124060

Peters, P. C. 1974, Phys. Rev. D, 9, 2207, doi: 10.1103/PhysRevD.9.2207

Pompili, L., Buonanno, A., Estellés, H., et al. 2023, Laying the foundation of the effective-one-body waveform models SEOBNRv5: improved accuracy and efficiency for spinning non-precessing binary black holes. https://arxiv.org/abs/2303.18039

Pound, R. V., & Rebka, G. A. 1960, Phys. Rev. Lett., 4, 337, doi: 10.1103/PhysRevLett.4.337

Pratten, G., Husa, S., García-Quirós, C., et al. 2020, Physical Review D, 102, doi: 10.1103/physrevd.102.064001

Pratten, G., García-Quirós, C., Colleoni, M., et al. 2021, Physical Review D, 103, doi: 10.1103/physrevd.103.104056

Pretorius, F. 2005, Physical Review Letters, 95, doi: 10.1103/physrevlett.95.121101

Ptolemy. 1984, in Ptolemy's Almagest, ed. & translated by G. J. Toomer (Bristol Classical Press)

Punturo, M., Abernathy, M., Acernese, F., et al. 2010, Classical and Quantum Gravity, 27, 084007, doi: 10.1088/0264-9381/27/8/084007

Reitze, D., Adhikari, R. X., Ballmer, S., et al. 2019, Cosmic Explorer: The U.S. Contribution to Gravitational-Wave Astronomy beyond LIGO. https://arxiv.org/abs/1907.04833

Riemenschneider, G., Rettegno, P., Breschi, M., et al. 2021, Phys. Rev. D, 104, 104045, doi: 10.1103/PhysRevD.104.104045

Romero-Shaw, I. M., Talbot, C., Biscoveanu, S., et al. 2020, Monthly Notices of the Royal Astronomical Society, 499, 3295–3319, doi: 10.1093/mnras/staa2850

Schneider, P. 1996, MNRAS, 283, 837, doi: 10.1093/mnras/283.3.837

Schneider, P., Ehlers, J., & Falco, E. E. 1992, Gravitational Lenses (Springer Berlin), doi: 10.1007/978-3-662-03758-4

Schutz, B. 2009, A First Course in General Relativity; 2nd ed. (Cambridge University Press)

Schutz, B. F. 2011, Classical and Quantum Gravity, 28, 125023, doi: 10.1088/0264-9381/28/12/125023

Seo, E., Hannuksela, O. A., & Li, T. G. F. 2022, The Astrophysical Journal, 932, 50, doi: `10.3847/1538-4357/ac6dea`

Sereno, M., Jetzer, P., Sesana, A., & Volonteri, M. 2011, Monthly Notices of the Royal Astronomical Society, 415, 2773–2781, doi: `10.1111/j.1365-2966.2011.18895.x`

Shapiro, I. I. 1964, Phys. Rev. Lett., 13, 789, doi: `10.1103/PhysRevLett.13.789`

Shapiro, I. I., Pettengill, G. H., Ash, M. E., et al. 1968, Phys. Rev. Lett., 20, 1265, doi: `10.1103/PhysRevLett.20.1265`

Shapley, H. 1919, ApJ, 49, 311, doi: `10.1086/142469`

Shipman, H. L. 1975, Astrophys. Lett., 16, 9

Shiralilou, B., Hinderer, T., Nissanke, S. M., Ortiz, N., & Witek, H. 2022, CQGra, 39, 035002, doi: `10.1088/1361-6382/ac4196`

Siemonsen, N., & East, W. E. 2023, Phys. Rev. D, 108, 124015, doi: `10.1103/PhysRevD.108.124015`

Skilling, J. 2004, AIP Conference Proceedings, 735, 395, doi: `10.1063/1.1835238`

—. 2006, Bayesian Analysis, 1, 833 , doi: `10.1214/06-BA127`

Smith, G. P., Jauzac, M., Veitch, J., et al. 2018, Monthly Notices of the Royal Astronomical Society, 475, 3823, doi: `10.1093/mnras/sty031`

Speagle, J. S. 2020, MNRAS, 493, 3132, doi: `10.1093/mnras/staa278`

Srivastava, M., Chen, Y., & Shankaranarayanan, S. 2021, Phys. Rev. D, 104, 064034, doi: `10.1103/PhysRevD.104.064034`

Tahura, S., & Yagi, K. 2018, Phys. Rev. D, 98, 084042, doi: `10.1103/PhysRevD.98.084042`

Takahashi, R., & Nakamura, T. 2003, Astrophys. J., 595, 1039, doi: `10.1086/377430`

Taylor, J. H., & Weisberg, J. M. 1982, ApJ, 253, 908, doi: `10.1086/159690`

The FLINT team. 2023, FLINT: Fast Library for Number Theory

The LIGO Scientific Collaboration, The Virgo Collaboration, & The KAGRA Collaboration. 2024, Observation of Gravitational Waves from the Coalescence of a $2.5 - 4.5\ M_{\odot}$ Compact Object and a Neutron Star. `https://arxiv.org/abs/2404.04248`

Thompson, J. E., Fauchon-Jones, E., Khan, S., et al. 2020, Physical Review D, 101, doi: `10.1103/physrevd.101.124059`

Turner, M. S. 1997, Phys. Rev. D, 55, R435, doi: 10.1103/PhysRevD.55.R435

Uchikata, N., Yoshida, S., & Pani, P. 2016, Phys. Rev. D, 94, 064015, doi: 10.1103/PhysRevD.94.064015

Udall, R., Ashton, G., & Yarbrough, Z. 2022, Compact Binary Coalescence Workflow: CBCFlow, Free Software (MIT). https://git.ligo.org/cbc/projects/cbcflow

Ujevic, M., Rashti, A., Gieg, H., Tichy, W., & Dietrich, T. 2022, Phys. Rev. D, 106, 023029, doi: 10.1103/physrevd.106.023029

Van Rossum, G., & Drake, F. L. 2009, Python 3 Reference Manual (Scotts Valley, CA: CreateSpace)

Varma, V., Field, S. E., Scheel, M. A., et al. 2019, Physical Review Research, 1, doi: 10.1103/physrevresearch.1.033015

Veitch, J., & Vecchio, A. 2010, Physical Review D, 81, doi: 10.1103/physrevd.81.062003

Veitch, J., Raymond, V., Farr, B., et al. 2015, Physical Review D, 91, doi: 10.1103/physrevd.91.042003

Velho, B. 1568, Principio de vardadeira cosmographia

Venn, J. 1888, The Logic of Chance (Macmillan and Co)

Virtanen, P., Gommers, R., Oliphant, T. E., et al. 2020, Nature Methods, 17, 261, doi: 10.1038/s41592-019-0686-2

von Soldner, J. G. 1804, Berliner Astronomisches Jahrbuch, 161

Wade, L., Creighton, J. D. E., Ochsner, E., et al. 2014, Phys. Rev. D, 89, 103012, doi: 10.1103/PhysRevD.89.103012

Wagle, P., Yunes, N., & Silva, H. O. 2022, Phys. Rev. D, 105, 124003, doi: 10.1103/PhysRevD.105.124003

Walsh, D., Carswell, R. F., & Weymann, R. J. 1979, Nature, 279, 381, doi: 10.1038/279381a0

Wiener, N. 1949, Extrapolation, Interpolation, and Smoothing of Stationary Time Series: With Engineering Applications (The MIT Press), doi: 10.7551/mitpress/2946.001.0001

Wierda, A. R. A. C., Wempe, E., Hannuksela, O. A., Koopmans, L. e. V. E., & Van Den Broeck, C. 2021a, Astrophys. J., 921, 154, doi: 10.3847/1538-4357/ac1bb4

Wierda, A. R. A. C., Wempe, E., Hannuksela, O. A., Koopmans, L. V. E., & Van Den Broeck, C. 2021b, The Astrophysical Journal, 921, 154, doi: 10.3847/1538-4357/ac1bb4

Will, C. M. 1998, Phys. Rev. D, 57, 2061, doi: `10.1103/physrevd.57.2061`

—. 2014, Living Reviews in Relativity, 17, doi: `10.12942/lrr-2014-4`

Williams, D., Veitch, J., Chiofalo, M. L., et al. 2023, Journal of Open Source Software, 8, 4170, doi: `10.21105/joss.04170`

Williams, M. J., Veitch, J., & Messenger, C. 2021, Phys. Rev. D, 103, 103006, doi: `10.1103/PhysRevD.103.103006`

Wolfram Research, Inc. 2024, Mathematica. `https://www.wolfram.com/mathematica`

Wright, M., & Hendry, M. 2022, The Astrophysical Journal, 935, 68, doi: `10.3847/1538-4357/ac7ec2`

Wright, M., Hendry, M., Liu, A., Seo, E., & Wong, I. C. F. 2022, Gravelamps, Free Software (MIT). `https://git.ligo.org/mick.wright/Gravelamps`

Wright, M., Janquart, J., & Hendry, M. 2023, The Astrophysical Journal, 959, 70, doi: `10.3847/1538-4357/ad0981`

Wright, M., Janquart, J., & Johnson-McDaniel, N. 2024, Effect of Deviations from General Relativity on Searches for Gravitational Wave Microlensing and Type II Strong Lensing. `https://arxiv.org/abs/2403.08957`

Wright, T. 1750, An Original Theory or New Hypothesis of the Universe (Henry Chapelle)

Yagi, K., Stein, L. C., Yunes, N., & Tanaka, T. 2012, Phys. Rev. D, 85, 064022, doi: `10.1103/PhysRevD.85.064022`

Yang, H., Nichols, D. A., Zhang, F., et al. 2012, Phys. Rev. D, 86, 104006, doi: `10.1103/physrevd.86.104006`

Zhu, T., Zhao, W., Yan, J.-M., Gong, C., & Wang, A. 2023. `https://arxiv.org/abs/2304.09025`

Zwicky, F. 1937, Phys. Rev., 51, 290, doi: `10.1103/PhysRev.51.290`

Dying she could handle.
Dying without any answers seemed terribly cruel.

Caliban's War, James S. A. Corey